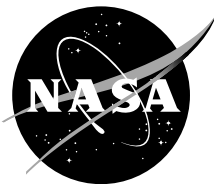


NASA/TM—2008–215466



# Heater Development, Fabrication, and Testing: Analysis of Fabricated Heaters

*S.M. Bragg-Sitton, R.E. Dickens, J.T. Farmer, J.D. Davis, M.R. Adams,  
J.J. Martin, and K.L. Webster  
Marshall Space Flight Center, Marshall Space Flight Center, Alabama*

*July 2008*

## The NASA STI Program Office...in Profile

Since its founding, NASA has been dedicated to the advancement of aeronautics and space science. The NASA Scientific and Technical Information (STI) Program Office plays a key part in helping NASA maintain this important role.

The NASA STI Program Office is operated by Langley Research Center, the lead center for NASA's scientific and technical information. The NASA STI Program Office provides access to the NASA STI Database, the largest collection of aeronautical and space science STI in the world. The Program Office is also NASA's institutional mechanism for disseminating the results of its research and development activities. These results are published by NASA in the NASA STI Report Series, which includes the following report types:

- **TECHNICAL PUBLICATION.** Reports of completed research or a major significant phase of research that present the results of NASA programs and include extensive data or theoretical analysis. Includes compilations of significant scientific and technical data and information deemed to be of continuing reference value. NASA's counterpart of peer-reviewed formal professional papers but has less stringent limitations on manuscript length and extent of graphic presentations.
- **TECHNICAL MEMORANDUM.** Scientific and technical findings that are preliminary or of specialized interest, e.g., quick release reports, working papers, and bibliographies that contain minimal annotation. Does not contain extensive analysis.
- **CONTRACTOR REPORT.** Scientific and technical findings by NASA-sponsored contractors and grantees.

- **CONFERENCE PUBLICATION.** Collected papers from scientific and technical conferences, symposia, seminars, or other meetings sponsored or cosponsored by NASA.
- **SPECIAL PUBLICATION.** Scientific, technical, or historical information from NASA programs, projects, and mission, often concerned with subjects having substantial public interest.
- **TECHNICAL TRANSLATION.** English-language translations of foreign scientific and technical material pertinent to NASA's mission.

Specialized services that complement the STI Program Office's diverse offerings include creating custom thesauri, building customized databases, organizing and publishing research results...even providing videos.

For more information about the NASA STI Program Office, see the following:

- Access the NASA STI Program Home Page at <http://www.sti.nasa.gov>
- E-mail your question via the Internet to [help@sti.nasa.gov](mailto:help@sti.nasa.gov)
- Fax your question to the NASA Access Help Desk at 301-621-0134
- Telephone the NASA Access Help Desk at 301-621-0390
- Write to:  
NASA Access Help Desk  
NASA Center for AeroSpace Information  
7121 Standard Drive  
Hanover, MD 21076-1320  
301-621-0390



NASA/TM—2008–215466



# Heater Development, Fabrication, and Testing: Analysis of Fabricated Heaters

*S.M. Bragg-Sitton, R.E. Dickens, J.T. Farmer, J.D. Davis, M.R. Adams,  
J.J. Martin, and K.L. Webster  
Marshall Space Flight Center, Marshall Space Flight Center, Alabama*

National Aeronautics and  
Space Administration

Marshall Space Flight Center • MSFC, Alabama 35812

---

*July 2008*

## **TRADEMARKS**

Trade names and trademarks are used in this report for identification only. This usage does not constitute an official endorsement, either expressed or implied, by the National Aeronautics and Space Administration.

Available from:

NASA Center for AeroSpace Information  
7115 Standard Drive  
Hanover, MD 21076-1320  
301-621-0390

This report is also available in electronic form at  
<<https://www2.sti.nasa.gov>>

## TABLE OF CONTENTS

1. INTRODUCTION—HISTORICAL THERMAL SIMULATOR DEVELOPMENT .....	1
1.1 General Requirements .....	1
1.2 Early Refractory Metal Heater Designs .....	11
2. CURRENT THERMAL SIMULATOR TESTING AND DEVELOPMENT .....	13
2.1 Refractory Metal Wire Wrapped Simulator Design .....	13
2.2 Carbon Fiber Braid Simulator Design .....	35
2.3 Sealed Thermal Simulator Configurations .....	40
2.4 Tantalum Wire Wrapped Heater Element .....	55
2.5 Tungsten Wire Wrapped Heater Element .....	59
2.6 Material Selection Criteria .....	70
2.7 Initial Conclusions from Thermal Simulator Tests .....	71
3. DEVELOPMENT OF SUPPORT HARDWARE .....	72
3.1 Gas Purification System .....	77
3.2 Water-Cooled Calorimeter .....	81
3.3 Data Acquisition System .....	87
3.4 Modified Power Interface .....	91
3.5 Component Cleaning and Chamber Preparation Procedures .....	92
4. ADVANCED THERMAL SIMULATORS: CURRENT STATUS .....	96
5. FUTURE TESTING AND DEVELOPMENT PLANS .....	100
5.1 Element Cooling Techniques .....	100
5.2 Advanced Thermal Simulator Development .....	101
6. CONCLUSIONS .....	105
APPENDIX A—GRAPHITE ROD HEATER ELEMENT .....	106
APPENDIX B—SPIRAL-WRAPPED SIMULATOR DESIGN, 0.625-IN ASSEMBLY .....	109
APPENDIX C—SPIRAL-WRAPPED SIMULATOR DESIGN, 0.400-IN ASSEMBLY .....	116

## TABLE OF CONTENTS (Continued)

APPENDIX D—TEMPERATURE-DEPENDENT RESISTIVITY OF SELECTED REFRACTORY METALS .....	121
APPENDIX E—TANTALUM HEATER ELEMENT MATERIALS ANALYSIS .....	122
APPENDIX F—RHENIUM HEATER ELEMENT MATERIALS ANALYSIS .....	136
APPENDIX G—KEY GOVERNING EQUATIONS AND SUPPORTING FORMULATIONS .....	149
APPENDIX H—THERMAL CROSS-SECTION CALCULATIONS .....	152
APPENDIX I—SINDA RESULTS: TEMPERATURE PROFILES .....	168
APPENDIX J—THERMAL ANALYSIS: CALORIMETER .....	172
APPENDIX K—THERMOCOUPLE THERMAL ERROR ANALYSIS .....	181
APPENDIX L—DESIGN DRAWINGS: MODIFIED POWER INTERFACE .....	187
APPENDIX M—BASIC MATERIAL CLEANING PROCEDURES .....	191
APPENDIX N—PURIFIED INERT GAS CONDITIONING .....	195
APPENDIX O—ADVANCED HEATER ELEMENT DESIGNS: CHANGING POWER PROFILE.....	198
APPENDIX P—ADVANCED HEATER ELEMENT DESIGNS: HEXAGONAL CROSS SECTION .....	202
REFERENCES .....	204

## LIST OF FIGURES

1.	Graphite rod heater element: (a) sketch and (b) photograph .....	3
2.	Graphite rod heater elements: (a) Batch of graphite rod heater elements and (b) identification of center taper geometry and power input design via Mo leads .....	5
3.	Integration of 48 simulators in SAFE 30 ( $\approx$ 23- by 20-cm ( $\approx$ 9- by 8-in) footprint) .....	7
4.	Integration of 183 simulators in SAFE 100 ( $\approx$ 26- by 29-cm ( $\approx$ 10.4- by 11.5-in) footprint) .....	7
5.	Integration of 57 simulators in SAFE 100a ( $\approx$ 18- by 16.5-cm ( $\approx$ 7- by 6.5-in) footprint) .....	7
6.	Integration of 37 simulators in DDG test article ( $\approx$ 16- by 18-cm ( $\approx$ 6.25- by 7.1-in) footprint). (Note: This core is inserted into a pressure vessel where the wires are not accessible after test article integration) .....	8
7.	Core face seal unit as configured for testing: (a) assembly on the test stand and placement of feedthroughs, (b) conflat style front cover plate, and (c) complete test configuration (without insulation shown) .....	9
8.	Integration of power with the LM core design using a core face seal concept: (a) core face seal extension showing power feedthroughs and (b) identification of ‘fuel tubes’ that house the resistive heater elements .....	10
9.	General configuration of the hairpin heater element design .....	11
10.	Generalized assembly configuration (not shown to scale) .....	22
11.	Test of W heater element at 3 kW (a) early in test and (b) later in test, revealing a spectral shift .....	23
12.	Alumina mandrel after removal of W wire, revealing (a) significant surface discoloration and (b) close-up view of contamination .....	25
13.	Test of Re heater element at (a) 5 kW and (b) 1.2 kW .....	26
14.	Posttest Al <sub>2</sub> O <sub>3</sub> mandrel (a) before and (b) after removal of Re wire, revealing slight surface discoloration .....	27

## LIST OF FIGURES (Continued)

15.	Tungsten wire-braid heater element wrapped on a 1.04-cm (0.410-in) $\text{Al}_2\text{O}_3$ mandrel. Close-up views are provided for (a) the power input end, (b) the nonpower end, showing wire wrap return for double helix configuration, and (c) the center section showing the five-wire braid .....	29
16.	Approximate TC locations on the Mo sheath .....	29
17.	Approximate two-dimensional model applied for W wire element thermal analysis (not to scale) .....	31
18.	Braid/mandrel/sheath geometry: (a) Annotated layout and (b) finite element model of determination of conduction shape factors .....	32
19.	Double-ended C fiber braid trail: configuration for rough checkout tests .....	36
20.	Carbonized C fiber braid wrapped in a double helix fashion around $\text{Al}_2\text{O}_3$ mandrel .....	37
21.	Basic configuration of the proposed heater/sheath geometry (not to scale) .....	43
22.	Approximate geometry used in the SINDA model .....	47
23.	Axial temperature profile for case 2 .....	52
24.	Axial temperature profile for case 3 .....	53
25.	Wire transition from the spiral wrap at end of mandrel (complete mandrel design with dimensions is included in figure 65) .....	55
26.	Posttest TA heater assembly showing wire failure .....	56
27.	Initial test data for a 0.5-mm (0.020-in) TA three-wire braid heater element in a He environment (the element failed at the start of the subsequent test day) .....	57
28.	Tantalum heater element power and resistance on subsequent test days for 0.64-mm (0.025-in) three-wire braid: (a) initial test data, July 1, 2005, and (b) final test data, July 5, 2005 .....	58
29.	Tantalum heater element power and resistance on the initial and final test days for 0.5-mm (0.020-in) three-wire braid: (a) initial test data, July 6, 2005, and (b) final test data, July 19, 2005 .....	60

## LIST OF FIGURES (Continued)

30.	Tungsten wire heater assembly—testing in a vacuum environment: (a) End view of element during test and (b) side view of element during test .....	61
31.	Mandrel distortion due to excessive heating .....	61
32.	Initial test data (day 1) for W three-wire braid: (a) Heater power chamber pressure and (b) element resistance and measured chamber and mandrel temperatures .....	62
33.	Final test data for W three-wire braid, 89–100 hr: (a) Heater power and chamber pressure and (b) element resistance and measured chamber and mandrel temperatures .....	63
34.	Test setup with sheathed heater element fitted inside a water-cooled calorimeter .....	64
35.	Initial and final test data for 0.25-mm (0.010-in) three-wire braided W element: (a) Initial test data, July 25, 2005, and (b) final 13 hours of test, August 8, 2005. Plots show total power delivered to the heater element and the calculated element resistance .....	65
36.	Test data for 0.25-mm (0.010-in) five-wire W braid (August 25–29, 2005) .....	66
37.	Test data for 0.25-mm (0.010-in) five-wire braid (Test 1, September 13–16, 2005) .....	67
38.	Test data for 0.25-mm (0.010-in) five-wire braid (Test 2, September 16–20, 2005) .....	68
39.	Test data for 0.25-mm (0.010-in) five-wire braid (Test 3, September 16–26, 2005). Data were broken into two separate plots due to limitations in Microsoft Excel plotting features: (a) Test data, 0–84 hr and (b) test data, 84–140 hr .....	69
40.	Color optical pyrometer setup .....	74
41.	Closeup of Mo heater .....	74
42.	Sample long-term pyrometer data .....	75
43.	Sample data with oxidation .....	76
44.	Test chamber gas mixture and purification system .....	78
45.	Inert gas purification system connected to test chamber .....	80
46.	Heater element calorimeter layout .....	82

## LIST OF FIGURES (Continued)

47.	Calorimeter coil fabrication tests .....	83
48.	Spring-loaded TC unit .....	84
49.	Calorimeter test chamber .....	85
50.	Calorimeter instrumentation .....	85
51.	LabVIEW thermal simulator application .....	88
52.	LabVIEW strip-chart application .....	89
53.	LabVIEW multigauge server .....	89
54.	Flowmeters: (a) LabVIEW gas flowmeter server and (b) installed thermal mass flowmeter .....	90
55.	LabVIEW data recorder .....	90
56.	Power interface for the DDG-cooled reactor tests .....	91
57.	Modified power interface conceptual design, using 37-pin DDG as a baseline concept .....	92
58.	Heater element placement inside DDG core block and TCs would be embedded in the Al <sub>2</sub> O <sub>3</sub> spacer region .....	98
59.	Thermocouple location on graphite heater element for preliminary testing .....	99
60.	Generalized simulator assembly with core block: cross-sectional view (not to scale) .....	100
61.	Heater element with a shifting axial power profile .....	104
62.	Mandrel design for a heater element with a hexagonal cross section .....	104
63.	Varying diameter graphite rod heater element, 0.375-in OD .....	107
64.	Constant diameter graphite rod heater element, 0.305-in OD .....	108
65.	Mandrel, 0.625-in assembly design .....	110



## LIST OF FIGURES (Continued)

66.	Coupler, 0.625-in assembly design .....	111
67.	Sheath, 0.625-in assembly design .....	112
68.	Endcap, 0.625-in assembly design .....	113
69.	Endcap assembly, 0.625-in assembly design .....	114
70.	Full assembly, 0.625-in assembly design .....	115
71.	Mandrel, 0.400-in assembly design .....	117
72.	Coupler, 0.400-in assembly design .....	118
73.	Endcap, 0.400-in assembly design .....	119
74.	Sheath, 0.400-in assembly design .....	120
75.	Resistivity of selected refractory metals as a function of temperature (data obtained from R. Kapernick, Los Alamos National Laboratory) .....	121
76.	Thermal conductivity of selected gases .....	152
77.	Axial temperature profile for case 1 .....	169
78.	Axial temperature profile for case 2 .....	169
79.	Axial temperature profile for case 3 .....	170
80.	Axial temperature profile for case 4 .....	170
81.	Axial temperature profile for case 5 .....	171
82.	Axial temperature profile for case 6 .....	171
83.	Cold wall/calorimeter primary tube and fluid circuit .....	174
84.	Predicted cold wall temperatures for the case of 6,000 W, He atmosphere, 19 L/min (5 gal/min) water flow .....	175
85.	Water temperatures for the case of 6,000 W, He atmosphere, 19 L/min (5 gal/min) water flow .....	176

## LIST OF FIGURES (Continued)

86.	Sheath temperature profile for the case of 6,000 W, He atmosphere, 19 L/min (5 gal/min) water flow .....	177
87.	Heater temperature profile for the case 6,000 W, He atmosphere, 19 L/min (5 gal/min) water flow .....	178
88.	Temperature vs. axial position for the sheath, heater, and cold wall for the case of 6,000 W, He atmosphere, 19 L/min (5 gal/min) water flow. (Axial position is the position along the longitudinal axis of the heater/sheath and zero represents the end of the cold wall) .....	179
89.	Temperature profile for TC error model; temperature profile corresponds to a bead contact conductance of 0.02 W/°C .....	183
90.	Close-up view of exposed TC wires in vicinity of the sheath and primary tube cold wall; temperature profile corresponds to a bead contact conductance of 0.02 W/°C .....	184
91.	Close-up view of conductor between the TC bead and sheath wall; temperature profile corresponds to a bead contact conductance of 0.02 W/°C .....	185
92.	Comparison of TC error versus bead contact conductance .....	186
93.	Cross-sectional view showing heater element pin formation for modified power interface .....	187
94.	Modified (conceptual) power interface showing positive and negative leads to heater element power terminals .....	188
95.	Modified power terminal connections for a single pin .....	189
96.	Modified power terminal connections for a single pin; axial view .....	189
97.	Modified power interface conceptual design showing series connection between neighboring pins .....	190
98.	Oxygen concentration (ppm by volume) in the heat pipe test chambers following successive dilutions with (a) UHP He or (b) UHP Ar fill gas .....	196
99.	Conceptual design, varying power profile .....	199
100.	Conceptual design, varying power profile .....	200

## LIST OF FIGURES (Continued)

101.	Conceptual design, varying power profile .....	201
102.	Conceptual design for hexagonal cross section, spiral-wound mandrel heater element .....	203

## LIST OF TABLES

1.	Identification of basic thermal simulator design requirements .....	3
2.	Thermal simulator test matrix: current status .....	14
3.	Maximum calculated element resistance at 140 V compared to measured resistance values at prescribed power levels .....	19
4.	Summary of resistance calculated for select refractory metal wires at 20 °C .....	20
5.	Measured sheath temperatures (K) for the braided W wire heater assembly. (The first temperature entry corresponds to the beginning of the test, the and the second to the end of the test) .....	30
6.	Calculated mandrel, wire, and sheath temperatures for the braided W wire thermal simulator .....	33
7.	Estimated costs* for additional heater element wire .....	34
8.	Effective gap conductance for different inert gases based on geometry depicted in figure 22 (radial gap size: 0.15-cm (0.058-in) properties at 1,273 K) .....	45
9.	Relative effect of radiation and gas conduction for baseline simulator geometry .....	46
10.	Thermal performance of combinations of optical property enhancements (assuming radiation heat transfer only) .....	47
11.	Performance of conductive gap filler concepts .....	48
12.	Impact of the sheath on heater temperatures experienced in vacuum testing .....	49
13.	Summary results from SINDA heater simulation (temperatures are in K) .....	51
14.	Suggested materials test matrix. (Work would entail an initial literature review to assess potential compatibility issues at certain test temperatures and durations, followed by testing of combinations of interest) .....	70
15.	SAES MonoTorr phase II 3000 performance guarantee for rare gases .....	79
16.	Desired advanced thermal simulator characteristics .....	102

## LIST OF TABLES (Continued)

17.	Summary of results from SINDA heater simulation (temperatures are given in Kelvin) .....	168
18.	Comparison of temperatures for various atmospheres and conditions .....	180
19.	Bounding contact coefficient and conductance between TC bead and sheath surface .....	181

## LIST OF ACRONYMS AND SYMBOLS

Al	aluminum
Al <sub>2</sub> O <sub>3</sub>	alumina
AlN	aluminum nitrate
Al-Ta	aluminum-tantalum
Ar	argon
BN	boron nitride
C	carbon
CH <sub>4</sub>	methane
Cl	chlorine
CO	carbon monoxide
CO <sub>2</sub>	carbon dioxide
CTE	coefficient of thermal expansion
Cu	copper
CVD	chemical vapor deposition
DDG	direct drive gas
EDS	Energy Dispersive Spectroscopy
EFF-TF	Early Flight Fission Test Facility
EWI	Edison Welding Institute
FBG	fiber Bragg grating
FEM	finite element model
FESEM	Field Emission Scanning Microscope
FLUINT	Fluid Integrator

## LIST OF ACRONYMS AND SYMBOLS (Continued)

GC	gas cooled
GHe	gaseous helium
H <sub>2</sub>	hydrogen gas
HCl	hydrochlorine
He	helium
Hf	hafnium
HF	hydrofluoric acid
HF/HNO <sub>3</sub>	aqua emporis
H <sub>2</sub> O	water
H <sub>2</sub> O <sub>2</sub>	hydrogen peroxide
HP	heat pipe
ID	inner diameter
IR	infrared
LM	liquid metal
Mo	molybdenum
MRI	Materials Research Institute
MSFC	Marshall Space Flight Center
MWt	mega-watt thermal
N	nitrogen
N <sub>2</sub>	nitrogen gas
Na	sodium
NaOH	sodium hydroxide
Nb	niobium
NB-1%Zr	niobium-zirconium

## LIST OF ACRONYMS AND SYMBOLS (Continued)

Ni	nickel
NRPCT	Naval Reactors Prime Contractor Team
N <sub>2</sub>	nitrogen gas
O <sub>2</sub>	oxygen gas
OD	outer diameter
ORNL	Oak Ridge National Laboratory
PPF	power peaking factor
Re	rhenium
Re <sub>2</sub> O <sub>7</sub>	rhenium oxide
RGA	residual gas analyzer
SAFE	safe, affordable fission engine
SBIR	small business innovative research
SINDA	Systems Improved Numerical Differencing Analyzer
SLIM	standard liters per minute
SP	space power
Ta	tantalum
TC	thermocouple
TF	trichlorotrifluorethane
TIG	tungsten inert gas
TM	Technical Memorandum
UDP	user datagram protocol
UHP	ultra-high purity
VPS	vacuum plasma spray
W	tungsten
Xe	xenon



## NOMENCLATURE

$A$	area
$C_P$	specific heat
$D$	diameter
$E$ or $\varepsilon$	emissivity function
$f$	factor of exchange
$I$	current
$k$	conductivity
$L$	length of gap
$l$	length of wire
$N$	number of surfaces
$P$	power
$Q$	heat transfer; input power
$R$	resistance
$S$	conductive shape factor
$T$	temperature
$V$	voltage
$\sigma$	Stefan-Boltzman constant
$\rho$	density
$r$	resistivity



## TECHNICAL MEMORANDUM

### HEATER DEVELOPMENT, FABRICATION, AND TESTING: ANALYSIS OF FABRICATED HEATERS

#### 1. INTRODUCTION—HISTORICAL THERMAL SIMULATOR DEVELOPMENT

The thermal simulators (highly designed heater elements) developed at the NASA Marshall Space Flight Center (MSFC) Early Flight Fission Test Facility (EFF-TF) are used to simulate the heat from nuclear fission in a variety of reactor concepts. When inserted into the reactor geometry, the purpose of the thermal simulators is to deliver thermal power to the test article in the same fashion as if nuclear fuel were present. Considerable effort has been expended to mimic heat from fission as closely as possible. To accurately represent the fuel, the simulators should be capable of matching the overall properties of the nuclear fuel rather than simply matching the fuel temperatures. This includes matching thermal stresses in the pin, pin conductivities, total core power, and core power profile (axial and radial).

##### 1.1 General Requirements

The initial development of the simulators was driven by past space reactor work and bounding parameters were purposely chosen to be as challenging as possible. For example, the target pin diameter was selected based on the previously developed space power-100 (SP-100) space reactor fuel. This would require simulator sizes to be as small as 0.648 cm (0.255 in) in diameter. Peak thermal simulator power was based on a very high core thermal power (>2 MW thermal (MWt)). Additionally, the simulators must be isolated from the core to prevent electrical shorting and to prevent contamination of the test article by the simulator at high temperatures (due to sublimation, outgassing, etc.). Operational requirements for the thermal simulators incorporate desired lifetime, thermal cycling, and test environment. The development path for the EFF-TF thermal simulators required that the simulators withstand thousands of hours of operation and hundreds of thermal (on/off) cycles. The simulators were also required to operate in a vacuum environment ( $\approx 0.1$  to  $10^{-4}$  Pa;  $\approx 10^{-3}$  to  $10^{-6}$  torr) in the initial simulator checkout testing or in the presence of a low-pressure, high-purity gas (helium (He), carbon dioxide (CO<sub>2</sub>), Argon (Ar), etc.) environment.

Significant development was required to determine the best method of providing an electrical hookup to the thermal simulators in all reactor concepts. For the heat pipe- (HP-) cooled reactor concept, the simulator leads/power input are not required to penetrate a pressure vessel, making hookup much easier to accomplish. However, for both the pumped liquid metal- (LM-) cooled and direct gas-cooled (GC-) reactor concepts, power feedthroughs (or the heater/sheath assembly in the LM system) must penetrate a pressure vessel to provide power to the simulators. In addition, if the simulator leads penetrate into a LM system, then the simulators must be configured to be compatible with the LM both from a materials and an electrical standpoint. This becomes increasingly difficult given the electrical conductivity and chemical activity of the LM, which can lead to heater shorting or the introduction of impurities into the system. The electrical leads on the simulators must be designed to not be larger (radial footprint) than the simulator itself. Due to the large number of simulators that must be integrated in a relatively small footprint (as many as 400 in a 38- by 38-cm (15- by 15-in) footprint), the design of the simulator must also be incorporated with the core layout and integration process.

As in most hardware development programs, cost was also a major driver in the development of the thermal simulators used in past electrically heated reactor testing programs at the EFF-TF. The development goal was to produce complete heater assemblies at a cost of less than \$1,000 per simulator; however, this goal may not be achievable for all concepts as the total simulator cost is highly dependent on materials and operating requirements.

Because each reactor concept has different requirements (pin power, axial power profile, operating environment, etc.), a single simulator design may not meet the needs of each test concept. Instead, each reactor concept must be approached individually, taking into account the basic requirements for the simulator and integration into the core. A decision can then be made for each concept, selecting the lowest cost design that is technically acceptable. For example, although the team strove to develop simulators with a 0.648-cm (0.255-in) diameter, the safe, affordable fission engine (SAFE) 100 core did not require this small simulator size. (The SAFE 100 HP-cooled reactor concept has a fuel tube clad with an inside diameter (ID) of 1.4 cm (0.55 in).) Using this approach, a graphite heater with alumina ( $\text{Al}_2\text{O}_3$ ) spacers (used to fill the gap between the graphite and the internal clad surface, providing electrical isolation and centering the simulator within each fuel tube) was selected for the SAFE 100 test series because it was able to meet the technical requirements of the test plan at a cost of \$200 per heater.

Each new reactor concept that is investigated maintains the basic parameter set identified in table 1 when selecting an appropriate simulator design. A successful simulator does not have to meet all of these parameters simultaneously, but may require a subset for a specific application.

Table 1. Identification of basic thermal simulator design requirements.

Parameter	Target Requirement
Temperature	1,400 K (clad)
Linear heat rate	≈100 W/cm (power per length)
Power density	≈100 W/cm <sup>3</sup>
Lifetime	10,000+ hours (per simulator, tested individually or in the reactor core concept)
Number of thermal cycles	200 or more (cycles to full temperature and power)
Axial power profile	Average pin power peaking of 1.33, cosine distribution
Simulator diameter	≈0.65 cm (0.255 in) and up The fundamental minimum size achievable for a given design is limited by the area available for power hookup and the number of pins that must be connected in a relatively small footprint.
Pin conductivity	Match effective fuel pin conductivity— design/age dependent
Pin voltage	≤150 Vdc to avoid voltage breakdown in low-pressure environment
Electrical connections	Single ended (power access to only one end of the heater)
Fabrication repeatability	Simulator concepts must be sufficiently robust so that minor changes in materials, impurities, or process do not significantly affect lifetime or performance of the simulator
Number of pins	≈200 to 500 (per concept/core footprint, operating simultaneously)
Operating environment	Vacuum, CO <sub>2</sub> , GHe, Ar, N <sub>2</sub>
Compatibility	Thermal simulators must not introduce any significant impurities into the test article

To simplify insertion in each reactor test article and to minimize the impact of the thermal simulators on the ability to achieve a prototypic nonnuclear test article, a single-ended heater design was selected for use at the EFF-TF. The graphite rod essentially acts as a large resistor, with the rod itself axially split down the middle. Power is input at one end of the graphite, and current flows along the length of the rod, returning along the opposite half. This configuration is sketched in figure 1(a). Alumina pieces are inserted along the center of the two halves of graphite to prevent contact, which would short the element. Additional Al<sub>2</sub>O<sub>3</sub> insulator rings are used at three points along the length of the graphite heater element to electrically isolate the heater from the test article. A photograph of the complete graphite heater assembly is provided in figure 1(b).

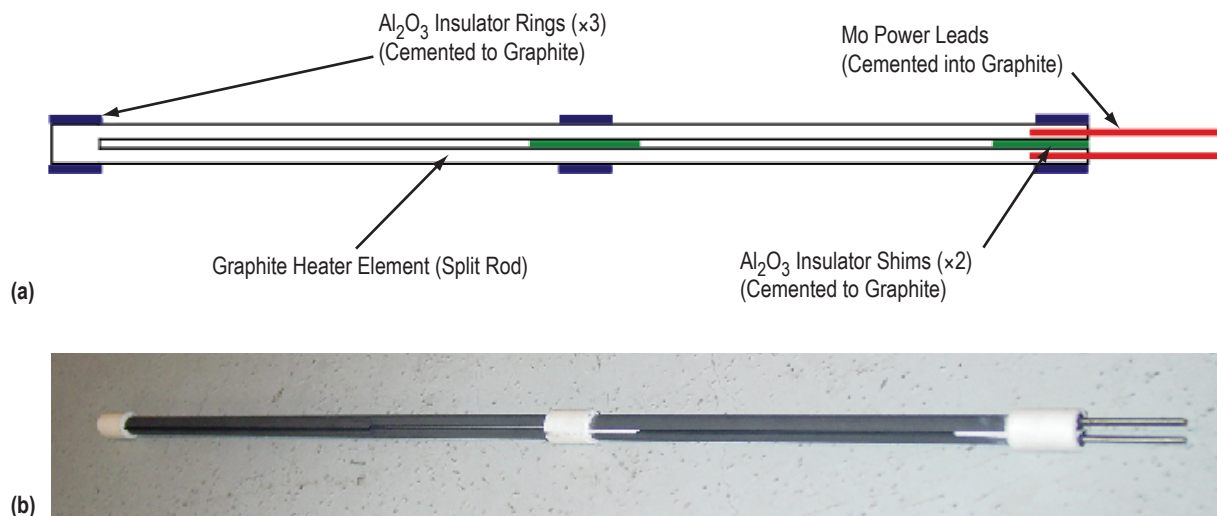


Figure 1. Graphite rod heater element: (a) Sketch and (b) photograph.

In a single-ended design, both power input and output are at the same end of the heater element. To connect the power to the element, molybdenum (Mo) couplers are cemented directly into the graphite rod using graphite cement. The coupler reduces the resistance from the interface back to the power source to ensure that a majority of the input power goes into the heater itself. The coupler serves three purposes:

- (1) It acts as the interface to the hot heater wire.
- (2) It reduces the resistance between the power supply and the heater element as a result of its material properties.
- (3) It lowers the temperature seen by the copper (Cu) lead wires. (The magnitude of the reduction is based on the length of the coupler pieces.)

The cold resistance (at room temperature) of the 0.95-cm (0.375-in) graphite rod is  $\approx 1 \Omega$ . As the graphite heats up, it initially decreases in resistance, reaching a minimum of  $\approx 0.5 \Omega$ ; the resistance again increases as temperature further increases, but never fully recovers to the room-temperature resistance. The characteristic full-load impedance of the power supply used to power the heater element is  $1.5 \Omega$ , therefore, when a single element is powered by the power supply, it operates in a current-limited fashion. To increase the resistance in the test article, the graphite rod heaters can be connected in series. Power supply use is most efficient when the resistance of the load matches the impedance of the power supply, allowing operation up to the full voltage and current capabilities of the supply (150 V, 100 A).

Graphite rod heaters can be designed to provide a flat axial power profile or a prescribed, shaped (cosine) axial power distribution. Constant diameter heaters provide uniform heat flux along their length. By cutting out a portion of the graphite along the axial center of the heater (using either a tapered cut or a squared-off cutout along a portion of the heater length), the power profile can be made to simulate that of an operating reactor. The initial set of varying diameter heaters had a 0.33-cm (0.130-in) diameter along a 10.2-cm (4.0-in) section at the axial center of the heater (engineering schematic provided in app. A). This degree of variation was adequate to show that anticipated requirements could be met. Tests have been conducted at the EFF-TF using both constant and varying diameter graphite rod heaters. Total operating hours (combined time of all individual simulators in all tests) for these simulators is in excess of 20,000 hr and hundreds of thermal cycles and a single set of three graphite rod heaters used in cyclic testing of a sodium HP performed well over 280 thermal cycles and no graphite rod heater has failed in any test to date. Figure 2 shows typical graphite elements with a varying axial power profile (center taper). To measure the temperature of the heater element at power, a type C thermocouple (TC) was sandwiched between layers of synthetic sapphire ( $\text{Al}_2\text{O}_3$  having a single crystal structure versus a multicrystal structure) and was inserted at the axial center of the graphite rod, between the split halves of the element. The measured element temperature was  $\approx 2,275 \text{ K}$  at 5 kW in a vacuum environment.

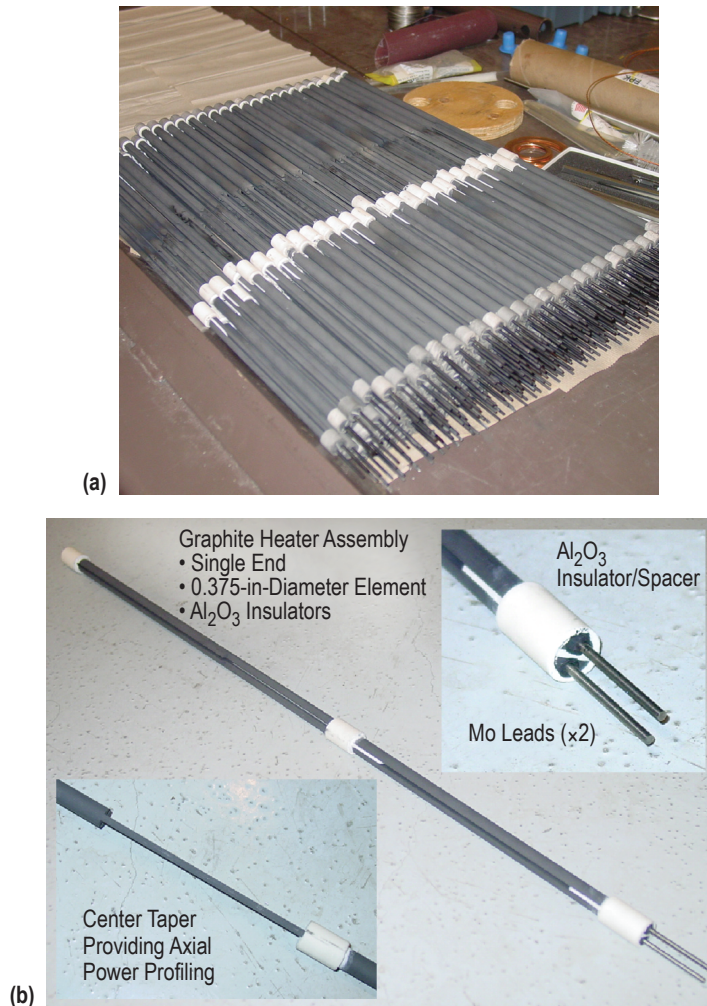


Figure 2. Graphite rod heater elements: (a) Batch of graphite rod heater elements and (b) identification of center taper geometry and power input design via Mo leads.

To date, all tests using the graphite rod heater elements have been 0.95 cm (0.375 in) in diameter (constant or varying), using 1.36-cm (0.535-in)  $\text{Al}_2\text{O}_3$  insulator rings to provide electrical isolation from the test article (1.37-cm (0.540-in) fuel tube ID). A more recent graphite rod element design reduces the graphite diameter from 0.95 to 0.77 cm (0.375 to 0.305 in), with the outer diameter (OD) of the  $\text{Al}_2\text{O}_3$  insulating rings of 1 cm (0.410 in). The overall length of the graphite element is 59.7 cm (23.5 in). These reduced diameter elements will be employed in the 37 pin LM-cooled reactor design that is currently being prepared for test at the EFF-TF. As will be discussed in a later section, the power integration into the LM design ensures that alkali metal cannot contact the thermal simulator. Detailed design drawings of the graphite heater elements are included in appendix A.



The minimum diameter that can be achieved for graphite elements is limited. The current design requires that the Mo couplers (0.32-cm (0.125-in) OD) be screwed directly into the graphite element, and reducing the total element diameter to much less than 0.77 cm (0.305 in) presents additional concerns in how to integrate the power. An alternate coupler design might allow the coupler cap to slip over the outside of the heater element to integrate the parts, but no design has been completed. The strength of the graphite material at reduced diameters also presents a concern, and the manufacturer of the graphite elements (POCO Graphite, Inc.) is reluctant to produce elements of significantly reduced diameter. The current design for the shaped graphite heater elements reduces the diameter of the element to just 0.33 cm (0.130 in) for the center and 10.2 cm (4 in) along the element's length. A reduced diameter graphite element may not have sufficient material to allow for axial shaping, although this is being investigated further.

To date, over 350 of these graphite rod simulators have been fabricated and tested with zero failures occurring within the element itself. In some cases, simulator refurbishment was required to reinstall power leads after multiple test cycles. This led to a redesign of the method of attaching the leads to the simulator elements in order to increase their strength over long periods of testing. The constant diameter graphite rod heater elements were used in the HP-cooled SAFE 30 kW thermal (kWt) test series (0.95-cm- (0.375-in-) OD elements) and will be used in the test circuit for the 37 pin liquid metal-cooled reactor design (0.77-cm- (0.305-in-) OD elements). The varying diameter graphite rod heater elements were used in the SAFE 100 (100 kWt) test article, the SAFE 100a test article (partial array HP core with gas flow heat exchanger), and the 37 pin direct drive gas- (DDG-) cooled test article. See VanDyke et al.,<sup>1-5</sup> VanDuyn et al.,<sup>6</sup> Godfroy et al.,<sup>7</sup> and Bragg-Sitton and Forsbacka<sup>8</sup> for additional details on some of these systems.

The electrical integration of the heater elements (thermal simulators) into the reactor core test article has evolved significantly from their introduction in the SAFE 30 test article to their use in the GC reactor design and their planned integration into the LM-cooled design. Integration is a function of the reactor type and operating environment. Simplifying the integration process continues to improve by using more flexible wire for power inputs and by developing a capability to more easily change out a control zone. The lessons learned from one reactor concept are typically applicable to other concepts. In developing an electrical interface to the core, it is important to take into account the total number of heater elements that must be powered in a relatively small footprint, where complexity significantly increases as the pin size is reduced and the total number of pins increases. Figures 3 through 6 show the integration of the thermal simulators in various core configurations.



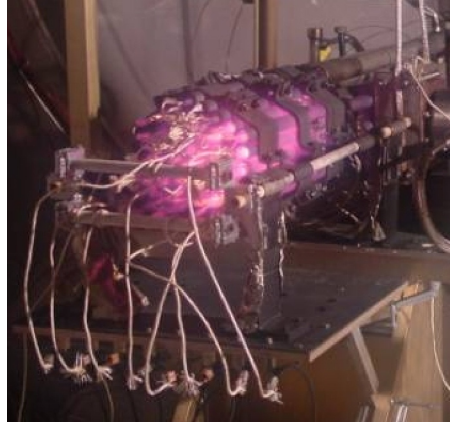


Figure 3. Integration of 48 simulators in SAFE 30 ( $\approx 23$ - by  $20$ -cm ( $\approx 9$ - by  $8$ -in) footprint).

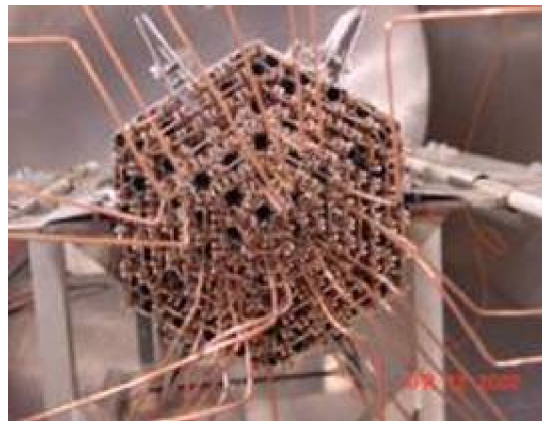


Figure 4. Integration of 183 simulators in SAFE 100 ( $\approx 26$ - by  $29$ -cm ( $\approx 10.4$ - by  $11.5$ -in) footprint).

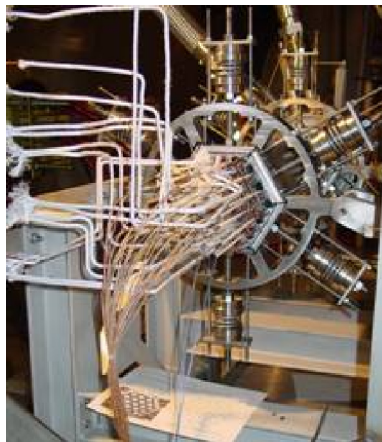


Figure 5. Integration of 57 simulators in SAFE 100a ( $\approx 18$ - by  $16.5$ -cm ( $\approx 7$ - by  $6.5$ -in) footprint).

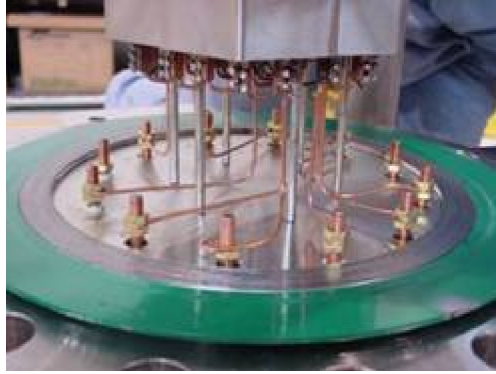


Figure 6. Integration of 37 simulators in DDG test article ( $\approx 16$ - by  $18$ -cm ( $\approx 6.25$ - by  $7.1$ -in) footprint). (Note: This core is inserted into a pressure vessel where the wires are not accessible after test article integration.)

The DDG reactor concept uses an electrical interface configuration that can be sealed after core integration and ‘flooded’ with gaseous helium (GHe) to fill the gaps between the thermal simulators and the clad, where the ‘clad’ is the inner surface of the test article (also referred to as a ‘fuel tube’). A proof-of-concept configuration experiment for a core face seal that would be integrated with an HP reactor design is shown in figure 7. Since this unit was not planned for test with an actual core, the design includes a series of heaters mounted along the back plane to provide a heat source (core simulator). The electrical connections enter from the side allowing front access to complete the integration process. A ‘flange’ would be sealed on the front of the apparatus and gas would be supplied through the top. Note that the back plate of the fixture simulated a core in this experiment. The actual back plate would be removed and the apparatus sealed around a lip of the core.

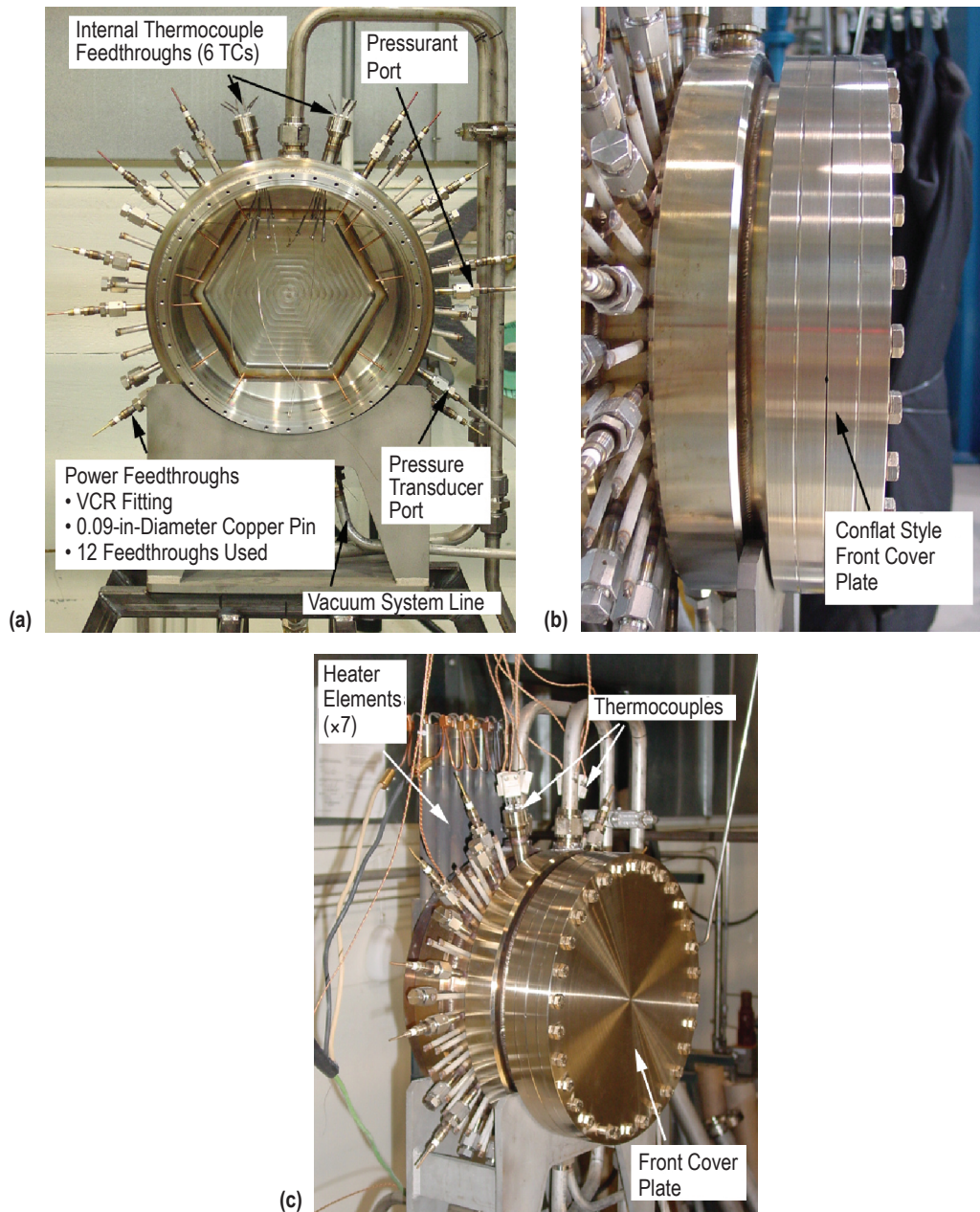


Figure 7. Core face seal unit as configured for testing: (a) assembly on the test stand and placement of feedthroughs, (b) conflat style front cover plate, and (c) complete test configuration (without insulation shown).

The core face seal concept is being implemented in the LM-cooled reactor concept that is being prepared for testing at the EFF-TF (see fig. 8). Due to the electrical conductivity of the LM, the power leads cannot be in contact with the coolant. To prevent the heaters from shorting, the fuel clad structure in the stainless steel test article was extended through the plenum. Each tube was then welded to the face seal to prevent leakage. With this configuration, the heaters could then be installed into each fuel tube without contacting the liquid metal flow.



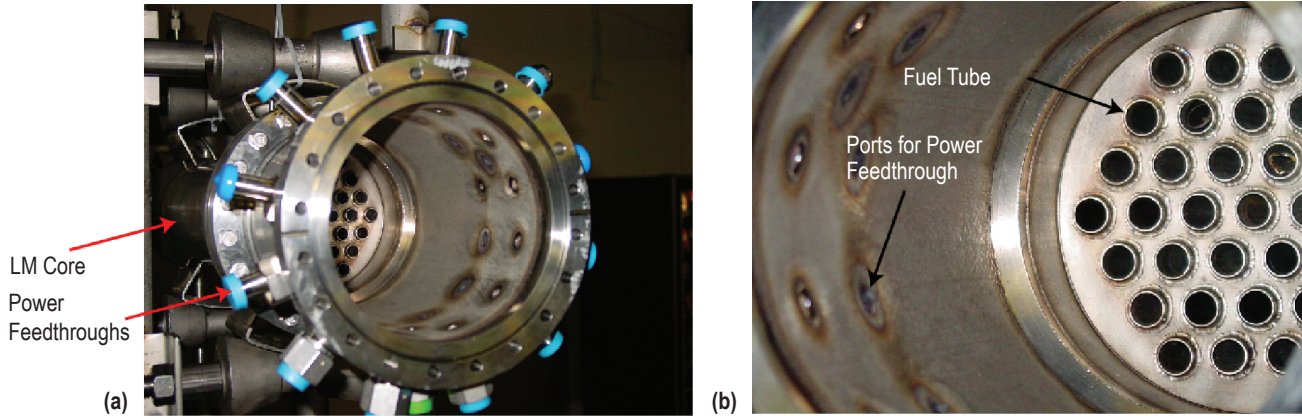


Figure 8. Integration of power with the LM core design using a core face seal concept: (a) core face seal extension showing power feedthroughs and (b) identification of fuel tubes that house the resistive heater elements.

Not only are improvements constantly being made to simplify integration, but investigation is also ongoing to determine how to better match thermal pin diffusivity (where diffusivity is calculated as the conductivity divided by the product of the density and heat capacity), among other properties, to that of nuclear fuel without affecting the test article. Steady state and dynamic thermal properties of the pin could be better matched to that of a nuclear fuel pin by modification of the complete heater element design. A proof-of-concept test using an updated graphite heater element design is currently being investigated. In this concept, the heater is sealed within a stainless steel tube using a high-temperature braze, backfilled with GHe, and then electrical leads are attached. If successful, this complete thermal simulator assembly will not only be a demonstration of the manufacturing process developed to fabricate the heater elements, but it will also demonstrate the ability of sealing an element within a tube identical to the cladding of the core structure (stainless steel, in the SAFE 100a case), ensuring there will be no material incompatibility between the simulator and the core. The first application makes use of a stainless steel sheath at relatively large pin diameters (0.95 cm (0.375 in) for the graphite rod, and 1.4 cm (0.540 in) for the sheath OD) to prove the manufacturing concept. In general, if the sealing method works with stainless steel, then a similar approach can be applied to refractory metal (Mo) or other metal alloy sheaths/tubes. After a lengthy series of testing on the stainless steel/graphite assembly, the design can be updated to accommodate the desired materials. Thermal analyses of the sheathed heater element design and potential refractory metal element designs are discussed in section 2.

## 1.2 Early Refractory Metal Heater Designs

Early investigation of potential refractory metal heater designs was conducted in 2002. The primary goal of the development effort was to build a very small diameter heater element that could achieve the power and temperatures necessary for the reactor designs that were being proposed at that time. Very small diameter elements are possible using a hairpin design. In this construction, a double-bore  $\text{Al}_2\text{O}_3$  tube is used, that allows a wire to be run down one bore, be bent, and returned down the opposite bore, hence the ‘hairpin’ terminology. Figure 9 provides a rough sketch of this design.

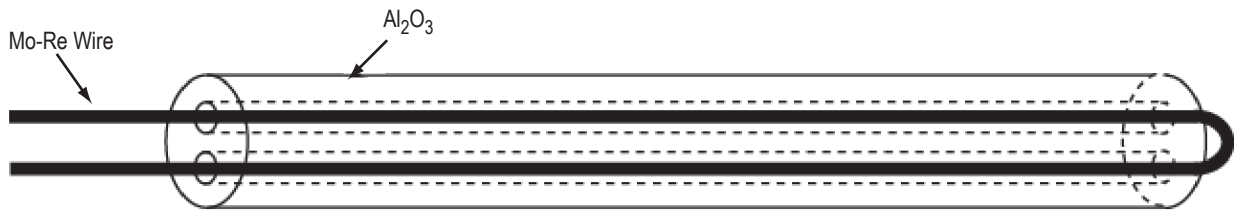


Figure 9. General configuration of the hairpin heater element design.

Several hairpin heater tests were conducted using molybdenum-rhenium (Mo-Re) wire of varying diameters. A 50/50 mixture of Mo-Re was selected to increase the ductility of the material over that of pure Mo. However, it was noted that, for larger diameter wires, the ductility at room temperature was still such that it was difficult to make the necessary bend to return the wire down the opposite bore. Heater fabrication at elevated temperature was not investigated. Tested wires ranged from 0.64 to 1.3 mm (0.025 to 0.05 in) in diameter. Each heater element required  $\approx 0.6$  m (2 ft) of wire, as opposed to the 3.7 m (12 ft) required for a spiral-wound heater design. Because of the very low resistance of the element (additional wire length is required to increase the resistance), the maximum power that could be deposited in these elements for the available 100 A of current was very low. For a 15-kW (150-V, 100-A) power supply, the maximum power that could be achieved with the hairpin design was  $\approx 1,600$  W. Because the wire was fully surrounded by  $\text{Al}_2\text{O}_3$  (there was no active heat removal from the element), wire temperatures were very high at these power levels. Additionally, a flat axial power profile is inherent to the hairpin design, and no flexibility is available to introduce a shaped profile.

The 1.1-mm (0.045-in) Mo-Re wire element, tested up to a maximum of 1,600 W, was submitted for complete materials analysis by the Metallurgical and Failure Analysis Team at MSFC. After removal from the  $\text{Al}_2\text{O}_3$  tube, the Mo-Re wire was found to be brittle with a pitted surface. Analysis found Mo and some Re deposits on the surface of the  $\text{Al}_2\text{O}_3$  insulator, but cross-section analysis of the insulator found no reaction between the wire and insulator and no reaction zone was found in the  $\text{Al}_2\text{O}_3$ . The cross section of the Mo-Re wire revealed large grain growth, resulting in the embrittlement of the material, and a surface reaction zone that was depleted of Mo-Re. Mo-Re grain growth is dictated by time at temperature. Mo-Re is typically fully annealed at temperatures above 1,600 K. Recrystallization of Mo-50%Re can occur at 1,473 to 1,673 K, with variation in the recrystallization temperature likely a result of processing history (material microstructure)

and material thickness. The Mo-Re material used in this element test was probably recrystallized material because significant grain growth would not be expected below 1,473 K for short times, but could occur for very long times. Because large grain growth was observed in the posttest analysis, it is likely that the element temperature exceeded 1,473 K for some period during the test. It was noted that the preferential oxidation of Mo was likely accelerated by the presence of water vapor in the test chamber, indicating the need for multiple purge cycles of the test chamber using dry nitrogen (N) or, preferably, high purity He or Ar gas before testing. The addition of a bakeout cycle would also help to remove volatile constituents before testing at high temperature.

Because of the various limitations described for the hairpin heater design, it was abandoned in favor of designs that offered additional flexibility in their application and that could achieve higher power in each pin.

## 2. CURRENT THERMAL SIMULATOR TESTING AND DEVELOPMENT

Investigation has commenced to assess alternate thermal simulator designs to replace the graphite rod heaters discussed in section 1. While the graphite heaters can accommodate most of the desired characteristics given in table 1, the limitations in the achievable pin size and the potential for graphite to contaminate a refractory metal test article has driven the simulator research effort toward other design concepts, such as refractory wire wrapped heater elements. Preliminary results for a carbon (C) fiber braid element will also be discussed. A matrix of the current and planned test hardware is provided in table 2.

### 2.1 Refractory Metal Wire-Wrapped Simulator Design

Refractory metal wire-wrapped heater element designs are investigated to develop a heater that will be compatible with refractory metal reactor concepts and to enhance the minimum achievable pin diameter. The wrapped wire heater element design considers various refractory metal wires wrapped in either a single pass or double pass fashion around a spiral groove etched along an  $\text{Al}_2\text{O}_3$  mandrel.

Initial tests use a mandrel having a constant pitch groove (for both the single pass and double pass helix), resulting in constant power density along the axial length of the heater element. The development effort will also consider cutting the mandrel with a constantly changing pitch to generate an axial power profile that mimics that of an operating reactor. Mandrels with a constantly changing pitch (corresponding to a prescribed equation determined by reactor designers at Los Alamos National Laboratory) have been produced to demonstrate manufacturability of the design, but the current work focuses on using the lower cost, constant pitch mandrels to assess materials performance for long-life thermal simulators. Several challenges addressed in concept development include the following:

- Identifying a wire manufacturer to make a small diameter refractory metal wire with adequate ductility to wrap around the mandrel without ‘unwinding’ once tension is released, but robust enough to withstand the long lifetime and high-temperature testing.
- Designing the electrical connection to the integrated system.
- Achieving power densities  $>1$  kW per element.
- Manufacturing a small diameter mandrel (0.65 cm (0.255 in) with a constantly changing, double pass pitch (to provide axial power shaping).
- Overcoming material compatibility issues.

Table 2. Thermal simulator test matrix: current status.

Simulator Type	Simulator Material	Configuration		Adhesives (Leads, Insulators, etc.)	Axial Power Profile (Peak to Avg)	Simulator Diameters (Heater Plus Sheath, Wire Diameter, Full Assembly)	Length	Chamber Environment*	Power Level/ Range (W)	Accumulated Test Time	Thermal Cycles	Test Status (Tested Configuration, Complete/Planned Tests)
		Sheathed vs. Bare	Cover Gas									
Poco Graphite	Graphite rod (Poco Graphite)	Bare rod Mo coupler	None	Power leads: Graphite cement Al <sub>2</sub> O <sub>3</sub> standoffs: Al <sub>2</sub> O <sub>3</sub> epoxy	Varying diameter (4-in section cutout at center), ≈1.33	0.375-in-OD, 0.130 in at center	20 in	≈10 <sup>-5</sup> torr	850 – 5,000	1,000's hr	100s	SAFE-30 SAFE-100 SAFE-100a DDG
					Varying diameter (4-in section cutout at center), ≈1.33	0.375-in-OD, 0.130 in at center	20 in	Mars environment (CO <sub>2</sub> )	25 kW total, distributed over 57 heaters (≈440 W per Heater)	≈30 hr	10	SAFE-30
					None (constant diameter)	0.375 in	20 in	≈10 <sup>-5</sup> torr	850 – 1,250	1,000's hr	100s	HP module tests
Sealed Tube	Graphite rod (Poco Graphite)	Stainless steel sheathed rod Mo coupler	None (un-sealed)	Power leads: Graphite cement Al <sub>2</sub> O <sub>3</sub> standoffs: Al <sub>2</sub> O <sub>3</sub> epoxy	None (constant diameter)	0.305 in	23.5 in	Not yet tested	Up to 5,000 W	Not yet tested — will be applied in LMR test		
					None (constant diameter)	0.375 in	20 in	≈10 <sup>-5</sup> torr	Not yet built or tested			
Wire Wrapped	W	Bare element, Al <sub>2</sub> O <sub>3</sub> mandrel	None	Seal: High temp. braze, RD material PALARO+3 V Wesgo Metals (Morgan Advanced Ceramics)	None	0.375-in graphite, 0.540-in stainless steel sheath	20 in	Conceptual design — Not yet built or tested				
					Unsuccessful test due to poor ductility of W wire at larger diameters — could not be wrapped around mandrel (0.040-in wire, with 0.410-in mandrel was attempted)							

\*Environmental conditions are estimated. No pressure gauges currently on the test chamber — estimated from pump capabilities.



Table 2. Thermal simulator test matrix: current status (Continued).

Simulator Type	Simulator Material	Configuration		Adhesives (Leads, Insulators, etc.)	Axial Power Profile (Peak to Avg)	Simulator Diameters (Heater Plus Sheath, Wire Diameter, Full Assembly)	Length	Chamber Environment*	Power Level/Range (W)	Accumulated Test Time	Thermal Cycles	Test Status (Tested Configuration, Complete/Planned Tests)
		Sheathed vs. Bare	Cover Gas									
<b>Wire Wrapped</b>	W braid	Bare element, Al <sub>2</sub> O <sub>3</sub> mandrel	None	Direct mechanical connection to power feedthrough	None	0.010-in-diameter wire, 5 wires, braided together, 0.410-in mandrel (0.625-in assembly)	20 in	10 <sup>-5</sup> torr	1200 – 3000	125 hr	16	Bare element testing (in progress)
	W braid	Mo sheathed	None, (un-sealed)	Direct mechanical connection to power feedthrough	None	0.010-in-diameter wire, 5 wires, braided together, 0.410-in mandrel (0.625-in assembly)	20 in	10 <sup>-5</sup> torr	1200 – 3000	115 hr	12	Sheathed element testing (in progress)
	Ta	Bare element, Al <sub>2</sub> O <sub>3</sub> mandrel	None	Direct mechanical connection to power feedthrough	None	0.040-in-diameter wire; 0.410-in mandrel (0.625-in assembly)	20 in	10 <sup>-5</sup> torr	1200 – 4000	150 hr	19	Bare element testing (in progress)
	Re	Bare element, Al <sub>2</sub> O <sub>3</sub> mandrel	None	Direct mechanical connection to power feedthrough	None	0.040-in-diameter wire; 0.410-in mandrel (0.625-in assembly)	20 in	10 <sup>-5</sup> torr	1200 – 5000	140 hr	18	Bare element testing (in progress)
	Hf	Bare element, Al <sub>2</sub> O <sub>3</sub> mandrel	None	Direct mechanical connection to power feedthrough	None	0.040-in-diameter wire; 0.410-in mandrel (0.625-in assembly)	20 in	10 <sup>-5</sup> torr	1200 – 3000	110 hr	13	Bare element testing (in progress) (did not stabilize —eliminated)
<b>C Fiber Braid</b>	General Comments: All wrapped wire configurations can be constructed to have the desired power profile by cutting the groove in the Al <sub>2</sub> O <sub>3</sub> mandrel with a constantly varying pitch. In this manner, the axial power profile can be set to any equation desirable, as a function of the selected reactor design. Direct mechanical connection to electrical feedthrough will be replaced by a Mo coupler in future testing. All wire-wrapped configurations met the basic requirement of operating at 1,200 W for 100 hr.											
	C fiber	Bare element, Al <sub>2</sub> O <sub>3</sub> mandrel	None	Mo coupler	None	0.1-in-diameter fiber braid; 0.410-in mandrel (0.625-in assembly)	20 in	10 <sup>-5</sup> torr	900	35		Bare element testing (in progress)
	C fiber, resin coated	Bare element, Al <sub>2</sub> O <sub>3</sub> mandrel, carbonized	None	Mo coupler	None	0.1-in-diameter fiber braid; 0.410-in mandrel (0.625-in assembly)	20 in	10 <sup>-5</sup> torr	1,200	10		Bare element testing (in progress)

\*Environmental conditions are estimated. No pressure gauges currently on the test chamber, estimated from pump capabilities.

Dozens of refractory metal wire heaters have been built and tested using various wire combinations. While several designs have proven successful, others have failed at high power levels due to the inability to efficiently remove heat from the element. Early element tests applied no active heat removal from the element. In this configuration, heat loss from the element is by radiation to the cool chamber walls. Because the test chamber was operated at vacuum, no conductive or convective cooling was possible. Under these conditions, the element temperatures can become very high. The spiral-wrapped refractory metal wire heater elements show promise for small pin diameters and excellent axial power profiling capabilities, and tests completed to date indicate that the maximum power per pin is only limited by the available power supply voltage. Modification of the boundary conditions in the test chamber to better mimic use of the element in the reactor simulator test article could allow higher pin power levels to be achieved without exceeding material temperature limitations in the heater elements (addition of heat removal mechanisms similar to those in the full test article); possible modifications will be discussed in section 2.3. Research and development continues on these element designs in an effort to resolve the issues that have been identified, and are reviewed in sections 2.4 through 2.6.

### 2.1.1 Engineering Design

Heater designs using spiral mandrels were pursued to reduce the overall diameter of the heater elements and to investigate the potential of using materials other than graphite in the thermal simulator applications to address compatibility concerns for each proposed test article. To date, materials tested on the spiral cut  $\text{Al}_2\text{O}_3$  mandrels include Re, tantalum (Ta), niobium (Nb), tungsten (W), hafnium (Hf), and C fiber, where tests incorporate the use of single wires or multiple braided wires. The braided material allows the use of smaller wire diameters, providing ductility required for manufacturability. As a result, the braided designs widen the possible range of heater element materials and designs, producing flexibility in meeting requirements. The C fiber braid design and tests will be discussed in section 2.2.

Initial efforts in the spiral-wrapped heater designs have been directed at developing a better understanding of the performance of potential materials that can be used to construct these elements. This provides a knowledge base that can be called on to quickly design a heater that will best meet the test article requirements once they have been established. To date, dozens of refractory elements have been built and tested to assess the applicability range of material selection. The basic requirement for all spiral-wrapped heater element designs was to produce an element capable of providing stable operation for a minimum of 100 hr at 1,200 W. Tests have been conducted over a range of 850 to 5,000 W with the goal power range of 1,200 to 6,000 W per element. Final designs for use in refractory metal systems will incorporate a sheath to ensure that oxygen ( $\text{O}_2$ ) from the  $\text{Al}_2\text{O}_3$  mandrel does not contaminate the test article.

**2.1.1.1 Heater Assembly: Mandrel Design.** The heater assembly designs entail four primary components: the heater, electrical connections, sheath, and end cap. For the spiral-wrapped wire heater designs, the ‘heater’ consists of a refractory metal wire wrapped around an  $\text{Al}_2\text{O}_3$  mandrel. To minimize variables from one test to the next, a 1.59-cm (0.625-in) assembly size was used for all preliminary material testing, as components required for these assemblies were standard (reducing development cost). This corresponds to the engineering drawings provided in appendix B for the

mandrel, coupler, and sheath. For this design, the OD of the  $\text{Al}_2\text{O}_3$  mandrel is 1.04 cm (0.410 in), with the groove in the mandrel cut with a radius of 1.6 mm (0.063 in) in a double helix fashion. The 1.59-cm (0.625-in) dimension corresponds to the OD of the flange on the sheath used with this design. Testing completed to date has primarily focused on the unsheathed heater elements to establish basic materials performance characteristics. Sheathed testing has been initiated with the Ta and W wire braid designs. Engineering specifications on the mandrel (and the sheath) fabrication require that it be held to a straightness of 0.13 mm (0.005 in) over full length. Current designs include a 0.064-mm (0.0025-in) radial clearance between the largest diameter on the mandrel (the insulator at the end of the wire wrapped region) and the ID of the sheath.

Currently, the smallest full assembly diameter (OD of the sheath flange) design is 1.02 cm (0.400 in) and the design includes the coupler and power integration strategy within this footprint. The minimum diameter is limited by the amount of power that is required per pin and by the ability to hook up the power within the given diameter. Smaller diameter assemblies have been manufactured, but the power integration issues have not been fully addressed to date. The limitations related to and the status of these smaller diameter designs will be discussed briefly in section 2.1.4. The 1.02-cm (0.400-in) design is shown in the engineering drawings provided in appendix C for the mandrel, coupler, coupler cap, and sheath. For this design, the OD of the  $\text{Al}_2\text{O}_3$  mandrel is 0.60 cm (0.235 in) (0.65 cm (0.255 in) at the nongrooved end sections), with the mandrel groove cut with a radius of 1.2 mm (0.048 in) in a double helix fashion. The 1.02-cm (0.400-in) dimension corresponds to the OD of the flange on the sheath used with this design. Although mandrels have been constructed with these dimensions, heater element testing for this configuration has not yet begun.

Testing has entailed two basic mandrel designs: single-pass and double-pass pitch, and all tests to date have been performed on the larger 1.04-cm (0.410-in) mandrel corresponding to the 1.6-cm (0.625-in) full assembly size. In all cases, the mandrel was constructed from 99.8% pure  $\text{Al}_2\text{O}_3$ . Alumina oxide is commercially available up to a purity of 99.99%. As heater development becomes more sophisticated, it may be desirable to obtain higher purity mandrel material to lengthen the operational lifetime of the heater elements and to minimize the potential of the heater components contaminating the test article.

While several heater elements have demonstrated successful performance, several elements 'broke down' at high power levels, presumably due to over-temperature conditions. Early spiral wound heater designs used 'one-pass' pitch mandrels, such that the wire was spiraled down the length of the mandrel (on the OD) and returned down a hole in the center of the  $\text{Al}_2\text{O}_3$  mandrel to allow for a single-ended heater element. Failures were noted in the center level at higher power levels. Because the center wire was fully surrounded by an  $\text{Al}_2\text{O}_3$  insulator, failure was likely due to inadequate heat transfer, which resulted in extremely high temperatures in the center wire. To date, element tests have applied no active heat removal from the element with heat loss from the element being by radiation to the cool chamber walls ( $\approx 50$  °C). The chamber walls are actively cooled by water, but the chamber end caps are not cooled and could be at elevated temperatures ( $\approx 150$  °C). The test chamber was operated at vacuum, preventing the possibility of no conductive or convective cooling.

The failures noted for the single-pass design led to the development of the double-pass helical mandrel. The double-pass mandrel improved the heater performance by bringing the wire completely to the outside surface of the Al<sub>2</sub>O<sub>3</sub> (improving the ability to remove the heat from the wire) and by increasing the length of the wire used to construct the element (from ≈2.4 to 3.65 m (≈8 to 12 ft)), increasing the total resistance of the element by a factor of 1.5.

Prior to wrapping the Al<sub>2</sub>O<sub>3</sub> mandrel with the desired wire, the mandrel and wire are cleaned with methanol and all components are handled with gloves. All tests are conducted in vacuum (≈1.3 mPa (≈10<sup>-5</sup> torr)). At the start of each run, ≈50 to 100 W is input to the heater element and it is allowed to bake out for a few hours. Testing begins on the following day at 1,200 W or higher. (Generally, heater elements reach the target 1,200 W in <30 s.) More extensive cleaning procedures will be adopted for higher fidelity element testing and prior to heater integration into each test article. Suggested procedures will be discussed in section 3.6.

**2.1.1.2 Heater Assembly: Wire Selection.** The use of refractory metal wires 0.5 to 1.5 mm (0.020 to 0.060 in) in diameter has been assessed with some materials demonstrating fabricability issues early on and, as a result, these elements were not tested. Selection of the appropriate wire diameter is a balance of resistivity, ductility, and integrity at temperature. As the ductility of the wire decreases, it becomes increasingly difficult to wrap the wire down the length of the mandrel. Generally, while the larger diameter wires have decreased resistance (such that, in a voltage limited case, the element can pass more current and reach a higher power level for the same voltage relative to the small diameter wires), they face limitations in ductility that impact manufacturability. Smaller diameter wires, on the other hand, are more ductile, simplifying heater fabrication, but they have increased resistance, so they pass less current in a voltage limited scenario. Additionally, smaller diameter wires are more prone to failure at high temperature due to materials limitations (such as temperature-induced grain growth, degradation of material, corrosion, etc.). Braiding three or more small diameter wires mitigates the high resistance problem by offering parallel paths for the current, providing the capability to reach higher power levels similar to that achieved with a single, larger diameter wire while offering the ductility of small diameter wires. Use of braided wire configurations widens the range of potential materials that can be used to construct the heater elements. The element resistivity could also be adjusted using material doping, but this could generate ‘hot spots’ as a result of nonuniform doping, which could lead to wire failure. Maintaining high purity for any refractory wires can increase their operational lifetime. Any impurities that might exist in the wire material affect the resistance of the wire and generate higher power deposition and higher temperature at the point of the impurity. For a small diameter wire, the resulting increase in temperature at impurity points can lead to wire failure more quickly than for larger wire diameters. All refractory metal wires have been obtained at the highest purity level available, ≈99.9%. (With the exception of Re, all wire has been obtained from ESPI Corp., Inc. and Re wire was obtained from Rhenium Alloys, Inc.)

Of the refractory metals, Nb exhibits the most ductility and W the least ductility. Therefore, a large 1.5-mm- (0.060-in-) diameter Nb wire was acquired to conduct a feasibility study for using this wire size. Because significant difficulty was encountered in wrapping the 1.5-mm (0.060-in) Nb wire, other refractory metals, which would have reduced ductility, were not acquired at this large diameter. In this case, the Nb was used to ‘bound’ the range of possibilities, eliminating several

potential options from the test scope without additional expenditure of time and funds. The 1.5-mm (0.060-in) Nb wire was successfully wrapped around the 1.04-cm (0.410-in) Al<sub>2</sub>O<sub>3</sub> mandrel but has not been tested to date.

The current test setup provides power to the heater element via a 150 V power supply at a maximum of 100 A (15 kW maximum). Although multiple power supplies could be used to power the heater elements to test to higher voltages, this has not been done to date because operation at higher voltages in a vacuum environment can lead to voltage breakdown. The amount of power that can be pushed into an element at a given voltage is set by the element’s resistance. From the basic Ohm’s law, power (*P*) is given by the product of the current (*I*) and the voltage (*V*), or it can be written in terms of the resistance (*R*) using the relationship that voltage is given by the product of the current and the resistance:

$$P = IV = I^2R = \frac{V^2}{R} \quad (2)$$

To prevent operation of the power supply near its 150 Vdc limit, it is desirable to determine the maximum resistance element that can provide the desired power level at a more reasonable level of 140 V. This calculated value is provided in table 3. The right-hand side of the table provides experimentally measured resistances of the tested spiral wound elements. For the Hf and W wire braid tests at 3 kW, note that the input voltage was pushed to the absolute maximum for the power supply, 150 V. To date, most successful refractory wire elements have run for at least 30 hr at a power of 800 W (reaching a temperature of ≈1,300 K), while the 0.5-mm (0.020-in) wires appear to be limited to ≈850 W.

Table 3. Maximum calculated element resistance at 140 V compared to measured resistance values at prescribed power levels.

Power Level (W)	Current @ 140 V (A)	Maximum Element Resistance @ 140 V (Ω)	Measured Resistance During Test (Ω)				
			Ta (1 mm, 0.040 in)		Re (1 mm, 0.040 in)	Hf (1 mm, 0.040 in)	W, Five-Wire Braid (0.25 mm, 0.010 in (× 5))
			No Sheath	With Sheath			
1,200	8.6	16.3	–	3.2 (63 V, 19 A)	3.6 (67 V, 19 A)	6.6 (95 V, 15 A)	5.9 (90 V, 15 A)
2,000	14.3	9.8	3.3 (85 V, 26 A)	3.6 (85 V, 24 A)	–	–	–
3,000	21.4	6.5 (7.5 @ 150 V)	3.5 (104 V, 30 A)	–	3.9 (110 V, 28 A)	7.4* (150 V, 20 A)	7.3 (150 V, 21 A)
4,000	28.6	4.9	–	–	4.0 (130 V, 33 A)	–	–
6,000	42.9	3.3	–	–	–	–	–

\*Note that the measured Hf resistance did not stabilize at power—the value provided is estimated from the test runs completed.

At higher power levels, the small diameter wires failed, possibly due to locally elevated temperatures. Elevated temperatures could occur at localized positions due to impurities on the wire

that cause elevated power deposition at that point. Impurities could cause fracture more rapidly in small versus large diameter wires. If this is the case, adoption of more rigorous cleaning procedures could remove additional surface impurities and may allow use of smaller diameter wires in heater construction.

To reduce the voltage required to provide a set power level, a lower resistance element would be required. For instance, to reach a power level of 3 kW, a 5-W element would require 122 V (24 A). A 3-W element would require only 95 V (32 A). A lower resistance element is also required to increase pin power for a fixed voltage ( $P = V^2/R$ ). For instance, the relatively high resistance of the 1-mm (0.040-in) Hf and the five-wire W braid limited the achievable power per pin to  $\approx 3$  kW with the 150-V power supply. The element resistance can be reduced by selecting a material with a lower resistivity ( $\rho_R$ ) or by increasing the diameter of the wire used to construct the element. The resistance of a wire is given in equation (2):

$$R = \rho_R \frac{l}{A} \quad , \quad (2)$$

where  $A$  is the cross-sectional area of the wire and  $l$  is the wire length. Table 4 provides the calculated resistance (at 20 °C) of various refractory metals using the resistivity values provided by the wire manufacturer, ESPI Corp., Inc. Calculations assume a wire length of 3.6 m (2 ft), the approximate length required to wrap the 1.04-cm (0.410-in) mandrel in a double helix fashion. For refractory metals, the resistance increases with temperature. (Graphite is unique in the fact that its resistance first decreases with temperature before reaching a minimum and then increasing again.) Detailed expressions for the resistivity of some of these materials as a function of temperature are included in appendix D.

Table 4. Summary of resistance calculated for select refractory metal wires at 20 °C.

Material	Resistivity* @ 20 °C $\rho_R$ , ( $\mu\Omega$ - cm)	Number of Wires	Cold Resistance for 3.6 m Length ( $\Omega$ )		
			OD 0.25 mm (0.010 in)	OD 0.5 mm (0.020 in)	OD 1 mm (0.040 in)
Re	19.3	1	13.94	3.49	0.87
Ta	13.5	1	9.75	2.44	0.61
Nb	12.5	1	9.03	2.26	0.56
W	5.5	5 (braid)	0.79	0.20	0.05
Hf	35.1	1	25.35	6.34	1.58
Mo	5.2 (@ 0 °C)	1	3.76	0.94	0.23

\*Resistivity data from manufacturer.<sup>9</sup>

To balance the tradeoff between resistivity and ductility, 1-mm- (0.040-in-) diameter wire was selected as a baseline for initial refractory metal wire heater element tests. Selection of the same diameter wire for all material options reduces the number of variables between materials, offering the ability to better assess the benefits of each material. Additional wire diameters could be tested as the development effort for the heater elements is focused to a defined set of requirements. Results from testing Ta and W are discussed in sections 2.4 and 2.5.



**2.1.1.2 Heater Assembly: Electrical Integration.** The electrical connections to the heater assembly incorporate the power leads and the junction between the power leads and the heater itself, which could be made via direct mechanical connection (used for preliminary testing) or by use of a low resistance coupler. The coupler serves three purposes:

- (1) It acts as the interface to the hot heater wire.
- (2) It reduces the resistance between the power supply and the heater element (as a function of its material properties).
- (3) It lowers the temperature seen by the Cu lead wires (as a function of the length of the coupler pieces).

Heater element design is fundamentally limited by the capability to provide electrical hookup to the element. This limitation is established by the physical wire size relative to the element size and the amount of power that can be pushed into the element. To push a large current into the element, while maintaining minimum resistance in the power leads, the feed wires become too large relative to the element footprint. As the assembly size is reduced, it also becomes increasingly difficult to seal the element (around the diameter and around the small lead wires), a requirement for the sheathed heater designs.

For the graphite rod heater elements, Mo couplers were used to connect the Cu lead wires from the power feedthrough to the graphite element. The threads of the coupler are covered with graphite cement and then screwed directly into the graphite, securing them into place. Initial tests of the refractory wire elements have not used a coupler; instead, the refractory wire elements were fed directly from the element to the power feedthrough without using any intermediate, low-resistance wire between the element and the feedthrough. However, it is desirable for all the input power to go into the element, requiring lead wires to have very low resistance to minimize the power deposition in these components. To accomplish this, a mechanical connection is required between the refractory wire and the power lead wires to ensure a good electrical connection. The engineering drawings for the redesigned couplers for the 1.6- and 1.02-cm (0.625- and 0.400-in) assemblies (corresponding to the 1.04- and 0.60-cm (0.410- and 0.235-in) mandrels, respectively) are provided in appendices B and C, respectively. The maximum coupler size is limited by the ID of the sheath. The 1.6-cm (0.625-in) design uses a bolted, mechanical hookup, but, the hardware used to provide this connection was too large for the 1.02-cm (0.400-in) assembly. As a result, the coupler design is modified for the smaller assembly design simply to account for the reduced diameter, and the final design uses a sleeve/compression hookup for the smaller assembly. In both cases the coupler is constructed from Mo.

To prevent contamination of the test article by the heater element and to seal an inert gas (He) inside the sheath to improve the thermal conductivity across the element, a high integrity seal must be developed. The sheath is manufactured as a tube and two end caps are used to provide a closed-end unit. The upper end cap (no power feedthrough) can be welded to the body of the sheath before the heater element is inserted. On the opposite end, a metal or ceramic end cap that is designed to allow the coupler to feed through is used. This general configuration is shown

schematically in figure 10. The mandrel is inserted into the sheath such that the heater element is centered axially, allowing room for the coupler assembly at the power feedthrough end cap. If a metal end cap is used, insulating material (electrically nonconductive) must be included around the coupler feedthrough surface. The metal cap could then be welded to the sheath around the OD, but brazing would still be required at the coupler/cap interface due to the presence of the insulating material. Alternately, if a ceramic cap is used, no additional insulating material is required around the coupler feedthrough, but it must be sealed by brazing around the OD and at the coupler feedthrough. Two concerns emerged with regard to this braze as the design proceeded: the desired maximum temperature of the braze joint exceeds that of current braze technology and brazing in a He (or other inert gas) environment may not be possible. Possible techniques for sealing the heater elements inside a sheath and the associated thermal analysis will be further discussed in section 2.3.

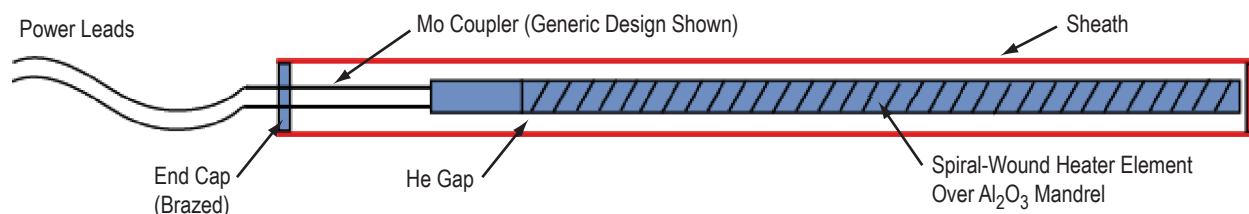


Figure 10. Generalized assembly configuration (not shown to scale).

## 2.1.2 Hardware Testing

Hardware testing to date has considered Ta, Re, Hf, and W wire heater elements. In all cases, the wire was wrapped around the 1.04-cm (0.410-in)  $\text{Al}_2\text{O}_3$  mandrel at a constant pitch (producing a flat power profile) and the wire used to form the heater element was mechanically connected directly to the electrical feedthrough. This connection is nonideal and nonprototypic, since all the input power from the power supply should go into the spiral-wound element itself rather than into the lead wires. However, for material and concept acceptance testing, there is no need to build and connect additional couplers. Elements selected for additional tests will incorporate the Mo coupler discussed above. After all potential element materials have been tested at 1,200 W (minimum test requirement of 1,200 W for 100 hr), the most desirable materials will undergo further testing at higher power levels.

**2.1.2.1 Tantalum.** Initial tests conducted on Ta wire used a 1-mm (0.040-in) wire wrapped around the 1.04-cm (0.410-in)  $\text{Al}_2\text{O}_3$  mandrel. Tantalum was tested over a range of 1,200 to 4,000 W for a total test time of  $\approx 150$  hr. Two Ta heater elements have been tested. The first Ta element was tested at 1,200 W for 101 hr, 1,600 W for 17.5 hr, and 2,000 W for 15.5 hr. The second was tested at 3,000 W for 50 hr and at 4,000 W for 5 hr. Bakeout of each heater was accomplished by applying  $\approx 50$  to 100 W to the element for several hours. Testing began on the following day, so that the startup to the desired power level would be from a cold element.



For the first Ta heater element run at 1,200 W, resistance measurements made before and after a 100-hr run indicated a  $< 9\%$  increase in the measured cold resistance of the element ( $\approx 0.8$  to  $0.87$  W). After an additional 34 hr at 1,600 to 3,000 W, the measured element resistance (after cooling for 12+ hr) had not changed, indicating that Ta was stable before and after operation at high power levels. Current and voltage were stable during all runs at power. ‘Stable’ heater operation was defined as an element that maintained approximately constant resistance before and after test, indicating that operation at power did not introduce any fundamental changes to the material properties. To be defined as stable, the element should also operate at a constant, stable current throughout testing at a constant power. The cold Ta element had a measured resistance of  $\approx 0.8$  W, and at 3 kW, the resistance increased to  $\approx 3$  W. From a cold startup condition, the heater was able to reach power in  $< 30$  s.

The first Ta heater element was tested both inside and outside of a stainless steel sheath. The sheath was unsealed, leaving a vacuum gap between the heater element and the sheath. During the 2-kW run, the heater was removed from the sheath for the remainder of testing. At this power level, the element produced a consistent glow from end to end, suggesting uniform performance and temperature along the length of the heater element. The element was run for an additional 8 hr at 3 kW. During the 3-kW test, photos of the hot Ta element revealed differential heating at localized positions along the helical conductor wire. Figure 11(a) shows the heater element early in testing where there are two points at which the Ta winding does not glow as brightly as the adjacent winding. The photo in figure 11(b), taken later in the 3-kW testing period, indicates that the differential heating locations have shifted to alternate positions and the overall coloration of the image has red shifted. Because some of the element testing was performed inside the stainless steel sheath, there was some concern that the sheath may have contaminated the Ta wire, producing the observed differential heating. Posttest materials analysis revealed that a lower temperature was most likely produced due to variations in the emissivity of the element over time.

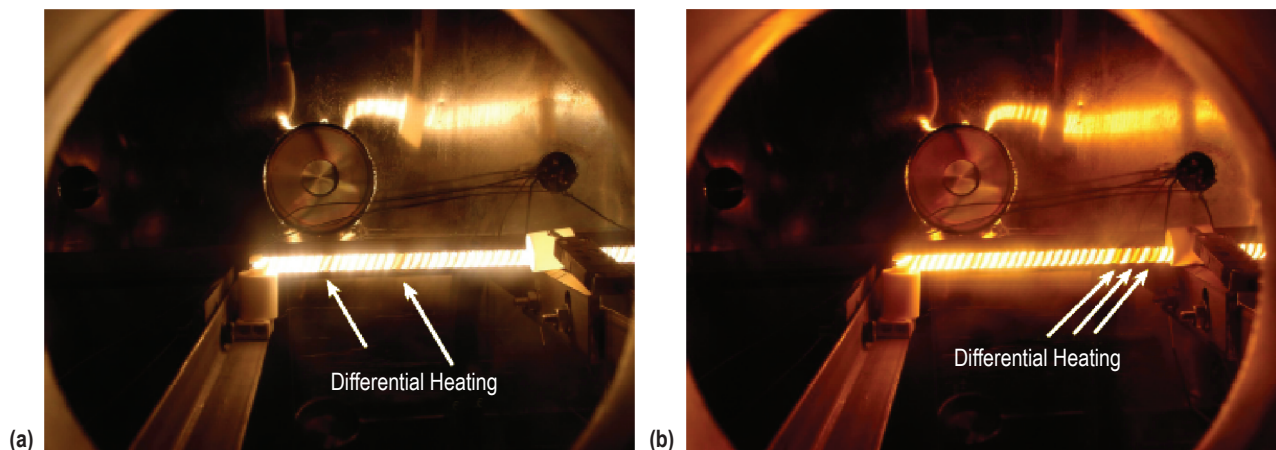


Figure 11. Test of W heater element at 3 kW (a) early in test and (b) later in test, revealing a spectral shift.

Test of a second Ta heater, constructed from the same wire lot, was performed to reproduce the differential heating observed during testing of the first element. This heater element was run bare (no sheath) at 3,000 W for a total of 50 hr. Visual observations indicated that the second Ta heater element demonstrated differential heating at high power operation, as was observed during testing of the first element. Hence, this behavior was not a result of contamination from the stainless steel sheath in the previous element test. Figure 11 (a) and (b) shows that the location of the differential heating on the Ta element moved to new positions at different times during the tests, suggesting that it was not a result of fixed surface contamination. Instead, this behavior may be due to changes in the surface emissivity as a function of time, which could be caused by oxidation or local contamination of the surface, producing an effective local reduction in the element emissivity. With time, the coil could be burning off the contaminant or it could be absorbing emitted gases such as  $O_2$  (based on the solubility of the material for these gases), resulting in a variable surface condition.

A complete visual inspection, after opening the chamber, revealed that the wire appeared to still be ductile. Power was increased to 4,000 W for a duration of 5 hr. Additional testing was not possible because the heater was accidentally knocked off the support stand while performing activities outside the chamber between tests.

After testing was completed, the Ta heater wire maintained a shiny silver metallic color while the white  $Al_2O_3$  mandrel had a bluish-black discoloration. The first Ta element was submitted for complete materials analysis to assess the overall heater performance. The complete analysis report, performed by G. Jerman of MSFC, is included in appendix E. When the wire was removed from the mandrel, it began to fracture in a brittle fashion and after approximately one-third of the wire had been unwound, the insulator fractured near the base of the mandrel where the Ta enters and exits the assembly. After the wire was completely removed from the mandrel, more significant discoloration of the  $Al_2O_3$ , which appeared to penetrate into the  $Al_2O_3$ , was noted (fig. 12). The complete materials analysis indicated that the discoloration was likely caused by the formation of an intermetallic aluminum-tantalum (Al-Ta) coating on the insulator surface. Carbon bearing contamination in the heater assembly reduced some of the  $Al_2O_3$  insulator surfaces under vacuum to form metallic Al. The hot Al metal then reacted with the Ta and reduced vaporized tantalum oxide to form a conductive intermetallic coating on the  $Al_2O_3$  insulator. Vapor deposited tantalum oxide on the sight glass window resulted in the overall red shifted image shown in figure 11(b), which was taken later in the test.

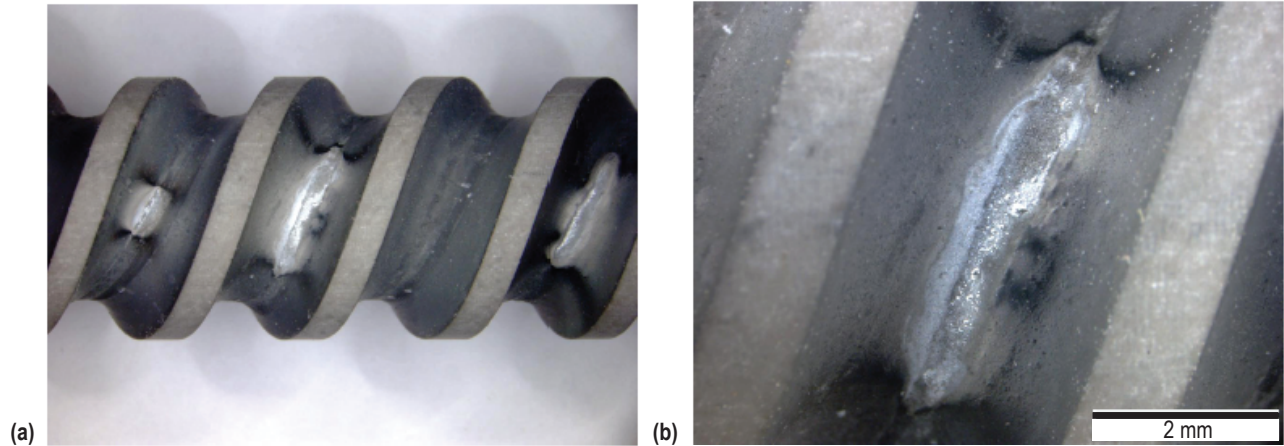


Figure 12. Alumina mandrel after removal of W wire, revealing (a) significant surface discoloration and (b) close-up view of contamination.

Detailed analysis using scanning electron microscopy indicated significant surface contamination on the Ta wire including C, O<sub>2</sub>, sodium (Na), and chlorine (Cl). The presence of these elements suggests that contamination may be due to human handling. This contamination could be reduced by thoroughly cleaning the wire to remove any oils or other volatile C bearing contamination before assembly. After assembly, bakeout under vacuum would remove any remaining volatile components. Additional cleaning and preparation procedures that may be adopted will be discussed in section 3.6.

The Al<sub>2</sub>O<sub>3</sub> used to construct the mandrel begins to melt at 2,072 °C and the maximum recommended operating temperature of Al<sub>2</sub>O<sub>3</sub> is 1,800 °C. Analysis indicated that localized melting may have occurred in regions in which the Ta wire was in intimate contact with the Al<sub>2</sub>O<sub>3</sub> mandrel. Constructing the mandrel from a ceramic with a higher temperature capability such as boron nitride (BN) (powder consolidated) or pyrolytic BN (vapor deposited), which does not break down until 3,000 °C, may be desirable. However, discussions with manufacturers of solid BN components have indicated that the maximum length component that could be fabricated is ≈46 cm (18 in), including the length of the ends necessary to hold the component during the fabrication process). As a result, elements using solid BN components in their construction may be significantly less flexible in their application than those using Al<sub>2</sub>O<sub>3</sub>. Additional higher power tests of braided Ta wire in vacuum and He environments, considering both sheathed and unsheathed configurations, are discussed in section 2.4.

**2.1.2.2 Rhenium.** Tests conducted on Re wire used a 1-mm (0.040-in) wire wrapped around the 1.04-cm (0.410-in)  $\text{Al}_2\text{O}_3$  mandrel. The Re heater element demonstrated stable performance at 1,200 W for the required 100 hr of run time. Operation for >100 hr indicated a reaction between the Re wire and the  $\text{Al}_2\text{O}_3$  mandrel, but because the heater met the minimum run time requirements without failure, the Re heater element is still being considered for further testing. The possibility of coating the mandrel with BN, or of constructing the mandrel from BN, is being investigated to mitigate the evident materials incompatibility issue between the Re and the  $\text{Al}_2\text{O}_3$ . Sealing the heater in a refractory metal sheath to prevent contamination is also being pursued and will be discussed further in section 2.3. Sealing techniques for the sheathed heater design are currently being investigated with industry.

As noted for the Ta heater, the cold Re element was capable of reaching a power level of 1,200 W (67 V, 19 A) in <30 s. The measured cold resistance dropped from 0.92  $\Omega$  at the start of day one to 0.91  $\Omega$  at the start of day two. No change in resistance was noted between the second and third testing days. The Re heater element was tested for a total of 100 hr at 1,200 W. Current and voltage remained stable throughout the element test at a given power level. After meeting the basic requirements for an acceptable heater element, power was increased to ensure that the element was not ‘on the edge’ of its performance capabilities. Testing continued for 24 hr at 3,000 W, 9 hr at 4,000 W, and 8 hr at 5,000 W. Unlike in the previous Ta wire tests, no differential heating was observed in the Re element. Photographs taken during the Re element test at 5,000 and 1,200 W are provided in figure 13. Rhenium has much lower  $\text{O}_2$  solubility at temperature than does Ta, so that the same  $\text{O}_2$  absorption would not be expected as was postulated from the Ta test results. After testing, the Re heater wire maintained a shiny silver metallic color while the white  $\text{Al}_2\text{O}_3$  mandrel had a bluish-grey discoloration.

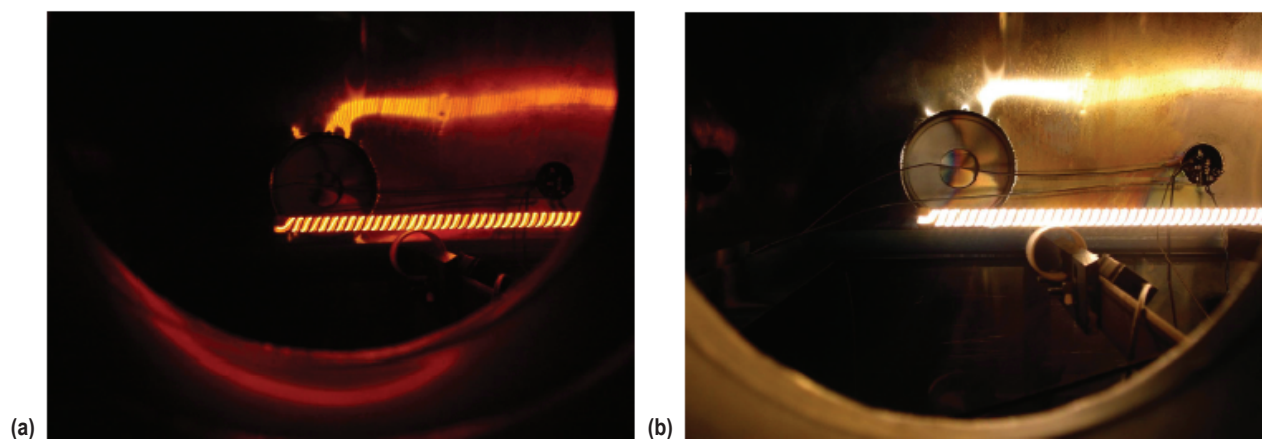


Figure 13. Test of Re heater element at (a) 5 kW and (b) 1.2 kW.



After test completion, the Re heater element was submitted for complete materials analysis to assess the overall heater performance. The complete analysis report, performed by G. Jerman of MSFC, is included in appendix F. When the wire was removed from the mandrel it was ductile and no wire was broken. After the wire was completely removed from the mandrel, variations in the discoloration of the  $\text{Al}_2\text{O}_3$  mandrel were noted. Localized surface coloration changes varied from bluish-grey to white streaks and dark bluish-grey spots, as shown in figure 14(b). Analysis indicated that this discoloration was caused by the deposition of Re oxides. The deposition of these low temperature oxides protected the  $\text{Al}_2\text{O}_3$  mandrel from high temperature degradation during the thermal testing. Because the Re oxides preserved the integrity of the mandrel and the conductor wire retained a large amount of ductility, the material analysis determined that the Re/ $\text{Al}_2\text{O}_3$  combination was superior to the Ta/ $\text{Al}_2\text{O}_3$  combination. Impurities contained in the heater element resulted in the formation of the Re oxide that actually acted as a protective layer to reduce further damage of the wire and mandrel, but because the protective Re oxidation begins to degrade at 1,000 °C, operation of an uncleaned Re element above this temperature is not recommended. Although Re performed very well in the thermal simulator tests, it was found that each order of Re wire from Rhenium Alloys, Inc. varied significantly in its purity levels. As a result, it may be more desirable to fabricate heaters with Ta or braided W wire (see sec. 2.1.2.4) due to the reproducibility of the specifications for these wires.

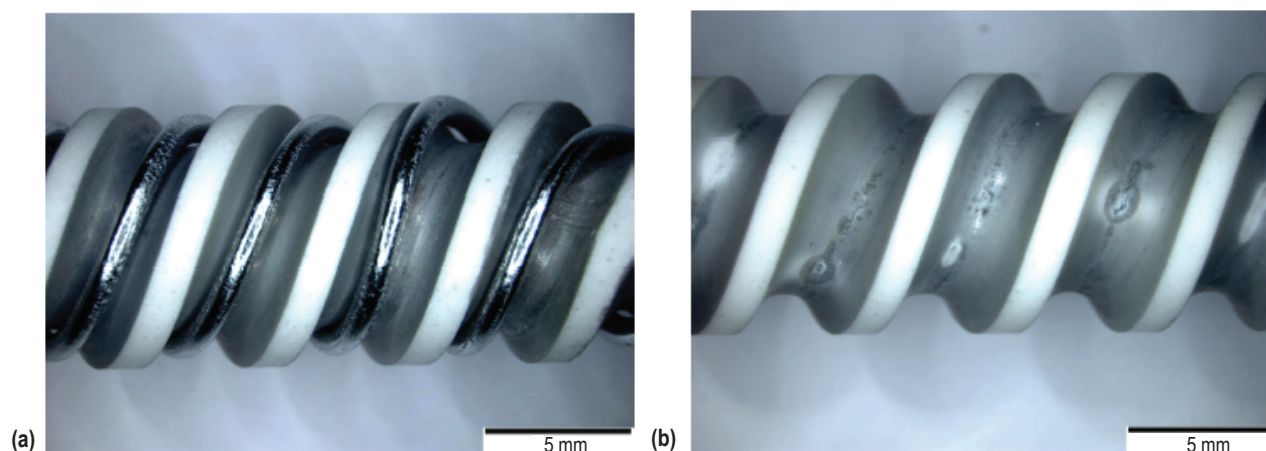


Figure 14. Posttest  $\text{Al}_2\text{O}_3$  mandrel (a) before and (b) after removal of Re wire, revealing slight surface discoloration.

**2.1.2.3 Hafnium.** Tests conducted on Hf wire used a 1-mm (0.040-in) wire wrapped around the 1.04-cm (0.410-in)  $\text{Al}_2\text{O}_3$  mandrel. Although the Hf met the minimum test requirement of 1,200 W for 100 hr, the element resistance never stabilized over the run time. Prior to test, the element resistance (cold) was  $\approx 1.5 \Omega$ . At the end of each day of testing, the measured element resistance had increased, and upon completion of the 100 hr of testing at 1,200 W, the cold resistance had increased to  $\approx 3.5 \Omega$ . Additional testing was performed at 3 kW for 10 hr. Although the resistance was relatively stable at 1,200 W, operation at higher power caused the resistance to drop slightly throughout the test.

Although no materials analysis was conducted, the continually increasing cold resistance could indicate that the Hf element suffered oxidation during test. Alternately, material incompatibilities or impurities in the test components could have altered the microstructure of the wire, causing it to become porous and slowly reducing its effective electrical conductivity path. After testing, the Hf wire was very brittle.

Because Hf did not demonstrate stable operation, it is not recommended for further testing at the current requirement levels. Although stability at power is a necessary requirement for any heater element, Hf has not been entirely eliminated from the list of potential heater materials. Depending on the final series/parallel configuration of the power hookup, Hf could, in fact, be a desirable choice for a reactor simulator that requires lower power density per pin due to its high resistivity.

**2.1.2.4 Tungsten.** Construction of W wire-wrapped heater elements has considered use of a single 1-mm (0.040-in) wire or braided wire, constructed from five 0.25-mm (0.010-in) wires braided together. Initial investigation indicated that the ductility of the 1-mm (0.040-in) W wire was such that the wire was very difficult to wrap around the 1.04-cm (0.410-in) mandrel, so no heater element was constructed using a single W wire. Use of smaller diameter wires in a braided configuration mitigated the manufacturability problem that was encountered with the single wire. The number and diameter of wires in the braid can be adjusted to vary the resistivity and current-carrying capacity of the heater element, per the requirements of a given reactor design. The current work has considered 0.25-, 0.38-, and 0.5-mm (0.010-, 0.015- and 0.020-in) wires because larger wire diameters encounter the ductility problem. Heating the W wire while it is being wrapped could allow use of larger diameter wires, but this would introduce additional complexity to the heater fabrication.

The braided W wire tests (five 0.25-mm (0.010-in) wires) have accumulated  $\approx 240$  hr of test time over a total of 30 thermal cycles. Pretest pictures of the braided W wire element are provided in figure 15. Tests of the W braid have assessed performance of both the unsheathed (bare) and the sheathed heater element. Unsheathed tests included 101 hr of testing at 1,200 W over 13 thermal cycles and an additional 24 hr at 3,000 W over 3 thermal cycles. The sheathed tests used a 1.6-cm- (0.625-in-) diameter Mo sheath (99.9% pure). The element was slid into the sheath but the sheath was not sealed, such that the environment between the heater and sheath and external to the sheath were at vacuum ( $\approx 1.3$  mPa ( $\approx 10^{-5}$  torr)). At 1,200 W, the measured resistance of the sheathed element was  $\approx 6 \Omega$ .

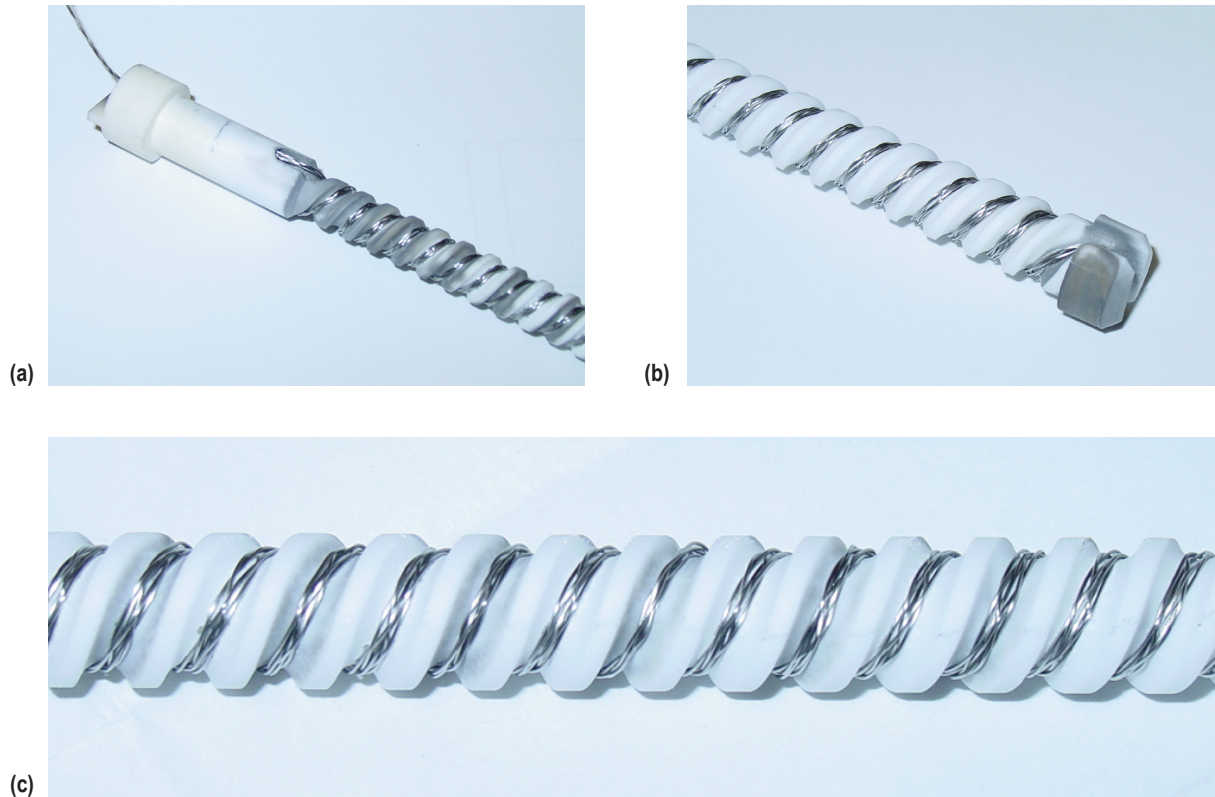


Figure 15. Tungsten wire-braid heater element wrapped on a 1.04-cm (0.410-in)  $\text{Al}_2\text{O}_3$  mandrel. Close-up views are provided for (a) the power input end, (b) the non-power end, showing wire wrap return for double helix configuration, and (c) the center section showing the five-wire braid.

For element testing inside the Mo sheath, the sheath was instrumented from end to end with type C TCs. A piece of nickel (Ni) foil was first welded to the sheath surface, and the TC was then welded to the foil (all welding was performed in air). Measured temperatures indicated a range from 950 to 1,400 °C at 1,200 W (variation in temperature along length of heater). The exact location of each TC was not measured, but approximate locations are identified in figure 16. Because they are bonded to the Mo sheath via Ni foil, the TCs are slightly cooler than the sheath. In addition, the TCs act as small fins, locally cooling the Mo and producing a temperature measurement that is somewhat lower than the actual sheath temperature.

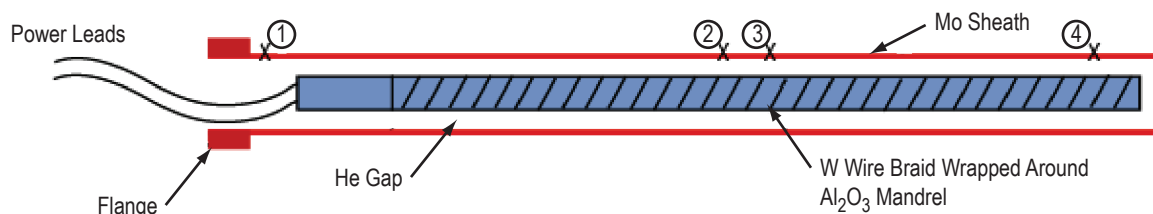


Figure 16. Approximate TC locations on the Mo sheath.

During the test, it became apparent that TC 2 may have lost contact with the surface of the sheath, as its temperature dropped to  $\approx 630$  K (relative to  $\approx 1,200$  K in previous test days). Early test data (prior to complete loss of TC 2) are provided in table 5. Two measurements are provided for each test day: one taken at the beginning of testing, and one taken at the end of the test day prior to turning off the power supply. (All temperatures are reported in kelvin.) The significant variability in the TC measurements along the length of the sheath may be related to their location on the sheath, but it is more likely (especially in the case of the relatively closely positioned TCs 2 and 3) that TCs attached to the outer surface of the sheath may not have provided reliable temperature measurement for thermal simulator evaluation. The temperature variation noted in the test data from day to day, particularly for TCs 3 and 4, may be due to reduction of the sheath surface emissivity (thereby elevating the temperature necessary to reject the heater power), off-gassing impurities from the sheath exterior surface, or off-gassing impurities from the foil connecting the sheath to the TC (thereby limiting cooling of the foil due to radiation). Alternate temperature measurement techniques will be discussed in section 3.1.

Table 5. Measured sheath temperatures (K) for the braided W wire heater assembly. (The first temperature entry corresponds to the beginning of the test, the second to the end of the test).

Power Level (test date)	TC Location			
	1	2	3	4
1,350* W (Feb. 8, 2005)	1,272	1,217	1,598	1,371
	1,267	1,217	1,600	1,402
1,350* W (Feb. 9, 2005)	1,260	1,217	1,593	1,413
	1,262	1,208	1,672	1,430
1,350* W (Feb. 10, 2005)	1,256	1,222	1,708	1,427
	1,262	1,207	1,760	1,439
1,350* W (Feb. 11, 2005)	1,259	1,219	1,785	1,455
	1,264	1,202	1,776	1,483

\*A total power of 1,350 W corresponds to  $\approx 1,200$  W in the heater element (assuming losses in the lead wires).

A thermal analysis was initiated after the testing was performed to assess the measured temperatures of the W wire braid element and the Mo sheath in the as-tested configuration and to determine the impact of varying environmental boundary conditions on the element and sheath temperatures. Calculations consider environment conditions both inside and outside the sheath, assuming either a vacuum test environment (as in the current experiment setup) or a 9 kPa (70 torr) He environment. In a vacuum environment, the only means of heat removal from the element is by thermal radiation to the cool chamber walls. If the chamber is backfilled with ultra-high purity gas, thermal conduction through the gas reduces the element temperature.

Analyses were performed using both Mathcad®, a Parametric Technology Corporation product, and Systems Improved Numerical Differencing Analyzer (SINDA)/Fluid Integrator (FLUINT). Use of both tools provided a quick check in formulations employed in the Mathcad model. The modeling approaches employed in each tool were similar. The key governing equations and supporting



formulations applied in the thermal analyses are included in appendix G. The simplified cross-section geometry shown in figure 17 was the basis of the thermal model, and also, there was an attempt made to model the braid/mandrel geometry shown in figure 15(c) (including details of the braid). Additional thermal analyses on sealed heater assembly configurations are included in section 2.3.

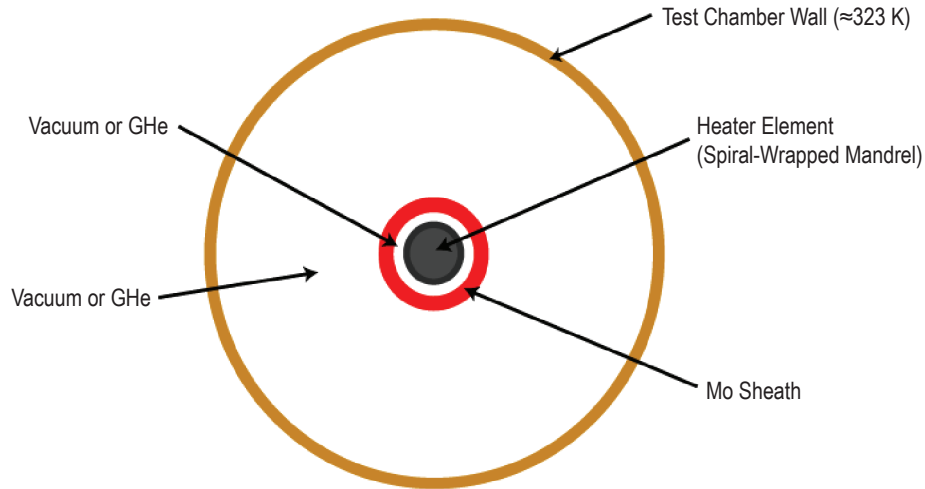


Figure 17. Approximate two-dimensional model applied for W wire element thermal analysis (not to scale).

All calculations assumed that the heater element wire, mandrel, and sheath were each isothermal and that the test chamber was maintained at a constant 323 K. The braid was modeled as a cylinder with the same cross-sectional area as the braided wire. The braid was thermally coupled to the mandrel and sheath via radiation and gas conduction depending on the case being evaluated. The emissivities of braid, mandrel, and sheath were assumed to be temperature independent and equal to 0.2, 0.4, and 0.2, respectively. For the radiative heat transfer calculations, the appropriate two-dimensional view factors and radiation exchange factors were hand calculated, based on figure 18(a). For the cases that incorporated gas (He) in the heater element/sheath gap, the gas conductance was assumed constant and equal to 0.427 W/m-K (corresponding to He at 1,273 K). A finite element model (FEM) mesh, shown in figure 18(b), was used to determine the two-dimensional conduction shape factors for the W wire-wrapped mandrel. The conduction shape factors and radiative exchange factors were then used in the Mathcad and SINDA models to compute the temperatures corresponding to the various configurations.

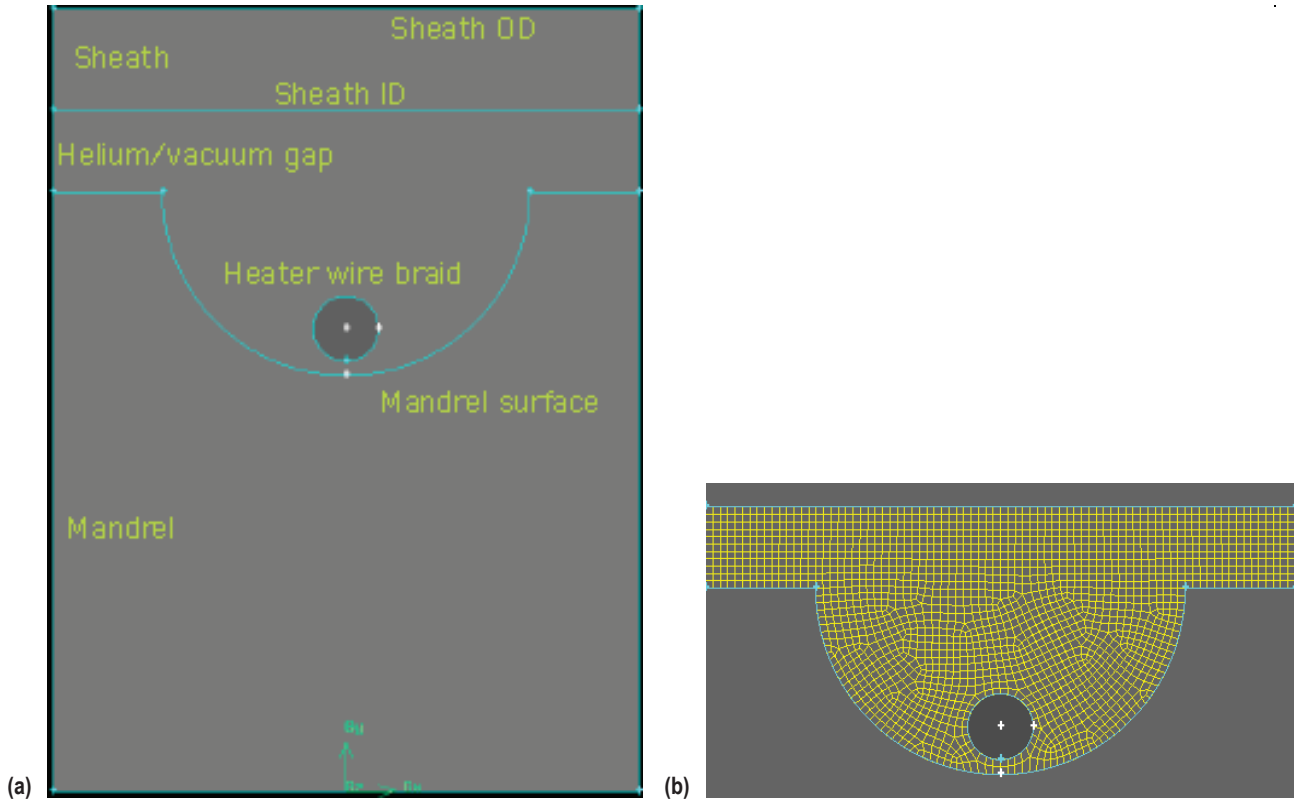


Figure 18. Braid/mandrel/sheath geometry: (a) Annotated layout and (b) finite element model of determination of conduction shape factors.

The results of the preliminary thermal analysis at a heater power of 1,200 W are provided in table 6. Case 2 (sheathed element, vacuum conditions) corresponds to the test conditions that were presented in table 5. A direct comparison of the two test results reveals a mixed picture. Experimental results indicated a sheath temperature ranging from  $\approx 1,256$  to 1,785 K along the length of the sheath and over several test days. The average measured sheath temperature for each test day presented in table 5 ranged from 1,364 to 1,431 K. The predicted sheath temperature, using both the SINDA and Mathcad models, was 1,486 K for this test configuration. The lower average measured temperature could result from the fact that the TCs are not bonded directly to the Mo sheath, but are separated from the sheath by a piece of Ni foil, causing them to be at a slightly lower temperature than the sheath. In addition, the differences in results could be due to differences between the emissivity value used in the model and the actual emissivity of the sheath external surface. For example, if the emissivity of the sheath were 0.1 (instead of 0.2 used in the model), the sheath temperature estimate would increase to over 1,700 K.

Table 6. Calculated mandrel, wire, and sheath temperatures for the braided W wire thermal simulator.

Case	Configuration	Calculated Temperature (K)		
		W Wire	Al <sub>2</sub> O <sub>3</sub> Mandrel	Mo Sheath
1	Sheath w/He	1,623	1,508	1,368
2	Sheath w/vacuum	2,405	1,863	1,486
3	No sheath w/He	1,271	1,161	N/A
4	No sheath w/vacuum	2,178	1,026	N/A

Thermal analysis results indicate the significant benefit of adding gas to the heater assemblies. The analysis predicts that the addition of thermal conduction across the heater/sheath gap will reduce the wire temperature by 782 K (from 2,405 to 1,623 K) in the sheathed heater element configuration and by 907 K (from 2,178 to 1,271 K) in the bare heater (no sheath) configuration. For both vacuum and He-filled environmental conditions, the sheathed configuration results in significantly higher wire and mandrel temperatures than for the equivalent unsheathed geometry. This results from the fact that the sheath acts as a radiation shield between the heater element and the cool chamber walls, reducing radiation heat transfer from the wire and mandrel. This effect is reduced when conduction is present, but the temperature differential between the sheathed and unsheathed configurations is still significant. Thermal analyses that consider additional details of the heater element and sheath geometry will provide additional insight to the expected temperatures in the heater assemblies. These calculated values could be further verified by incorporating enhanced diagnostics on the heater assemblies and on the test chamber itself. Tests of W wire-wrapped elements at higher power levels (up to 6 kW) were performed on three-, four-, and five-wire braids using the 0.25-, 0.38-, and 0.5-mm (0.010-, 0.015-, and 0.020-in) wire diameters. Results of these tests and the resulting thermal management issues are discussed in section 2.5.

### 2.1.3 Preliminary Conclusions

Testing of the refractory wire-wrapped heater element designs as of March 2005 indicated that the 1.6-cm (0.625-in) assembly with the 1.04-cm (0.410-in) Al<sub>2</sub>O<sub>3</sub> mandrel worked well for tests at 1,200 to 5,000 W. This series of testing provided information on desirable materials for the heater element, buildup of a complete heater assembly (as it relates to a desirable minimum assembly diameter), and power hookup. Materials recommended for continued development include Re, Ta, and W braid. All have successfully run for over 100 hr at 1,200 W. Brief runs of up to 4,000 W for Ta, 5,000 W for Re, and 3,000 W for W braid also produced desirable performance. No failures have been noted in the baseline tests (1-mm (0.040-in) wire or wire braid) for the single-ended, double-helix element designs tested to date. The success of the braided W wire element tests may open up the possibility of using other low ductility refractory wires, such as Mo. The 1.02-cm (0.40-in) assembly components are currently being procured and will be tested with Re, Ta, and W wires. These tests are covered in sections 2.4 through 2.6. If all wires are acceptable for the thermal simulator application, cost and ease of fabrication should also be considered in making the final material selection before fabricating a large number of heater assemblies for the reactor test article. Table 7 provides current estimates for the cost of each of the three refractory wires that will undergo further testing.

Table 7. Estimated costs\* for additional heater element wire.

Wire Diameter	W (3N8 Purity) (\$)	Ta (3N8 Purity) (\$)	Re (3N Purity) (\$)
0.25 mm (0.010 in)	2.00/m	7.40/m	107.00/m
0.38 mm (0.015 in)	3.30/m	7.90/m	70.50/m
0.5 mm (0.020 in)	4.00/m	8.00/m	43.50/m
1.0 mm (0.040 in)	—	23.50/m	356.50/m
<b>Comments</b>	Smaller W wire diameters necessary due to low wire ductility. The braided wire construction will cost an additional \$250/braid ( $\approx$ 4-m length).		

\*Quotes obtained from manufacturer.<sup>9</sup>

Future testing will seek to overcome challenges introduced by further reducing the assembly diameter. Previous testing (in 2003) on smaller element designs indicated significant difficulty in further reducing the complete assembly size. Because of the complexity associated with fabricating very small diameter, detailed mandrels and sheaths, it was difficult to find a vendor to produce the pieces. Mandrels having an OD of 0.53 cm (0.210 in) were manufactured from  $Al_2O_3$  with a constantly varying pitch. These mandrels were designed to fit inside a 0.65-cm (0.255-in) OD sheath, producing a full heater assembly with a total diameter of 0.65 cm (0.255 in). However, tests conducted using 0.5-mm (0.020-in) Re and W wires were not successful. In fabricating the element, it was very difficult to hold sufficient tension on the wire so that it did not unwrap from the mandrel while the sheath was pulled over the element. Tests of these elements were conducted in vacuum, so heat removal from the element was purely by thermal radiation. Tests at 1,200 W resulted in wire failure, presumably due to the inability to effectively remove heat from the element. Incorporation of a trapped high-purity gas in the heater element/sheath gap would improve the heat transfer by introducing conduction across this gap. Performing the test with the vacuum chamber backfilled to low pressure with ultra-high purity (UHP) inert gas (He or Ar) would also assist in removing heat from the element. These modifications to the test parameters could indicate significantly different results in the potential use of these small diameter heater assemblies. However, development to date has not addressed the issue of power integration with these very small diameter heater elements. As discussed previously, the coupler and power integration should fit within the diameter of the assembly so that it will not interfere with the neighboring heater assembly when integrated into a test article. Very small element diameters introduce a new challenge in providing input power to achieve the desired power per pin (to push higher currents necessary to reach the desired power levels, the power lead wires become relatively large). This challenge in power integration would have to be overcome before a reduction in assembly diameter could be considered feasible.

The element diameter could be further reduced by removing the requirement for sealing the heater element inside a sheath. In this case, the minimum element diameter would be driven by the limitations for fabricating the mandrel and the power integration issues discussed above. Although the heater would no longer be physically isolated from the test article (electrical isolation would still be required to prevent shorting), the achievable pin size could be beneficial. In the current mandrel design, at either end of the mandrel section that is grooved for the wire, the mandrel has a slightly larger diameter to allow the element to be self-isolating (e.g., unless it relaxes over time, the wire physically cannot touch the sheath due to the  $\text{Al}_2\text{O}_3$  mandrel ‘standoffs’). For the 1.02-cm (0.40-in) assembly, the mandrel diameter at the ends of the grooved section is 0.65 cm (0.255 in). To maintain a 0.13-mm- (0.005-in-) radial clearance, this element could fit into a 0.6-cm (0.270-in) fuel-clad surface (allowing a 0.13-mm (0.005-in) tolerance on the mandrel diameter and 0.13 mm (0.005 in) for mandrel and fuel-clad straightness). Alternately, the delta between the mandrel ends and the OD of the grooved portion could be reduced to bring the sheath closer to the wire element, reducing the width of the gap and, consequently, the OD of the sheath.

The noted interactions between the  $\text{Al}_2\text{O}_3$  mandrel and some refractory metal materials at elevated temperature (see materials analyses, app. E and F) do not eliminate these materials from use in heater construction. With over 100 hr of run time, these elements have performed well at the current requirements (1,200 W). Future endeavors will investigate reducing the interaction between materials by employing a BN coating over the  $\text{Al}_2\text{O}_3$  or replacing the  $\text{Al}_2\text{O}_3$  with solid BN. Using a BN mandrel, however, introduces additional issues to the heater fabrication. Boron nitride has significantly less strength than the  $\text{Al}_2\text{O}_3$  currently in use, so at small diameters, it will have a tendency to fracture if any significant tension is required to wrap the heater element wire. Additionally, as indicated in the above discussions, solid BN is limited to a maximum fabrication length of  $\approx 46$  cm (18 in). As a result, elements using solid BN components in their construction may be significantly less flexible in their application than those using  $\text{Al}_2\text{O}_3$  mandrels. Developing a BN coating that could be applied to the  $\text{Al}_2\text{O}_3$  and wire using a vapor deposition process for electrical insulation and improvement of materials compatibility may be a more promising option than employing solid BN.

Investigation of methods for heater encapsulation to prevent contamination to the test article will be discussed in section 2.3.

## **2.2 Carbon Fiber Braid Simulator Design**

Graphite C fiber braid is being investigated for use in thermal simulators in an effort to reach small pin sizes (0.65 cm (0.255 in)) and high power levels (1,200 W to 6,000 W per simulator) at high temperatures. One fabrication technique involves taking a C fiber braid, wrapping it around a mandrel, and melting the mandrel away while simultaneously carbonizing the fiber. This would require the use of a mandrel constructed of a material, such as Al, that could be melted near the temperature required for carbonization. Selection of the mandrel material must also take into account compatibility with refractory metal sheaths should any traces of the material remain

after the carbonization process. Alternately, the same  $\text{Al}_2\text{O}_3$  mandrel design discussed for the refractory wire heater elements can be applied for the C fiber braid elements. The challenges facing the C fiber braid simulator design include:

- Finding an appropriate method of attaching the C fiber braid which has the approximate consistency of yarn, to the  $\text{Al}_2\text{O}_3$  mandrel.
- Determining the best carbonizing method (furnace temperature and treatment time).
- Creating a support structure for the mandrel that holds the braid to the mandrel, but does not interfere with the mandrel melting process (using an Al mandrel).
- Designing the electrical connection to the integrated system.
- Achieving the desired power levels given the high resistance of the carbon fiber braid.

Tests run to date using the C fiber braid material have been directed at verifying material capabilities at temperature and initial results look promising for the power levels set forth in the requirements. Research and development has just begun on this concept, with the initial braid tests showing great promise—the primary issues with this concept are related to manufacturability.

### 2.2.1 Engineering Design

Preliminary tests were conducted using 3,000 fiber, 0.25-cm- (0.10-in-) diameter C braid material acquired from A&P Technology (type RM3793). The tension required to wrap a C fiber braid material around a mandrel is much less than that required for a refractory wire, simplifying heater fabrication over the design discussed in the previous section. Rough ‘checkout’ tests involve wrapping a section of braid material ( $\approx 0.6$  m ( $\approx 2$  ft)) around a 2.5-cm (1.0-in)  $\text{Al}_2\text{O}_3$  tube and connecting either end to the power supply, creating a double-ended heater design (see fig. 19). Additional tests have been performed using the 1.02-cm- (0.410-in-) OD mandrel (where the complete heater assembly would utilize the 1.6-cm (0.625-in) sheath design) that was employed in the refractory metal wire element tests (see fig. 20).

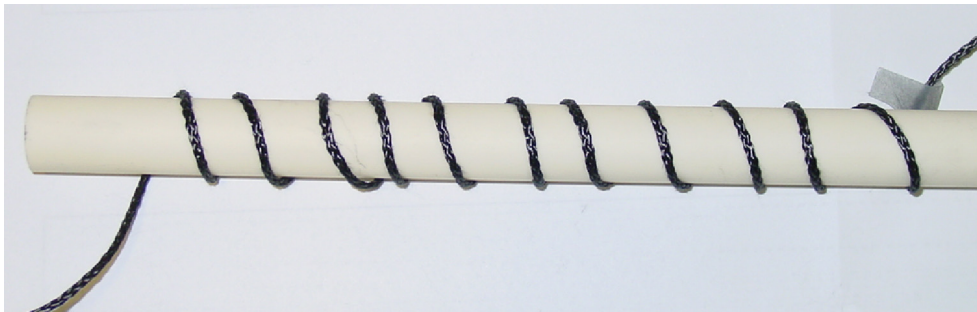


Figure 19. Double-ended C fiber braid trail: configuration for rough checkout tests.





Figure 20. Carbonized C fiber braid wrapped in a double helix fashion around  $\text{Al}_2\text{O}_3$  mandrel.

Power is provided to the C fiber braid assembly via a Mo coupler. The ends of the braid are fed through the holes at the end of the  $\text{Al}_2\text{O}_3$  mandrel, the coupler is coated with graphite cement, and the coupler is then pushed into the holes in the  $\text{Al}_2\text{O}_3$  mandrel to bond the coupler to the braid material. Copper lead wires are then connected via the Mo coupler. The electrical connection method has not yet been worked out for the carbonized version in which the Al mandrel is melted away, leaving only a stiff C coil.

An acceptable method of carbonizing the braid material, while simultaneously melting away the mandrel material (Al), must be developed if this approach is selected. This method will require a test fixture to support the mandrel during the carbonization process. The initial attempt to produce a mandrel-free carbonized element used a very simple support structure in which the element was rested in a V-shaped 'trough' such that one end of the element was higher than the other. The C fiber braid was dipped in resin (necessary to carbonize the material) and wrapped around the Al mandrel. The entire assembly, including the trough support, was then placed in a vacuum furnace to melt the Al mandrel. The resin-dipped material carbonizes at  $800\text{ }^\circ\text{C}$  or higher, and the Al melts at  $660\text{ }^\circ\text{C}$ , and once melted, just a stiff, carbonized braid should remain. In the initial test of this carbonization method, the braid was successfully carbonized and the Al melted and successfully fell away from the braid material, but a melted pool of Al remained at the lower end of the element, leaving  $\approx 90\%$  of the C composite spiral clear with the remaining 10% in the pool. Should the C fiber braid material be pursued, alternate, more sophisticated support structure designs will be investigated.

### 2.2.2 Hardware Testing

To date, versions of the C fiber braid element have been run for over 140 hr. The initial checkout tests of the material used a piece of C braid ( $\approx 0.6$  m ( $\approx 2$  ft)) that was wrapped around a constant diameter ( $\approx 2.5$ -cm ( $\approx 1$ -in)) Al tube and strung between electrical inputs, creating a single-pass spiral, double-ended heater design as shown in figure 19. The mandrel was not grooved to establish a specific pitch to the spiral for this initial rough test. This element was run for a total of 100 hr at 1,200 W, remained stable throughout the run, and the material maintained a similar appearance before and after the 100-hr test. Heating appeared to be even from end to end. At 140 Vdc from the power supply, the very high resistance of the C fiber element limited the current that could be pushed through the element, and the maximum achievable power level at 140 V was reduced. Regardless of the heater material and design, in a voltage-limited operational regime, to reach 1,200 to 6,000 W at (or less than) 140 V (allowing a 10 V margin before reaching the limitation of the power supply), a resistance of no greater than 16.3 and 3.3  $\Omega$ , respectively, is required. At the maximum 150 V that could be provided by the power supply, the measured current in the element was 6.3 A, yielding a resistance value of 23  $\Omega$ . As was noted for the graphite rod heater elements, the resistance of the C fiber braid material decreased with temperature, from 28  $\Omega$  at room temperature to the measured 23  $\Omega$  during test at 950 W. Operation of multiple C fiber braid elements in parallel would reduce the total resistance (two parallel elements would have resistance of  $R = 1/(1/28+1/28) = 14$   $\Omega$ ), but independent operation of elements at high power with a single power supply would be limited in the maximum power that could be achieved due to the high resistance.

The second test of a C fiber braid element utilized a braid material coated with resin in an attempt to lower the resistance and to allow the braid to be carbonized. This element was constructed using the 1.04-cm (0.410-in)  $\text{Al}_2\text{O}_3$  mandrel applied in the refractory metal wire heater tests, creating a double-pass, single-ended heater element (using  $\approx 0.3$  m ( $\approx 12$  ft) of braid material versus  $\approx 0.6$  m ( $\approx 2$  ft) in the previous test). Photos taken after completion of testing are shown in figure 20. The element was coated by dipping the entire assembly (mandrel and braid) in resin. This resulted in resin coating the entire surface of the element, including both the spiral-wrapped braid and the raised  $\text{Al}_2\text{O}_3$  pieces between each rotation of the braid. Because the resin is conductive, resin fully coating the element would create a dead short. To remove the excess resin from the mandrel, a buffing wheel was used to clean out the  $\text{Al}_2\text{O}_3$  between the wrapped braid. In the future, to maintain a consistent mandrel diameter after removal of the excess resin, a better method might be to manufacture the mandrel at a slightly larger than required diameter while maintaining the diameter to the lowest surfaces of the groove. After dipping the element in resin, it could then be machined down to the desired diameter. With the resin coating, 150 V produced a measured current of 7.7 A, yielding a resistance of 19  $\Omega$ —a drop of 4  $\Omega$  from the previous test. However, the resin-dipped C braid did not appear to have even heating (one end of the heater produced a dull glow relative to the remainder of the element), possibly due to an uneven coating of resin on the element. This element was tested at 1,200 W for  $\approx 10$  hr.

A third C fiber braid element was constructed using the same C braid material and was wrapped around the 1.04-cm (0.410-in)  $\text{Al}_2\text{O}_3$  mandrel, but no resin was applied to the element and the braid was not carbonized. The element demonstrated good performance at 900 W over 35 hr of run time. The power supply was set to its maximum 150 V and the current measured through the element was  $\approx 6$  A, yielding a resistance of 25  $\Omega$ .



### 2.2.3 Preliminary Conclusions

Tests run to date using the C fiber braid material have been directed toward verifying material capabilities at temperature. Initial results look promising for the power levels set forth in the requirements if elements can be operated in parallel in order to reduce the total resistance seen in the power supply. Because the  $\text{Al}_2\text{O}_3$  mandrels of the other simulator concepts have a possibility of melting at high temperature/high power combinations (the maximum recommended operating temperature of  $\text{Al}_2\text{O}_3$  is 1,800 °C), using C fiber material is quite attractive, as the material can be wrapped, carbonized, and the mandrel melted away, leaving a true C braid heater. Note, however, that the mandrel temperatures will decrease when additional heat removal methods are incorporated in the element tests. In addition to potentially higher temperature operation, the tension required to wrap C fiber is much less than that required for refractory wire, simplifying heater element fabrication.

Carbon braid has allowed continuing evaluation of C for the manufacturability of smaller diameter heaters, but continued study is necessary. For instance, it was found that when C fiber is braided, some of the fibers have a tendency to fracture (a small fraction of the 3,000 fibers used to produce the braid), resulting in a 'hairy' appearance of the braid material. This is much like taking a green stick and bending it without folding it in half, causing some fraying of the stick, but no fracture. A similar result is obtained when C fiber is braided and wrapped around a mandrel. Although the test elements exhibited this type of fraying, it did not appear to affect the integrity of the material as a heating element. However, it is desirable to better understand the behavior of the C braid material and to find a potential solution to the fraying problem so that consistent elements can be produced. This problem has been discussed with the material manufacturer, A&P Technology, and they have suggested that a heavier resin coating on the fiber may reduce fraying. The second C fiber braid heater element, which was carbonized, did not have this frayed appearance after the carbonization process.

Research and development has just begun on this concept, but the C fiber braid tests show great promise, and the primary issues with this concept are in regard to manufacturability. The effort to develop an acceptable C fiber braid heater element was temporarily sidelined to focus on the development of refractory metal heater elements. Because some of the proposed reactor concepts would incorporate refractory metals in their design, C may not be the material of choice in the heater element design due to potential interactions between C and the refractory metal at temperature. Refractory metals, however, are also adverse to  $\text{O}_2$  at elevated temperatures, which may preclude the use of an  $\text{Al}_2\text{O}_3$  mandrel for any of the proposed heater element designs. Potential incompatibilities can be averted by selecting an alternate material for the thermal simulator assembly or by altering its geometry or means of isolation from the test article. For instance, a BN coating could be applied to the C fiber-wrapped heater assembly using a vapor deposition process to provide electrical insulation and to improve materials compatibility. This coated assembly could then be inserted into a sheath of appropriate material for compatibility with the test article, or the sheath could also be built up in a vapor deposition process, with bonding provided by using a functional gradient between the sheath material and the BN coating. If the sealed assembly design is selected, development of an acceptable hermetic seal for the heater/sheath assembly will be critical to its success. This will be discussed further in the following section. Additional investigation of the various material options will address compatibility issues for the requirements set forth by the selected reactor designs.

## 2.3 Sealed Thermal Simulator Configurations

Sheathed thermal simulators are considered to prevent contamination of the reactor test article from the heater material (testing at high temperature over time can cause the heater to degrade) and to better emulate actual nuclear fuel pin designs by matching conductivity across the pin. This section addresses the initial design and analysis for a sealed thermal simulator in which the heater element is sealed inside a sheath with a low-pressure inert gas fill.

### 2.3.1 Engineering Design

Three methods are being investigated to seal the heater inside the sheath with an inert gas fill, both to prevent contamination of the reactor simulator test article from the heater element and to emulate a better model of a nuclear fuel pin. The processes currently being considered include active metal brazing, plating the ceramic coupler cap and then brazing the sheath to it, and plating (encapsulation) the ceramic to the metal interface.

To prevent contamination of the test article and to seal an inert gas (He) inside the sheath, a high integrity seal must be developed. The sheath is manufactured as a tube and two endcaps are used to provide a closed-end unit. The upper endcap (blank cap, no power feedthrough) can be welded to the body of the sheath before the heater element is inserted. On the opposite end, the metal or ceramic endcap is designed to allow the coupler to penetrate. This general configuration was shown schematically in figure 10. If a metal endcap is used, insulating material (electrically nonconductive) must be included around the coupler feedthrough surface. The metal cap could then be welded to the sheath around the OD, but it must be brazed to the coupler. The ceramic to metal interface could be plated using a vacuum plasma spray (VPS) deposition, which would create a uniform bond without any gaps, ensuring a good seal. Alternately, if a ceramic cap is used, no additional insulating material is required around the coupler feedthrough, but it must be sealed by brazing around the OD and at the coupler feedthrough. Two concerns emerged with regard to this braze as the design proceeded: (1) The desired maximum temperature of the braze joint exceeds that of current braze technology and (2) brazing in a He (or other inert gas) environment may not be possible.

Finding an appropriate high-temperature braze material to seal the sheath was difficult. Current metal to ceramic brazing technology limits the temperature of the braze joint to  $\approx 800$  °C, significantly lower than the temperature required for the original sheathed heater design ( $\approx 1,000$  °C). In the original design, the end of the mandrel was positioned  $\approx 1.9$  cm ( $\approx 0.75$  in) from the end of the sheath, where the braze joint is located. To reduce the temperature at the braze joint, the sheath and coupler were lengthened by  $\approx 7.6$  cm ( $\approx 3$  in). Investigation continues to identify a higher temperature braze so that the brazed sheath option is fully understood. Under contract with MSFC, Edison Welding Institute (EWI) is developing a metalizing seal, where the ceramic is first plated with a metal such as Ni and then brazed, providing improved bonding to  $\text{Al}_2\text{O}_3$ . Additionally, Materials Research International (MRI) is working to develop an active metal brazing technique using an alloy braze material made by Morgan Advanced Ceramics that can maintain its integrity at high temperature.

Discussions with potential vendors that would perform the braze operation also led to concerns about sealing He inside the sheath. The brazing operation must be performed in a vacuum furnace. The current assembly plan would perform this braze with the furnace filled to low pressure ( $\approx 10$  kPa ( $\approx 76$  torr)) with UHP He gas, allowing the gas to be sealed into the assembly during the sealing process. However, the additional conductivity provided by the He gas in the furnace would transfer a significantly greater amount of heat to the walls of the furnace than would be transferred by thermal radiation alone. As a result, vendors are presently concerned about increased temperatures damaging the vacuum furnace during the brazing procedure. If this concern cannot be addressed, an alternate method of filling the assembly with low pressure He may be required.

In an alternate assembly sequence, the nonlead endcap assembly could be used as a gas fill location. This could be accomplished by first welding and brazing the power feedthrough end of the assembly, and then performing the final weld of the nonlead endcap assembly in an inert gas (He) environment. If this is not possible, then an alternate solution would perform all welding and brazing of the endcaps in a vacuum environment. The nonlead endcap assembly could then be used as a fill location for filling the heater assembly with a partial atmosphere of He gas once the ends are sealed and leak checked. A 1/8-in-diameter tube connected to the nonlead endcap would be suitable for filling the heater assembly with UHP gas, and after fill, the tube would be flattened and electron beam welded to form a leak tight seal.

The primary concern that emerged from this investigation is that the desired maximum temperature of the braze joint,  $\approx 1,273$  K ( $\approx 1,000$  °C), exceeds that of current braze technology. Although a redesign of the heater sheath and coupler allowed the temperature at the braze joint (moving the joint a greater distance from the heated section), alternate solutions were pursued.

Discussions continue with potential brazing shops in an attempt to develop a high-temperature braze for dissimilar materials that will allow a gas to be sealed inside the assembly. Possible vendors include Summation Research, MRI, General Atomics, and Altair Technologies, as well as in-house engineering groups. The in-house design group has finalized machine design drawings for a brazing jig and potential machine shops to fabricate the part are being identified. While industry has successfully brazed the heater assembly components together in a manner that relieves the mechanical stress on the electrical connection, a seal that successfully captures He inside the sheath has yet to be demonstrated. Lessons learned from industry will be employed in the in-house effort, along with a redesign of some of the components.

Examination of an alternate sealing effort using a mechanical seal option for thermal simulator assemblies has been initiated. Although this type of seal would be nonhermetic, it may be acceptable if the materials selected for the reactor core and the thermal simulators are compatible over long test times at elevated temperature. If this proves to be a viable option, continued pursuit of a high-temperature braze joint may not be required. The focus of the mechanical seal development work is on manufacturing components with tight tolerances (to achieve as tight a seal as possible) and on investigating commercially available mechanical seals that could be used in the heater assembly.

### 2.3.2 Hardware Testing

A sheath design has been developed and will be sealed with a ceramic or metal cap using one of the brazing techniques discussed above. Initial tests consider the use of a graphite heater element in the sheath, as these heaters have an extensive test history and have been demonstrated to be very work-hardy in all test conditions. Future applications could consider other heater element designs, such as the refractory wire wrapped or C fiber braid designs discussed above. The sheath material or design may be altered as a function of the application. Electrical hookup varies with heater design, and integration in the reactor simulator (test article) must be taken into consideration in the overall design process.

MRI and EWI have not been successful in initial attempts to make the high-temperature braze seal. No assemblies have been received to date with He inside. The first attempt by MRI revealed a hairline crack in the  $\text{Al}_2\text{O}_3$  endcap, and a second attempt appeared to be successful, but the resistance measurements made upon receipt at MSFC indicated that all He had leaked out of the assembly. Generally, brazing shops do not handle parts that are on the order of the heater lengths ( $\approx 51$  to  $64$  cm ( $\approx 20$  to  $25$  in)) and there is a lack of sufficient knowledge on braze materials that can maintain integrity at the target sustained operating temperature of  $1,000$  °C. Additionally, vendors are reluctant to perform the braze operation inside a He-filled vacuum furnace (required to trap He in the assembly) because of the potential damage to the furnace. (Helium increases conduction to the furnace walls, potentially increasing the wall temperature above design specifications.)

### 2.3.3 Preliminary Thermal Analysis

Preliminary calculations and analyses have been conducted to assess the performance of high-temperature heater elements as bare elements and inside a sealed sheath. These analyses were performed in parallel with the testing program discussed above and, as yet, have not fed back into the element design. Thermal analyses will be utilized in refining the simulator designs. The overall goal of the test and analysis work has been to identify and evaluate candidate materials and resistive heater configurations to establish a database of design concepts that could be used to meet the requirements of the simulator designs once the particular fuel rod design options have been specified for nonnuclear reactor testing.

The initial phase of the simulator thermal analyses has focused on the following tasks:

- Assessment of simulator cross-section design, with emphasis on design aspects such as internal geometry, internal conduction, and radiation performance and enhancements. The impact of the sheath design on heater temperatures is also considered.
- Assessment of end effects and interface temperatures, particularly on the electrical leads.

As stated, these analyses are preliminary in nature and sophistication, and it is expected that, as the development proceeds, the complexity and specificity of these analyses will increase. A brief synopsis of the results generated thus far is provided in the following sections. Most of the analyses were performed using Mathcad or SINDA/FLUINT. More details of each analysis are provided in appendices H and I.

**2.3.3.1 Cross-Section Analysis.** The primary focus for the simulator cross-section analyses was to identify and evaluate means of enhancing the heat transfer from the resistive heater element to the sheath. Figure 21 shows the basic sheathed heater configuration and associated dimensions used for the cross-sectional thermal calculations. Improving the heat transfer across the gap reduces the heater temperatures that are reached for a given input power due to the greater efficiency of transferring the heat into the core. (Input power is selected so that the entire heater/sheath assembly mimics the power and temperature for a nuclear fuel pin in a given reactor design.) Reducing the heater temperatures allows consideration of a greater variety of heater materials and design options and potentially increases heater element life.

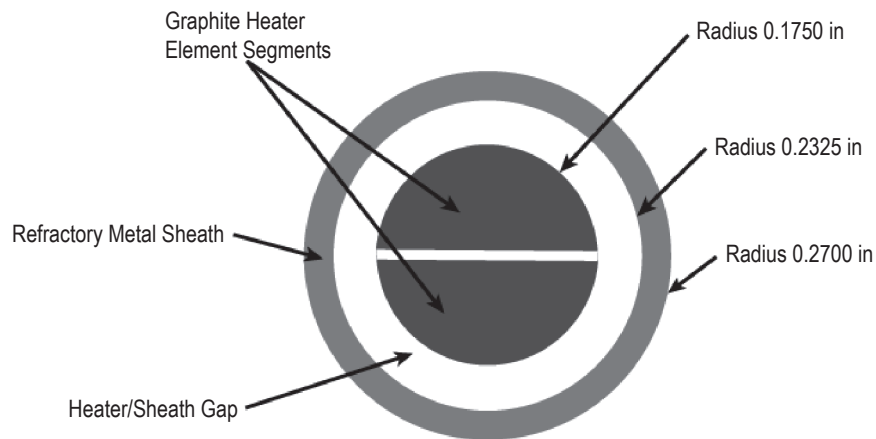


Figure 21. Basic configuration of the proposed heater/sheath geometry (not to scale).

The heater/sheath length used for the various calculations was 50.8 cm (20 in). While this solid graphite heater element configuration was used as the basis for the calculations, most of the trends identified in the analysis will still hold for other heater configurations, such as braided or solid wire wrapped around a ceramic insulating mandrel. The majority of the thermal analyses applied a heater power of 6,000 W to establish a conservative estimate of the maximum temperature differential that might be observed across the heater/sheath gap. All cross-section analyses considered a constant sheath temperature of 1,273 K to represent a target heat source (fuel pin) temperature that was assumed to be isothermal. In practice, the heater power and desired heat source temperature (at the sheath surface) will be specifically selected for each reactor design and test condition.



Enclosing the heater element in a sheath introduces a series of thermal resistances that must be overcome to transfer heat from the heater element into the reactor simulator. While the sheath provides some thermal resistance, the relatively high thermal conductivity of the metal composing the sheath transfers heat efficiently. The gap between the heater and the sheath and possibly the gap between the sheath and reactor core introduce the most significant resistances from the heater to the core block. Initial designs consider a heater/sheath gap that is filled with either a low conductivity inert gas or is under vacuum conditions. Under vacuum conditions, the primary mode of heat transfer is thermal radiation. When the gap is filled with an inert gas, the dominance of radiation versus conduction is dependent on temperature, emissivity (of both the heater element and sheath), and gap size. As the gap size increases, the benefit of conduction in removing heat from the element decreases. While the high operating temperature of the heater improves the radiative heat transfer, the thermal resistance is still appreciable. Use of radiative heat transfer alone to move heat from the heater to the sheath necessitates relatively high heater temperatures to reach the desired sheath temperature and input power. A number of configuration changes were identified to enhance the heat transfer across this gap, including:

- Selecting the proper gas to fill the gap.
- Reducing the size of the gap.
- Increasing the radiative properties (absorptivity and emissivity) of the heater and sheath.
- Adding conductive gap fillers, such as powders or solid liners.

Each of these suggested modifications are described below with their potential enhancements. The level of enhancement is quantified in terms of two values: the thermal conductance and the temperature differential across the gap. The temperature differential is that difference in temperature between the heater and the sheath necessary to transfer 6,000 W between the two.

2.3.3.1.1 Improvement of Thermal Conductance Due to Gas Selection. The gas selected for use inside the sheath at these extremely high temperatures should be nonreactive to preserve the integrity of the heater and sheath materials and to prevent contamination of the test article (reactor simulator) if the gas leaks out of the sheath containment. As such, the use of inert gases, such as Ar, He, and xenon (Xe), should be considered for inclusion into the sheathed heater design. As indicated by the thermal conductance values summarized in table 8, He is by far the most thermally conductive of the gases considered. Note that the values provided are solely based on conduction across the gap and correspond to gas properties at the sheath temperature of 1,273 K. A more accurate estimate of the gap conduction would allow the gas conductivity to vary depending on the local gas temperature as well as the sheath and heater temperatures. Because gas conductivity typically increases with temperature, the expected thermal conductance would increase if the average temperature were applied rather than the temperature at the sheath. Hence, the effective gap conductances presented in table 8 may provide a conservative (low) estimate of the heat transfer across the gap.

Table 8. Effective gap conductance for different inert gases based on geometry depicted in figure 21 (radial gap size: 0.15-cm (0.058-in)) properties at 1,273 K).

Gas in Gap	Thermal Conductance (W/K)
He	4.8
Ar	0.56
Xe	0.29

Derived properties: He,<sup>10,11</sup> Ar,<sup>12</sup> Xe,<sup>11,13</sup>

2.3.3.1.2 Reduction of Gap Size. The thermal conductance of He, which is an order of magnitude higher than that of either Ar or Xe, necessitates a temperature differential of over 1,251 K across the gap to drive 6,000 W from the heater to the sheath. To maintain a sheath temperature of 1,273 K would require the heater temperature to be over 2,400 K. The temperature differential required for Ar or Xe fill gas would be significantly greater. Other gases, such as halogens, can be evaluated, with special attention given to their potential for reacting with the sheath or heater materials.

2.3.3.1.3 Reduction of Gap Size. The thermal conductance of a gas-filled gap roughly scales with the reciprocal of the gap size. As the gap size is reduced, the conductance can increase significantly. For example, at the current radial gap size of  $\approx 0.15$  cm ( $\approx 0.058$  in) the gap conductance (considering conduction alone) through the He gas is  $\approx 4.8$  W/K, as listed in table 8. However, if the radial gap size is reduced to  $\approx 0.25$  mm ( $\approx 0.010$  in), the conductance improves to over 26 W/K (gas conduction alone). This reduces the temperature differential from 1,251 K (gap size 0.15 cm (0.058 in)) to  $\approx 225$  K and results in a heater temperature of  $\approx 1,500$  K (versus 2,400 K for a gap size of 0.15 cm (0.058 in)) to maintain the sheath at 1,273 K. Appendix H provides a curve of conductance and temperature differential for a number of other gap sizes.

Although small gap sizes improve the heat transfer from the heater element to the sheath, small gaps introduce concern over achieving tight manufacturing tolerances, the ability to assemble the thermal simulator, and the effects of differential thermal expansion at elevated temperature, which could result in inadvertent electrical contact between the heater and sheath. Coating the heater element with a dielectric material, such as BN, before inserting it into the sheath could prevent heater to sheath shorting even if the element were to bow at elevated temperatures. If the gap width is reduced by increasing the sheath wall thickness, while maintaining a constant sheath OD, then the axial conductance of the sheath will increase due to the additional material. This increased axial conductance can diminish any axial temperature gradients (power profile) designed into the heater to match the heat distributions inherent in the nuclear fuel rods. Therefore, the complete heater/sheath assembly must be considered when tailoring the heater profile to achieve the desired heat flux profiles.

2.3.3.1.4 Sensitivity to Optical (Thermal Radiative) Properties. At the high temperatures achieved in the heater testing for application to nonnuclear testing of a reactor simulator (in concert with the low conductive and convective conditions), radiative and conductive heat transfer contribute almost equally to the heat transfer across the heater/sheath gap. Table 9 provides estimates of the temperature differential across this gap for conduction, radiation, and their combined

effects. These calculations assume a gap width of 0.15 cm (0.058 in) per figure 21. For contribution due to conduction, the annular gap was filled with He gas at a pressure of 101 kPa (760 torr). For the radiation-only calculation, a vacuum gap was assumed.

Table 9. Relative effect of radiation and gas conduction for baseline simulator geometry.

Configuration	Temperature Differential (K)
Gas conduction only	1,251
Vacuum gap (radiation only)	1,242
Gas conduction and radiation	763

The radiative heat transfer calculation in table 9 assumes that the heater and sheath are diffuse and gray. Their respective emissivities are 0.5 (representing a mid-range emissivity ceramic substrate, such as  $\text{Al}_2\text{O}_3$  or BN instead of the graphite heater element) and 0.2 (representing a clean/slightly polished metallic sheath, such as stainless steel or a refractory metal). Using gas conduction in coordination with radiation significantly reduces the temperature differential across the gap, demonstrating the benefit of having a gas filled versus a vacuum gap in the thermal simulator design.

The temperature differential across the gap can be further reduced by increasing the emissivities of the heater and sheath surfaces. Table 10 provides the estimated temperature differentials that would result from using various combinations of surface optical properties. The conditions used for these calculations are based on the geometry depicted in figure 22. A sheath temperature of 1,273 K is imposed, and the sheath is assumed to be isothermal. These calculations suggest a few possible design enhancements that could be pursued. First, the emissivity of the sheath inner surface may be enhanced. This may be possible by coating the inner surface with a high emissivity material or by chemically reacting ('oxidizing' or 'nitriding') the surface to create a stable, high emissivity surface. Emissivity coatings that may be applicable to the heater design are currently under development via a small business innovative research (SBIR) contract with MSFC. Note that chemically modifying the sheath inner surface could adversely affect the sheath if it is constructed from a refractory metal. Alternately, the heater element design could be altered or its component materials could be selected to enhance the emissive properties. The analyses discussed thus far have assumed that heat transfer from the heater to the sheath is relatively insensitive to the heater type (a solid graphite resistive element or spiral wound braid or wire, such as C fiber, Re, etc.). However, the emissivity of each of these potential heater elements is significantly different, so that the radiative heat transfer across the heater/sheath gap is highly dependent on the selected materials. The solid graphite used in heater designs tested in multiple test articles at the EFF-TF has an inherently high emissivity. For wire/mandrel heater configurations, other high emissivity ceramic substrates, such as weapons grade aluminum nitride (AlN), could also be investigated to enhance the emissive properties of the heater.



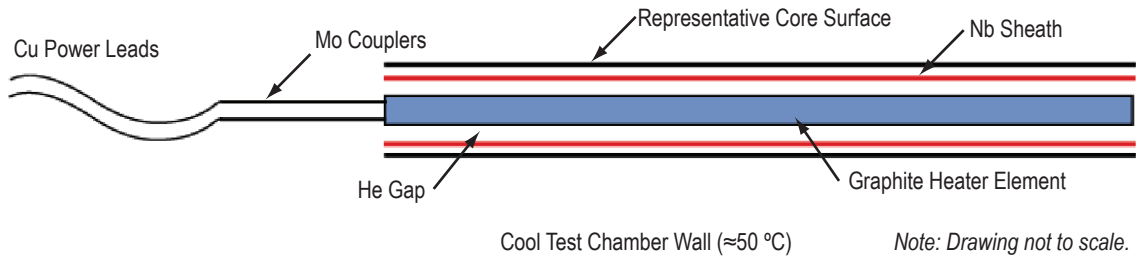


Figure 22. Approximate geometry used in the SINDA model.

The results presented in table 10 indicate that enhancing either the sheath or the heater should improve the performance of the heater assembly by improving radiative heat transfer across the gap. Improving the sheath inner surface emissivity from 0.2 to 0.7 appears to induce a more significant reduction in the temperature differential than changing the emissivity of the heater surface. Combining both emissivity enhancements reduces the temperature differential still further. As some of these enhancements require coatings or chemical treatments, subsequent evaluation and testing are required to ensure chemical compatibility and longevity of the altered designs. While the addition of gas to the heater/sheath gap will improve the overall performance of the thermal simulator, reducing its temperature and possibly improving the longevity of the heater assembly, it could also retard outgassing of the emissivity coatings, improving the integrity of the coatings over long test times.

Table 10. Thermal performance of combinations of optical property enhancements (assuming radiation heat transfer only).

Heater Emissivity	Sheath Emissivity	Temperature Differential (K)	Comments
0.5	0.2	1,242	Ceramic heater substrate—slightly polished sheath inner surface
0.5	0.7	840	Ceramic heater substrate—coated or chemically modified sheath inner surface
0.9	0.2	1,130	Graphite style heater element or high emissivity ceramic substrate—slightly polished sheath inner surface
0.9	0.7	637	Graphite style heater element or high emissivity ceramic substrate—coated or chemically modified sheath inner surface

2.3.3.1.5 Conductive Gap Fillers. An alternative way to further enhance heat transfer across the gap is to fill the gap with a more conductive material (nongas). This could entail filling the gap with a thermally conductive, electrically isolating powder (BN powder) or inserting a single solid liner (or a segmented solid liner) having the same thermal and electrical attributes (thermally conductive, electrically isolating). In a recent microgravity experiment development activity, BN powder was studied as a gap filler in a similar application that required enhanced conduction at high temperature.<sup>14</sup> This concept has a number of advantages including enhanced thermal performance, electrical isolation, geometric conformability, and tolerance of differential thermal expansion. However, previous experience indicated that it was difficult to uniformly distribute and pack the powder to prevent axial or circumferential voids, leading to nonuniform heat distribution. The solid liner concept is an attempt to address this packing issue. This liner would essentially consist of a ceramic

tube sized to fit in the gap between the heater and the sheath, consuming as much of the gap as possible to minimize the resulting circumferential voids between the heater and the sheath. Table 11 provides preliminary calculations for these two concepts. Both cases use BN ceramic, in a powder or solid liner form. The assumed heater/sheath gap (unfilled) is  $\approx 0.15$  cm ( $\approx 0.058$  in) as in the previous analyses. Either approach to filling the heater/sheath gap must take into account thermal expansion at elevated temperature in producing the final assembly design.

Table 11. Performance of conductive gap filler concepts.

Configuration	Temperature Differential (K)	Comments
BN powder w/He	220	Properties of He at 1 atm are used — powder assumed uniform
BN liner w/He	228	Liner thickness = 80% of original gap thickness

The suggested conductive gap configurations could significantly reduce the temperature differential between the heater and the sheath, allowing the target sheath temperature to be maintained at heater temperatures that are quite manageable for a number of materials. While both concepts produce similar temperature differentials, it is important to note the sensitivity of each to the presence of He. The powder concept will produce slightly degraded, but still useful, performance if the He is not present in the interstitial gaps between the grains of powder as was observed in previously discussed testing for the microgravity experiment. (This design utilized a different powder material.) Although some voids may exist in the absence of He, the acceptable performance is likely a result of the particle-to-particle contact that exists whether the He is present or not. On the other hand, if no He is present in the liner concept, then there is only radiation across the smaller gaps that are not filled by the liner. Because there are now two serial gaps where there used to be only one, the liner acts as a radiation shield, which actually increases the radiative resistance and increases the temperature differential. Consequently, the solid liner appears to have merit only for a gas-filled gap configuration.

A BN layer could also be added by a method such as plasma vapor deposition, which could apply a solid layer to increase the element diameter to correspond to just less than the ID of the sheath, allowing it to be inserted with minimal gap. Addition of this layer would not only enhance electrical isolation, but could enhance thermal performance by shrinking the gap, as just mentioned, and by increasing the emissivity of the wire or braid being coated. However, consideration of differential thermal expansion is critical. Centerless grinding could also be used to grind the element to the appropriate size to slide into the sheath if it is built up to a slightly larger diameter. This technique can meet  $\pm 0.076$  mm ( $\pm 0.003$  in) variation on the element OD, allowing the gap between the element and the sheath to be as small as possible. Plasma vapor deposition could also be used to build up the sheath, setting a fractional gradient to transition from the BN layer to the sheath material to establish a strong bond between the materials without any gap. The sheath could be built up to a diameter that is slightly greater than that required, so that it could then be ground to the proper diameter using the centerless grinding technique. One potential concern associated with a full buildup of the simulator using plasma vapor deposition (allowing no gaps between component layers) is differential thermal expansion of the various materials used in the simulator. Additional analysis would be required to ensure that the individual simulator layers would not be subject to cracking during test at elevated temperatures.

Each of the suggested modifications to the sheathed thermal simulator design (addition of gas, reducing the gap size, improving the emissive properties of the components, or adding conductive gap fillers) was shown to improve the overall heat transfer across the gap and to lower the heater temperature necessary to drive the required heat flux. In most cases, potential weaknesses of each concept were also briefly identified. While the selection of a specific heater/sheath assembly would likely depend on the specific application, including the desired temperature and power levels, the most straightforward design modifications would be to add He gas to the gap (assuming the He gas can be contained) and to shrink the gap size either by enlarging the heater diameter or by shrinking the sheath ID. The final assembly design will be based on reactor design constraints and heater capabilities.

2.3.3.1.6 Impact of the Sheath on Thermal Performance. The impact of encasing the heater inside a sealed sheath on the heater temperatures was also assessed. In the typical heater element test setup, a bare heater is suspended in the center of a large stainless steel vacuum chamber and electricity is applied. The test specimen is allowed to run in this condition for extended periods of time, after which it is removed and examined to evaluate its tolerance of high temperature conditions. For the general surface characterization of the test chamber, the inner surface of the chamber is assumed to be uncoated and free of significant oxide buildup or grime, providing a basis for estimating surface emissivity. A simple analysis was performed to estimate the test conditions for comparison of the expected bare element temperatures with the expected temperatures for the element encased inside the sheath and put under the same load. Initial calculations assumed heat removal by radiative heat transfer alone. The results of this analysis are provided in table 12. The analysis assumed a vacuum environment around the heater and inside the sheath, and as previously discussed, gas conduction would help to significantly reduce the sheath configuration temperatures. In all cases, calculations assumed a constant diameter graphite rod heater configuration. Similar scoping calculations for a braided W wire heater element were presented in section 2.1.2.4. Calculations allowed the sheath temperatures to float while maintaining the vacuum chamber wall temperature at a constant 50 °C.

Table 12. Impact of the sheath on heater temperatures experienced in vacuum testing.

Configuration	Heater Power (W)	Sheath Temp (K)	Heater Temp (K)	Comments
No sheath	1,000	–	1,096	–
Sheath	1,000	1,422	1,740	Sheath emissivity = 0.2
No sheath	6,000	–	1,712	–
Sheath	6,000	2,224	2,726	Sheath emissivity = 0.2
Sheath	6,000	1,638	2,057	Sheath emissivity = 0.7

Table 12 summarizes results that indicate that the sheath acts like a radiation shield, imposing a significant thermal resistance the value of which depends primarily on its optical properties and operating temperature. However, encasing the heater element inside a sheath more closely approximates the geometry of a nuclear fuel element for use in the nonnuclear test article (while the bare heaters offer convenient testing options, in practice, these heaters will probably never be used in a bare configuration). These results also suggest that care should be taken in

selecting the proper sheath and power combinations to avoid over-temperature conditions within the sheath or heater materials. Finally, while most of the endurance testing has been completed (in most cases without a sheath present), additional high-temperature endurance testing of materials may be warranted once the design space (operating temperature, power level, heater design, sheath design, etc.) has been narrowed to evaluate these materials at or near use conditions. Note that in the test article configuration, the reactor coolant system (LM HPs, pumped gas, or pumped LM) will actively remove heat from the surface of the sheath and heat removal will no longer be solely by radiation to the vessel wall, significantly reducing the heater and sheath temperatures relative to the single element (heater and sheath) testing for the same power level. For instance, the sheath temperatures indicated in table 12 would be on the order of 1,400-1,500 K (core block temperature  $\approx 1,273$  K) at full power (6 kW per pin) in a cooled core case, resulting in a lower heater temperature for the same power level.

**2.3.3.2 Assessment of End Effects and Heater Lead Wire Thermal Conditions.** In addition to examining the gross performance and design of the heater and sheath, the end effects and thermal conditions within the electrical lead wires and Mo transition pieces (couplers) are also of interest relative to potential material-over-temperature conditions. The present analysis considers a graphite rod heater element and Cu wire leads. Molybdenum transition pieces are used between the Cu wire and the graphite to reduce the temperature experienced by the Cu leads.

A simplistic SINDA model was constructed to analyze the thermal conditions within this assembly and the basic components of the model are shown in the sketch provided in figure 22. The dimensions of the graphite heater rod assembly (heater and sheath) were provided in figure 21. A constant diameter graphite rod heater (0.89-cm- (0.350-in-) OD) is assumed for these calculations for both uniform and cosine-shaped power distributions. The cosine-shaped axial power distributions apply a peak to average power factor of 1.33. The heater is enclosed in a Nb sheath having the dimensions previously cited in figure 21. The heater/sheath gap and the sheath/core block gaps are filled with He at 101 kPa (760 torr) and no emissivity enhancements are considered. A brief investigation was performed to determine the effect of gas pressure on the conductance across the heater/sheath gap. As discussed in section 2.3.1, the intended pressure in the heater/sheath gap is 10 kPa (76 torr). For the given gap width (0.15 cm or 0.058 in), the gas is still in the continuum flow regime at this pressure. (It begins to approach the mixed flow regime at  $\approx 4$  kPa ( $\approx 30$  torr)) and the difference in gas conductivity at 101 kPa versus 10 kPa is  $<0.1\%$ .

The graphite heater design is single ended, so the input and output power leads are at the same end of the graphite element. Each lead is connected to a 10.2-cm- (4-in-) long Mo transition piece (coupler). The details of the connection were not incorporated in the model, but the connection between the Mo and the graphite is assumed to be intimate (or near ideal) with no additional resistance modeled between the two materials. Each Mo piece, in turn, connects to a Cu lead wire. Both the Mo and the Cu wires are sized to American wire gauge (AWG) 11. The connection between the Mo and the Cu wires is also assumed ideal with no thermal resistance modeled between the ends of each piece. The Cu wires were extended to 0.9 m (36 in) in length.

As previously stated, the heater is enclosed in the Nb sheath and transfers heat to the sheath via thermal radiation and gas conduction with heater and sheath emissivities assumed to be 0.9 and 0.3, respectively. In the cross-sectional analyses, the sheath temperature was assumed fixed. In this analysis, however, the sheath temperature is allowed to reach a value necessary to transfer the heater power to a core boundary condition. The boundary is intended to represent the fuel tube (clad) or core block in which the heater/sheath assembly is inserted. In this case, the HP reactor design, which does not include a fuel clad, is assumed and the boundary condition is set to 1,325 K, equivalent to the expected boundary condition on a HP-cooled reactor design. The radial gap between the sheath and the core block is assumed to be 0.25 mm (0.010 in), and is assumed to contain pure He.

In the thermal model, the sheath rejects heat to the representative core boundary by thermal radiation and gas conduction and the core inner surface emissivity is assumed to be 0.3. A limited amount of heat may also transfer from the sheath to the boundary through low pressure line and point contacts and through end welds or seals, but this is not yet modeled. Thermal analysis using radiative and conductive heat transfer (through the He gas) establishes temperature trends. However, the current model does not currently include temperature-dependent electrical resistivity, so to obtain more realistic correspondence between heater input power and heater temperature, subsequent improvements must be incorporated.

The Mo couplers are assumed to be adiabatic (neither Mo piece is allowed to exchange heat with any boundary directly; it only exchanges heat with the heater element and the Cu wire), providing a conservative estimate of the temperatures reached in these pieces. The Cu lead wires are allowed to radiate to a cool boundary (50 °C). This assumption may be somewhat unrealistic given the proximity of the leads to the reactor body, unless active cooling of the electrical interface is employed (as would be the case for a gas-cooled reactor design). Heat generated in the Mo couplers and Cu lead wires (by virtue of the  $\approx 60$  A current flowing through them) is also included in the model. In one case (case 6 in table 13), the ends of the Cu lead wires are assumed to be clamped to the cool 50 °C boundary, providing cooling via contact conductance (simulating the Cu wire attachment to the power feedthrough at the chamber wall).

Table 13. Summary results from SINDA heater simulation (temperatures are in K).

Case	Cu Lead		Mo Transition		Heater Element		Sheath		Comments
	Min	Max	Min	Max	Min	Max	Min	Max	
Case 1	778	1,069	1,107	1,475	1,468	1,471	1,348	1,349	1 kW; PPF*=1
Case 2	778	1,085	1,126	1,547	1,545	1,813	1,362	1,417	3 kW; PPF=1.33
Case 3	778	1,119	1,165	1,707	1,709	1,712	1,394	1,395	3 kW; PPF=1
Case 4	778	1,122	1,168	1,720	1,723	2,153	1,398	1,508	6 kW; PPF=1.33
Case 5	778	1,176	1,232	1,985	1,993	2,001	1,462	1,464	6 kW; PPF=1
Case 6	332	1,121	1,168	1,720	1,723	2,153	1,398	1,508	6 kW; PPF=1.33; cooled lead end

\*power peaking factor

Based on the design of the graphite heater element, the axial power profile could be uniform (constant heater diameter) or could exhibit a simple cosine distribution along its length (smaller heater diameter at the axial center of the heater) to approximate the heat flux profile of a fuel rod in a nuclear reactor. The model considers both uniform and shaped power distributions but, a constant element diameter (0.89 cm (0.350 in)) is assumed in both cases. The SINDA model discretizes the heater into 100 equally sized nodes (0.51 cm (0.2 in) per node).

At present, the model has not been correlated with test data. Consequently, the characteristics observed in the results are subject to change once the model has been verified. A number of cases have been run to characterize the general heater element configuration. Summary results are provided in table 13. Plots of temperature versus axial position (for the heater element, sheath, couplers, and lead wires) are provided for cases 2 and 3 (3 kW, cosine and flat power distributions, respectively) in figures 23 and 24. The corresponding plots for the remaining cases are included in appendix I.

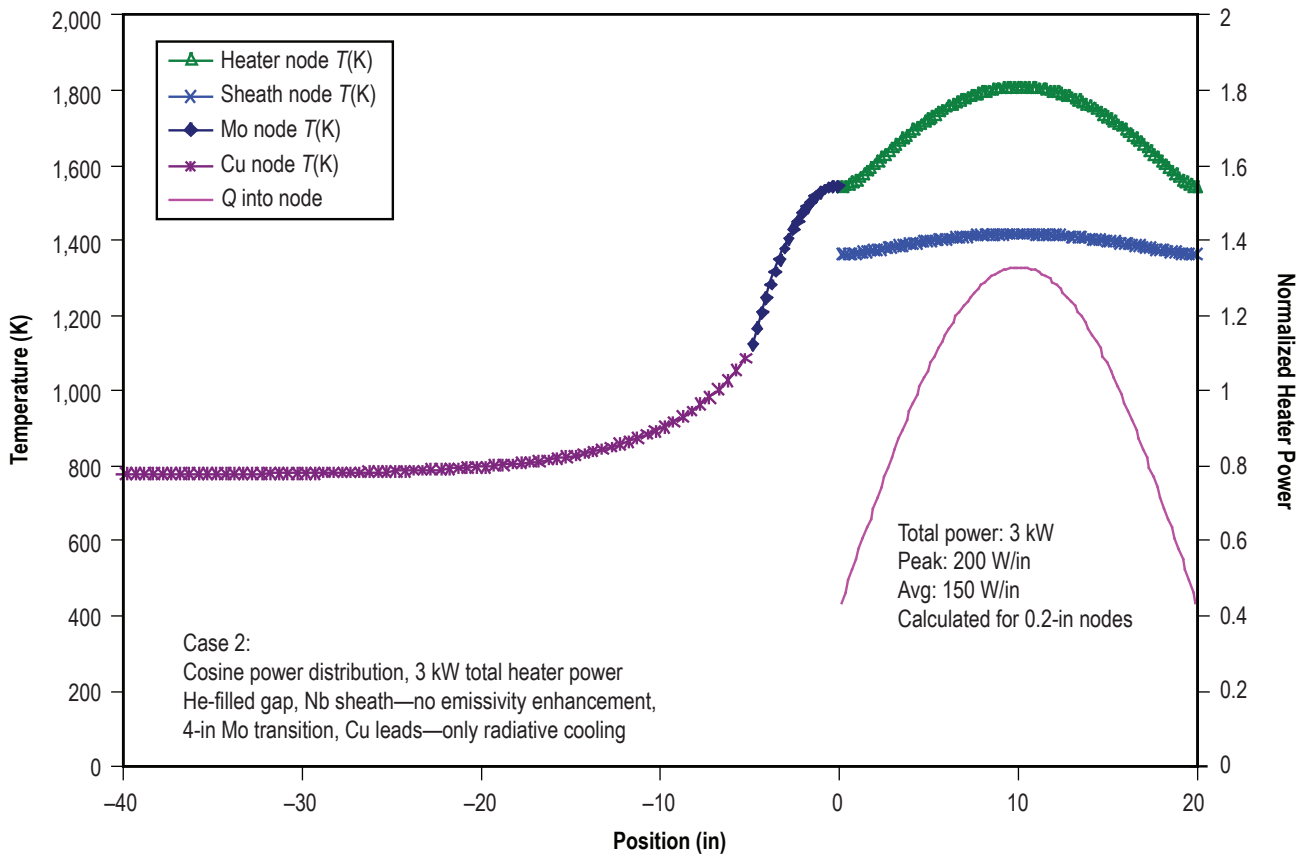


Figure 23. Axial temperature profile for case 2.



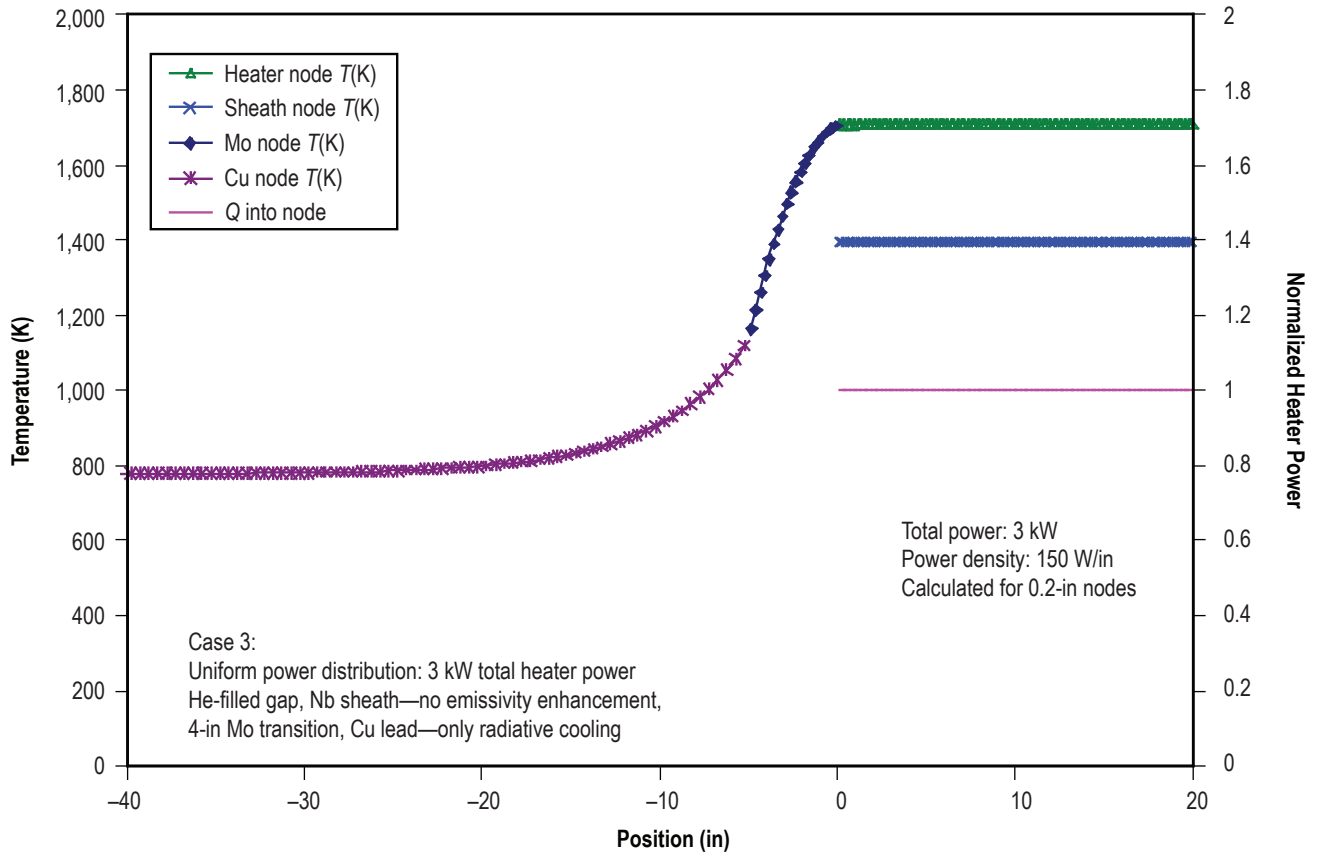


Figure 24. Axial temperature profile for case 3.

Figure 23 and 24 show the temperature profile for various components of the heater/sheath assembly for cases 2 and 3. Both cases assume 3 kW total heater power ( $Q$ ), applying a cosine power distribution with a power peaking factor (peak to average power) of 1.33 (fig. 23), or a uniform power distribution (fig. 24). This input power is calculated at each node-defined heater node in the model and is indicated as ‘ $Q$  into node’ in the corresponding plots. As discussed previously, the model assumes a graphite heater element encased in a Nb sheath (no emissivity enhancements) with a He-filled gap and power input is provided via 10.2-cm (4-in) Mo transition pieces (couplers) connected to Cu leads wires. A position of zero on the  $x$ -axis corresponds to the start of the heater and negative position corresponds to the lead wires and transition pieces.

The current analysis applies a constant cross section for both power distributions. To accomplish a shaped power distribution with a graphite rod heater, the diameter of the element is reduced for a portion of its length at the axial center of the element. The estimated temperatures (using a constant cross section) are probably lower than they might be if the cross section had been contoured because (1) the constant cross section probably helps reduce temperature gradients by maintaining a larger heat flow path, (2) the contoured element has less surface area, driving up the temperatures necessary to reject the local heating, and (3) the gap between the graphite and the sheath is increased, at the center of the contoured element, reducing the heat transfer by conduction across the gap. Because the wire-wrapped heater elements have a constant diameter regardless of power profile

(the profile is accomplished by varying the pitch of the wire wrap rather than by contouring the element diameter), the differential heat transfer for the flat versus shaped power profiles will not present the same difficulties as noted for the graphite elements.

In case 2, the sheath temperature varies from 1,362 to 1,417 K in order to reject the heater power to the 1,325 K boundary representing the core block. The maximum heater temperature reaches 1,813 K. The temperature differential between the sheath and the heater varies with the local heat input. A slight elevation is seen in the temperature of the transition piece for this case. The local maximum results from the fact that the heat generated in the Mo transition is not allowed to transfer directly to any boundary. The Cu wire, on the other hand, exchanges heat radiatively with the cool boundary (chamber walls), causing its temperature to drop despite the fact that heat is being generated in it due to electrical resistance. The Cu reaches a fairly uniform temperature once it is well away from the coupler. The heater temperatures for case 3, which assumed uniform power distribution, was  $\approx 1,712$  K (calculations indicate a range of 1,709 to 1,712 K) and the sheath temperature was 1,395 K. Because the local heat input was uniform along the length of the element, the temperature differential between the sheath and the heater was nearly constant.

In examining the results of the various cases, a number of characteristics are observed. First, by allowing the sheath temperature to vary, the sheath and heater temperatures are higher than were seen in the cross-sectional analysis as a result of the differences in the established boundary conditions. Cross-section analyses fixed the sheath temperature at 1,273 K; the current analysis establishes a reactor boundary condition (a core block temperature of 1,325 K) outside the sheath and adds a significant resistance between the sheath and the reactor boundary. The resulting increased sheath temperature illustrates the significance that the external (to the sheath) heat rejection efficiency can have on the operation of the heater assembly.

Second, the 10.2-cm (4-in) Mo transition pieces appear to sufficiently reduce the temperature extremes seen in the Cu lead wires. The addition of low-pressure, high-purity gas in the test chamber would provide additional reduction in the Cu lead temperatures. Given cooling by radiation alone, the Cu temperatures near the Mo interface do not exceed 1,176 K, which is well below the melting point of Cu (1,358 K). Further analyses are planned to evaluate the impact of lengthening the Mo couplers to assess the impact of this parameter on the temperature of the braze joint. Given that ideal connections were assumed in the current model, the details of the interface between the Mo and the Cu leads should be evaluated more closely. Various options may be available to enhance the cooling of the Cu, but this depends strongly on the reactor simulator design constraints. In the current model, the Cu emissivity was assumed to be 0.1. More detail is needed to examine the thermal impact of the various electrical insulation options under consideration.

Third, for most of the cases evaluated, the temperature at the end of the Cu opposite the heater is allowed to float (boundary condition set to  $dT/dx = 0$  at the end of the Cu lead). This is probably not realistic and, in fact, produces a temperature that may adversely impact electrical connections outside the chamber. In case 6, the end was assumed to be clamped in such a way that it could be cooled via a contact conductance to the 50 °C boundary (simulating the Cu wire attachment to the power feedthrough at the chamber wall). This cooling was based on performance achievable with typical thermal compounds used to cool electronics. In this case, the

clamped end of the Cu cooled down substantially, as expected, but the temperature of the end in contact with the Mo transition was not reduced due to the relatively long length of the lead wires.

Finally, it appears that the heater temperature profile, while impacted slightly by the heat transfer through the transition and lead wires, is not very sensitive for the cases evaluated.

## 2.4 Tantalum Wire-Wrapped Heater Element

Initial Ta wire-wrapped heater elements were fabricated using a 1-mm (0.040-in) wire wrapped around the 1.16-cm (0.460-in)  $\text{Al}_2\text{O}_3$  mandrel. As discussed in section 2.1.2.1, these element tests indicated exceptional performance at 1,200 W, with the tested element achieving 101 hr of operation in vacuum, accumulated over multiple thermal cycles. The goal of the tests discussed below was to reach 6 kW per element and to operate the element for a minimum of 100 hr at this elevated power. Both 0.5- (0.020-in-) and 0.64-mm- (0.025-in-) diameter Ta wires, configured in a three-wire braid, were tested.

### 2.4.1 Element Testing in Vacuum

Four separate attempts were made to test braided Ta wire in vacuum, considering both sheathed and unsheathed configurations. In each case, the heater element was constructed from three braided Ta wires and both 0.5- (0.020-in-) and 0.64-mm- (0.025-in-) diameter wires were attempted.

**2.4.1.1 Test 1: Tantalum Three-Wire Braid, Sheathed, Vacuum Environment.** The first and second elements tested were encased in a Mo sheath. These tests were terminated when the Ta wire shorted out to the sheath during the test. Because of thermal expansion, the wire contacted the sheath when it achieved operating temperatures. Therefore, for this wire diameter, the groove depth cut into the mandrel (currently 1.6 mm (0.063 in)) should be increased to prevent the wire from expanding beyond the edge of the mandrel and coming into contact with the sheath. Additionally, the transition of the wire from the spiral wrap through the hole that prevents unwrapping, shown in figure 25 with design details shown in appendix J, should be improved. Because of the limited ductility of the wire, this transition was not smooth in the constructed heater elements, which caused the wire to sit slightly above the  $\text{Al}_2\text{O}_3$  mandrel and allowing easier contact with the sheath.

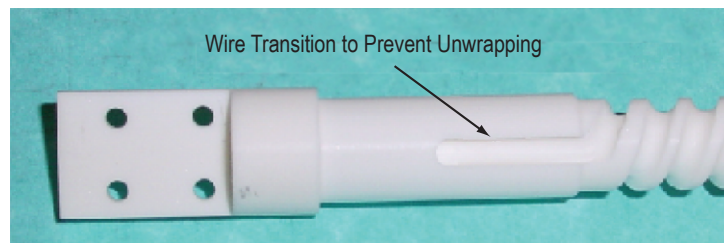


Figure 25. Wire transition from the spiral wrap at end of mandrel (complete mandrel design with dimensions is included in figure 65).

**2.4.1.2 Test 2: Tantalum Three-Wire Braid, Unsheathed, Vacuum Environment.** The third and fourth Ta vacuum tests were performed without the sheath. The third attempt ended when the lead wire sagged sufficiently to contact the Ni foil used to support the TC connector. No real damage to the heater was observed, but one power lead was slightly shorter after the event. The same heater element (0.64-mm (0.025-in) three-wire braid) was reconnected for the fourth attempt. In this attempt, 6,000 W was achieved and held for 3.5 hr. However, heat removal by radiation alone, resulting from operation in vacuum, was insufficient at this power level. As a result, the heater reached excessive temperatures and subsequently melted, as seen in figure 26. Tests of the Ta heater element were repeated in a high-purity He gas environment, as discussed in the following section.

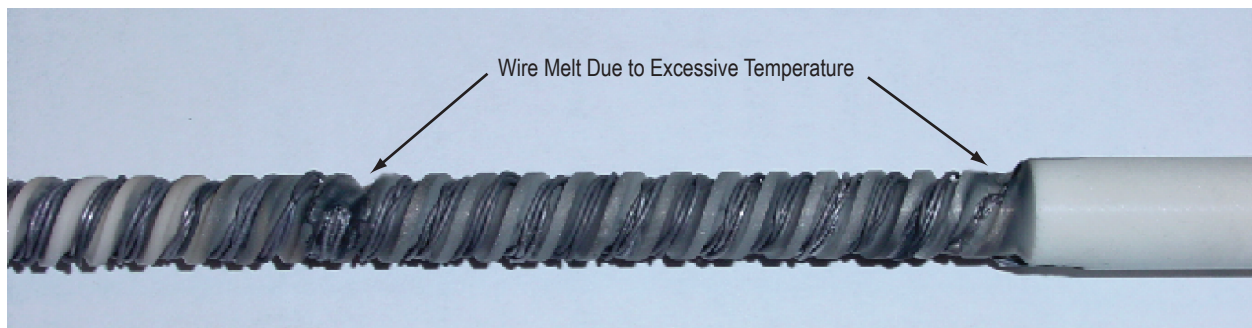


Figure 26. Posttest TA heater assembly showing wire failure.

## 2.4.2 Element Testing in Helium Environment

For subsequent Ta element testing, a bottle of UHP He gas was connected to the test chamber to allow for backfill of the chamber to a low pressure. This bottle will be replaced by the gas purification system when it is ready for operation (see sec. 3.1). The addition of He to the chamber allows heat to be removed from the element by conduction in addition to radiation, significantly reducing the operating temperature of the heater element.

**2.4.2.1 Test 1: 0.5-mm (0.020-in) Tantalum Three-Wire Braid, Sheathed, Helium Environment.** A 0.5-mm (0.020-in) Ta three-wire braid element was assembled using the 1.17-cm- (0.460-in-) diameter  $\text{Al}_2\text{O}_3$  mandrel. This element was installed inside a 1.37-cm (0.540-in) Mo sheath for testing at 5.5 kW. After a ramp up to the desired 5.5 kW over  $\approx 45$  min, the element operated for  $\approx 7$  hr with no observed problems (fig. 27). Shutdown was required at the end of the work day. On the subsequent test day, the element failed when it was brought up to 6 kW of power from a cold condition at the start of the test. At low temperature, the resistance of a refractory metal element is low and then increases as the element temperature increases. Because the full power was applied at the start of the test, it is likely that the element experienced significant thermal stress as the temperature rapidly increased, resulting in element failure. These results suggest that, in order to achieve high power levels, the wire material requires a ramp time to reach the appropriate power level. This allows the element temperature and, correspondingly, its resistance, to slowly increase, minimizing the thermal stress places on the element. Future testing will determine the required

ramp time. Testing at 1,200 W did not require power ramping at the start of test so the full desired power could be applied to a cold heater element due to the smaller change in temperature over this power range. In contrast to the refractory metal elements, C is unique in that it drops in resistance as it heats up. Previous testing experience with C fiber braid and graphite rods demonstrated that C-based elements are very robust under all thermal conditions. If C braid can be acquired in the resistance range needed for thermal simulators, power ramping may not be required to achieve the 6 kW power level. This would potentially allow the application of full power at the start of the test with no ramp time.

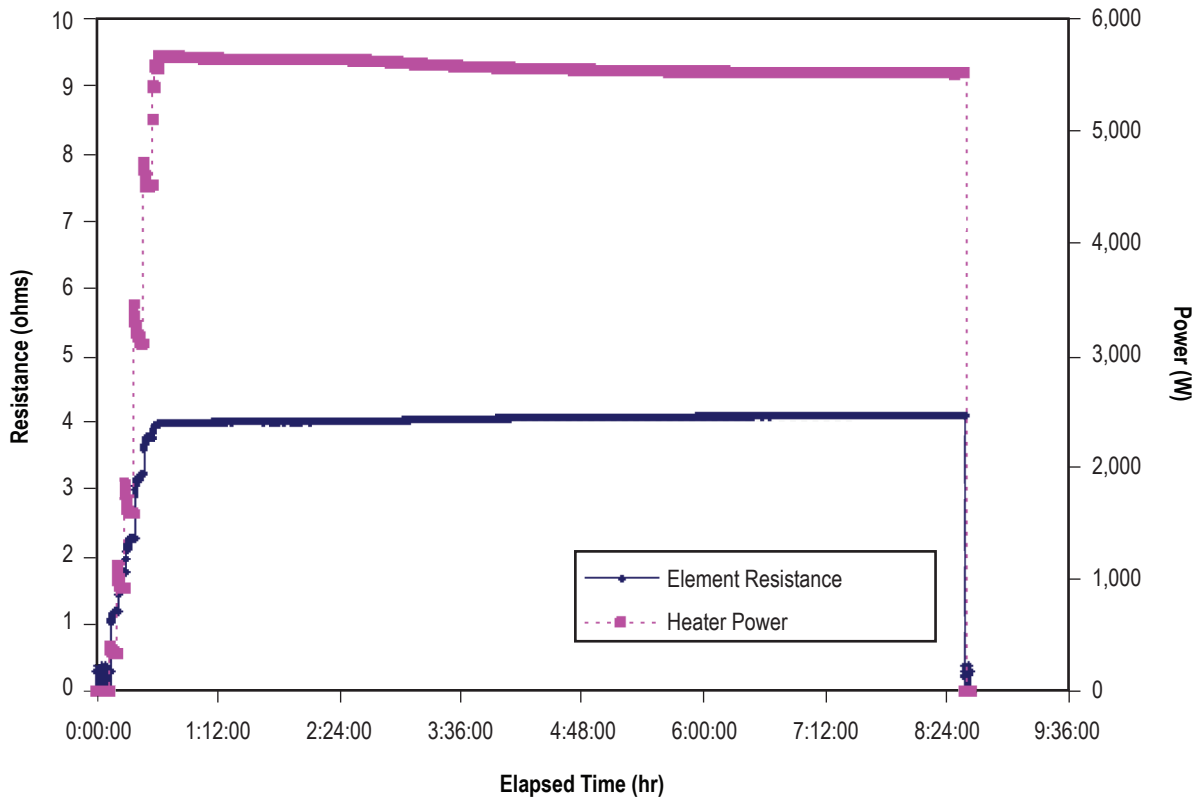


Figure 27. Initial test data for a 0.5-mm (0.020-in) TA three-wire braid heater element in a He environment (the element failed at the start of the subsequent test day).

Two additional Ta elements were tested after the initial power ramping failure discussed previously. In these tests, which considered three-wire braided elements using wire diameters of 0.64 and 0.5 mm (0.025 and 0.020 in), power was increased gradually to allow the heater temperature to increase at a more reasonable rate. Both elements were tested inside a Mo sheath with the chamber backfilled to  $\approx 6$  kPa ( $\approx 45$  torr) He to provide additional heat removal from the element. However, the same size mandrel was used in these assemblies (1.17-cm (0.460-in) OD, 1.65-mm (0.065-in) groove depth) as in the previous element tests. Therefore, although testing in an inert gas environment was expected to significantly reduce the maximum temperature of the heater element wire, it was uncertain whether or not there would be sufficient clearance for the wire at 6 kW.

**2.4.2.2 Test 2: 0.64-mm (0.025-in) Tantalum Three-Wire Braid With Power Ramping, Sheathed, Helium Environment.** A three-wire braid element using 0.64-mm- (0.025-in-) diameter Ta wire was tested on July 1, 2005, and July 5, 2005. On the first day of test, the desired power level of 6 kW was approached very slowly, reaching the full power after  $\approx 3$  hr. The element continued to operate an additional hour of run time at the full power level. On the second test day, the element failed  $\approx 45$  min into the test, during the power ramp procedure. Heater power and calculated element resistance for each test day are shown in figure 28. This failure occurred when the heater element wire came in contact with the sheath due to excessive thermal expansion. This wire diameter will not be tested further until redesigned mandrels having deeper grooves are procured.

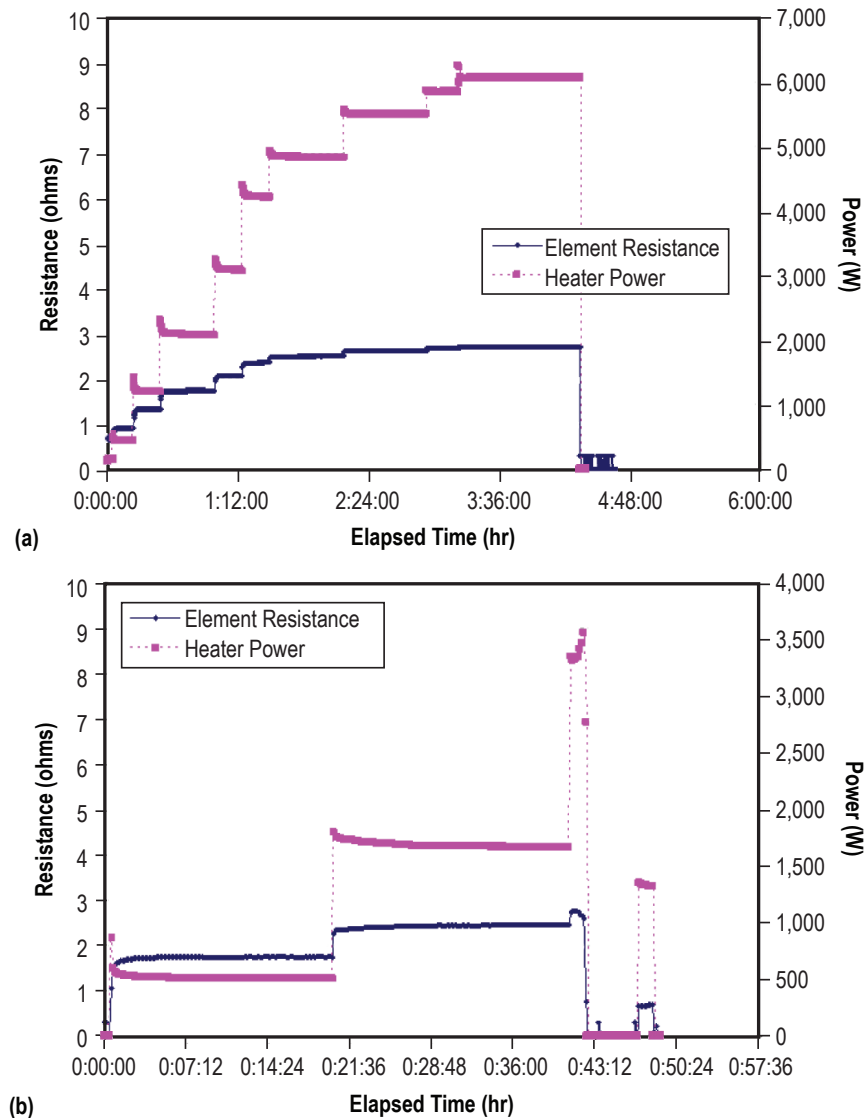


Figure 28. Tantalum heater element power and resistance on subsequent test days for 0.64-mm (0.025-in) three-wire braid: (a) Initial test data, July 1, 2005, and (b) final test data, July 5, 2005.



**2.4.2.3 Test 3: 0.5-mm (0.020-in) Tantalum Three-Wire Braid With Power Ramping, Sheathed, Helium Environment.** A final Ta element was assembled using a three-wire braid constructed from 0.5-mm- (0.020-in-) diameter wire. Due to the previous failures of Ta at high power levels, the stated goal of this test was to first achieve 100 hr of operation at 3.6 kW before moving to the higher power levels. This testing commenced on July 6, 2005, and ran until the element failed after 71 hr of operation at 3.6 kW on July 19, 2005 (fig. 29). Because the automated control system was not yet operational, the element was started and shut down on each test day. (Later tests have incorporated continuous runs with the addition of automated control and safety systems.) The calculated element resistance was relatively stable at  $\approx 3.3 \Omega$ , indicating that no fundamental changes occurred in the element from one thermal cycle to the next. Element failure occurred at 71 hr when the data acquisition system reported an open circuit. Posttest analysis of the assembly indicated that the heater element wire had welded itself to the interior surface of the sheath. The automated data acquisition system was not yet available during this test. Observations, however, indicated that a brief disruption may have occurred in the water flow to the test chamber, which may have resulted in an elevated heater temperature. If this is the case, the increased temperature may have resulted in slightly greater thermal expansion of the wire, causing it to contact the sheath.

Tantalum wire followup testing may consider a braid composed of 0.69-mm- (0.027-in-) diameter wire; however, this will require a mandrel with deeper grooves to accommodate the increased wire thickness. A short trial test was attempted with the 0.69-mm- (0.027-in-) diameter wire (and an existing mandrel with a 1.6-mm (0.063-in) groove depth), resulting in a short circuit condition to the Mo heater sheath. A new mandrel design to evaluate the larger braids has been produced and submitted to the procurement process and this configuration will allow the braid to lie flatter in the mandrel groove, minimizing the potential for shorting to the sheath. In addition, this new deeper groove design introduces the possibility of developing a mechanical seal configuration (designed to seal the heater inside the sheath) for a heater assembly with an OD as small as 1.4 cm (0.540 in) at the sheath OD (1.6-cm (0.625-in) flange). Element sealing options will be discussed in section 3.4.

## **2.5 Tungsten Wire-Wrapped Heater Element**

Initial investigation of W wire-wrapped heater elements considered 0.25-, 0.38-, and 0.5-mm (0.010-, 0.015-, and 0.020-in) W wire. Use of larger wire diameters was not feasible due to the reduced ductility of W as the wire diameter is increased. A five-wire braid, using 0.25-mm (0.010-in) wire, wrapped around the 1.17-cm (0.460-in)  $\text{Al}_2\text{O}_3$  mandrel accumulated 240 hr of test time over 30 thermal cycles, meeting the minimum requirement of 100 hr at 1,200 W in an unsheathed, vacuum environment. Additional testing of the five-wire braid in the initial test series was performed at higher power levels (3,000 W, 24 hr) in a sheathed configuration. Details of these early W element test results can be found in section 2.1.2.4. Based on initial success with W wire, it was recommended for further testing at higher power levels.

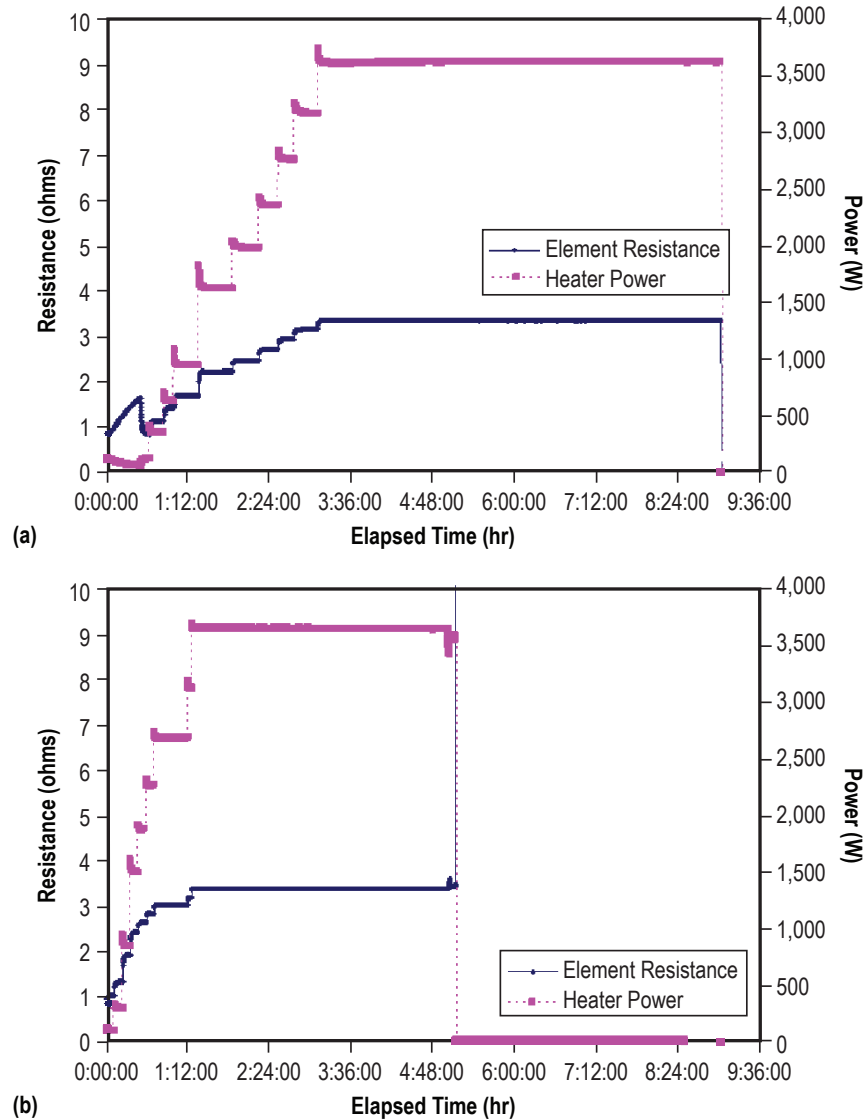


Figure 29. Tantalum heater element power and resistance on the initial and final test days for 0.5-mm (0.020-in) three-wire braid: (a) Initial test data, July 6, 2005, and (b) final test data, July 19, 2005.

Tests of W wire-wrapped elements at higher power levels (up to 6 kW) were performed on three-, four-, and five-wire braids using the 0.25-, 0.38-, and 0.5-mm (0.010-, 0.015-, and 0.020-in) wire diameters. Results of these tests indicate that W is capable of reaching these high power levels over long periods of time, but that thermal management becomes a significant concern as the power level is increased.

### 2.5.1 Bare Element Testing in Vacuum

Vacuum testing was performed on a three-wire braid, using 0.5-mm- (0.020-in-) diameter W wire, wrapped around a 1.17-cm (0.460-in)  $\text{Al}_2\text{O}_3$  mandrel (see fig. 30). This element operated for 100 hr at 6,000 W in an unsheathed configuration under a 1.3-mPa ( $10^{-5}$ -torr) vacuum. A check of the cold resistance of the heater prior to running on each test day indicated that the resistance was stable, measuring 0.40 to 0.43  $\Omega$ . At this elevated power level, thermal management becomes a concern for the mandrel if testing is performed in a vacuum environment. Because heat was only being removed by radiation, the mandrel became extremely hot, and sagged in unsupported regions, as shown in figure 31. However, despite the drastic change in shape from the start of test, the heater did not fail. If tested in the sheathed configuration, the additional increase in temperature could cause the mandrel to melt if additional heat transfer mechanisms are not added to the test configuration. Further testing could be conducted to better establish the limits of the heater element design and material selections. The addition of inert gas to the test chamber can drastically reduce temperatures, allowing operation at much higher power levels.

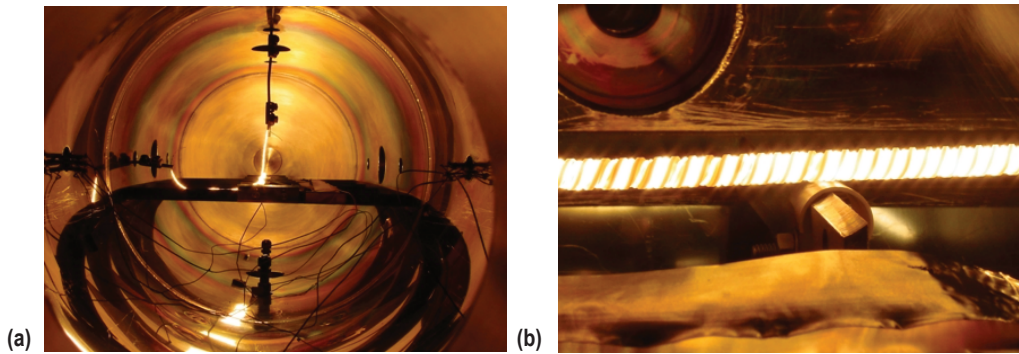


Figure 30. Tungsten wire heater assembly—testing in a vacuum environment: (a) End view of element during test and (b) side view of element during test.

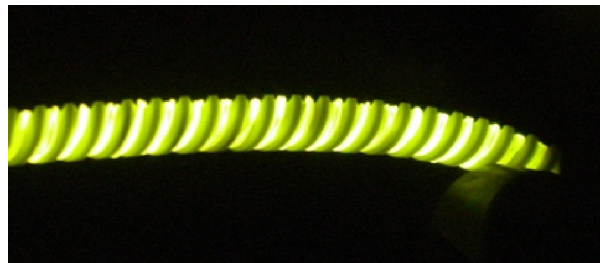


Figure 31. Mandrel distortion due to excessive heating.

Data for the initial and final days of testing are shown in figures 32 and 33. During the first day of testing, a slow heating rate was applied to bakeout the heater element. Two TCs were operational during test. One TC was lying on the bottom of the test chamber (TC3) and an additional TC was placed on the mandrel (TC5). The melting point of  $\text{Al}_2\text{O}_3$  is 2,313 K (2,040 °C). The plastic deformation of the mandrel indicates that the measured mandrel temperature of  $\approx 2,300$  °C on the first day of testing was likely correct. However, later test data suggest that neither TC was reading accurately. Although TC3 maintained a higher temperature measurement of  $\approx 2,300$  °C throughout testing, the mandrel temperature reported by TC5 dropped to less than 1,000 °C, as shown in figure 33(b), despite the observed plastic deformation, suggesting possible TC failure. Data shown in figures 32(b) and 33(b) indicate that the element resistance was stable throughout the test at 6,000 W. The total of 100 hr of testing was accumulated over eight thermal cycles.

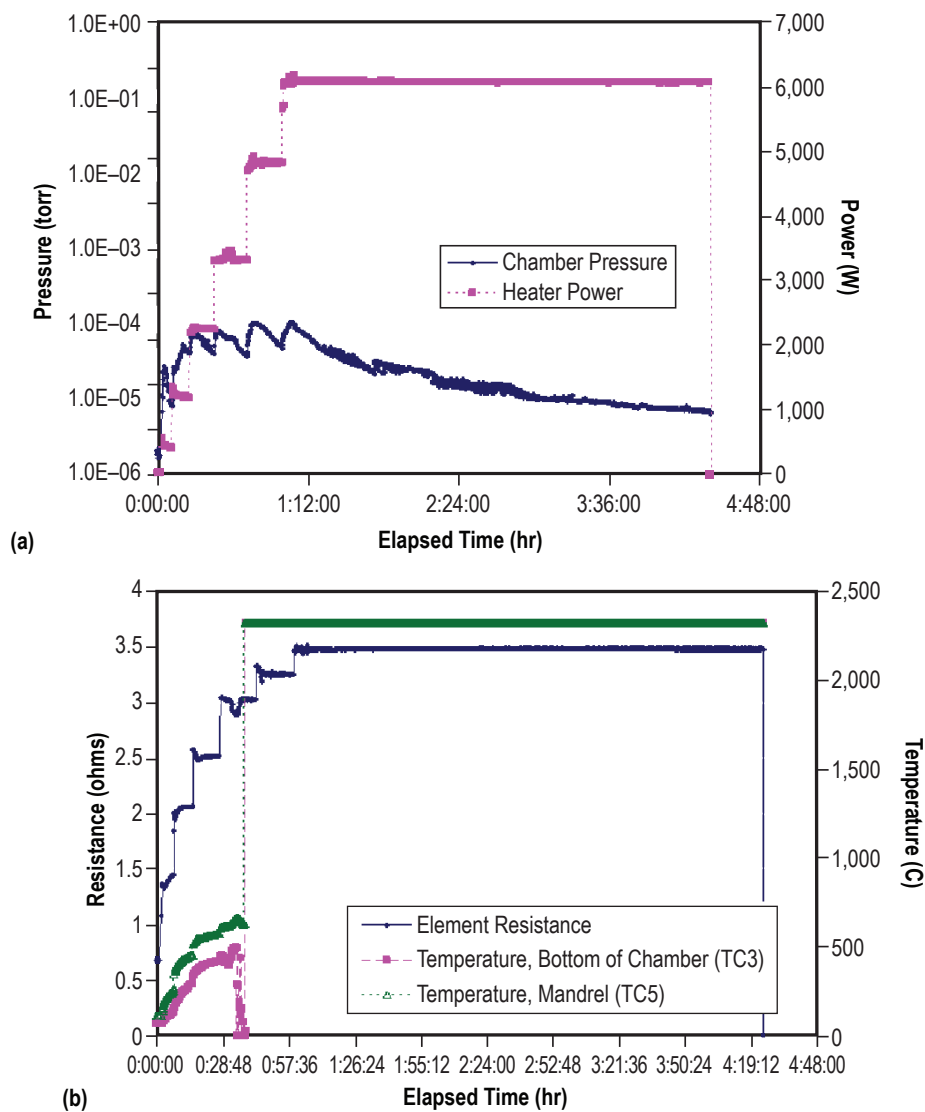


Figure 32. Initial test data (day 1) for W three-wire braid: (a) Heater power chamber pressure and (b) element resistance and measured chamber and mandrel temperatures.

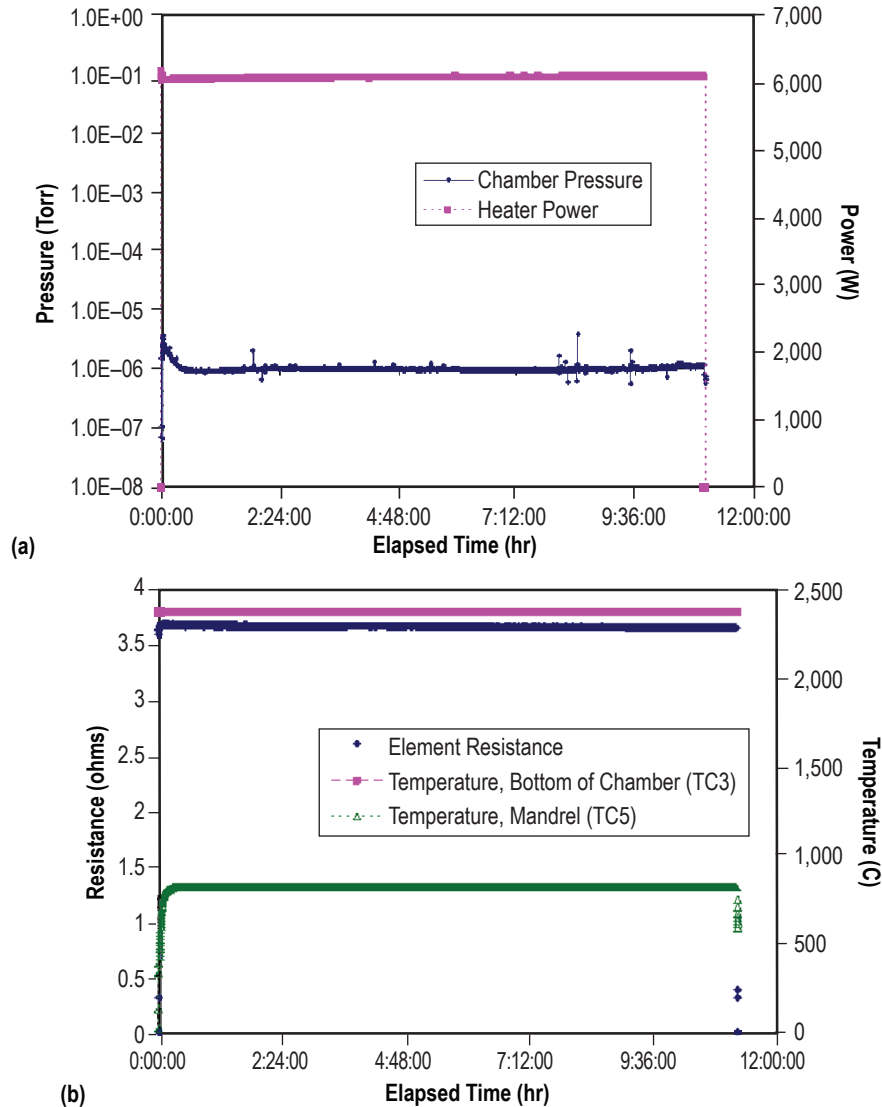


Figure 33. Final test data for W three-wire braid, 89–100 hr: (a) Heater power and chamber pressure and (b) element resistance and measured chamber and mandrel temperatures.

Results of the 0.5-mm (0.020-in) three-wire braid W element vacuum test indicate that a refractory wire element can be designed and built to achieve the highest stated power requirement under extreme conditions (well above expected operating temperatures in a core array and given element deformation). In this case, heat removal by radiation alone allowed the heater element temperature to become excessive, resulting in the mandrel deformation that was seen in figure 31. This result indicates that improved thermal management (operation of the heater in a low pressure inert gas environment) should be implemented at these high power levels. Additionally, differential heating was noted in the coils on the power inlet side of the center heater element support. Every other coil from the support back to the power input appears dimmer, as seen in figure 30(b). This suggests that the coil could be losing some power due to contact with the support or, given that the differential heating appeared to wander during the test, it is very likely that the observed differential heating results from emissivity changes in the element at elevated temperatures.

## 2.5.2 Sheathed Element Testing in Helium Environment

All subsequent tests of W wire-wrapped elements were performed with the heater element inside a Mo sheath and with the vacuum chamber backfilled with high purity He gas to  $\approx 5.3\text{--}6$  kPa ( $\approx 40\text{--}45$  torr). Tests considered a 0.25-mm (0.010-in) three-wire braid, 0.25-mm five-wire braid, and a 0.38-mm (0.015-in) four-wire braid. All wires were wrapped around a 1.17-cm (0.460-in)  $\text{Al}_2\text{O}_3$  mandrel and were tested inside a 1.37-cm- (0.540-in-) diameter Mo sheath. All sheathed element tests were performed with the assembly housed inside a water-cooled calorimeter. This calorimeter, shown in figure 34, was a basic shell-in-tube design having a single flow path. It was not designed to achieve a specified sheath temperature. Development of a highly designed calorimeter for application to thermal simulator testing is discussed in section 3.2, but testing of this calorimeter will not be covered in this Technical Memorandum (TM).

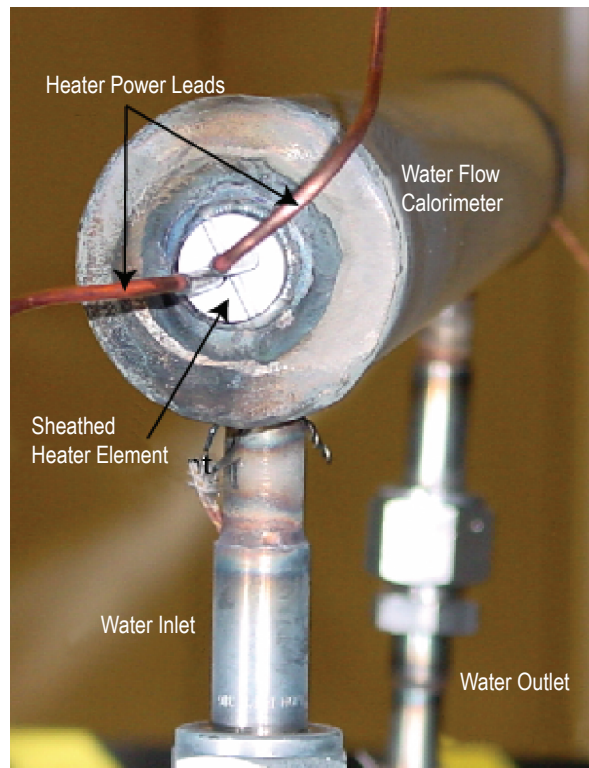


Figure 34. Test setup with sheathed heater element fitted inside a water-cooled calorimeter.

**2.5.2.1 Test 1: 0.25-mm (0.010-in) Tungsten Three-Wire Braid With Power Ramping, Sheathed, Helium Environment.** The initial objective of the 0.25-mm (0.010-in) three-wire braid test was to achieve 100 hr of testing at 2.4 kW. Because the test configuration differed from previous tests, it was desirable to first study W element operation at lower power levels before stepping up



to the ultimate goal of 6 kW. In addition, the total power that can be delivered to the element using a single power supply is limited by the element resistance and the maximum voltage that could be delivered (150-V, 100-A supply). A total of  $\approx 108$  hr were acquired at 2.4 kW over 10 thermal cycles, with the ramp to 2.4 kW taking  $\approx 1$  hr on each test day. (Test data are provided in fig. 35). Testing was performed in an  $\approx 6$  kPa ( $\approx 45$  torr) He environment. To ensure high-purity He in the test chamber, the chamber was pumped to vacuum ( $\approx 1.3$  mPa ( $\approx 10^{-5}$  torr)) and backfilled with He three times prior to the start of test. This procedure significantly reduces the potential contamination in the test chamber. The measured cold resistance of the element, taken prior to the start of each test run, was consistent at  $\approx 1.21 \Omega$  and measured resistance at 2.4 kW was also consistent at  $\approx 9.2 \Omega$  throughout testing.

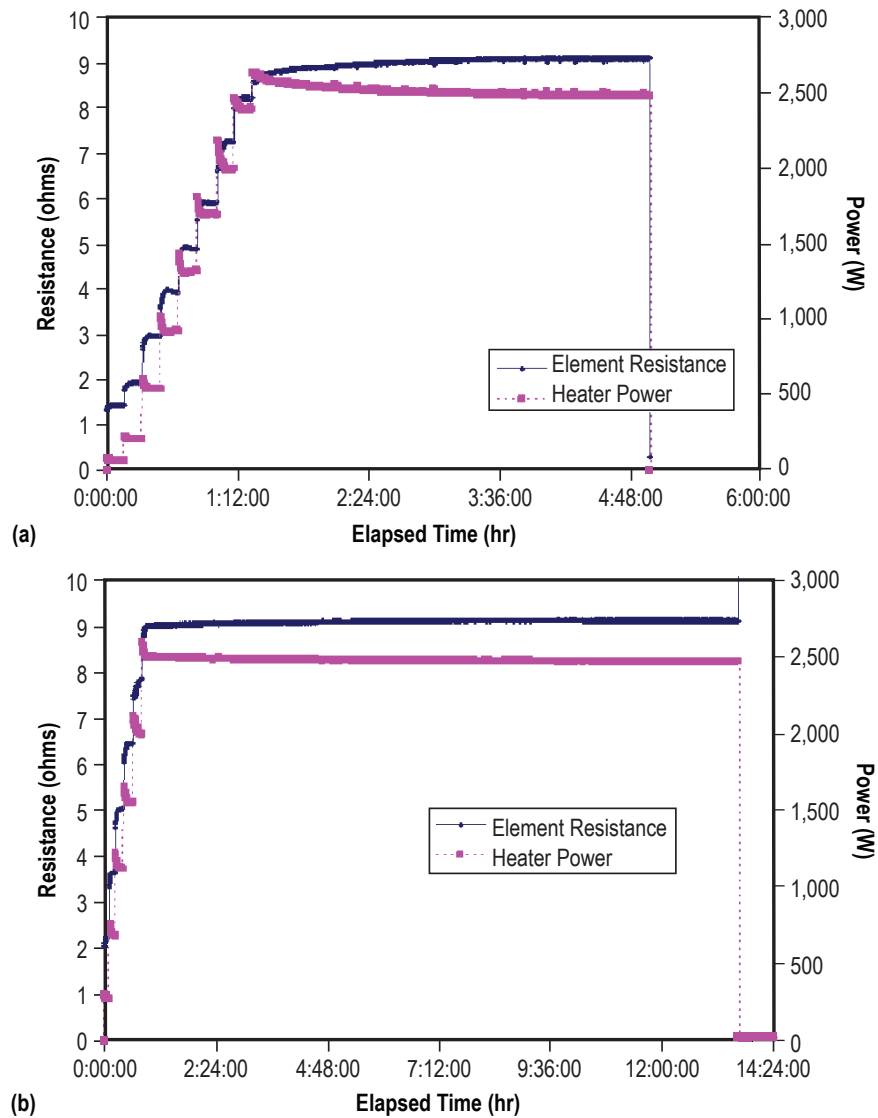


Figure 35. Initial and final test data for 0.25-mm (0.010-in) three-wire braided W element: (a) Initial test data, July 25, 2005, and (b) final 13 hr of test, August 8, 2005. Plots show total power delivered to the heater element and the calculated element resistance.

**2.5.2.2 Test 2: 0.25-mm (0.010-in) Tungsten Five-Wire Braid With Power Ramping, Sheathed, Helium Environment.** Upon successful operation of the three-wire braid for more than 100 hr at 2.4 kW, a 0.25-mm (0.010-in) five-wire W braid was assembled for test at 3.6 kW in the same test environment (Mo sheath, 6 kPa (45 torr) He, water-cooled calorimeter). The additional two wires in the braid configuration dropped the element resistance at temperature from 9.2 to 6  $\Omega$ , increasing the maximum power that could be delivered to the element by the 150-V supply; at 6  $\Omega$ , the 15 kW supply could provide up to 3.75 kW to the element. Testing from August 12 to September 2, 2005, recorded more than 100 hr of test time at 3.6 kW. After completing the initial requirement of operation for a minimum of 100 hr, this element was used to assist in debugging the test automation software, allowing additional test time to be accumulated. In total, this element was allowed to reach over 300 hr of total test time, accumulating over 40 thermal cycles, without experiencing element failure. This is a significant improvement over previous tests, indicating the effect of active heat removal (inert gas environment and operation in a water-cooled calorimeter) to achieve operating temperatures that are more representative of a heater element operated in a reactor core array. The longest single run, using the automated test operation and data acquisition system, was initiated on August 25, 2005, and ran for 95 hr, accumulating a total of 10 thermal cycles on the heater element. Data for this test run are shown in figure 36. The final element shutdown is not shown in this plot due to a limitation in the total number of data points that can be displayed by Microsoft Excel in a single plot. The plot indicates that the element resistance remained relatively stable at  $\approx 6 \Omega$  throughout the duration of the cyclic test that was consistent with the calculated resistance at power on other test days as well.

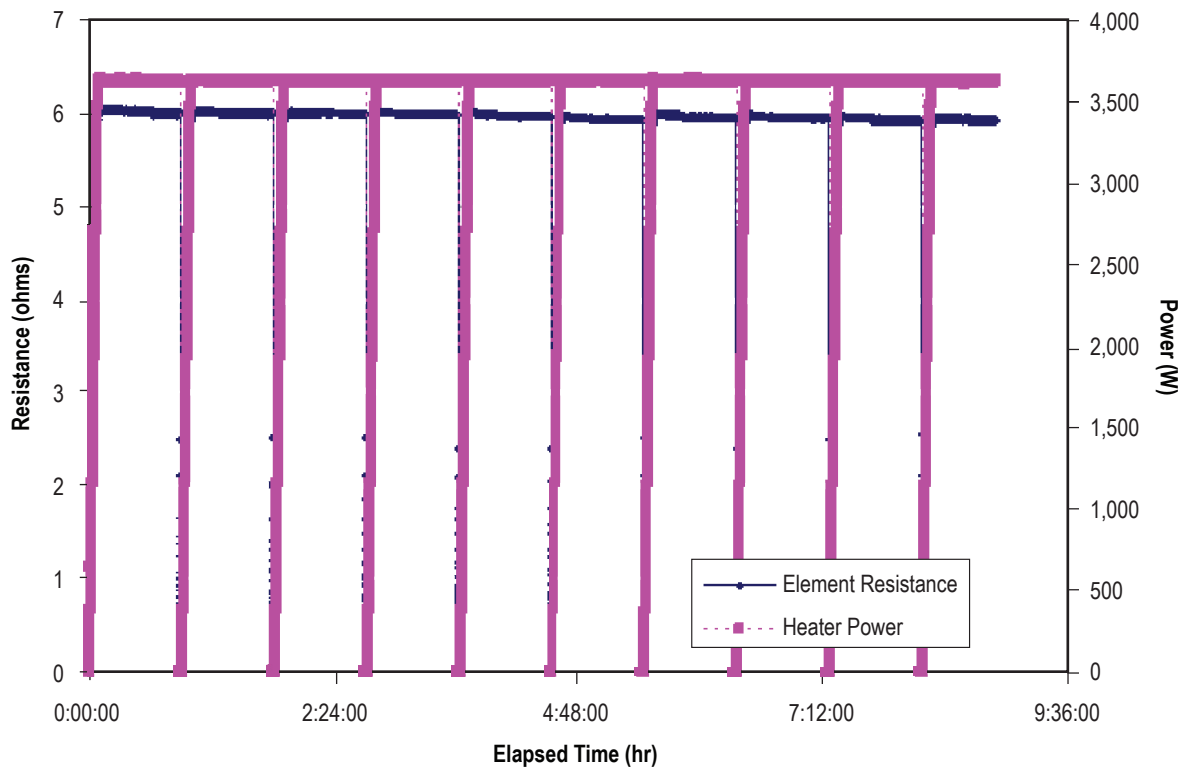


Figure 36. Test data for 0.25-mm (0.010-in) five-wire W braid (August 25–29, 2005).

**2.5.2.3 Test 3: 0.38-mm (0.015-in) Tungsten Four-Wire Braid With Power Ramping, Sheathed, Helium Environment.** An additional W heater element was assembled for testing at 5.0 kW using 0.38-mm- (0.015-in-) diameter, four-wire braid. Braiding the 0.38-mm-diameter W wire was difficult. Although no problems were encountered with the 0.25-mm or 0.5-mm wire, the 0.38-mm wire experienced breakage at random lengths during the braiding process. There was no evidence of problems with the braiding machine, suggesting potential variability in the wire manufacturing process. The manufacturer was questioned as to the potential fabrication differences that might exist between the different wire diameters, but no response was received. A total of 3.7 m (12 ft) of braided wire is required to wrap the 1.17-cm (0.460-in) mandrel. This length was achieved after several failed attempts and the assembled heater element was installed for testing on September 9, 2005. All testing was conducted with the element installed inside a Mo sheath and with the entire assembly fitted inside the water-cooled calorimeter shown in figure 34. The chamber was again backfilled to 6 kPa (45 torr) with high-purity He gas. The heater element burned out after only 4 hr of testing. The control system detected an over-current condition, and the power to the heater was automatically shut down before the circuit opened, per specifications set in the automated control system.

A second 0.38-mm (0.015-in) four-wire braid element was assembled and installed for testing on September 13, 2005. Initially operated at 4 kW for  $\approx$ 16 hr, the heater power was then increased to 5 kW in an attempt to reach over 100 hr at the elevated power level. This element failed during its fifth thermal cycle after operating for 36 hr at 5 kW. Corresponding data are shown in figure 37.

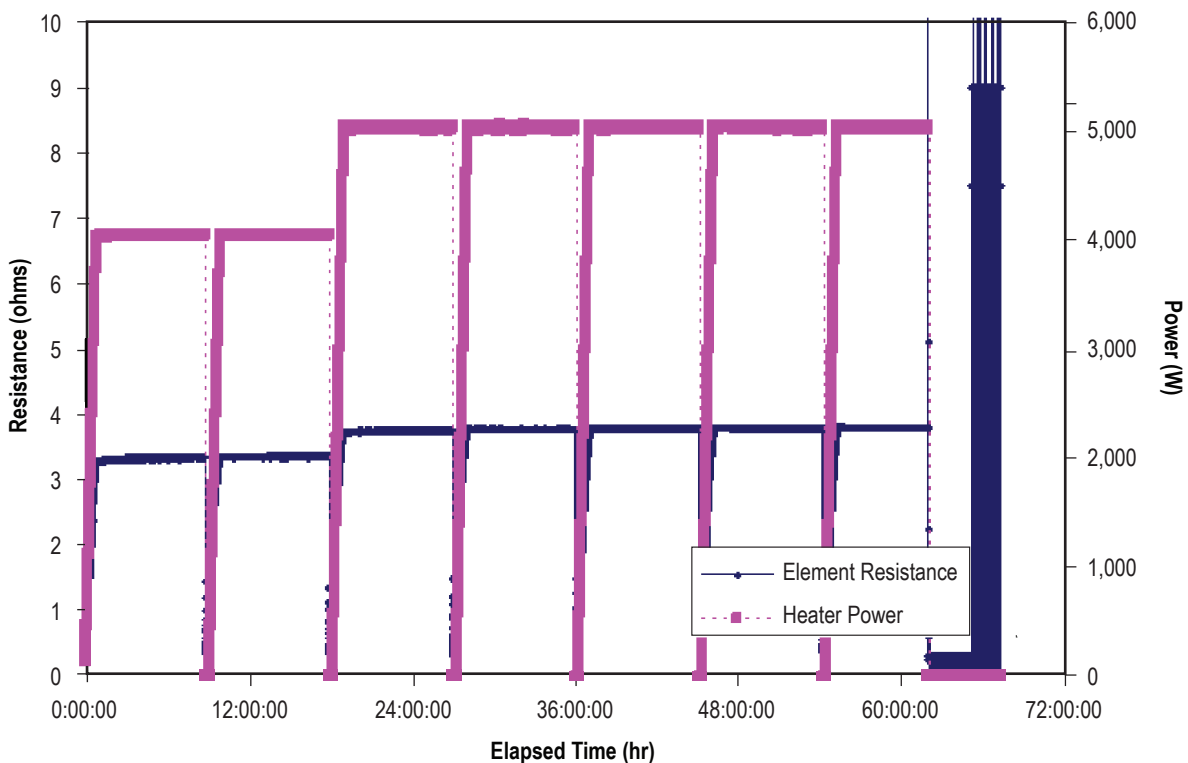


Figure 37. Test data for 0.25-mm (0.010-in) five-wire braid (test 1, September 13–16, 2005).

A third 0.38-mm (0.015-in) four-wire braided W element was tested during September 16–26, 2005) (figs. 38 and 39). This element was operated continuously throughout this time period, utilizing the automated control and data acquisition system. The element was first allowed to operate for more than 130 hr at 5 kW (14 thermal cycles) and for an additional 100 hr at 5.4 kW (11 thermal cycles). Hence, despite the initial difficulty noted with regard to wire breakage and failure of the first two 0.38-mm four-wire braid W elements, this configuration was operated well in excess of the minimum required test time of 100 hr at power levels at or above 5 kW. It is possible that the previous two 0.38-mm wire elements had microbreaks in the braided wire that resulted in early element failure. Additionally, the refractory wire elements were hand wrapped on the mandrel. Varying amounts of tension applied during the wrapping process can significantly affect the stress placed on the wire and can affect how tightly the wire lies on the spiral-cut mandrel. The variability incurred in a manual process could affect the success or failure of the resulting element during testing. The reproducibility of the refractory material and the assembled heater elements must be assessed if these heaters are to be used in a full core array. Element reproducibility was very good for earlier tests of graphite rod elements manufactured to specifications set by MSFC (see sec. 2.2), suggesting that the use of graphite elements should be reassessed if materials compatibility issues do not exist with the final core design.

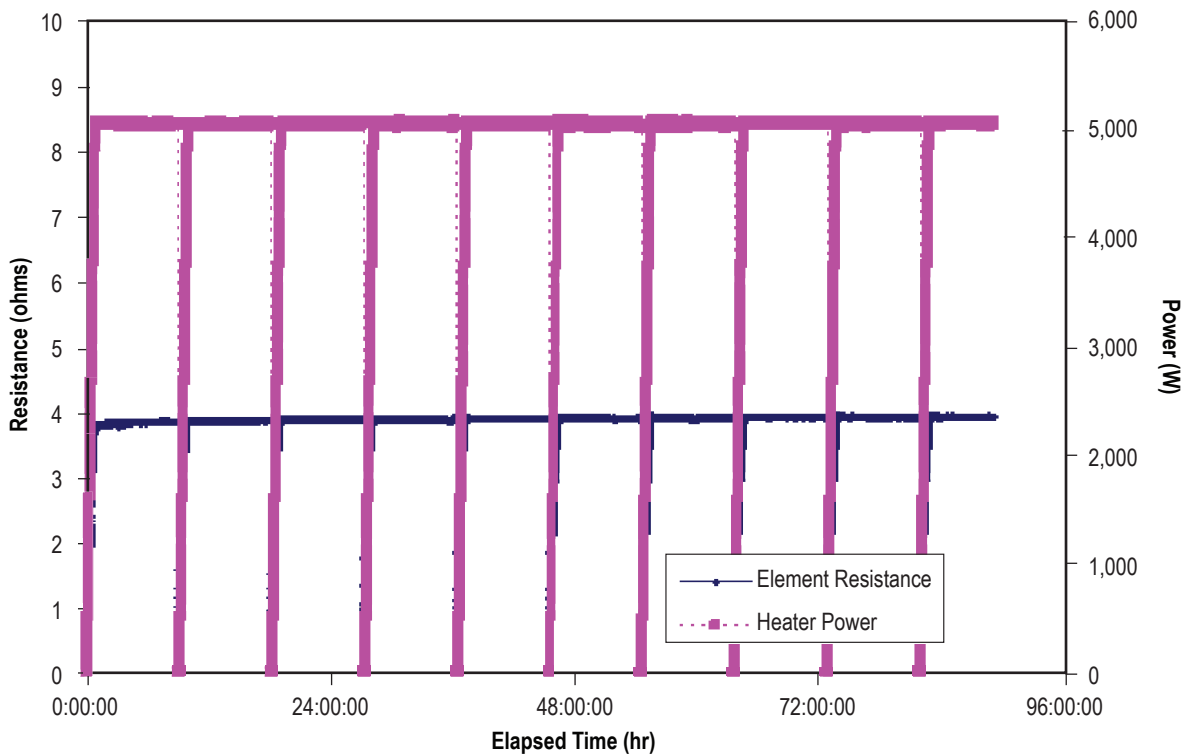


Figure 38. Test data for 0.25-mm (0.010-in) five-wire braid (test 2, September 16–20, 2005).

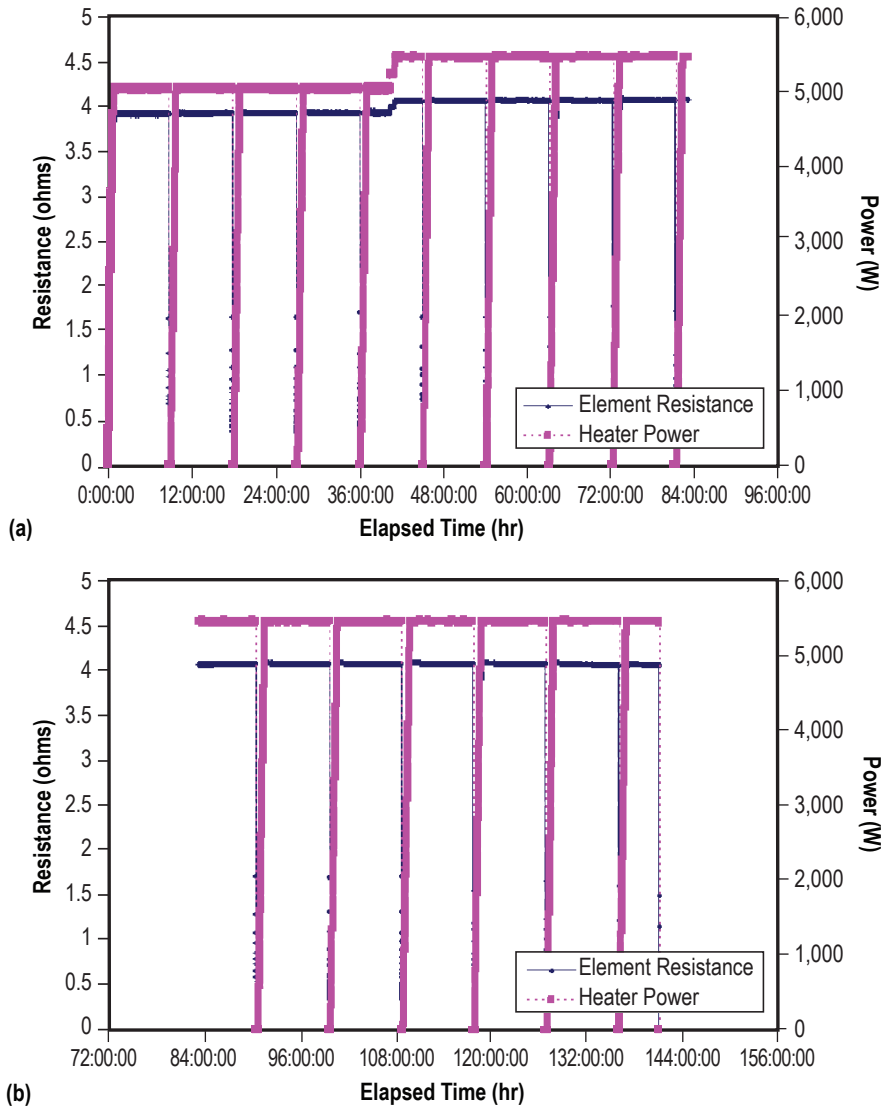


Figure 39. Test data for 0.25-mm (0.010-in) five-wire braid (test 3, September 16–26, 2005). Data were broken into two separate plots due to limitations in Microsoft Excel plotting features: (a) Test data, 0–84 hr and (b) test data, 84–140 hr.

## 2.6 Material Selection Criteria

Heater material compatibility issues are being investigated for a number of potential core, sheath, and heater element materials. Specific issues are contamination of the core materials from heater assemblies, coefficient of thermal expansion (CTE), and interfacial diffusion during long time exposures at high temperatures. Quick, cost-effective testing of subscale samples by inductive and resistive heating is planned for existing materials test chambers at the Propulsion Research Laboratory at MSFC. A matrix of potential core, heater (wire, mandrel, central rod, power connections, etc.), and sheath materials has been established as a baseline to prepare a comprehensive assessment of materials compatibility issues over time (table 14). If compatibility issues are not expected to arise over the planned lifetime of a heater element (hundreds of hours), these material combinations may preclude the need for developing a hermetic seal for the heater element (sealing the central element inside the sheath). In all cases, it is expected that a mechanical seal will be necessary to develop elements that can properly mimic the static and dynamic characteristics of a nuclear fuel element, allowing layering of materials in the overall buildup of the element, but removing the need for a hermetic seal may significantly reduce the cost of developing an advanced thermal simulator.

Development of a thermal simulator that more closely mimics the characteristics of a nuclear fuel element, taking into account various material compatibility issues, will be discussed further in section 3.

Table 14. Suggested materials test matrix. (Work would entail an initial literature review to assess potential compatibility issues at certain test temperatures and durations, followed by testing of combinations of interest.)

Potential Heater Element and Sheath Materials \ Potential Core Materials	Poco Graphite	C Fiber Braid	Al <sub>2</sub> O <sub>3</sub>	BN	W	Ta	Re	Mo
Mo-47.5%Re								
Astar								
Ta-10%W								
SiC								
FS85								



## 2.7 Initial Conclusions From Thermal Simulator Tests

After completion of the initial test series at 1,200 W, refractory materials recommended for continued development and testing included Re, Ta, and W. The Re material has not been received to date and was not included in the current round of testing at higher power levels. The supplier has missed delivery dates in the past and has not proven reliable in providing the necessary material. Therefore, due to the limited supply, expense, and available quality of the material, Re is not recommended for future use in thermal simulator development.

The results presented in this TM suggest that W is the most desirable material for thermal simulator assembly should the reactor design dictate refractory metal elements. The final W simulator assembly achieved well over the stated test requirements, operating for more than 100 hr at 5 kW and for an additional 100 hr at 5.4 kW without failure. Tantalum element tests failed to achieve the minimum requirements at high power levels. Although none of the tested elements could go from zero to full power (5–6 kW) in a single step, given either a vacuum environment (sec. 2.4.1) or an inert gas environment (sec. 2.4.2.1), power ramping over  $\approx 1$  hr was successful. Additional testing must be performed to determine the maximum power ramp rate from a cold condition that can be applied without element failure. Once at operating temperature, the power to the element can be turned to zero and reset to the full power level without failure, allowing thermal cycling during the extended test period. During the automated power cycling, the element temperature was not allowed to decrease between power cycles.

It may also be appropriate to investigate hardening effects during wire braiding. Three different W wire diameters were investigated: 0.25, 0.38, and 0.5 mm (0.010, 0.015, and 0.020 in). Although each of these wire diameters was braided (using three, four, or five strands per braid), the 0.38-mm wire had problems with breakage during the braiding process. Braiding was attempted with two separate lots of each tested diameter, with the same results in each case. This variability between potential wire diameters should be further investigated if W is selected for use in core thermal simulators.

Aside from reproducibility of the material and fabricated elements, one potential problem noted with the use of W wire was the limited material ductility. It may be desirable to investigate the possibility of increasing the W ductility to improve fabricability of the heater elements. If a blend of materials (doping) is necessary to improve ductility, however, localized hot spots caused by uneven distribution of materials could become a concern.

Previous testing indicated that graphite rod heater elements are significantly more robust than any of the tested refractory wire elements, allowing instantaneous power changes without affecting the integrity of the heater. Element variability was also avoided in earlier testing of graphite rod elements that were manufactured to specifications set by MSFC (see sec. 2.2). The use of graphite heater elements should be reassessed if materials compatibility issues do not exist with the final core design.

### 3. DEVELOPMENT OF SUPPORT HARDWARE

In early 2005, heater element testing was performed with a minimum of diagnostics on the test chamber or on the elements themselves. The current test chamber is equipped with a roughing pump and a turbopump to provide pump down to vacuum. Vacuum gauges were present on the chamber to make regular pressure measurements during earlier testing and development. Based on these earlier measurements, it is estimated that the current tests were conducted at a pressure on the order of 1.3 mPa ( $10^{-5}$  torr). Future testing will incorporate vacuum gauges and other pressure gauges to allow for specification of chamber conditions for testing either at vacuum or in a high-purity inert gas environment. To properly conduct thermal simulator testing in relevant environments, a significant amount of support hardware must be developed. Discussions with the Naval Reactors Prime Contractor Team (NRPCT) indicate that the desirable sheath temperatures could range from 1,100 to 1,700 K at power. Achieving specified sheath temperatures requires that the test environment be manipulated through the addition of gas to the test chamber (providing conductive heat transfer from the element) and by the use of a highly designed noncontact calorimeter to actively remove heat from the element under test.

Data acquisition and control systems were installed in late 2005 and activated on the thermal simulator test chamber. The system is capable of recording temperatures and pressures, and provides automated control for the heater power supply. All future tests will be conducted with the data acquisition system operational. Chamber pressure is determined using three pressure gauges to cover the range of pressures expected in the chamber: a capacitance manometer is used for pressures from 0.1 to 100 kPa (1 to 1,000 torr), a convector from 0.1 to 100 Pa ( $10^{-3}$  to 1 torr), and a lower range convector from  $10^{-5}$  to 0.1 Pa ( $10^{-7}$  to  $10^{-3}$  torr). The data acquisition system is currently set up to record eight temperatures, with wiring for type C TCs run up to the chamber feedthrough. These TCs can be connected to the heater assembly or to other structures in the test chamber, as desired for a given experiment. The control system is configured to remotely operate the heater power supply, with read back to record the actual power delivered to the assembly. The control system also has the capability to establish set points for voltage and current, and if either should exceed the predetermined set point, the power can be automatically shut down. To operate the test chamber in a round-the-clock fashion, additional cutoffs must be programmed (a flow switch would be required to monitor water flow through the test chamber walls because loss of water would require a power down of the experiment), but the currently installed data acquisition and control systems will provide for higher fidelity in the future thermal simulator tests.

To better assess heater performance, diagnostics should be incorporated on the heater assemblies to provide data that can be compared to thermal analysis results. To monitor overall operation of each heater assembly during initial testing (outside of the full test article), temperature measurements are required. One test of the graphite heater element (bare) included a type C TC placed at the center of the element between two pieces of synthetic sapphire. Some tests attempted to obtain a sheath temperature using a TC tack welded to the outer surface of the sheath. This connection, however, failed during the test, and temperature measurements were not accurate. It may

be desirable to incorporate a noncontact method of temperature measurement. Previous tests used an infrared (IR) camera, which viewed the heater through one of the zinc selenide viewing windows, to estimate element temperature. Future testing may incorporate an IR camera, and/or an optical pyrometer could be positioned to view the test article through one of the viewing windows to obtain a temperature measurement at a specific location on the element.

TCs provide inexpensive temperature measurement, but they have a number of negative issues related to their use. First, they are a contact measurement technique requiring direct attachment to the surface of the heater assembly. This can be troublesome since they can frequently debond from the surface to which they are attached. In addition, to achieve a successful bond (especially in the case of refractory metals), an intermediate material, such as Ni foil, is typically required. The foil is bonded to the refractory metal surface and the TC is then bonded to the foil. This intermediate material could diffuse into the sheath material over long periods of testing, potentially resulting in undesirable and/or unknown effects. Type C TCs, which are available with a 26% Re content (the balance being W), may have sufficient Re to allow them to be spot welded directly to the sheath surface, but testing would be required. However, the use of spot welding in general is not recommended, as it can result in pitting of the heater sheath surface and potentially embed or trap impurities. In addition, the TC leads act as fins, locally cooling the location where the measurement is taken, and the long-term degradation of the TC wires over time at high temperature also introduces unknowns. If TCs are employed, they will be used in pairs to provide backup at each measurement location.

The two-band optical pyrometer is a remote unit-mounted, noncontact measuring technique that makes use of a lens to focus the field of view on the location where the temperature measurement is required. The two-color, IR sensing device uses a ratio technique between the emissivity at two overlapping wavelength ranges to determine temperature rather than using the emissivity at just a single wavelength. The result is a temperature measurement that is somewhat independent of emissivity, target size/shape, and dust/contamination on the windows in the optical path. The noncontact technique simplifies setup (no internal TC wires) and eases operations involving loading and unloading of the heater elements.

The range of wavelengths used by the two-band pyrometers typically falls between 0.70 and 1.15  $\mu\text{m}$ . (For example, the Ircon model M5-R uses the ranges of 0.75 to 1.05 and 1.0 to 1.1  $\mu\text{m}$ ). As such, the type of sight glass selected is an important factor in the unit's performance. The suggested view port material type is quartz fused-silica (available from vacuum product vendors such as Kurt J. Lesker). Zinc selenide windows have a wavelength of 8 to 14  $\mu\text{m}$ , appropriate for infrared thermometry used previously but not applicable in combination with the suggested 0.70–1.15  $\mu\text{m}$  pyrometer, requiring that the existing viewing windows in the test chamber be changed if optical pyrometers are adopted. Figure 40 illustrates a general laboratory pyrometer setup used to assess the operation of a two-band unit to support another program. The heated element is a Mo-sheathed graphite heater operated in vacuum and equipped with several type K TCs. Figure 41 shows a closeup of the heater area being monitored where the TC is visible at the top, and spot welded to the Mo sheath using an intermediate Ni foil.

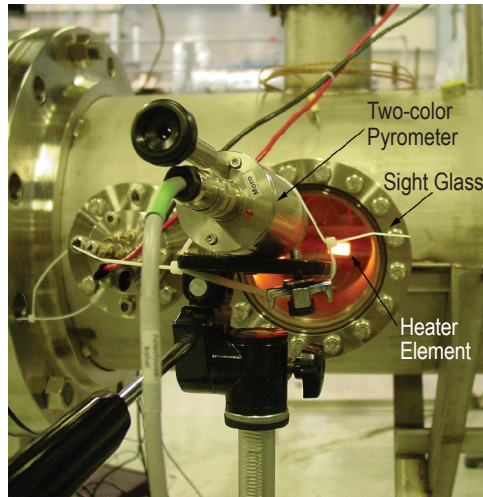


Figure 40. Color optical pyrometer setup.

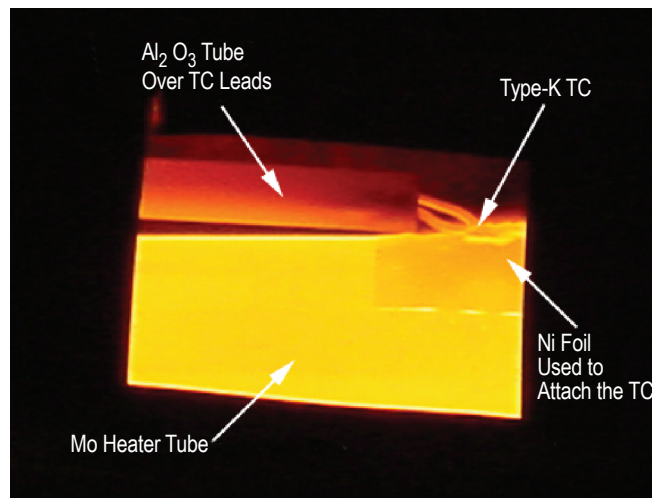


Figure 41. Closeup of Mo heater.

Heating tests were performed to examine trends between the pyrometer and TC rather than absolute values of temperature (due to time and equipment limitations). These ‘heat and hold’ tests were conducted in a vacuum environment ( $\approx 1.3$  mPa ( $\approx 10^{-5}$  torr) or lower), and an emissivity slope of 1.06 was used for the pyrometer (typical value for Mo suggested by manufacturers). Figure 42 shows temperature traces over  $\approx 5$  hr for both the pyrometer and TC (type K). There is a difference of  $\approx 42$  °C between the readings, but both readings track very well over the interval. The TC measurements are unadjusted for losses, which typically produce lower readings (fin effect, etc.). The stated accuracy of the pyrometer and TC are  $\pm 0.5$  and  $\pm 2.0\%$ , respectively.

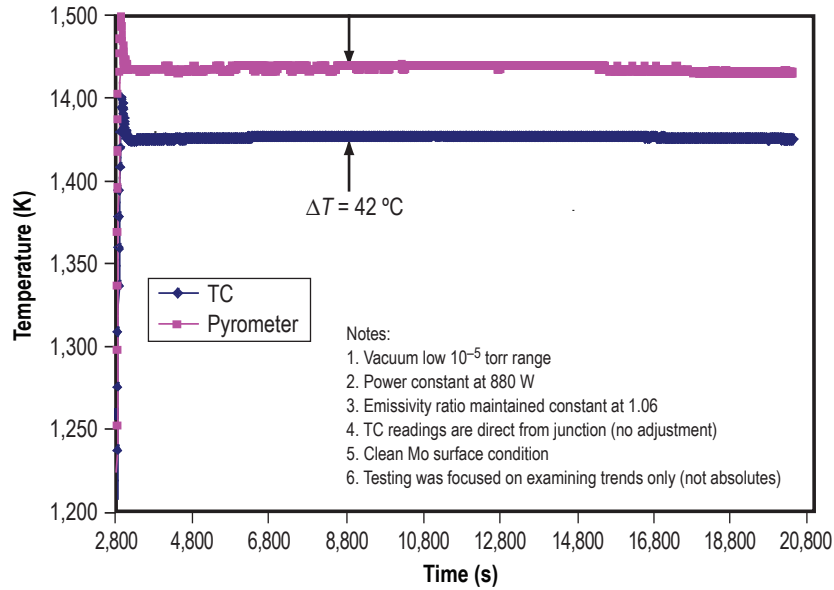


Figure 42. Sample long-term pyrometer data.

An additional test examined the effect of oxidation on the temperature readings by injecting air into the vacuum chamber and monitoring the resulting trends. Figure 43 illustrates one of these cycles in which air was briefly introduced while the turbo pumps continued to operate (causing the vacuum level to return to  $\approx 1.3$  mPa ( $\approx 10^{-5}$  torr) fairly quickly after injection). The Mo tube was already slightly oxidized at the beginning of this test due to previous air exposure experiments. Very small amounts of air injection resulted in higher sheath temperatures, primarily due to better thermal conduction from the hot graphite heater to the sheath. The temperature peaked and then dropped off again as the gas was evacuated (typically to a lower temperature due to some oxidation). In the case of a large air injection, the sheath temperature dropped rapidly, stabilizing at a much lower temperature due to the increased oxidation. (The vacuum level rapidly returned to  $\approx 1.3$  mPa ( $\approx 10^{-5}$  torr) after injection). After the large air injection, the Mo tube was dark gray (when inspected posttest at room temperature). During these transients, the pyrometer and TC readings trended in the same directions at similar response rates, and as expected, there was a variation in their difference. However, these differences were within the accuracy of the diagnostics and were reasonable considering no calibration or corrections were made for thermal losses, etc.



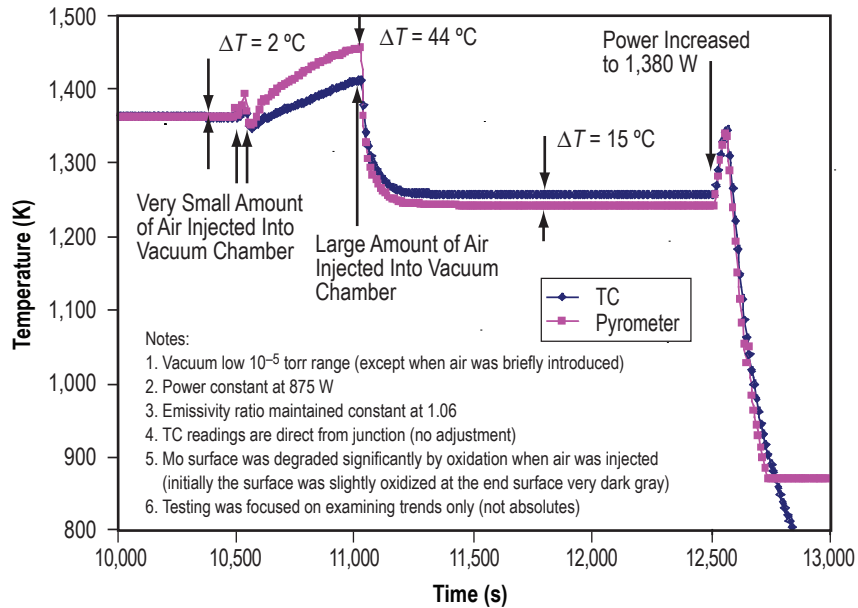


Figure 43. Sample data with oxidation.

To improve the absolute temperature measurement for a two-band optical pyrometer the emissivity slope for the material of interest must be determined. These ratios are available in literature for common materials, but they must be determined experimentally for special cases or applications. One possible method for determining this parameter is to fabricate a small blackbody cavity of the material to be tested. The cavity could be a piece of 2.5-cm- (1-in-) diameter tubing (of the correct material) with sealed ends and a small, 0.64-cm- (0.25-in-) diameter opening at one end. The internal surface finish should have a roughness of  $>0.25 \mu\text{m}$  to produce a diffuse emission. The tube should be equipped with a TC (with a lead wire length of at least 15 diameters inside the heated cavity to minimize loss effects) and an external heater. This assembly should be fully insulated (with the 0.64-cm hole exposed) and placed in a small vacuum chamber with a sight glass. With the pyrometer looking into the blackbody and focused in the 0.64-cm hole, the emissivity ratio is unity and the pyrometer and TC temperature readings should read essentially the same (within their accuracy bands). Shifting the pyrometer focal point so that it is on the outer surface of the tube next to the hole (a graybody) results in a temperature shift. The pyrometer's emissivity ratio is adjusted in this configuration until its reported temperature agrees with that found during the blackbody measurement. This approach assumes that the tube is isothermal (with no drastic temperature drop across the thickness of the tube, a good assumption, if care is taken with the layout of the heaters and overall geometry).

A typical two-band system (such as the Iacon series 5R model 1410 with a temperature range of 600 to 1,400 °C) retails for \$3,100 (estimate received in 2005). This device is equipped with lens options that allow for measurement spot sizes as small as 0.3-cm- (0.12-in-) diameter at a distance of 30 cm (12 in) and sighting of the measurement location is done through the lens for easy alignment.



The current recommendation is to incorporate both a limited number of TCs and a two-band optical pyrometer to measure the sheath surface temperature during testing. This will reduce the overall effort involved in setting up, attaching, and maintaining TCs on the assembly sheath and will offer duplication of temperature measurements as the pyrometer is being tested. In addition, the two-band system will be completely external to the chamber, allowing for rapid replacement or troubleshooting should it be required. TCs will also be incorporated to measure environmental conditions on the support stand and the test chamber.

In summary, a significant amount of support hardware must be developed to properly conduct thermal simulator testing in relevant environments and at characteristic temperatures prior to full core or partial core array testing.

### **3.1 Gas Purification System**

The gas purification system adopted for use with the thermal simulator test chamber was originally designed for use with lifetime testing of refractory metal HPs that utilize a LM working fluid. Therefore, it was designed to achieve very high gas purity (<1 ppb O<sub>2</sub> contamination) over extended test times. The system incorporates two independent gas purifiers to accomplish this goal: a once-through SAES Pure Gas, Inc. MicroTorr® purifier that is used to initially cleanse the gas from the supply bottles and a recirculating SAES MonoTorr® purifier that is used to continually filter contaminants from the chamber fill gas as it is recycled through the system during testing. The gas purification system is designed to operate with any desired mixture of He and Ar gas (set by the partial pressure of each gas), which can be premixed from independent K-bottles. The premixed gas is contained in a mixed gas bottle and once the recirculating gas system is brought up to the desired gas pressure, the supply bottle is isolated and the mixed gas is continuously cycled through the test chamber and gas purification system. The design of the gas mixture and purification system, shown in figure 44, is such that the recirculating gas system can be fully isolated from the gas mixing/fill system using the hand valve G-HOV9, allowing the gas mixture bottle to be charged with an appropriate He/Ar mixture prior to test chamber fill.

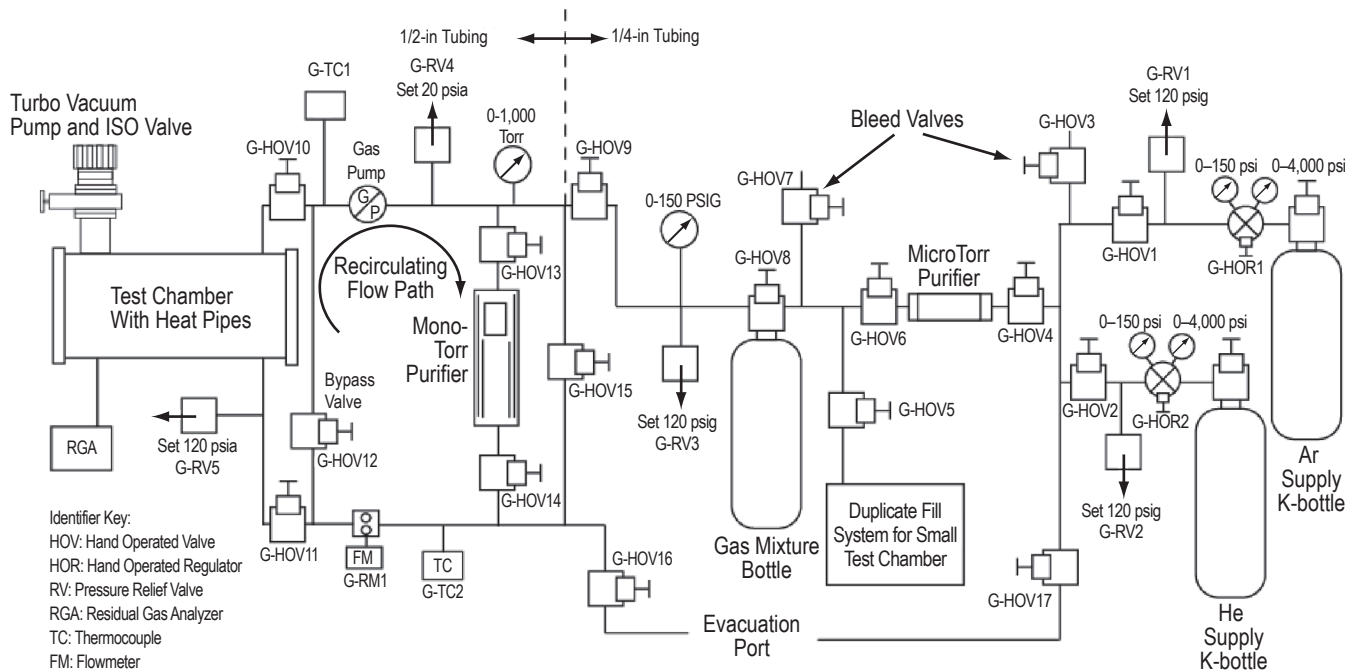


Figure 44. Test chamber gas mixture and purification system.

The MicroTorr Purifier, which has an advertised performance for purifying both He and Ar to a final  $O_2$  concentration of 1 ppb, is employed on the inlet flow line. With a vacuum chamber initially filled with air, the  $O_2$  concentration in the test chamber can be significantly reduced over multiple gas dilution cycles with high purity He or Ar. After only two dilution cycles starting from atmospheric pressure, the final  $O_2$  impurity concentration is just 0.1 ppb at a 10 kPa (76 torr) test chamber pressure. This condition meets the acceptable  $O_2$  concentration ( $\approx 0.28$  ppb) for testing Mo-Re alloys (per the design specification set for lifetime HP testing) and is well within an acceptable range for testing prospective thermal simulators.

Within the MonoTorr purifier, getter materials are used to irreversibly trap gaseous impurity molecules that are captured on the surface of the materials and, upon heating, diffuse into the bulk of the getter. Note that if the getters inside the MonoTorr are inadvertently exposed to air, they will be immediately filled, and the unit will require extensive overhaul before it can be applied again in the purification loop. The internal heater within the MonoTorr device has an operating temperature of 400 °C and, as a result, gas exiting the MonoTorr will have an elevated temperature up to as much as 400 °C, which may require that the lines be cooled by water circulation downstream of the MonoTorr. For this reason, the gas pump is located upstream of the MonoTorr purifier to prevent overheating of the pump internals. When used with Ar or He, the MonoTorr purifier can remove molecules of water ( $H_2O$ ),  $O_2$ , hydrogen gas ( $H_2$ ), carbon monoxide (CO),  $CO_2$ , nitrogen gas ( $N_2$ ), and methane ( $CH_4$ ). The performance of the purifier is dependent on the pumping speed at which it is operated. Table 15 provides a summary of the performance guarantee for the SAES MonoTorr Phase II 3000 for rare gases.

Table 15. SAES MonoTorr phase II 3000 performance guarantee for rare gases.

Impurity	Pumping Rate	
	0-20 slpm (ppb)	20-50 slpm (ppb)
O <sub>2</sub>	< 1	< 1
H <sub>2</sub> O	< 1	< 1
CO	< 1	< 1
CO <sub>2</sub>	< 1	< 1
N <sub>2</sub>	< 1	< 10
H <sub>2</sub>	< 1	< 10
CH <sub>4</sub>	< 1	< 10

When the gas purification system is incorporated in thermal simulator testing, the test procedure will include an initial bakeout of the system (under vacuum), which will assist in driving out volatile impurities (primarily water, if the system is clean and degreased) from the test components and gas lines to reduce additional impurities in the system. An endothermic process, desorption (or outgassing) is accelerated by increased temperature. The rate at which gas appears to emanate from a surface is referred to as the outgassing constant and this value is usually given in torr-L/s-cm<sup>2</sup>. It is advisable to begin a degassing program by first pumping down the system at room temperature to remove physically adsorbed water before commencing the baking cycle. If heat is applied at atmospheric pressure, it could result in activated chemisorption of physically adsorbed gas, which would require a prolonged heating cycle to remove.

Residual gases in a vacuum chamber derive from the original gas content of the chamber, gas emission from the chamber walls, or hardware in the chamber, or leaks from the outside of the chamber. To determine the actual gas content in the test chamber and to assess the effectiveness of the bakeout and gas purification processes, a residual gas analyzer (RGA) should be employed to verify the partial pressure of various gaseous components in the test chamber throughout test. A DYCOR® Dymaxion™ Mass Spectrometer (an Ametek Process Instruments product), model DM100M) will be employed in the test system. The DYCOR mass spectrometer utilizes a quadrupole mass analyzer. A hot filament in the RGA is used to create electrons of a suitable energy that then generate a stream of ions, where the rate depends on the pressure, temperature, and species of the individual molecules. The stream of ions is then electrostatically focused toward the mass filter. A quadrupole mass filter consists of four metal rods having a time-varying electrical voltage applied, selected to only allow ions of a particular mass to enter along the axis and to pass through to the opposite end. After passing through the mass filter, ions are focused toward a Faraday cup and the current is measured using a highly sensitive ammeter. The resulting signal is proportional to the partial pressure of the ion species that was passed by the mass filter. Because the current produced by residual gases is very small, a sensitive signal amplifier is also required in the system to detect very small partial pressures of the various gases that may be present. The DYCOR DM100M can be used to detect masses up to 100 AMU at a minimum detectable partial pressure of  $6.7 \times 10^{-10}$  Pa ( $5 \times 10^{-12}$  torr).

The gas purification system has been installed in the MSFC thermal simulator test laboratory and is connected to the thermal simulator test chamber, as shown in figure 45. This system is intended to purify the gas (reduce the potential for contaminants) contained within the test chamber. The test chamber gas thermally couples the calorimeter and heater element by means of a static gas gap to achieve the required power/temperature balance. A complete leak check was conducted and all leaks on the low pressure side of the system (recirculating section) were located and repaired.

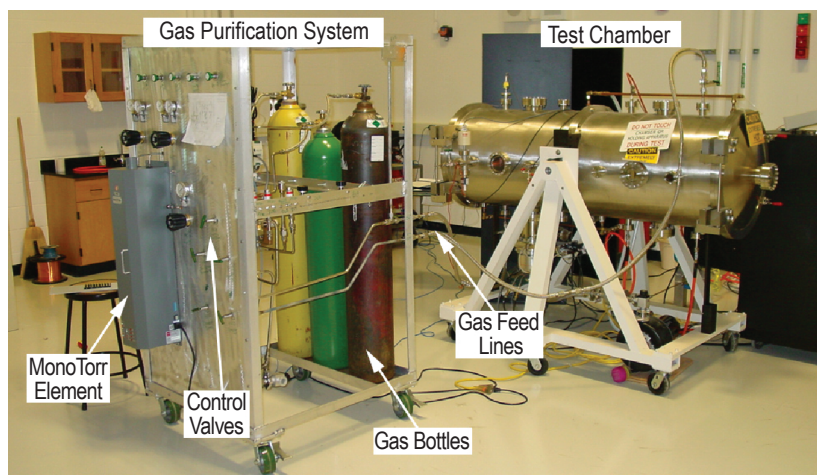


Figure 45. Inert gas purification system connected to test chamber.

Flow, temperature, and pressure measurement instrumentation on the gas purification rack have been tied into a data acquisition system and initial checkout tests have been performed to evaluate gas loading and flow performance of the system. In an effort to conserve its capacity, the MonoTorr purifier element has not been activated in tests performed to date. It will be employed at a later date after the RGA has been integrated with the system and all gas purification system lines have been bakedout to minimize potential contaminants in the system. Initial checkouts were performed with air and pure He to determine flow performance in the gas purification system. Results of air flow tests at a pressure of 1 atm indicate a volumetric flow rate of  $\approx 20$  L/min, in agreement with manufacturer reported capability. As operating pressure is reduced, the volumetric flow (as reported by the thermal mass flowmeter) remains approximately constant, as expected, since the pump is a diaphragm design with a constant volume displacement. However, below 20 kPa (150 torr), the flowmeter indicates substantial drops in the volumetric flow, reporting  $\approx 9$  L/min at 6.7 kPa (50 torr). It is currently believed that the actual volumetric flow rate is approximately constant even at the reduced operating pressure and the reduction in the reported flow rate could be attributable to error in the thermal flowmeter since it is being operated well below its designed operating and calibrated pressure range. Note that accurate flow measurements are not important for this application since the flowmeter is only intended to provide an indication of flow in the purification loop, much like a flow switch.

For the baseline He case at a test chamber pressure of 13 kPa (100 torr), the gas inventory was  $\approx 0.012$  kg. This gas was cycled throughout the purifier at a rate of 0.023 kg/hr, resulting in about two gas exchanges per hour. To monitor the gas conditioning process, the DYCOR RGA was set up to sample the gas purification loop and thermal simulator chamber. The RGA was successfully operated after resolving some initial communication problems between the analyzer and the control computer. The RGA was used to sample the recirculation line with He present in the system and the unit was used to display the partial pressure of each species in the system. At this time, however, the circulation system tubing has not been vacuum baked, resulting in a high background floor (as read on the RGA). Heater tape will be applied to all tubing and components on the gas purification loop and the system baked out for a minimum of 24 hr prior to use with the thermal simulator test chamber and prior to incorporation of the MonoTorr purifier (testing to date has used the MonoTorr bypass flow path). The SAES MonoTorr purifier, which will be used to scrub the recirculation flow, has been operated briefly to ensure proper operation of the complete purification loop. Initial results indicate that it has a higher than anticipated pressure drop, resulting in a lower flow rate which corresponds to an increase in the time required to fully circulate the gas inventory in the system, but this is not expected to adversely affect the proper operation of the test chamber.

Initial operational procedures have been laid out and checkout operations of the gas purification system have been initiated, as previously discussed. Actual use of the purification system to support day-to-day operations will be held off until additional operating experience has been gained so that its implementation will not impact currently scheduled test activities.

### **3.2 Water-Cooled Calorimeter**

As discussed in the test results in section 2.5.2, a noncontact water-cooled calorimeter has been specifically designed to allow testing of individual thermal simulators in a relevant thermal environment. This calorimeter is designed to achieve a specific sheath temperature at a given power level, simulating the conditions that the thermal simulator assembly would see in the full core assembly. A series of thermal calculations was performed to initially size a calorimeter for anticipated simulator testing. Coupling of the calorimeter to the heater element is controlled by a static gas gap containing He, Ar, or a mixture of these gases. Water flow rates through the calorimeter are assumed to range from 0.4 to 7.6 L/min (0.1 to 2 gpm) for initial calculations. In shifting from pure He gas to a mixture of He and Ar, it is noted that the reduced thermal conductivity arising from the addition of Ar to the gas mix increases the sheath temperature by a few hundred degrees kelvin depending on the power levels and the mixture ratio. Desired boundary conditions for heater testing were obtained from NRPCT. The current state of the reactor designs indicate that the fuel pin OD temperature could range from 1,100 to 1,700 K, with power per pin of up to 6,000 W. However, it is anticipated that the final design will set the fuel OD temperature closer to 1,400 to 1,500 K. The calorimeter design attempts to meet this range of conditions, but it is likely that multiple calorimeters will be necessary to cover the full range of test parameters.

The current calorimeter concept uses a series of Cu coils attached to a central Cu tube that completely surrounds the sheathed heater element. Operational conditions include holding a given power throughput in the heater (up to 6 kW) while maintaining a prototypic fuel pin surface



temperature on the heater element (up to 1,700 K, as specified by the reactor design). The individual Cu coils that form the calorimeter assembly are positioned with a slight separation to provide access to the surface of the heater sheath for TC and optical pyrometer measurements.

A thermal and flow analysis was performed for the initial noncontact water calorimeter design. Key operating parameters included: sizing of the conduction gas gap width, cooling water flow rate, water temperature rise, water pressure drop, and bulk Cu operating temperature. The design heater boundary conditions used in this analysis include a power level of 6,000 W at temperatures of 1,700, 1,400, and 1,100 K. The basic engineering layout for a wrapped coil type configuration uses off-the-shelf Cu tubing and hardware components. Two methods were identified to meet the heater operating power and temperature conditions. First, each test boundary condition could be accomplished by fabricating three different calorimeter units with gas gap widths set to meet each of the operating temperature conditions. Alternately, a fixed gas gap geometry could be used and the desired sheath temperature could then be achieved by varying the composition of the conduction gas to adjust the gas conductivity. Figure 46 illustrates the basic calorimeter layout that includes six individual cooling coils separated by  $\approx 0.64$  cm ( $\approx 0.25$  in) to allow for TC/optical pyrometer access. Four coils have 13.5 revolutions of Cu tubing while the remaining two have 6.5 revolutions. To test fabrication techniques, 4-in-long coil segment samples were wrapped on the central support tube and brazed in place (fig. 47). Initial trials using a furnace braze method resulted in good bonding of the 0.64-cm- (0.25-in-) diameter flow coils to the central tube and each other; however, the tri-cusp area between coils was not filled due to the limited amount of braze material which could be added. A hand-brazing technique was then employed (allowing more filler braze material to be added) and this technique resulted in good bonding between adjacent coil tubes and nearly filled all the tricusp cavities. Due to the high thermal conductivity of Cu and the close packing of the cooling coils, complete filling of the tricusp gaps is not necessary to meet the desired operating conditions.

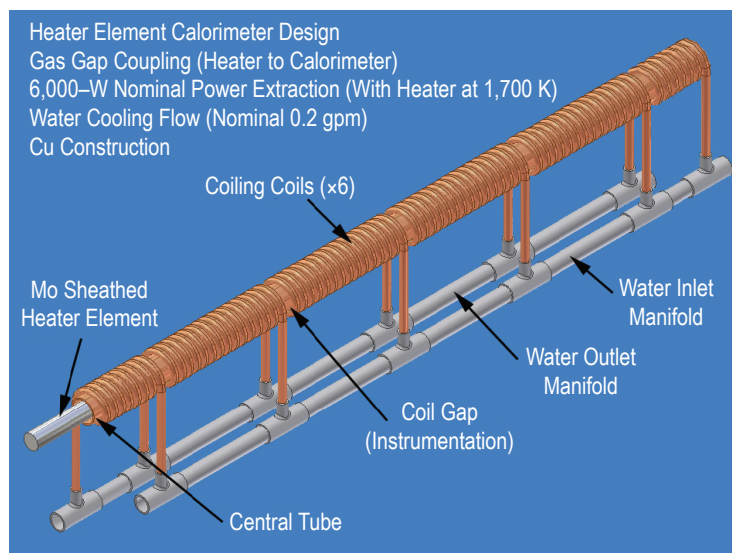


Figure 46. Heater element calorimeter layout.





Figure 47. Calorimeter coil fabrication tests.

After initial success with the hand-brazing technique, it was noted that the high temperatures required for this braze resulted in a reduction of the central tube strength, introducing difficulty in maintaining concentricity between the heater element and the calorimeter. Therefore, low-temperature hand-brazing and soldering tests were conducted to further perfect the technique of attaching the Cu coils to the central calorimeter tube. Due to difficulties encountered during repeated brazing attempts, the initial as-built configuration did not include braze or solder connecting the coils to the central tube. There may be sufficient contact between the coils and the tube by virtue of the wrapping procedure and this contact conductance may be complimented by the existence of a very thin, sufficiently conductive gas gap. Testing is necessary to fully assess these assumptions. Differential thermal expansion between the central tube and the water-filled coils might enhance contact pressure and the conductance between the coils and the primary tube. If this concept does not provide sufficient cooling during initial testing, additional braze applications will be attempted or other coupling techniques (such as thermal epoxy or thermal grease) will be evaluated. To complete the connection to the Cu coil assemblies, silver solder is used to connect the water supply/return headers.

Thermal analysis, performed in parallel to the assembly of the initial calorimeter concept, assumes some preliminary values for coil-to-central-tube contact and gas gap conductance. This analysis indicates that for a pure He gas gap between the coils and the primary tube, sufficient cooling is available to extract 6,000 W while maintaining the maximum sheath temperature at or near the 1,700 K target. The analysis further shows that if the gap contains pure Ar or vacuum conditions, excessive sheath and heater temperatures will ensue. Unless initial testing indicates that the preliminary assumptions in the model are too conservative, some means of directly coupling the coils to the central tube should be implemented to allow lower sheath temperatures to be achieved, or to provide any ‘tunability’ to reach alternative conditions. Analysis results also suggest that a thicker wall central tube with a smaller sheath/central tube gap would be helpful

in meeting desired target ranges. The initial calorimeter thermal testing should help to quantify the thermal conductances and provide a basis for correlation of the calorimeter thermal model to the actual test hardware. More detailed discussion of the thermal model and results are provided in appendix J.

Spring-loaded TCs were built to allow monitoring of the heater element sheath temperature at five locations. Figure 48 illustrates the TC probe layout in which exposed bead TC probes will be used in the final assembly. The spring loaded TC allows the assembly to be fitted to the calorimeter and ensures that direct contact between the TC and sheath will be maintained. However, initial thermal analysis suggests that the TC thermal conduction error for this configuration can be very large, ranging from tens to hundreds of degrees kelvin. A detailed analysis of the potential error associated with spring-loaded TCs is provided in appendix K. Additional temperature measurements will be obtained at the same axial positions (rotated by 180°) using two-band optical pyrometers to better assess the element temperature. The calorimeter test chamber and the instrumented test configuration are shown in figures 49 and 50.

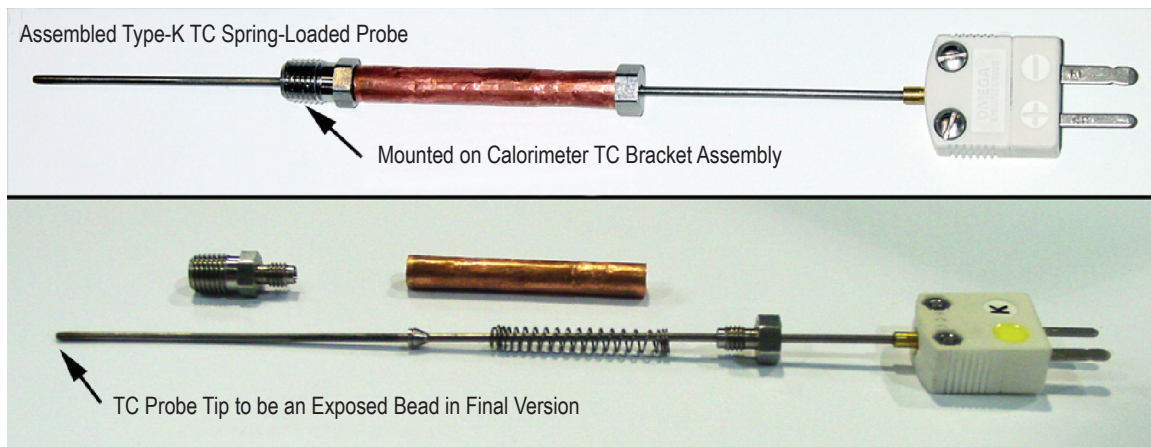


Figure 48. Spring-loaded TC unit.

The heater element will be centered in the calorimeter using thin Mo spacer rings. The selected approach uses two spacer rings, one placed at each end of the sheath in the unheated regions. The Mo heater sheath is not expected to sag significantly at the planned operating temperatures, so the need for a central spacer ring is not anticipated at this time, but could easily be added if necessary. The Mo spacer rings were fabricated from 0.25-mm- (0.010-in-) thick plate stock and machined to a knife edge along the contact perimeter in order to minimize heat transfer through the ring itself. An approximate 0.13-mm (0.005-in) clearance is provided on the inner and outer ring diameters to allow for easy assembly and to account for thermal expansion.

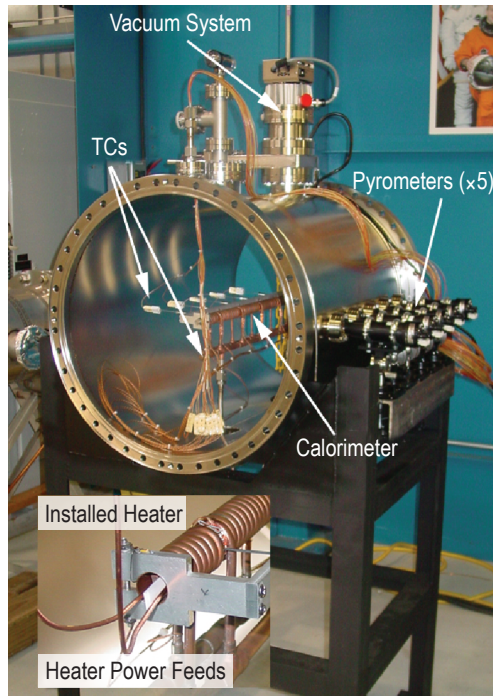


Figure 49. Calorimeter test chamber.

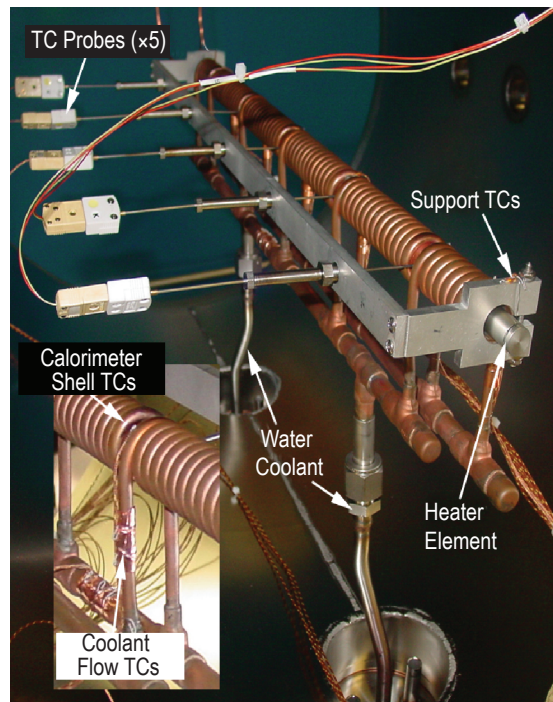


Figure 50. Calorimeter instrumentation.



The thermal simulator test chamber with integrated calorimeter assembly has been set up and auxiliary support systems such as vacuum hardware, inert gas supply, and water-cooling components have been connected. To measure coolant water flow rate, a paddle wheel style flowmeter was installed. The test chamber shown in figure 49 is separate from the one currently used for refractory wire-wrapped heater testing discussed in section 2. Once calorimeter checkout tests are complete, the two independent thermal simulator test chambers will be used in heater checkout and lifetime testing. Figure 49 shows the current setup with the calorimeter and heater element installed. TC and optical pyrometer instrumentation have been attached to select calorimeter locations to monitor its operation, allowing comparison with thermal models. Figure 50 provides a closeup of the test configuration with a number of instrumentation locations identified. Before use in the current thermal simulator testing, the calorimeter will be fully checked out using proven heater elements to minimize any potential impact on the thermal simulator test program. For initial testing, a 46-cm- (18-in-) long graphite heater element, powered by a 15-kW dc power supply, has been installed. At the expected operating temperature, heater element resistance will be  $\approx 0.6 \Omega$  dissipating 6 kW, limited by the power supply maximum current output of 100 A (operating voltage would be 60 Vdc in this condition).

A successful low power checkout test of the power supply and data system was performed, bringing the heater to a temperature of 50 °C. (The test chamber was open to the air during these tests.) Following the checkout, the calorimeter assembly and test chamber were He leak checked. Results indicate that all vacuum chamber penetrations and connections are leak tight (as measured to  $10^{-10}$  Std  $\text{cm}^3/\text{s}$  He); however, leaks were noted on the calorimeter assembly, which includes several mechanical fittings and low-temperature braze joints. A water bubble test (with the calorimeter assembly pressurized) was used to isolate the visible leaks and they were repaired. The calorimeter was reinstalled in the test chamber and He leak checked to verify its integrity. The low-temperature braze joints on the Cu calorimeter fittings were suspect due to their close proximity to each other since the high thermal conductivity of Cu tends to significantly heat all the joints around the repair location. To address this issue should future repairs be required, an alternative to brazing is to perform a tungsten inert gas (TIG) weld at the joint locations. A sample joint (which was brazed) was TIG welded to test the welding process and to examine the interaction of the braze material with the weld. The operation was very successful, producing a final weld that looked good and passed a He leak test on the first try. Therefore, welding will be used to repair or manufacture new calorimeter components.

During a second checkout test, the test chamber was evacuated and the calorimeter assembly water cooling system with integrated flowmeter was temporarily connected to a facility potable water connection. Checkout testing indicated that the flow could be adjusted (using a throttling hand valve on the calorimeter exit) from 0.95 to 13.2 L/min (0.25 to 3.5 gal/min) at a service pressure of  $\approx 0.4$  MPa ( $\approx 60$  psi). This range of flow rate is expected to be sufficient for the planned tests. However, the thermal model calculations, provided in full in appendix K, assume a maximum water flow rate of 19 L/min (5 gal/min) and a maximum service pressure of 0.55 MPa (80 psi). During the checkout testing, the input heater power was held at 500 W, resulting in a heater sheath temperature of  $\approx 1,073$  K ( $\approx 900$  °C) and the Cu calorimeter temperature remained essentially uniform, ranging from 302 K (29 °C) at the water inlet to  $\approx 308$  K ( $\approx 35$  °C) on the

uncooled portion of the shell (midway between cooling coils). During this operation, the chamber vacuum level initially spiked into the 1.3 mPa ( $10^{-5}$  torr) range, followed by a slow fall into the  $\approx 0.5$  mPa ( $\approx$ mid  $10^{-6}$  torr) range. This response is typical when baking out vacuum systems. These initial test results, performed in a vacuum environment, have not yet been used to correlate thermal model results in order to determine the actual contact and gap conductances. As shown in the results presented in appendix J, the thermal model predicts a maximum sheath temperature that is appreciably higher than that measured. Subsequent examination is warranted to understand the differences between the experimental and predicted results, but the lower measured temperature is promising with regard to achieving sheath temperatures in the range of interest.

### 3.3 Data Acquisition System

A computer controlled user interface (data acquisition and control) has been developed for automated thermal simulator testing, incorporating multiple safety cuts to allow round-the-clock testing in the absence of support personnel. The control interface is comprised of five LabVIEW® (a National Instruments product) applications that include: main thermal simulator application, strip-chart application, multigauge server, gas flowmeter server, and data recorder.

The thermal simulator application, shown in figure 51, provides the following functionality:

- Manual control of the heaters, where the user specifies a current and voltage.
- Automatic power control, where the application automatically adjusts the voltage setpoint to achieve the user-specified power setting.
- Automatic control of heater power over time to a user-specified profile for a user-specified number of cycles, allowing the heaters to be cycled repeatedly over a long period of time without user intervention.
- Checks for out-of-limit conditions. Each limit violation is indicated on the display. If a limit violation occurs when cutoffs are enabled, the application automatically interrupts the power to the heater.

Out-of-limit conditions are established such that the power to the heater simulator is automatically shut down if any one of the limits is exceeded. Currently, the application can monitor the following:

- Up to 20 TCs for individually specified limits.
- Chamber pressure for a specified upper and lower limit (shutdown will also occur in the event of a loss of signal from the vacuum gauge server).
- Heater element power for a specified percent tolerance over the setpoint.
- Calculated element resistance for a specified percent tolerance relative to a specified resistance.

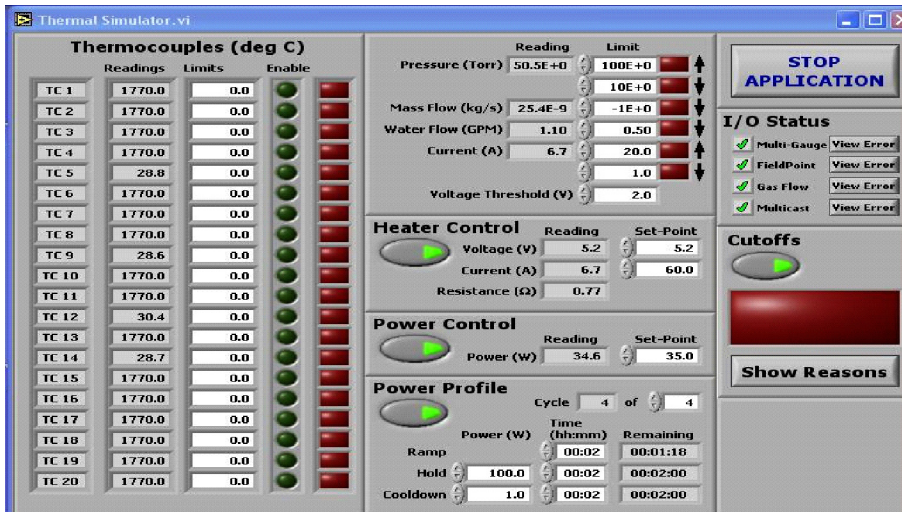


Figure 51. LabVIEW thermal simulator application.

- Mass flow rate of gas through the recirculating gas purification system below a specified limit (shutdown will also occur in the event of a loss of signal from the gas flowmeter server).
- Mass flow of cooling water through the walls of the thermal simulator test chamber and the heater calorimeter (shutdown will occur given a low or no flow condition).

The application monitors measurements for limit violations and updates display indicators appropriately. If cutoffs are enabled and an out-of-limit condition occurs, the power to the heater is immediately shut down and the limit indicators are latched. The indicators are unlatched when cutoffs are disabled by user intervention. Before enabling cutoffs, the user must verify that all limit indicators are off to prevent the cutoff from immediately tripping. Additionally, a signal light was installed to indicate the system status: when the system cutoffs are enabled and no cutoff has occurred, the light is green; during a cutoff condition, the light flashes red, and when cutoffs are disabled, the light is off.

The strip-chart application, shown in figure 52, plots up to 24 hours of pressure, TC, voltage, current, resistance, and power data. All data are recorded to a data file for post processing.



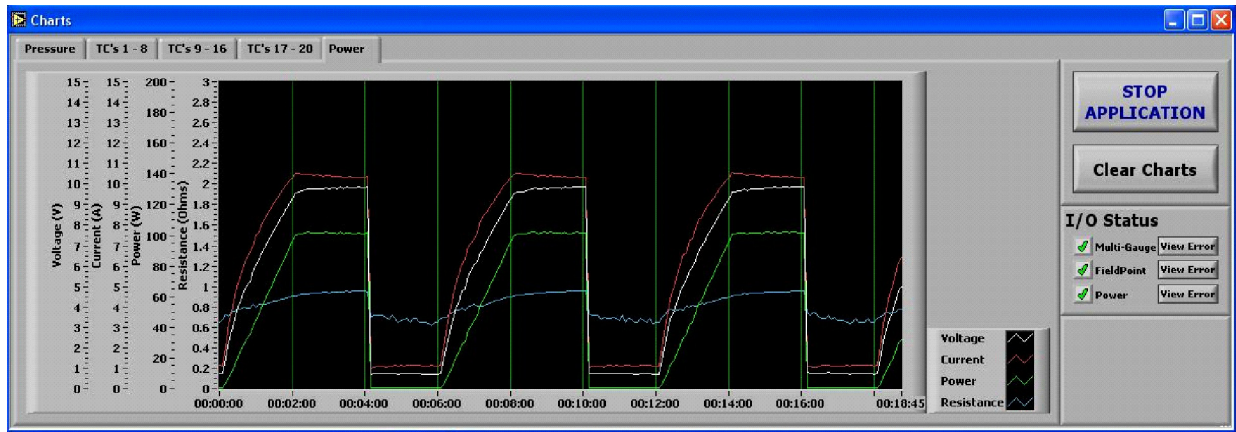


Figure 52. LabVIEW strip-chart application.

The multigauge server, shown in figure 53, acquires data from the vacuum gauges and uses the user datagram protocol (UDP) to distribute the data to other applications. The multigauge server handles the serial communication interface with the multigauge vacuum controller.

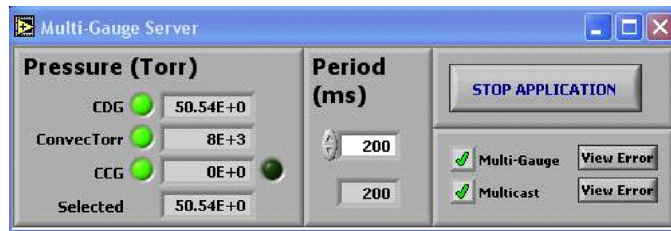


Figure 53. LabVIEW multigauge server.

The gas flowmeter server, shown in figure 54, acquires data from a thermal mass flowmeter and converts the reading from standard liters per minute (SLM) of  $N_2$  to the actual mass flow of a mixture of two gases and then uses the UDP to distribute the results to other applications. The conversion uses the mole fraction and the specific heat of each gas to compute the specific heat of the mixture. The ratio of the specific heat of  $N_2$  to that of the gas is then used to convert from the standard  $N_2$  reading to the actual reading for the mixture. The specific heat is necessary for the conversion because the meter is a thermal mass flowmeter and the sensor reading is proportional to the specific heat of the gas as well as the mass flow.

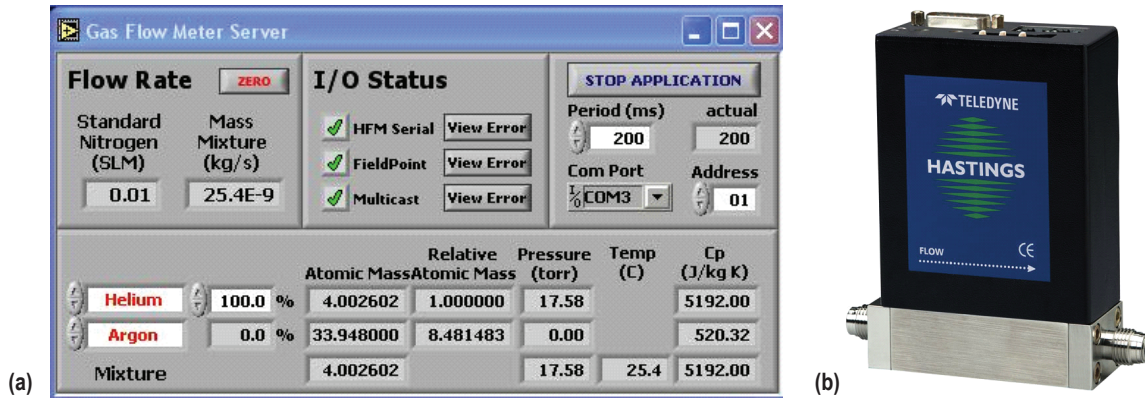


Figure 54. Flowmeters: (a) LabVIEW gas flowmeter server and (b) installed thermal mass flowmeter.

The data recorder, shown in figure 55, acquires data from the data acquisition hardware, the multigauge server, the gas flowmeter server, and the thermal simulator applications. These data are then recorded to a tab delimited file, which can be loaded into a spreadsheet. The recorder supports various user-specified record rates and allows the user to specify comments to be inserted into the data.



Figure 55. LabVIEW data recorder.

### 3.4 Modified Power Interface

In response to the 2005 NRPCT downselect to a direct gas-cooled reactor design, the power interface to the electrically heated reactor module was reinvestigated. The original power interface used in testing the SAFE HP-cooled reactor and the DDG cooled reactor allowed heater power leads to extend from the base of the core in order for Cu wire to be connected for power input to the heaters. This configuration is shown in figure 56 for the DDG test series. To minimize impact on the gas flow through the inlet plenum in gas-cooled reactor designs, a conceptual design for a modified power interface was developed for implementation in the next phase of thermal simulator designs. This power interface will minimize the interference of the electrical system with the flow plenum, better mimicking an actual reactor design. The current design assumes single-ended heater elements (power in/out at the same end), removing the need to account for axial thermal expansion from the power interface design. Additionally, the proposed concept assumes that the power interface is on the inlet flow plenum, as in the original DDG design. This assumption allows the use of existing power feedthroughs in the DDG pressure vessel, but power feedthroughs could be moved to the exit flow plenum if it is desired in subsequent reactor prototypes.

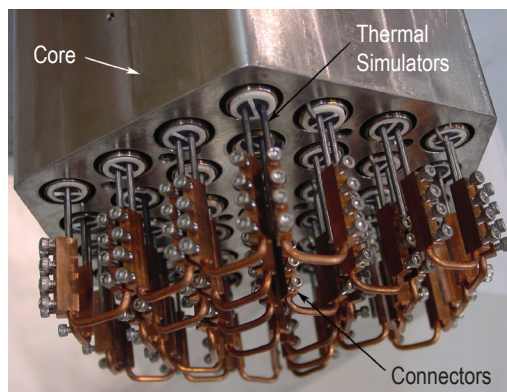


Figure 56. Power interface for the DDG-cooled reactor tests.

Initial conceptual designs have been prepared for a 2.5-cm- (1.0-in-) diameter heater (outer sheath diameter, corresponding to the outer clad diameter), within the range of potential fuel pin sizes in the reactor designs under evaluation by NRPCT. The power interface incorporates a ‘motherboard’ type design to bring power into the core with minimal disruption to the gas flow. The conceptual design appears to be feasible, but could become significantly more complicated with a larger number of fuel pins. The 37-pin DDG layout was used as a baseline for the initial design study. Figure 57 shows the conceptual design; detailed design drawings are included in appendix L.

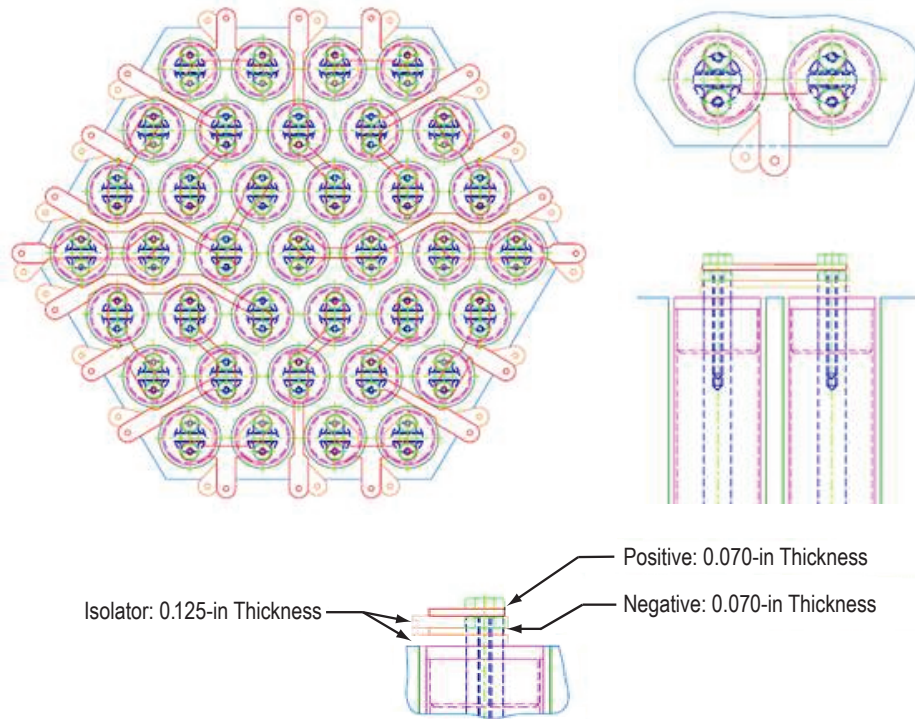


Figure 57. Modified power interface conceptual design, using 37-pin DDG as a baseline concept.

### 3.5 Component Cleaning and Chamber Preparation Procedures

The current test preparation procedures do not incorporate rigorous cleaning of test components, but some rough cleaning is performed. Prior to wrapping the  $\text{Al}_2\text{O}_3$  mandrel with the desired wire, both the mandrel and the wire are cleaned with methanol and all components are handled with gloves. The chamber startup and operation procedures are as follows:

- (1) Initialize roughing pump on the vacuum chamber. Allow to run for  $\approx 1$  hr.
- (2) Initialize turbopump—it will take  $\approx 10$  min to get to operational conditions. It will take several hours for the pressure to reduce to an acceptable level if pumping down from atmospheric conditions. Between testing days, the turbopump is turned off but the chamber is not opened (so that an acceptable pressure is reached in a relatively short time on subsequent test days). Note: The current chamber configuration does not incorporate any vacuum pressure gauges. Pressure is estimated to be  $\approx 10^{-5}$  torr based on past experience with this pump and chamber.
- (3) Turn on cooling water to cool the chamber walls.
- (4) Turn on power supply. The heater elements operate in a voltage-limited mode, so the current on the supply is turned to its maximum 100 A and power is controlled by adjusting voltage.



(5) For initial testing of an element, apply 50–100 W and allow the element to bake out for a few hours. For subsequent test days, set the power supply to the desired power level (1,200 W).

(6) At the end of test day, turn off power supply and pumps. Allow the element temperature to drop below  $\approx 200$  °C before turning off chamber cooling. (Note: It will take  $\approx 30$  min for a bare element and  $\approx 1$  hr for a sheathed element to cool to the desired temperature.)

More extensive cleaning procedures will be adopted for higher fidelity element testing and prior to heater integration into each test article.

Posttest materials analysis of the W and Re heater elements indicates that the lack of thorough cleaning procedures may have impacted test results due to the presence of various residues on the heater assembly. To minimize the possibility of contaminants affecting the test results, more extensive cleaning procedures should be adopted for all components that will be in the test chamber: mandrel, heater wire, sheath, chamber, and support structure. Extensive cleaning will also be required before heater assemblies are integrated in the reactor test article to prevent any contamination of the test article. Proposed cleaning procedures for various materials are included in appendix M. Each procedure includes a series of steps that use Freon™ (a DuPont product), chemical cleaning, and ethanol to remove any grease, oil, and other contaminants from the material. Vacuum firing is also employed to remove moisture (water vapor) from the material.

In addition to thorough cleaning, all components should be fully baked out to remove all water vapor and other residual contaminants from the chamber and other structures. Tests will be conducted in a vacuum environment or in a low-pressure, high-purity inert gas environment per the test requirements and the boundary conditions that will exist when the heater assemblies are inserted into the full test article. The proposed procedure is derived from chamber preparation procedures outlined for HP life testing at the EFF-TF, with modification made for this specific application. Step 14 can be omitted if testing is to be performed in a vacuum environment. This procedure assumes that additional instrumentation has been incorporated in the test chamber. The procedure is as follows:

- (1) Clean heater unit using the approved procedure (see app. M) and handle only with powder-free, alcohol-cleaned surgical gloves.
- (2) Wipe down the test chamber with Freon and alcohol to remove any potential grease, solvents, fingerprints, etc. Also perform a complete visual inspection to verify that no foreign materials are present. Allow the test chamber to dry for a minimum of 1 hr.
- (3) Install cleaned heater assembly into the test chamber support bracket and secure.
- (4) Close the test chamber and secure all flanges using appropriate tightening sequence.

(5) Evacuate test chamber and inert gas feed system lines to 0.1 mPa ( $10^{-6}$  torr) or lower and perform a He leak check to a sensitivity of  $10^{-10}$  std cm<sup>3</sup>/s He on all flanges, feedthroughs, and view ports. Tighten any leaky fittings using the appropriate tightening sequence, exchanging any leaky view ports. Note: He leak checking is a fairly time-consuming process and it is not necessary to perform this check prior to every test. Leak checks will be performed on initial chamber check-out and will be repeated periodically (approximately monthly) to ensure that the chamber is still leak tight.

(6) Turn on the test chamber wall and inert gas feed system heater tapes and bring to a temperature of  $\approx 200$  °C ( $\approx 575$  K) to outgas all trapped water vapor and other volatiles.

(7) Measure the cold resistance of the heater assembly prior to heat-up. (This will be compared to the assembly resistance after outgassing, during test, and after test to assess stability of the heater element.) Turn on the heater element power supply and heat the element to  $\approx 200$  to  $400$  °C ( $\approx 575$  to  $775$  K) by applying a low-power level to the element ( $\approx 50$ – $100$  W). Hold at this heated condition for  $\approx 24$  hr or until pressure reaches the  $\approx 0.01$  mPa ( $\approx$ mid  $10^{-7}$  torr) range. Periodically monitor test chamber vacuum pressure. Note: Test chamber pressure should increase during heating and then begin to fall after a steady temperature has been maintained for 1 to 2 hr. If pressure continues to rise or does not drop, there may be a leak due to heating of the flanges. Perform a leak test while at temperature to locate the leak and tighten the offending flange.

(8) Verify that all data systems are operational and the temperature measurement system is properly set up (two-band optical pyrometer is focused on the desired heater assembly location and/or TCs are registering reasonable values).

(9) Increase the power to the heater element to continue the outgassing process. Power can be increased using a linear ramp over time, up to approximately two-thirds of the desired pin power level (800 W for a 1,200 W assembly test, reaching  $\approx 800$  to  $900$  K). Note: The test chamber pressure will increase as additional outgassing occurs. As the temperature is increased, the chamber pressure will drop again when the element is no longer outgassing.

(10) Maintain the heater at a constant temperature for  $\approx 2$  hr and monitor the test chamber pressure. The pressure should begin to fall off after reaching a high value.

(11) Turn off power system and all tape heaters and monitor the test chamber vacuum level as the system cools. The pressure should drop approximately one decade after the entire system is cooled to room temperature.

(12) Isolate the inert gas system from the vacuum chamber and charge the system with the required inert gas mixture ratio. (Typical gasses will be He and/or Ar, with the desired percent Ar specified by weight.) This is in preparation for multiple dilution cycles of the test chamber to sweep the environment. A discussion of the effect of multiple dilution cycles using UHP gas on the level of contaminants in the test chamber is included in appendix O.



(13) Isolate the test chamber from the vacuum system and then introduce the inert gas mixture purge into the test chamber to a pressure of  $\approx 9$  kPa ( $\approx 70$  torr). Isolate the test chamber and let stand for 2 min.

(14) Isolate the inert gas system and open the vacuum system to remove the inert gas mixture from the test chamber. Allow the vacuum to reach the 0.1 mPa ( $10^{-6}$  torr) range.

(15) Perform two more inert gas dilution cycles, and then bring the test chamber pressure to  $\approx 9$  kPa ( $\approx 70$  torr). (Note: This step is omitted for vacuum testing.)

#### 4. ADVANCED THERMAL SIMULATORS: CURRENT STATUS

Advanced simulator development includes efforts to embed instrumentation (TCs) within the thermal simulator structure and to develop simulators that better mimic the behavior of nuclear fuel elements. Discussions and initial investigations on advanced thermal simulator design and development have commenced. The current plan is to develop simple, advanced simulator models in-house to test techniques and methods for embedding instrumentation within the thermal simulator assembly and to assess fabrication ability with regard to matching key properties of nuclear fuel elements. Test articles will begin with graphite heater element cores. Rather than inserting the graphite element into a metal sheath with a gas fill in the heater/sheath gap, attempts will be made to fill it with an insulating powder to improve the conductivity across the thermal simulator. This technique was previously attempted by engineers that developed thermal simulators for testing at the Oak Ridge National Laboratory (ORNL) in the 1970s and 1980s.<sup>15,16</sup> These experiments led to limited success due to the method in which the filler material was inserted between the element and sheath. In the ORNL heater elements, the insulating powder was poured into the gap, and tamped down periodically to remove voids, but no verification was performed to ensure that no voids existed. In addition to using the insulating powder layer, the future TCs will be embedded inside the sheath structure. External TCs and pyrometers will also be used to measure sheath temperature and to then assess the relationship between the internal and external measured temperatures.

In developing advanced simulators, the most important parameter to match is the dynamic response of the nuclear fuel element rather than the static characteristics, such as conductivity. It may be desirable to maximize the conductivity across the pin (radially), allowing significant capability to get heat out of the simulator and minimizing the temperature of the central element. The simulator design will then attempt to match dynamic characteristics at the outer radius of the simulator (at the sheath surface) to those at the outer radius of the nuclear fuel element (at the outer surface of the fuel clad structure).

Initial attempts at developing advanced simulators will take advantage of materials available in-house. This will include use of graphite heater elements with a buildup of ceramic material around the element with TCs embedded during the buildup process. Characteristics of various powdered insulating materials will be assessed to determine the best option for simulator construction. Methods of applying the insulating material will also be investigated. One option is to simply fill the gap with powder, tamping down the powder periodically to remove any voids that might exist. However, this method limits the ability to predict the packing density in the heater/sheath gap, which could lead to localized heating due to poor conductivity. Other possible techniques include VPS or chemical vapor deposition (CVD). If a plasma spray process is adopted, it may be possible to build up the heater element with the TCs already positioned in the heater/sheath gap, but this remains undetermined. The potential of using a metal 'shield' between the

heater and sheath to improve radial pin conductivity will also be considered as an option in heater element buildup. An analysis of the potential materials selection and layering will be completed, along with a materials compatibility study.

Thermal analysis associated with advanced thermal simulator development will entail an assessment of the axial heat flux at various layers of the proposed element to determine the ultimate external heat flux distribution at the outer sheath surface, both during steady state and dynamic conditions. This analysis will be run in parallel to initial element design and buildup and will feed into the future development of advanced simulators.

Initial advanced thermal simulator configurations can be evaluated using graphite heater elements. The samples would be fabricated using powder materials such as AlN, W, or Mo to fill the gap between the graphite heater and Mo sheath. However, caution should be taken when using W or Mo filler materials because, while both are thermally conductive, they are also electrically conductive and will require some type of insulator layer to prevent electrical contact between the heater and sheath. Alumina nitrate has a much higher thermal conductivity (140–200 W/m-K) than ceramics currently being used in simulator construction, such as Al<sub>2</sub>O<sub>3</sub> (18 W/m-K) or BN (40 W/m-K). The thermal conductivity values decrease at temperatures above 1,273 K (1,000 °C) but still provide some improvement over Al<sub>2</sub>O<sub>3</sub> or BN.

Alumina nitrate is also a good electrical insulator. Similar materials have been used on VPS Mo and Mo-Re HPs that had an Al<sub>2</sub>O<sub>3</sub>/AlN composite material on the OD for electrical isolation. If necessary, a thin, dense AlN coating (applied by a technique such as sputtering, CVD, etc.) can first be deposited on the graphite to electrically isolate the heater. This approach might allow the use of a metallic powder or solid gap filler with higher thermal conductivity. Tungsten and Mo, for instance, both have decent thermal conductivity as compared to ceramics. A spray deposition approach may also allow for a milling process that could be used to minimize the gap between the heater and the sheath to very small clearances. By overapplying the outer isolating layer, then machining the OD to match the ID of the sheath (keeping in mind the tolerances), very small gaps might be achieved depending on the machining tolerances of the sheath and the heater. If this small gap can be filled with He, then heater to sheath thermal conductances could be significantly improved over existing larger gap configurations. On the other hand, the sheath material could be sprayed directly onto the outer layer of the isolator if differential thermal expansion of the materials does not present potential problems.

Advanced fabrication techniques are also being investigated to fabricate assemblies with embedded TCs. These could be embedded within the powder material between the graphite heater element and the sheath. This can be done using processes such as VPS, CVD, or electroforming to close out machined grooves in refractory metal sheath materials. Net shaped multimaterial components are also possible.

Temperature measurements inside a heater element assembly could be accomplished using very fine TCs embedded in the insulation around the heater element, or fiber optic probes might be inserted along the length to obtain a complete description of the temperature in this region at multiple axial positions. Figure 58 shows the heater element placement inside the DDG core block, identifying the  $\text{Al}_2\text{O}_3$  spacer region that could be used to embed TCs.

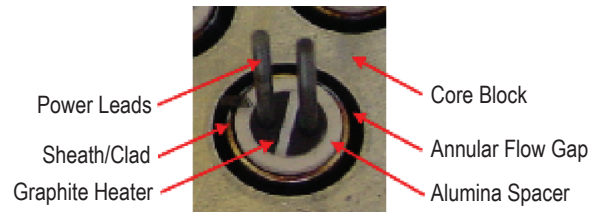


Figure 58. Heater element placement inside DDG core block and TCs would be embedded in the  $\text{Al}_2\text{O}_3$  spacer region.

Fiber optic temperature probes developed by Luna Innovations, Inc. are constructed with Bragg gratings spaced evenly (standard fiber optic design allows measurement of temperature at 1-cm increments) along the sensing length to obtain detailed temperature profiles. These fiber optics currently have a temperature limitation of 1,000 °C for testing over extended times and may not survive over long test times at elevated temperatures in the DDG core. Luna fiber optic probes tested on the SAFE-100 demonstrated superior ability in generating three-dimensional temperature profiles of the core.<sup>17</sup> Luna is currently working to extend the maximum operating temperature of the fiber optic sensors, which may qualify them for use as embedded temperature instrumentation in future advanced heater elements. Previous tests with these fiber optics were conducted by Luna, who brought the support hardware necessary to obtain and record data from the fiber optic probes to MSFC for temporary use. The EFF-TF is currently working to obtain an in-house capability to use fiber optic sensing techniques in future testing applications.

An initial series of tests was conducted to examine the possibility of embedding very fine (52 AWG) TCs between the heater and sheath. Because TCs are relatively inexpensive and are available in a wide range of sizes and configurations, it was feasible to test a proposed configuration in a relatively short period of time. A graphite heater element, fitted with three  $\text{Al}_2\text{O}_3$  spacer rings, was used for the test. Six 0.254-mm- (0.010-in-) diameter, Inconel<sup>®</sup>- (a Special Metals Corporation product) sheathed type K TCs with an ungrounded junction were procured to assess their applicability in planned DDG testing. Graphite heater elements used in the DDG testing are 0.985 cm (0.375 in) in diameter and are single ended (designed so that both inlet and outlet power leads are on a single end). These heater elements fit inside a 1.4-cm- (0.55-in-) diameter sheath, the OD of which forms the annular flow path. The heater is separated from the sheath using three  $\text{Al}_2\text{O}_3$  spacer rings to prevent contact between the graphite element and the metal sheath. The junction end of a TC was bonded to the graphite element at each  $\text{Al}_2\text{O}_3$  ring using  $\text{Al}_2\text{O}_3$  cement to obtain three temperature

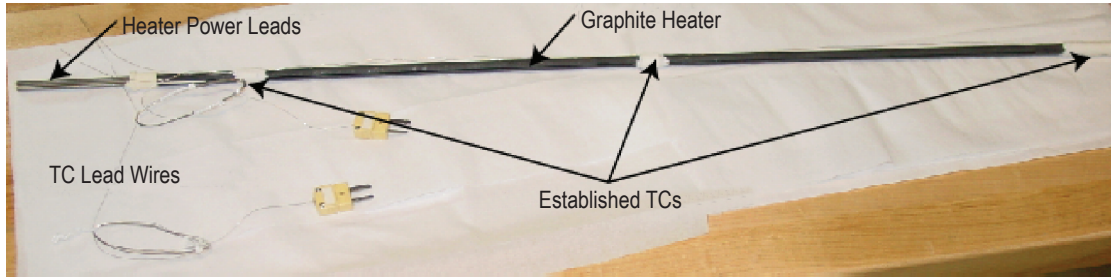


Figure 59. Thermocouple location on graphite heater element for preliminary testing.

measurements along each element, as shown in figure 59. During testing, several problems were noted with this configuration. Because the TC sheath was made of an electrically conductive material (Inconel), bonding the sheath to the heater in more than one location set up a parallel current path in the Inconel sheath. The current required to operate the heater element caused the sheath to vaporize and the 52-gauge TC wires did not survive. Future investigation will consider alternate methods of embedding TCs within the heater elements to obtain approximate ‘fuel’ temperature measurements (heater temperature measurement that can be directly correlated to the expected fuel temperature at comparable conditions).

## 5. FUTURE TESTING AND DEVELOPMENT PLANS

Future thermal simulator work will extend testing on the current materials and assembly designs, incorporating improved procedures to ensure that boundary conditions on the individual heater assembly tests will match those experienced when the heater assembly is incorporated in a reactor test article. These improvements include: enhancement of engineering in the incorporation of diagnostics (temperature and pressure) on the heater assembly and test chamber, improvement of the automated control system, refinement of cleaning and chamber preparation procedures, conduction of tests in both vacuum and high purity inert gas environments, incorporation of a heat removal method to better mimic the assembly boundary conditions in the full test article (using a calorimeter assembly around the heater assembly), and development of advanced thermal simulator designs that will seek to better match key properties of nuclear fuel elements and that will incorporate advanced instrumentation inside the heater assembly.

### 5.1 Element Cooling Techniques

Early testing was conducted at vacuum, to ensure that the only method of heat removal from the heater element was by thermal radiation to the cool chamber walls. This condition, however, is not typical of the boundary conditions that would be present for a heater assembly inserted into a reactor test article. Although each potential reactor design will have slightly different boundary conditions, attempts will be made to adopt a test configuration that can be made to simulate the conditions that would exist if the heater assembly were located in the core block test article. Testing at vacuum represents the most extreme condition that might be experienced by the heater. In any of the reactor designs, the heater elements would be actively cooled by the reactor coolant system (LM HP, pumped gas, or pumped LM), more efficiently removing heat from the element than by radiative cooling alone. A sketch of a single heater assembly (heater element plus sheath) as it fits into the full test article (represented by the core block) is shown in figure 60.

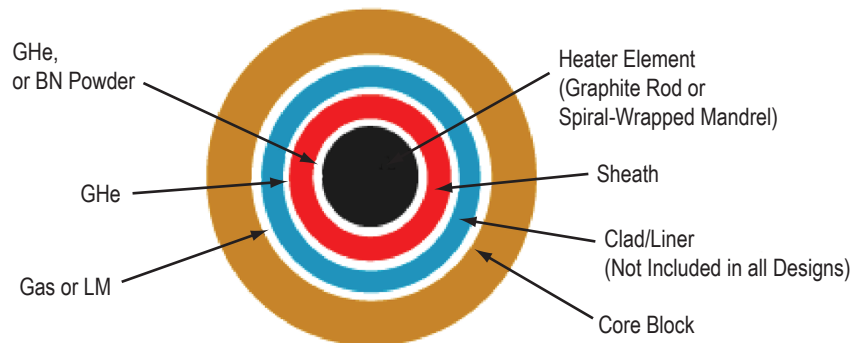


Figure 60. Generalized simulator assembly with core block: cross-sectional view (not to scale).



In the electrically heated configuration, the heater element and the sheath—the full thermal simulator assembly—are representative of the nuclear fuel element. This sheathed assembly would slide into (a) the clad/liner (bonded) for the gas-cooled reactor or LM-cooled reactor or (b) the core block itself for the HP-cooled reactor design. In each case, the boundary condition that will be held in the separate heater assembly tests is the temperature of the inner surface of the core block—whether there is a clad structure between this and the heater assembly (sheath) or not. The currently assumed design point temperature for the HP core block will be  $\approx 1,325$  K and for the gas-cooled reactor it will be  $\approx 1,225$  K. These boundary conditions can be held in the single heater assembly tests by using an adjustable heat removal device, such as a calorimeter. Calculations required to design the calorimeter will initially assume that the sheath/clad or the sheath/block gap will be  $\approx 0.25$  mm ( $\approx 0.010$  in) (radial gap).

For the individual heater assembly tests to examine heater checkout and characterization, the test configuration may or may not include the clad structure (using materials equivalent to what will be in the complete test article) in order to get the correct boundary conditions for the test. If no clad structure is incorporated, the calorimeter design could allow for operation at the temperature of the inner surface of the clad, calculated from the core block temperature and conduction through the clad/block gap and the clad/liner itself (in designs that include a clad in the full reactor core). This would be simpler for the single element tests, and should allow for testing at prototypic boundary conditions. Additional testing has been conducted in a He environment of 6 kPa (47 torr) and also with incorporation of a calorimeter, as noted in section 3.2.

## 5.2 Advanced Thermal Simulator Development

Development of more advanced thermal simulators will focus on designing a heater element that more closely mimics the characteristics of a nuclear fuel element, both at steady state and during transient conditions, to allow improved capability in testing and analysis of a fission reactor using electrically heated elements to mimic nuclear fuel rods. This will take into account both materials selection and heater element design in an attempt to match radial pin conductivity, element surface temperatures, and the time-dependent temperature response of nuclear fuel. Although it is unlikely that a single design will meet each of these characteristics simultaneously, each stage in the development of advanced heater elements keeps these characteristics as a focal point.

Current thermal simulator development work is directed toward meeting requirements established for power per pin, axial flux profile, maximum assembly diameter, materials compatibility, and operational lifetime. Proposed advanced thermal simulator development will look to achieve these basic requirements while attempting to match significant thermal properties to that of an actual fuel element. Properties that will be considered include thermal conductivity, heat-up rate (which can be expressed as the product of density and specific heat ( $\rho C_p$ )), thermal diffusivity, and thermal expansion characteristics. The design will also include advanced instrumentation housed within the thermal simulator for analysis of the axial temperature distribution during test. Criteria that should be established prior to significant investment in thermal simulator and internal temperature sensor development are summarized in table 16.

Table 16. Desired advanced thermal simulator characteristics.

Total power per pin	≈1–6 kW
Linear heat rate	≈100 W/cm (dependent on selected reactor design)
Pin power density	≈100 W/cm <sup>3</sup> (assumes 15-yr operation, 6% burnup, 1 MW-d/g energy from fission)
Axial power profile	Peaking factor per reactor specifications, ≈1.33 used in graphite rod designs Cosine distribution, per reactor specifications
Pin dimensions	Target range:
Diameter	≈0.65-cm (≈0.255-in) minimum to 2.5-cm (1-in) maximum (selected based on reactor design)
Length	≈50 cm nominal
Operating temperature	
Centerline	≈1,700 K nominal, reactor fuel dependent
Outer surface (sheath OD)	≈1,400 K nominal, reactor design dependent
Operational environment	Testing to include:
Vacuum/pressure	Operation in 10 <sup>-5</sup> Pa (10 <sup>-7</sup> torr) vacuum
Fill gas	Operation in ≈10 kPa (≈70 torr) He or Ar environment (UHP, O <sub>2</sub> < 1 ppm)
Operational lifetime (for cyclic testing)	≈ 10,000 hr
Basic geometry	
Heater element/sheath	Single-ended design
Heater element/sheath/clad	Clad structure dependent on reactor design
Effective thermal conductivity (centerline to inner clad diameter)	Thermal simulator will attempt to match—value dependent on selected reactor fuel
Specific heat (as a function of temperature)	
Density (as a function of temperature)	
Effective $\rho C_p$ (heater element + sheath)	
Thermal expansion characteristics (effective)	

The proposed advanced thermal simulator work will incorporate state-of-the-art techniques to fabricate the thermal simulator, incorporating advanced temperature sensors in the buildup process that will allow simultaneous determination of temperature at multiple axial positions. If desired, temperature measurements will be considered at both the centerline and the outer radius (inner clad wall) of the simulator. Inclusion of internal diagnostics becomes increasingly difficult as the size of the heater assembly is further reduced, and internal diagnostics may not be possible for all heater assembly configurations.

### 5.2.1 Plasma Spray Process

This effort will examine the use of the VPS process to build up a thermal simulator. This process begins with a mandrel and builds the simulator using multiple layers of material with layer thickness and porosity being defined in the process. In the layup of each material, materials can be bonded using a functional gradient, where the two adjacent materials are mixed over a few layers to guarantee that a bond is achieved. Depending on the layer thickness and overall element size, grooves can be left in preselected positions during the VPS process to allow placement of instrumentation (along the centerline and radius of the heater elements). Inconel tubing can be inserted into these channels, which can then be used to position temperature sensors (type C TCs or fiber optic Bragg grating sensors). Options for directly building up tubing during the VPS manufacturing process will also be investigated. The VPS layup of the heater element would be performed

in a low pressure ( $\approx 10$  kPa ( $\approx 76$  torr)), UHP He environment, trapping the He inside the element and improving the conductivity across the element. Heater leads could be embedded in the heater element during the VPS process. (The current proposal would include three-quarters of an inch of the heater lead embedded in the element.)

### 5.2.2 Advanced Temperature Sensors

The fiber Bragg grating (FBG) temperature sensors developed by Luna Innovations and previously tested in the SAFE-100 and 100a cores allow detailed determination of axial temperature distribution with a sensor that is only 0.2 mm (0.008 in) in diameter, minimizing both the number and size of the penetrations necessary to fully characterize the temperature distribution in the simulated reactor core or in a thermal simulator.<sup>18,19</sup> To protect the sensor itself, these fibers are encased in a stainless steel sheath that can be as small as 0.5 mm (0.02 in) in diameter. The FBG sensors are currently limited to a maximum temperature of  $\approx 1,000$  °C, but can be pushed to as high as  $\approx 1,100$  °C. Due to the temperature limitation, use of the FBG sensors to characterize the internal temperature of the thermal simulators during operation may not be a current option, but the sensors could be included in the representative core block in the heater element test chamber to assess temperature distributions along its length. Luna Innovations is seeking to extend the temperature range over which the FBG sensors are operational and successful advanced FBG sensor designs may be incorporated into the thermal simulators at a later date. As an alternative, more traditional means of embedded temperature measurement devices, such as high-temperature type C TCs, will be pursued in the initial phase of this proposed work.

### 5.2.3 Power Profiling

In an operating nuclear reactor, the axial power profile approximates a cosine distribution. For a selected reactor design, heater elements can be developed to match the corresponding axial power profile and the radial power profile of an operating reactor can be matched in a non-nuclear test article by operating the heater elements in independent zones using multiple power supplies. The advanced heater development work will also entail investigation into methods of better matching the power profile of the heater element to the reactor fuel elements, both during nominal and off-nominal operation. A conceptual design of a heater having two power profiles has been generated and is shown in figure 61. The complete design drawing is included in appendix O. The proposed design is essentially constructed from two heater elements, with the smaller diameter element fitting completely inside the larger diameter element. This design would allow the power density to be shifted quickly during test to simulate a failure condition. For instance, in a reactor that is controlled by sliding reflectors, a stuck slider could result in an off-nominal axial power profile. If the shifting power profile design cannot be manufactured, or if it is found that the center element would reach temperatures that exceed materials limitations, then several heater elements could be constructed with different axial power profiles. These elements would then be interchangeable in the reactor simulator, with changeout being achieved over 2 to 3 days, to test off-nominal conditions.

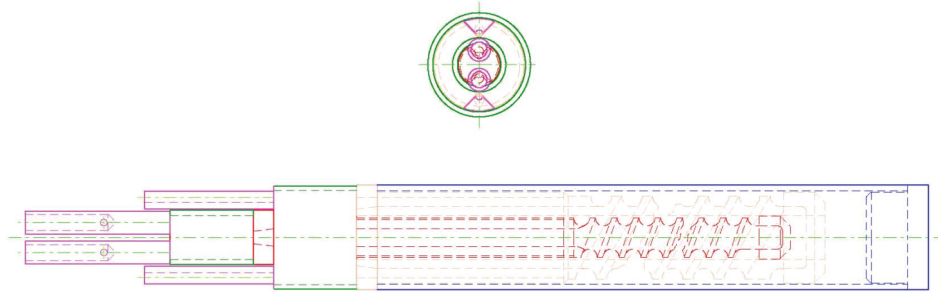


Figure 61. Heater element with a shifting axial power profile.

To allow for rapid transition from one test configuration to another, developing methods that will allow the heater elements to be removed and replaced in the reactor simulator in a simpler, more efficient fashion without damaging the elements or the input power leads will be investigated. Extended testing using the graphite rod heater elements (including hundreds of thermal cycles, testing up to high temperatures and power densities, and significant handling by the experimenters) has also made it evident that it will be necessary to develop a stronger lead connection mechanism that will endure extended testing and handling of the heater elements.

Alternate heater assembly cross sections are also being investigated. To date, all heater elements and sheathed assemblies have had a circular cross section. Depending on the reactor design, it may be desirable to develop a heater assembly with a noncircular cross section to better simulate the heat that would be produced in the corresponding nuclear fuel rod. A conceptual design for a hexagonal fuel rod has been developed and is shown in figure 62. A complete design drawing for the hexagonal heater element is included in appendix P.

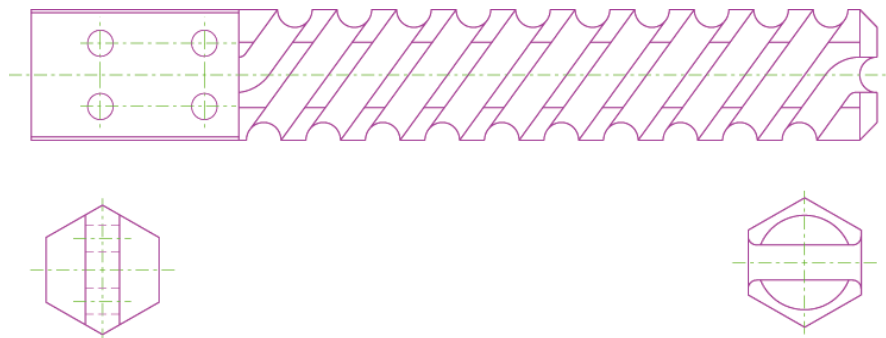


Figure 62. Mandrel design for a heater element with a hexagonal cross section.

## 6. CONCLUSIONS

The materials testing performed to date has provided a basic platform for future heater assembly development for simulated reactor testing. This series of testing has focused on establishing a minimum achievable assembly size, developing a sealing method to improve conductivity across the assembly, and preventing contamination of the reactor test article. Future testing will test the current heater elements to higher power levels (6,000 W/element), and will seek a broader materials list that could potentially be applied in heater elements in a variety of reactor test configurations. Investigation will continue to identify a method that reduces interaction between the heater materials and the test article in addition to developing an acceptable sealing procedure.

The current thread of thermal simulator development was concluded prior to completion of the stated objectives due to a change in program direction and a stop work order from NRPCT. To date, significant work has been completed on the engineering of refractory metal heater elements that may be suitable for use in a refractory metal core block to avoid any potential contamination of the core by the thermal simulators. However, should compatibility issues not be a concern based on the materials selection in the final core design, graphite heater elements have been demonstrated to be more robust and more reproducible in their fabrication than the corresponding refractory wire-wrapped heater elements. Planned future work entails the development of highly instrumented thermal simulators that better mimic the operation of nuclear fuel pins. Sample advanced simulator elements can be tested individually in relevant environments to assess their characteristics relative to thermal analysis predictions, and can then be applied in partial or full-array reactor core testing. Engineering of thermal simulators that better mimic nuclear fuel pins, both in their static and dynamic characteristics, can offer significant enhancement to realistic nonnuclear test methodologies, as discussed in Bragg-Sitton and Webster.<sup>19</sup> Initial design work has also been completed on a power interface assembly that minimizes the impact on the gas flow plena in a direct gas-cooled reactor design, per the down-select made by NRPCT in mid-2005. Each additional step toward developing an electrically heated test article (and integrated system) that is more prototypic of the planned nuclear system significantly enhances the value of the data acquired from the test, offering a vast knowledge base to be developed at a relatively small fiscal investment and over a short period of time as compared to a full nuclear test.

## APPENDIX A—GRAPHITE ROD HEATER ELEMENT

Figures 63 and 64 show the varying diameter (0.375-in-OD) and constant diameter (0.305-in-OD) graphite rod heater elements, respectively.





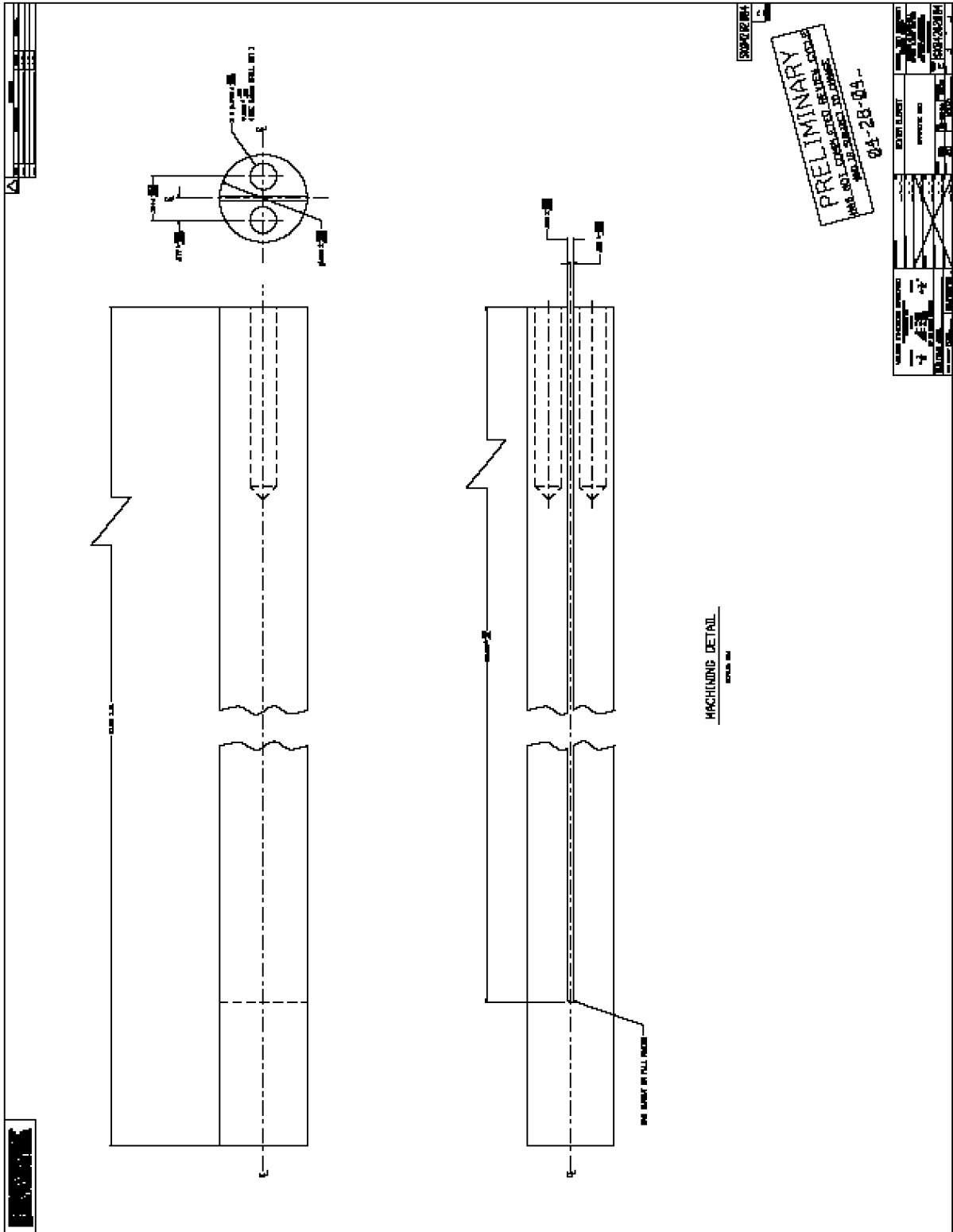


Figure 64. Constant diameter graphite rod heater element, 0.305-in OD.

## **APPENDIX B—SPIRAL WRAPPED SIMULATOR DESIGN, 0.625-IN ASSEMBLY**

Figures 65–70 show the mandrel, coupler, sheath, endcap assembly, and full assembly, respectively, (0.625-in) for the spiral-wrapped simulator design.

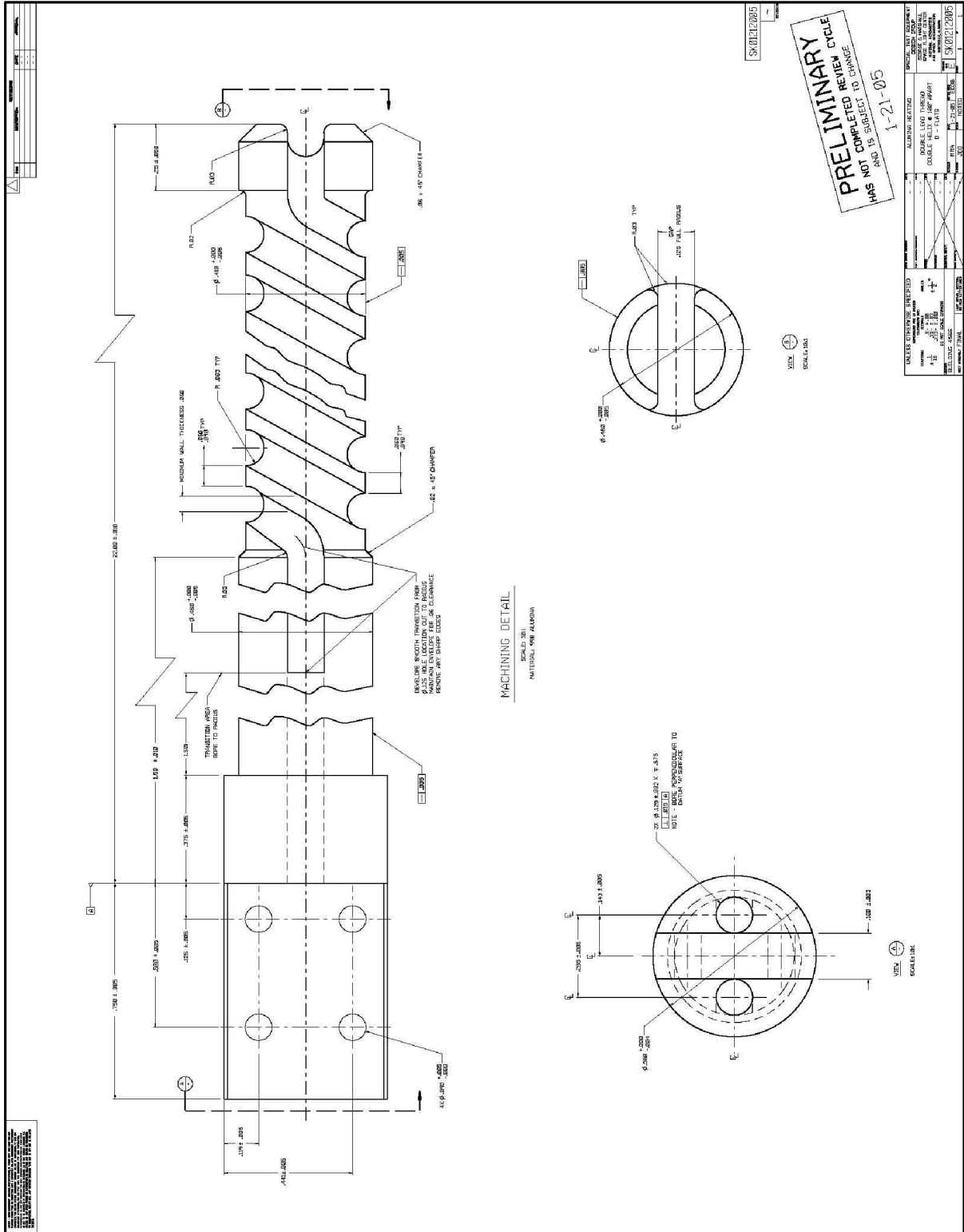


Figure 65. Mandrel, 0.625-in assembly design.

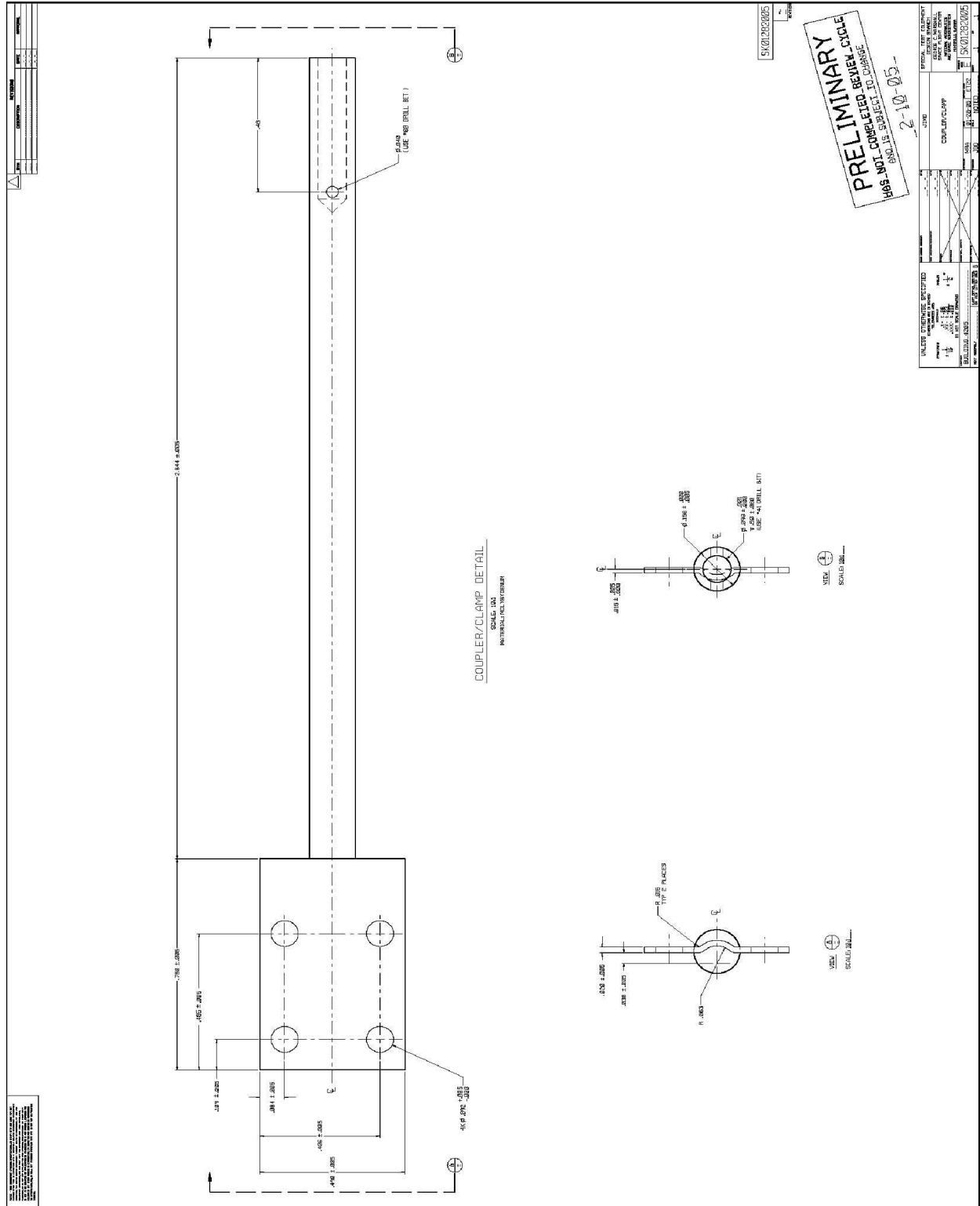


Figure 66. Coupler, 0.625-in assembly design.





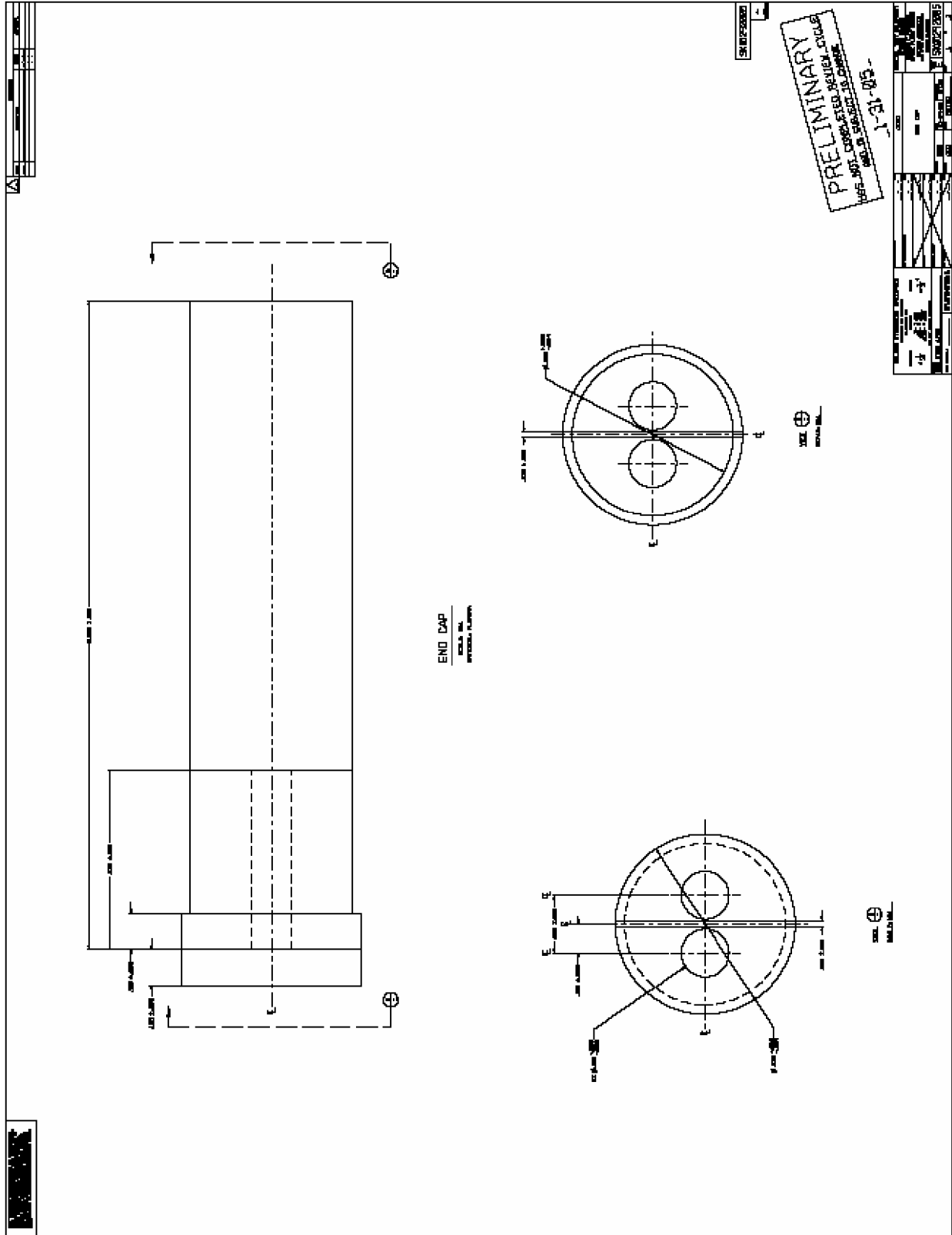


Figure 68. Endcap, 0.625-in assembly design.

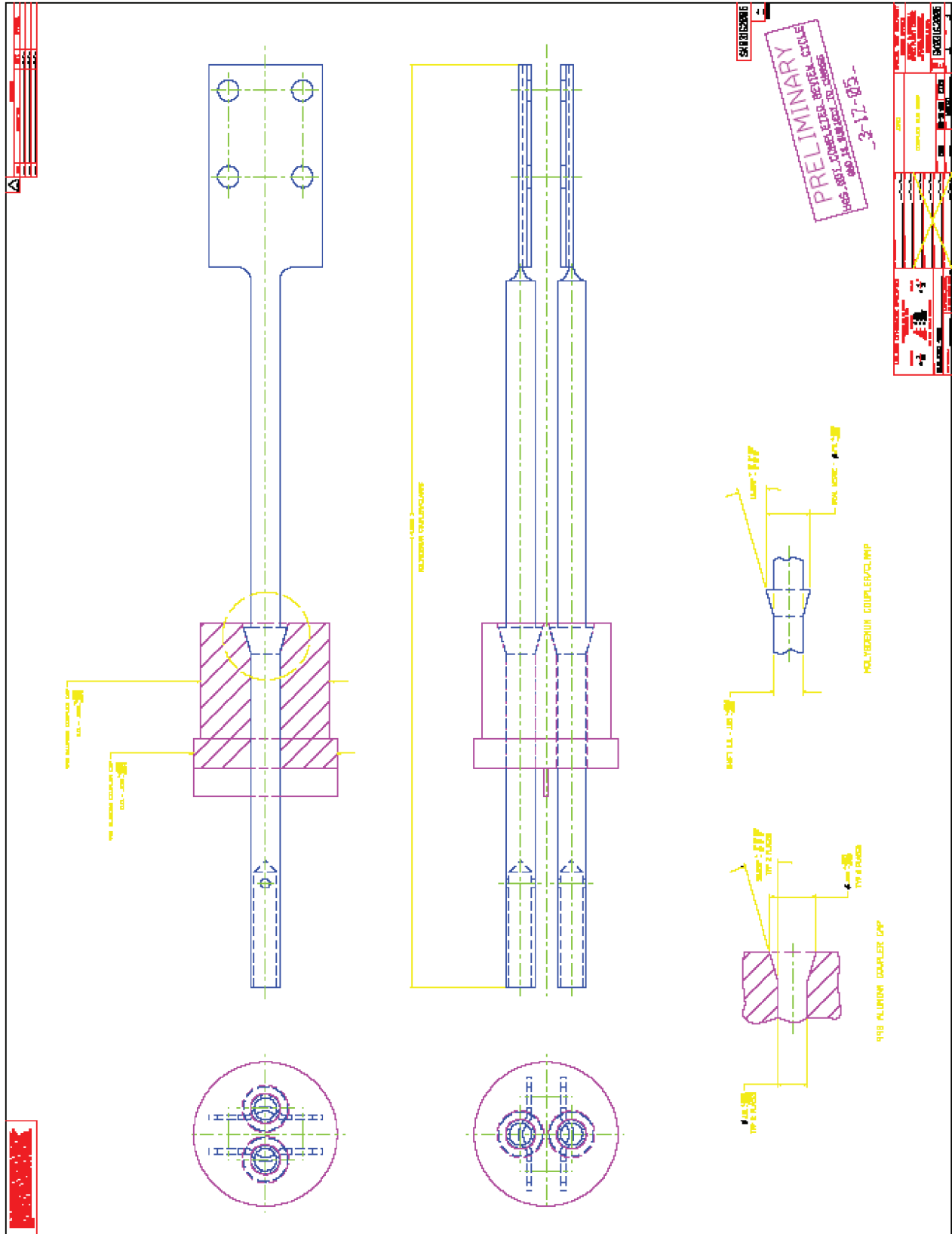


Figure 69. Endcap assembly, 0.625-in assembly design.

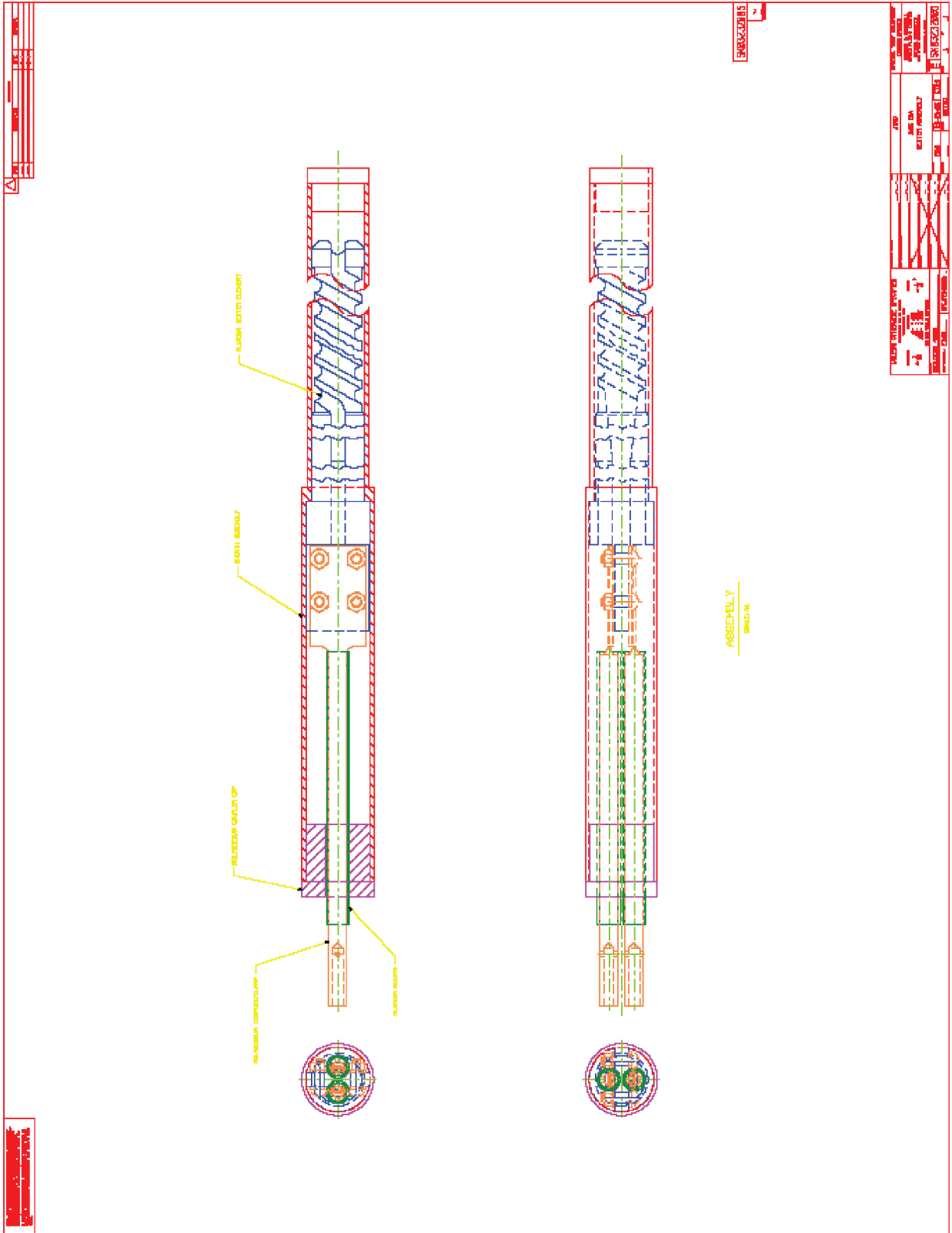


Figure 70. Full assembly, 0.625-in assembly design.

## **APPENDIX C—SPIRAL-WRAPPED SIMULATOR DESIGN, 0.400-IN ASSEMBLY**

The mandrel coupler, endcap, and sheath are shown in figures 71–74, respectively, for the 0.400-in assembly for the spiral-wrapped simulator design.







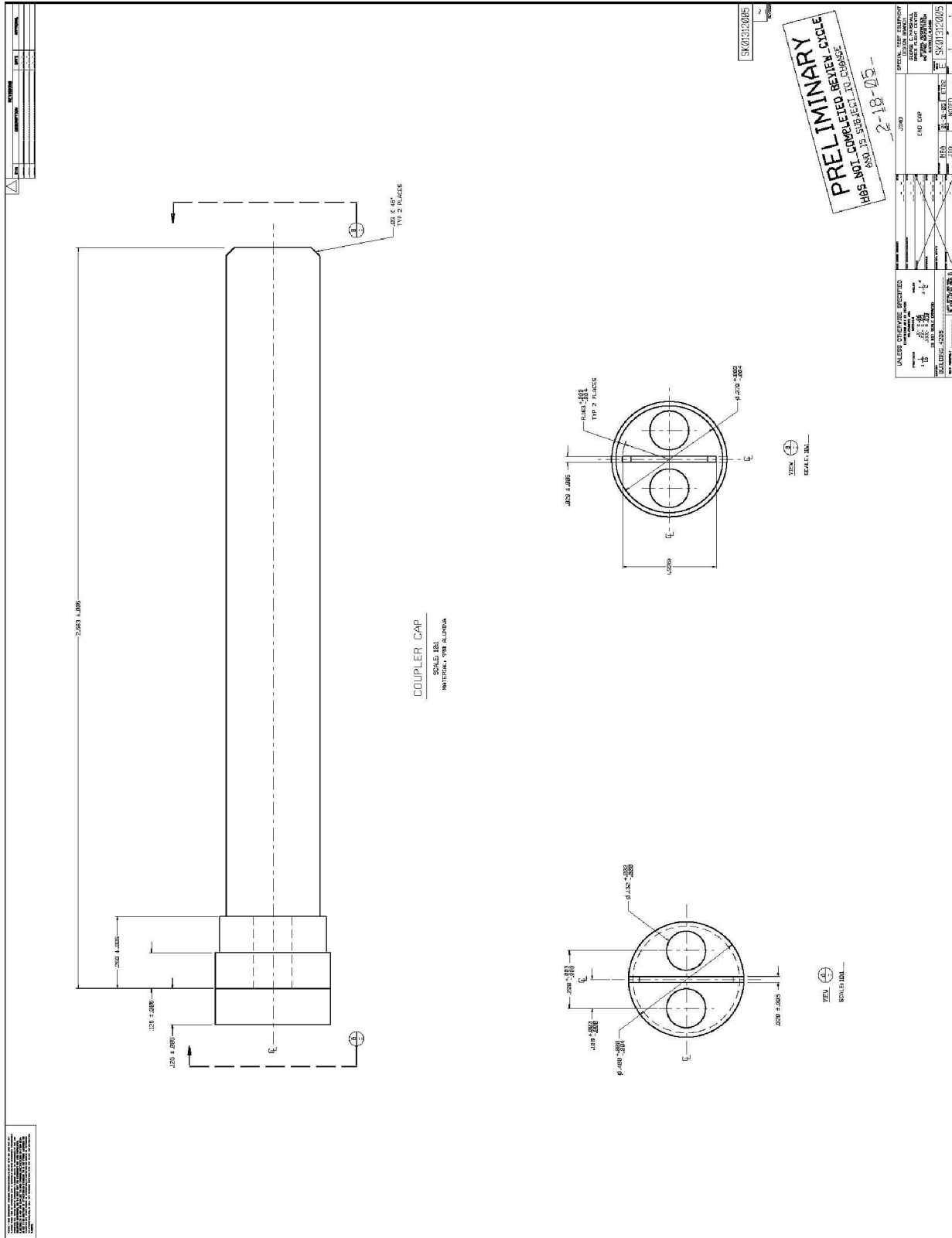


Figure 73. Endcap, 0.400-in assembly design.

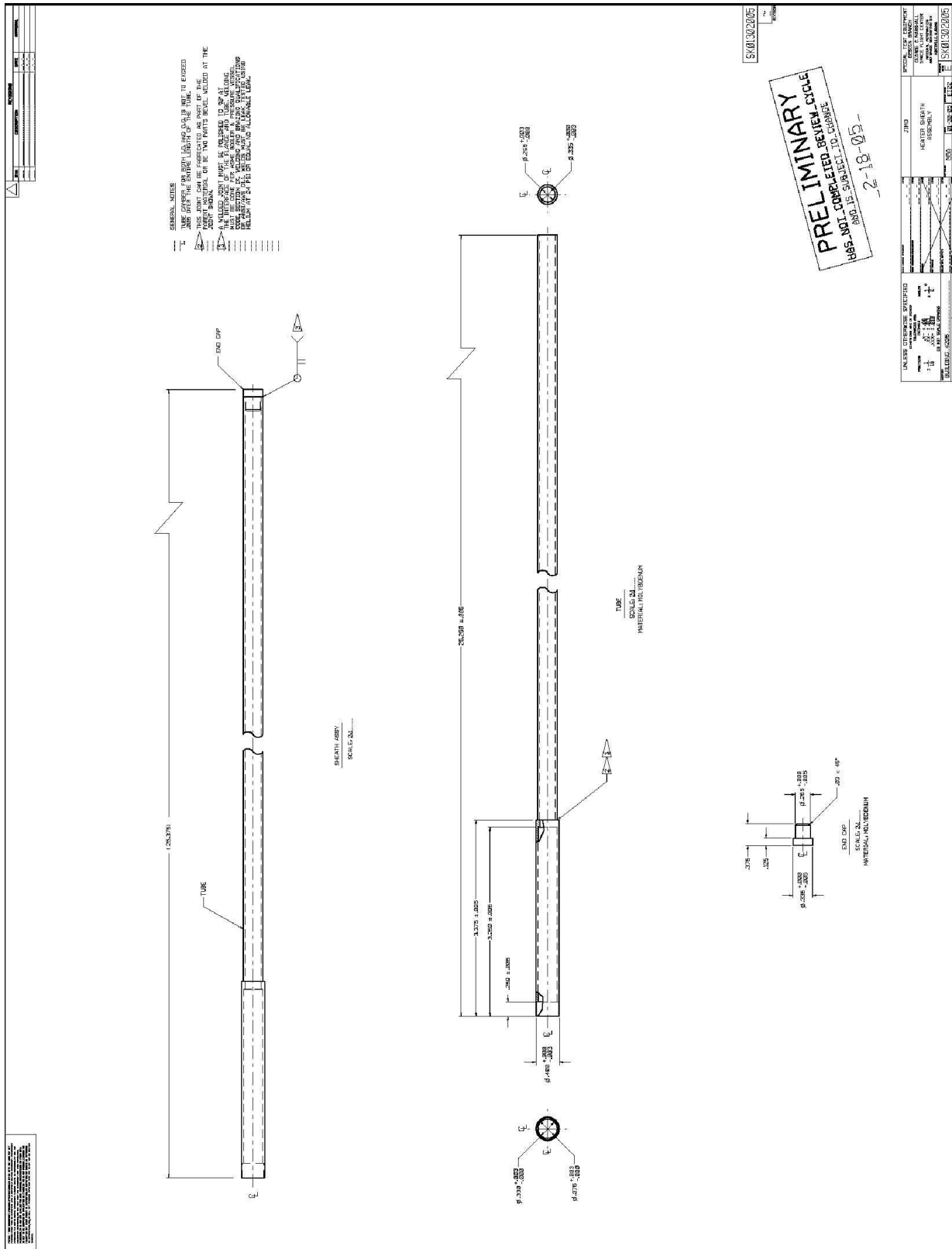


Figure 74. Sheath, 0.400-in assembly design.

## APPENDIX D—TEMPERATURE DEPENDENT RESISTIVITY OF SELECTED REFRACTORY METALS

The temperature-dependent resistivity of refractory metals of interest in the current work are summarized in equations D-1 to D-3, where resistivity  $r$  is given in  $10^{-6} \Omega\text{-cm}$  and temperature  $T$  is in K:

$$\text{Tantalum:} \quad \rho = -4.192 \times 10^{-6} T^2 + 4.16 \times 10^{-6} T + 5.571 \quad (3)$$

$$\text{Tungsten:} \quad \rho = -2.4019 \times 10^{-6} T^2 + 2.6255 \times 10^{-6} T + 2.8476 \quad (4)$$

$$\text{Rhenium:} \quad \rho = -8.100 \times 10^{-6} T^2 + 5.8613 \times 10^{-6} T + 7.5774 . \quad (5)$$

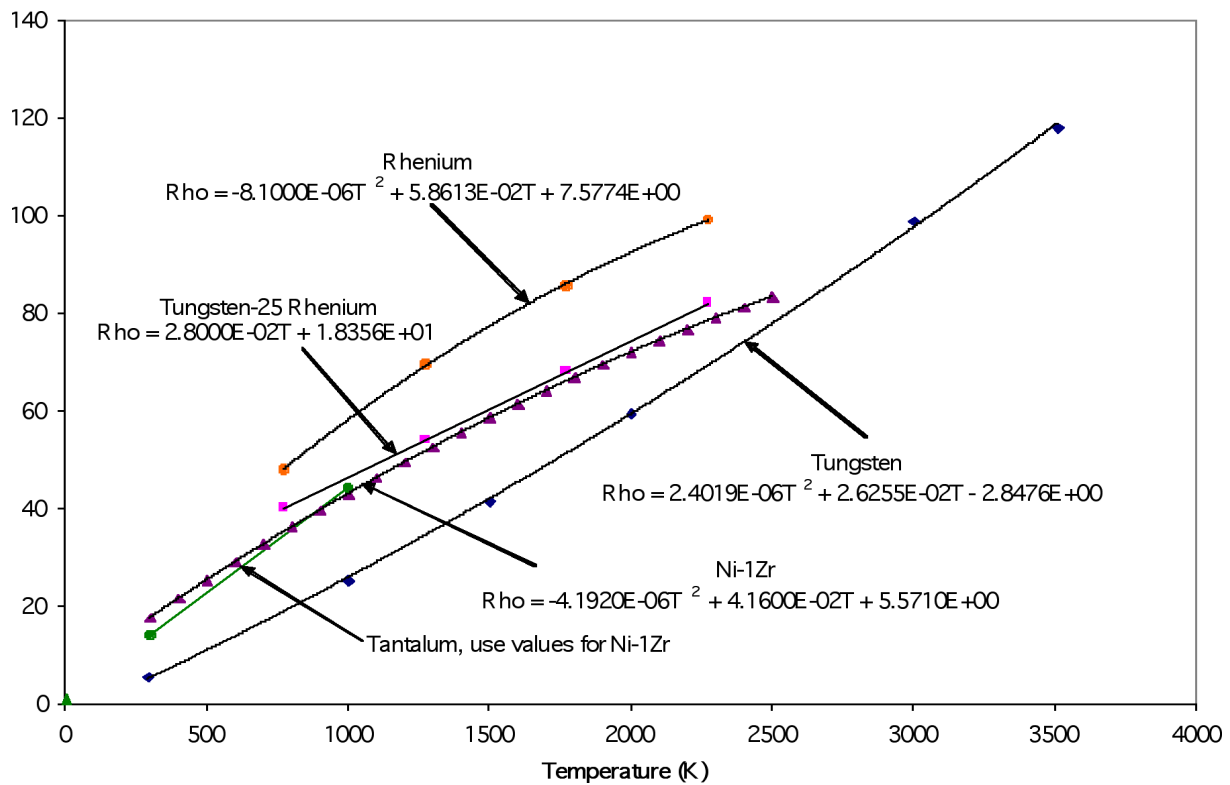


Figure 75. Resistivity of selected refractory metals as a function of temperature. (Data obtained from R. Kapernick, Los Alamos National Laboratory.)

## **APPENDIX E—TANTALUM HEATER ELEMENT MATERIALS ANALYSIS**

Appendix E is a NASA memo dated December 20, 2004, regarding materials analysis of the Ta heater element.



December 20, 2004

Reply to Attn of: (EM30 2004-092)

TO: ALLIED/R. Dickens

FROM: EM30/G. Jerman

SUBJECT: Failure Analysis of a Discolored Helical Alumina Insulator, Wire Wrapped by a Tantalum Heater Element (EM30 2004-726)

### **Introduction**

A 0.040 inch diameter tantalum (Ta) wire heater element was tested at high temperature in a vacuum chamber to simulate nuclear fission heating. During testing, images of the hot Ta element showed differential heating at localized positions along the helical conductor wire that twisted around a grooved alumina ( $Al_2O_3$ ) insulator. Figure 1 shows the heater element early in its testing. There are two places where the Ta winding does not glow as bright as the adjacent winding. Figure 2 shows the heater element later in the test. The locations of differential heating have shifted to alternate positions and the overall coloration of the image has red shifted. No voltage or current anomalies were noted during heater operation. Upon removal from the test chamber, the white alumina insulator had bluish-black discoloration. The Ta heater wire remained a shiny silver metallic color. The heater element was then submitted to the EM30 Materials Analysis Branch to determine the cause of the differential wire heating and the insulator discoloration.

### **Optical Microscopy**

In order to analyze the Ta heater wire and the alumina insulator separately, the Ta wire was unwound from the helical insulator. After unwinding the Ta wire a few turns, the wire began to fracture in a brittle fashion. Large variations in discoloration were noted on the insulator surfaces as the Ta wire was removed. Figures 3, 4, and 5 show localized insulator surface coloration changes including metallic spheroid deposits. After unwinding about a third of the way up the insulator, the insulator fractured. The fracture occurred near the base of the insulator where the Ta wire enters and exits the assembly. Discoloration also appears to have penetrated into the alumina as shown in figure 6. A second fracture was then induced in the alumina insulator to liberate a small segment for further analysis. Pieces of new and thermally tested Ta wire were also cut for further analysis. Figures 7 and 8 show the surface condition of the new and heated wire while figures 9 and 10 show the cross sections. Although the surface texture of the heated wire did not change, large grain growth can be seen in the wire cross section. Such a large average grain size with respect to the wire diameter probably caused the observed wire embrittlement during disassembly.

### **Scanning Electron Microscopy**

Surface morphology and chemistry information were collected from the insulator and conductor wires in a Field Emission Scanning Electron Microscope (FESEM). Figures 11 and 12 show secondary electron images of the helical insulator at a location that contained both discoloration and metallic spheroid deposits. Normally alumina is an insulator which requires conductive coating for FESEM imaging. Nonconductive samples collect an electrical charge from the electron beam and appear bright white under normal circumstances. The majority of the surface area in figures 11 and 12 have significant conductivity. Only the tops of the helical ridges and a limited portion of the valley were nonconductive like alumina should be. Because of the unexpected electrical conductivity, Energy Dispersive x-ray Spectroscopy (EDS) was performed in order to document the surface chemistry that was allowing conductivity. Figure 13 shows the chemistry of the general discoloration that covers most of the insulator. The general discoloration contains a combination of metallic aluminum (Al) and Ta. Metallic Al and Ta can form a variety of intermetallic compounds. Figure 14 shows a region of discontinuity in the general discoloration. This region contains more Al than the general discoloration, but it also contains some oxide. Figure 15 shows the metallic spheroids that were seen optically in figure 5. They are composed of pure metallic Al. In figure 16, a region that charged electrically was analyzed. It was composed mainly of alumina, but it also contained Ta which was also possibly in oxide form. Finally, the new and used Ta conductor wires were analyzed by FESEM/EDS. The surface of the new wire is shown in figure 17. It is composed of pure Ta, but some traces of carbon and oxygen are present. Figure 18 shows the same Ta wire after thermal testing. The surface morphology has changed little and small amounts of carbon and oxygen are still present. Figure 19 shows the composition of surface contaminants on the new Ta wire. The contaminant contains significant amounts of carbon, oxygen, sodium, and chlorine which indicates it may be related to human handling.

### **Discussion of Differential Heating and Image Red Shift**

There are three reasons why local sections of the Ta heater wire glowed less than neighboring wire locations during operation: current loss, thermal dissipation, or emissivity changes. No significant roughness or chemical changes were noted on the Ta wire surfaces, therefore the emissivity of the wire did not change during testing. No emissivity change means no red shift. A large temporary change in thermal dissipation would require a large localized improvement then loss of thermal conductivity in the insulator, which is highly unlikely. The only likely mechanism for the observed localized change in wire heating is loss of electrical current. Alumina is an insulator, but FESEM/EDS analysis showed a conductive metallic Al-Ta coating covers the insulator surface. If the coating was thick enough, a parallel electrical circuit along the insulator surface could draw current away from the Ta wire temporarily. Current flow to ground would not change, so from the heater instrumentation standpoint, no current or large voltage change would be noticeable. Since the conductor was producing a small amount of Ta oxide vapor, it would coat the entire vacuum chamber including the sight glass window. A vapor deposited oxide coating would limit light transmittance through the sight glass resulting in the red shifted image.

### **Discoloration Discussion**

The presence of pure metallic Al on the insulator indicates the alumina was being reduced to



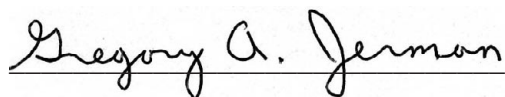
metallic Al and it was reacting with Ta to form an intermetallic layer on the insulator surface. Alumina is known to break down in a vacuum environment in the presence of carbon. Since the new and tested Ta wires contained measurable amounts of surface carbon contamination, this was a possible source of degradation. Metallic Ta melts at 2996 °C but its oxide melts at 1872 °C. The calculated operational temperature of the tantalum wire could have varied between 1933 and 2500 °C. In this temperature range, the wire would not have melted, but any oxide formation would have vaporized then condensed on lower temperature surfaces. Since the insulator kept its shape and no wide spread slumping or distortion was seen in the insulator rod, the general insulator temperature was probably close to the targeted 1000 °C output temperature of the heater assembly. Alumina melts at 2072 °C, so it is possible that some localized insulator melting occurred where the Ta wire was in intimate contact with the insulator surface. The maximum recommended operating temperature for alumina is 1800 °C, so the use of alumina with such high contact temperatures is not recommended.

### **Conclusions**

1. Discoloration of the alumina insulator was caused by the formation of an intermetallic Al-Ta coating on the insulator surface.
2. Carbon bearing contamination in the heater assembly reduced some of the alumina insulator surfaces under vacuum to form metallic aluminum.
3. The hot aluminum metal then reacted with and reduced vaporized tantalum oxide to form a conductive intermetallic coating on the alumina insulator.
4. Vapor deposited tantalum oxide on the sight glass window resulted in the later red shifted test image.

### **Recommendations**

1. The tantalum wire and insulator should be thoroughly cleaned to remove any oils or other volatile carbon bearing contamination before assembly.
2. After assembly, the heater should be baked out under vacuum at approximately 150 °C in order to vaporize any remaining volatile components without causing decomposition of organic molecules that could lead to carbon deposits.
3. The helical insulator should be manufactured from a ceramic with higher temperature capability such as boron nitride (powder consolidated) or pyrolytic boron nitride (vapor deposited) which doesn't break down until 3000 °C.



Gregory A. Jerman  
EM30 Materials Analysis

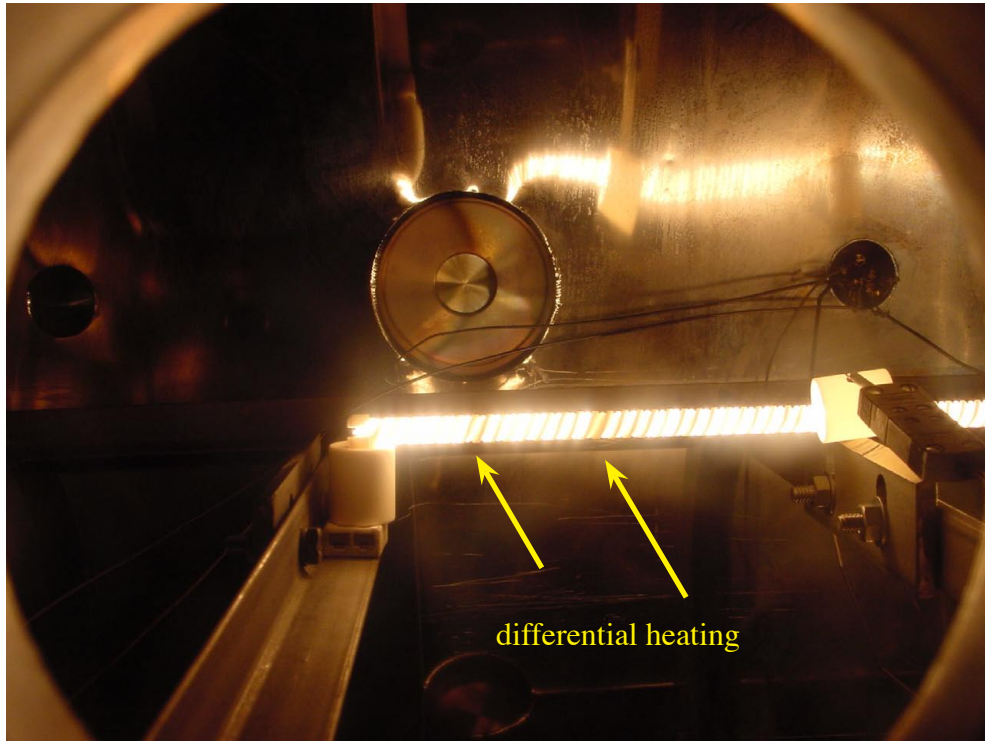


Figure 1. Initial thermal test image showing differential heating.

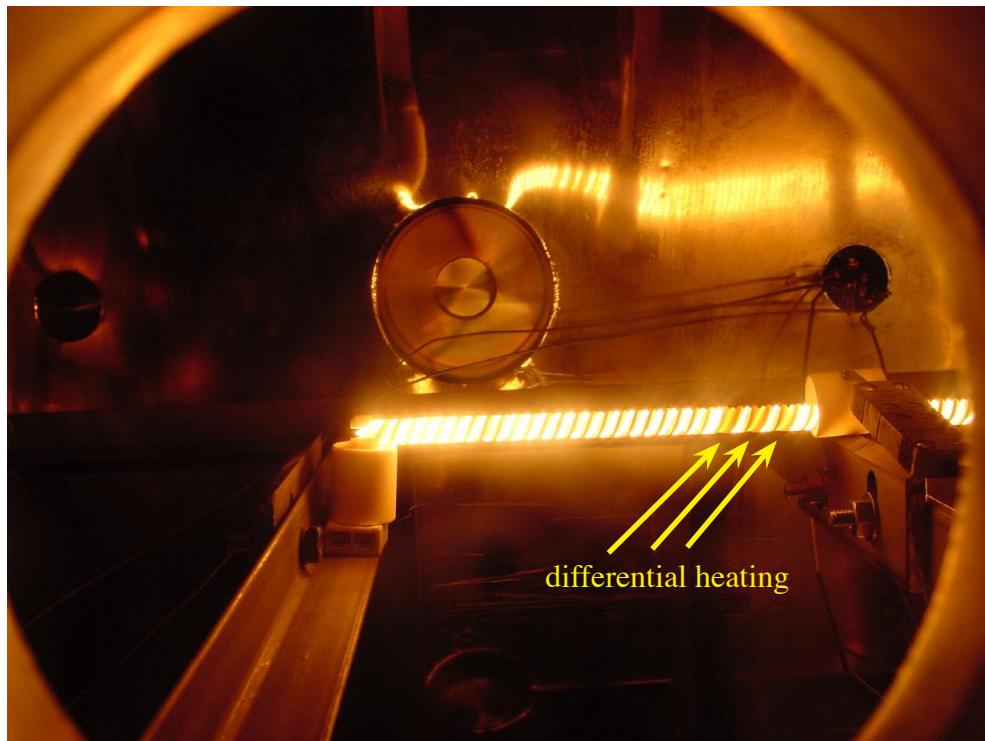


Figure 2. Later thermal test image showing a red color shift and differential heating.

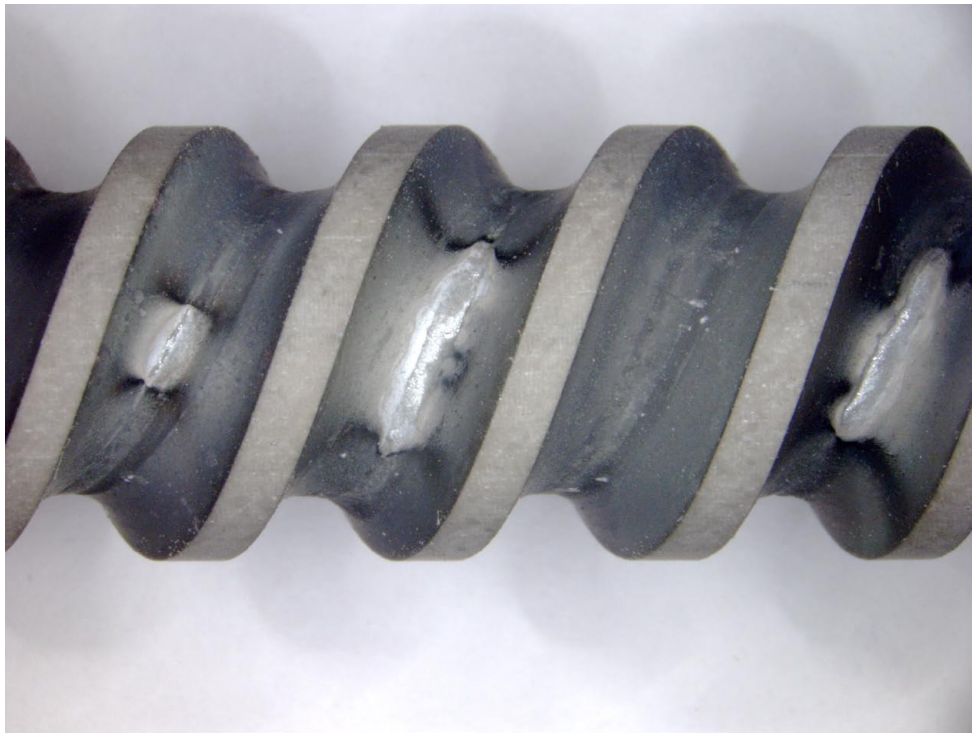


Figure 3. Surface condition of the alumina insulator, after testing, with the Ta wire removed.

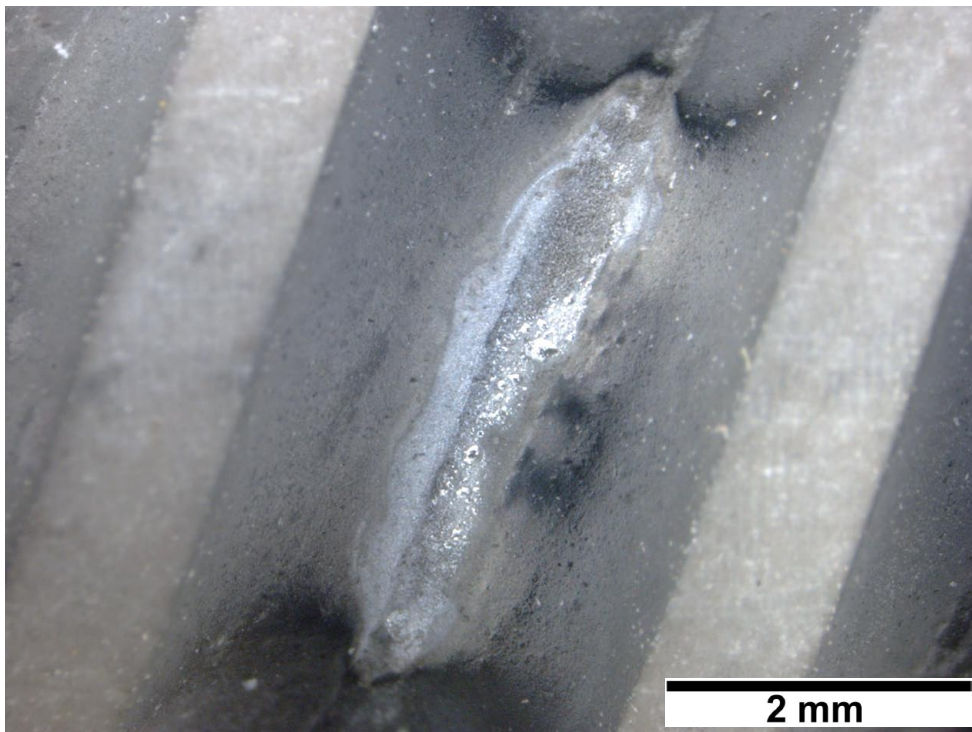


Figure 4. Surface reaction zone on the alumina insulator, after testing, with the Ta wire removed. (20x)



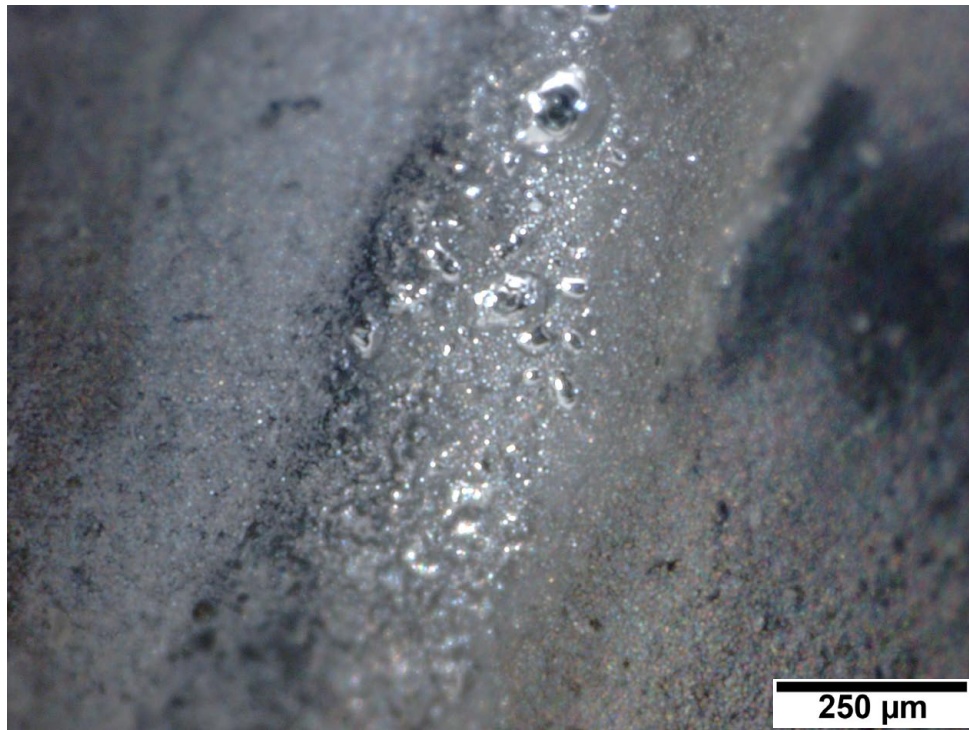


Figure 5. Metallic droplets in the alumina insulator surface reaction zone. (100x)



Figure 6. Penetration of surface discoloration into the insulator cross sectional thickness. (10x)

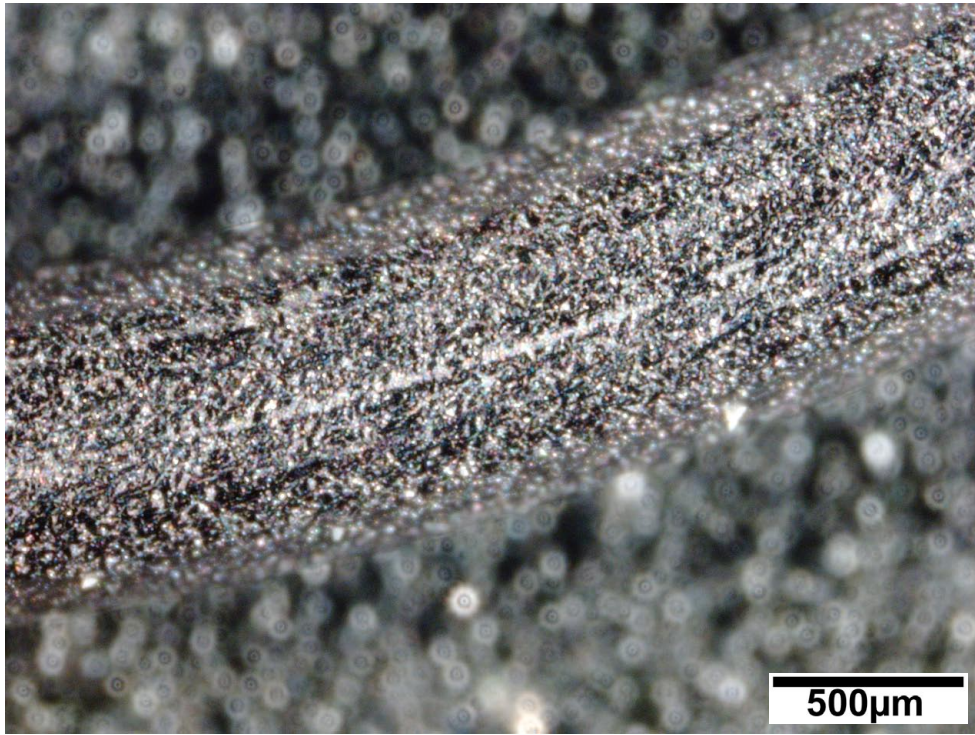


Figure 7. Optical view of the new Ta wire surface condition. (50x)

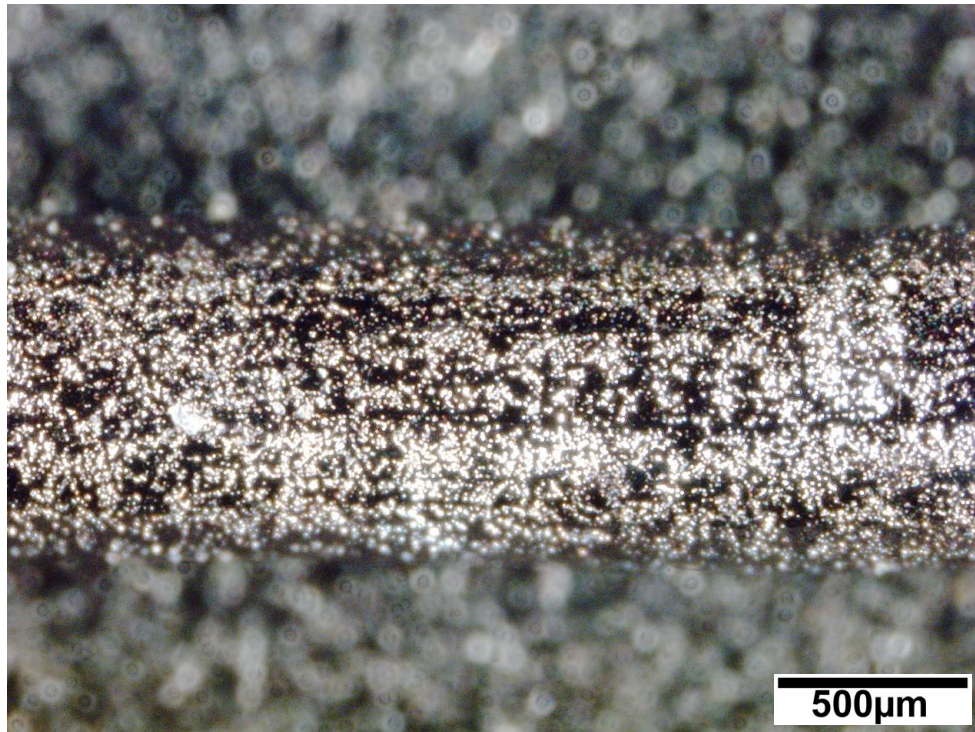


Figure 8. Optical view of the tested Ta wire surface condition. (50x)



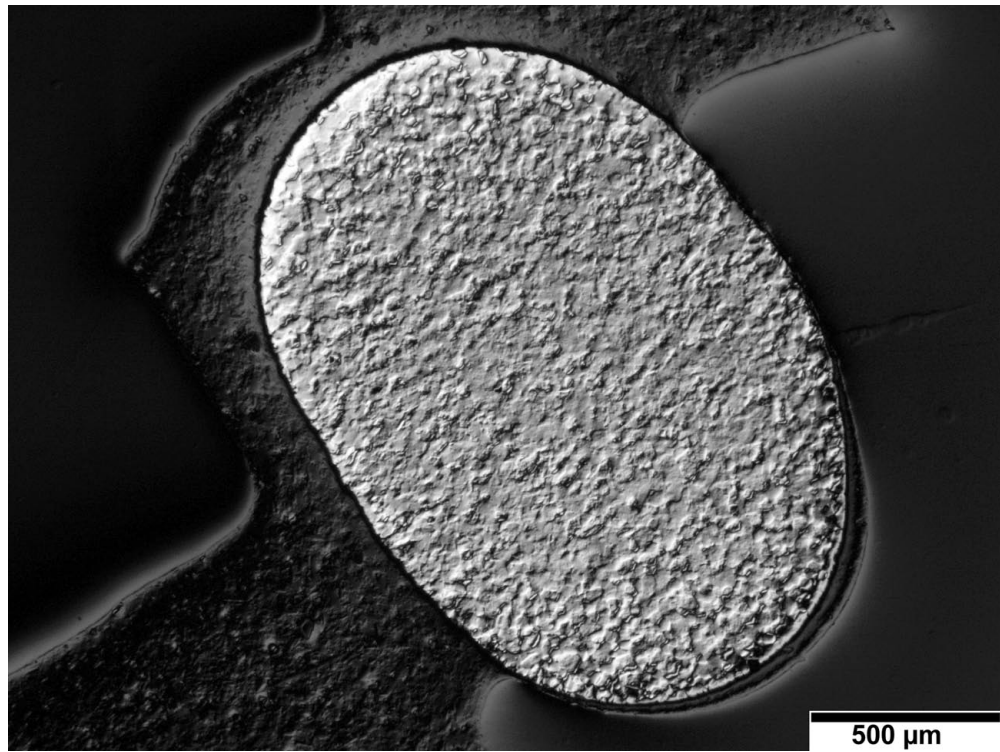


Figure 9. Optical cross sectional view of the new Ta wire grain structure. (50x)

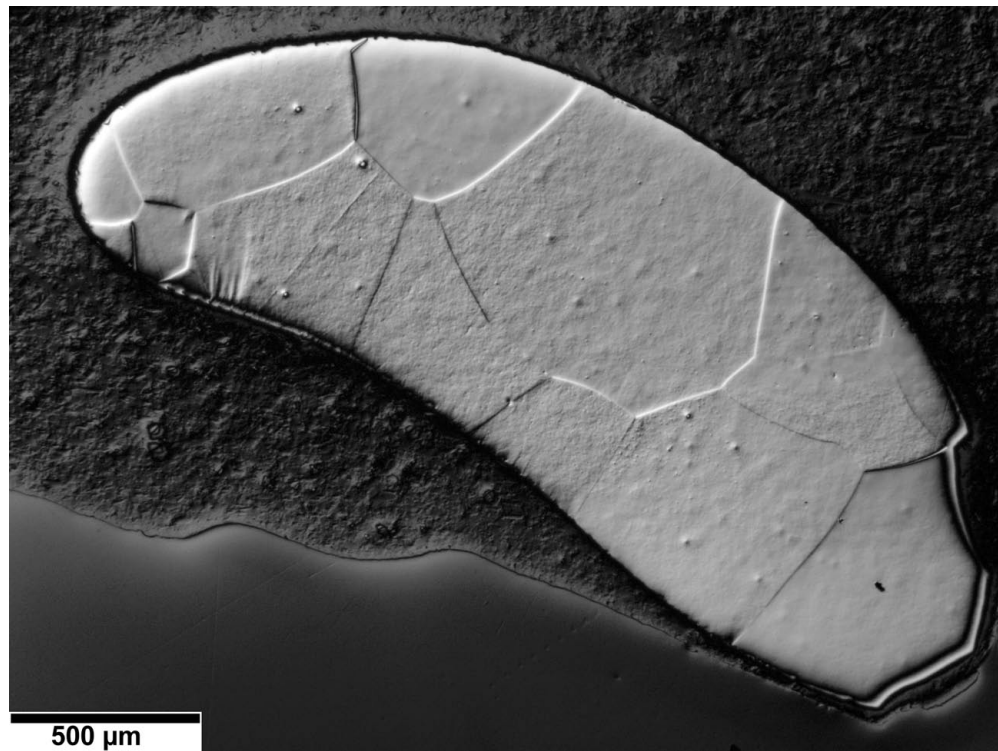


Figure 10. Optical cross sectional view of the tested Ta wire grain structure. (50x)



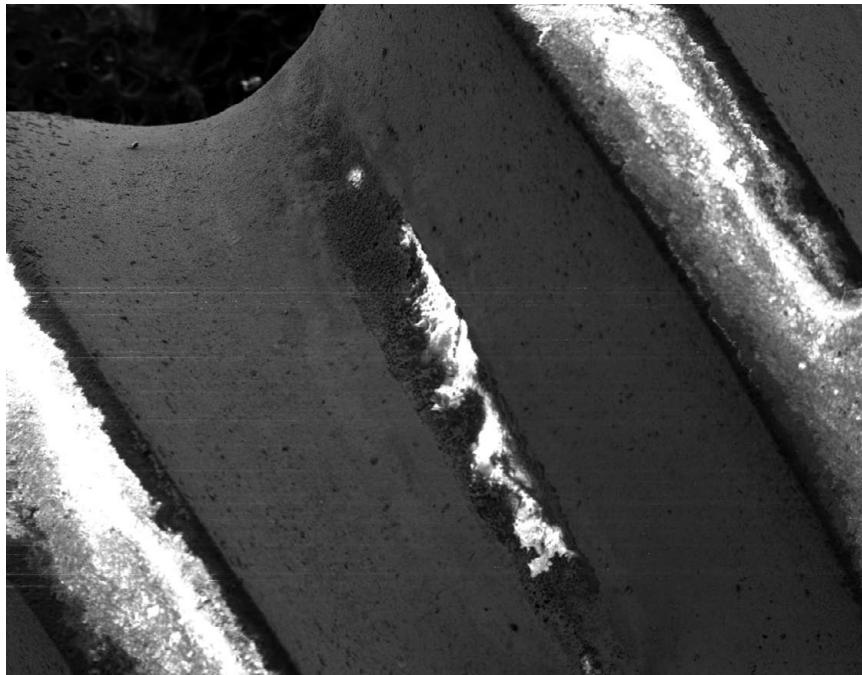


Figure 11. Low magnification FESEM view of the helical groove in the alumina support insulator. (20x)

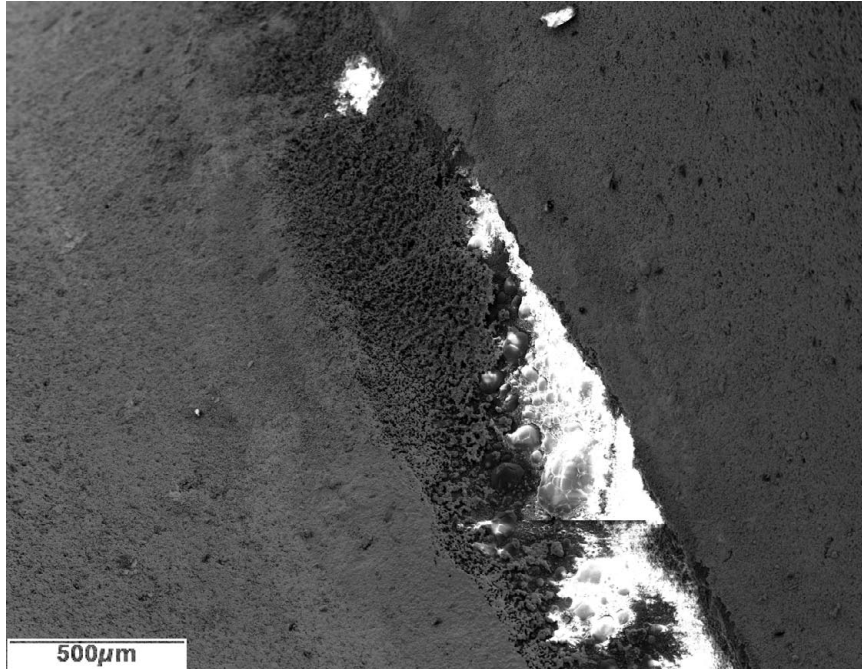


Figure 12. Low magnification FESEM view of the deposits at the bottom of the helical groove in the alumina support insulator. (50x)

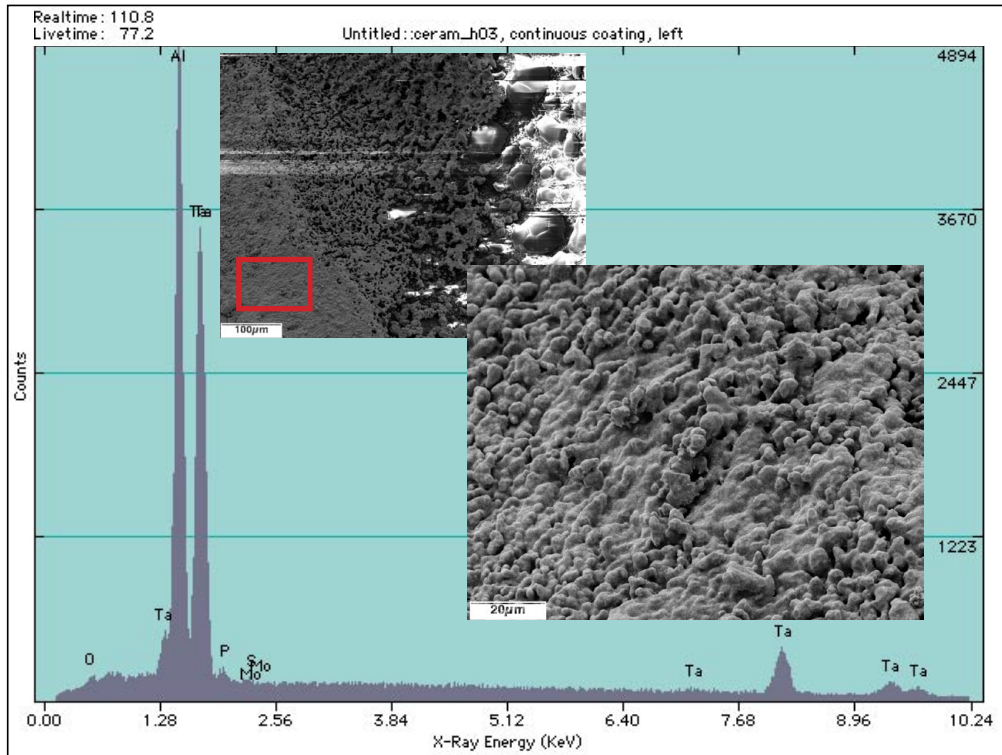


Figure 13. FESEM/EDS analysis of the uniform coating that covers the most of the helical alumina insulator groove.

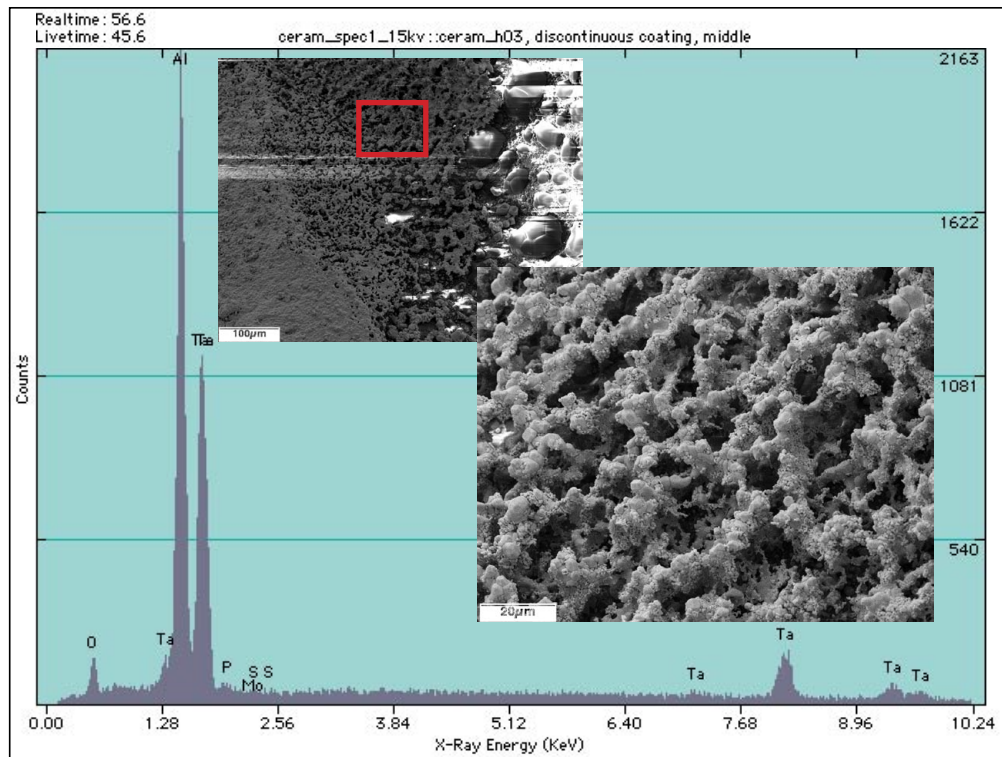


Figure 14. FESEM/EDS analysis of the discontinuous coating that covers a small portion of the helical alumina insulator groove.

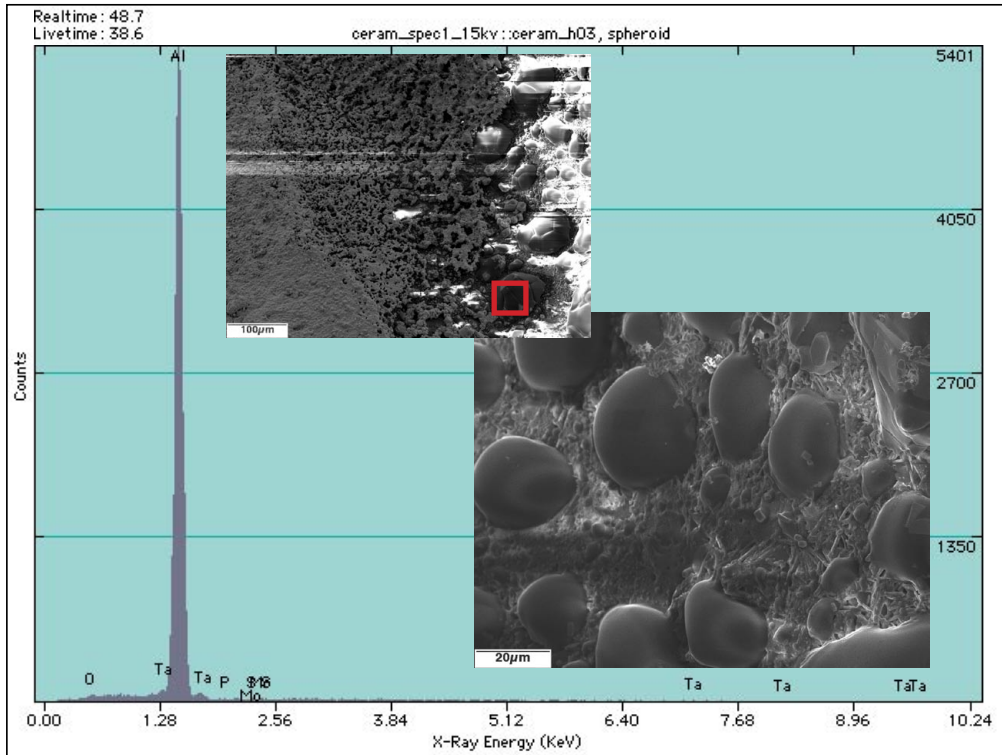


Figure 15. FESEM/EDS analysis of the spheroidal formations at the bottom of the helical alumina insulator groove.

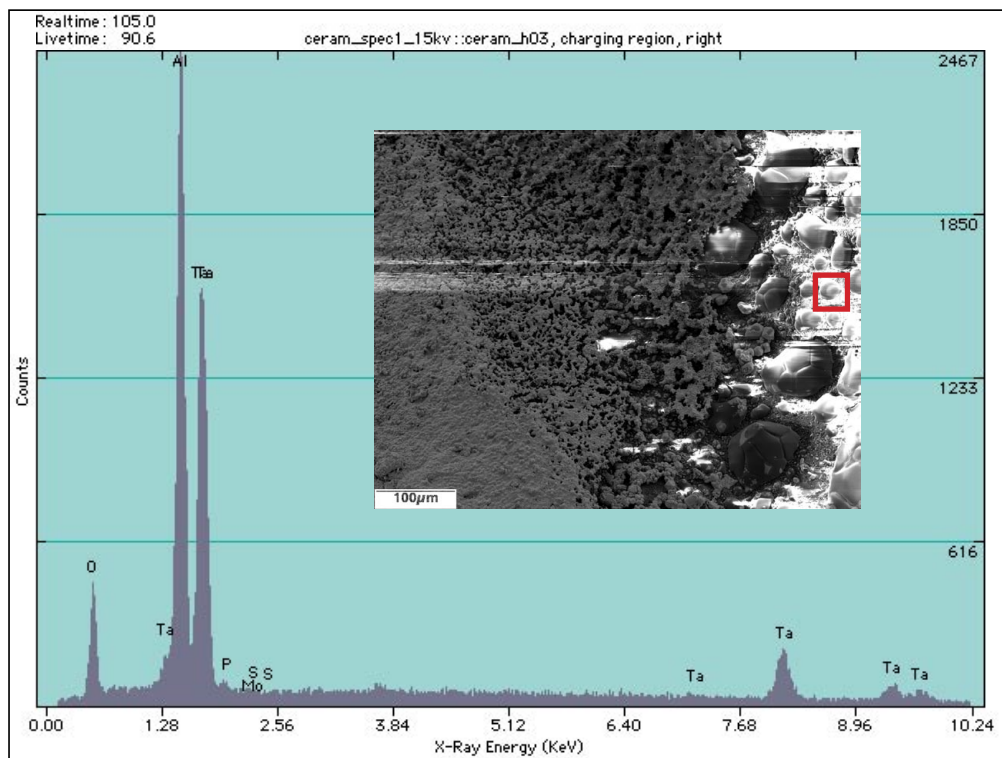


Figure 16. FESEM/EDS analysis of the region that electrically charges at the bottom of the helical alumina insulator groove.



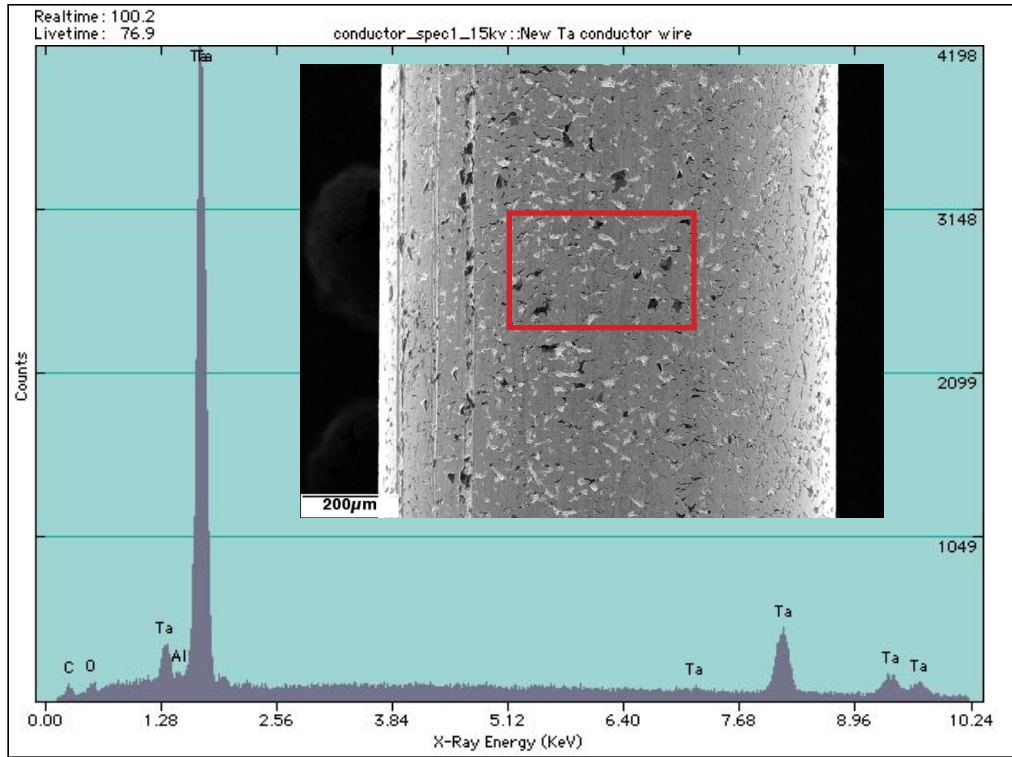


Figure 17. FESEM/EDS analysis of new Ta wire from the same lot installed on the helical alumina insulator.

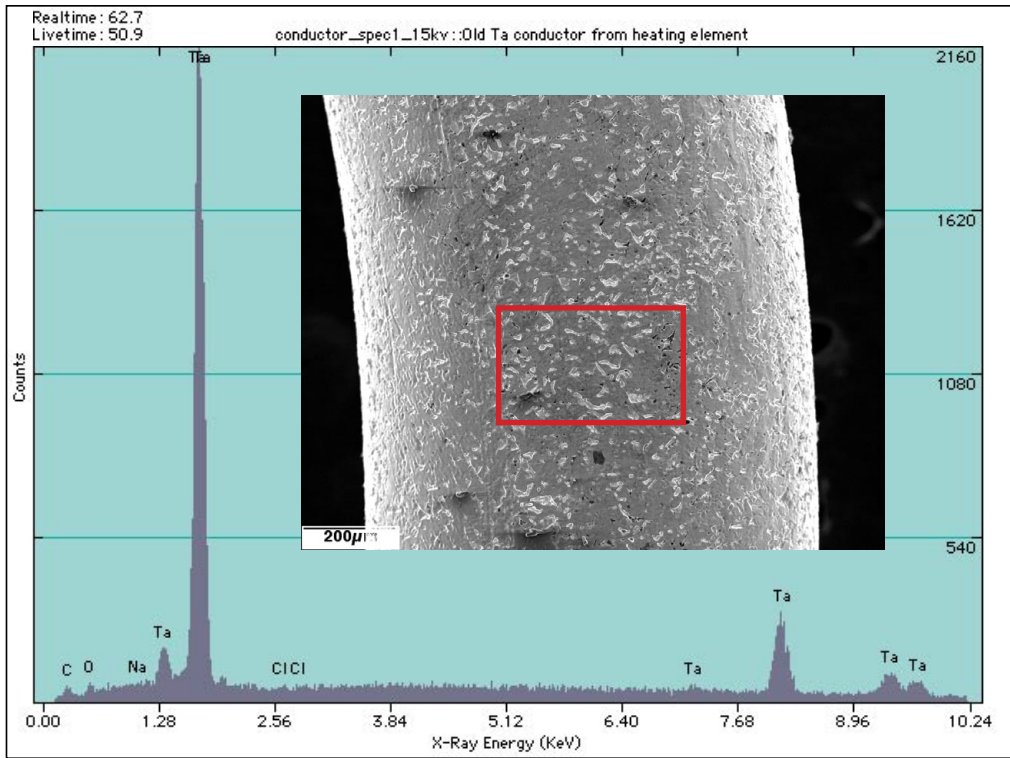


Figure 18. FESEM/EDS analysis of the thermally tested Ta wire that was installed on the helical alumina insulator.

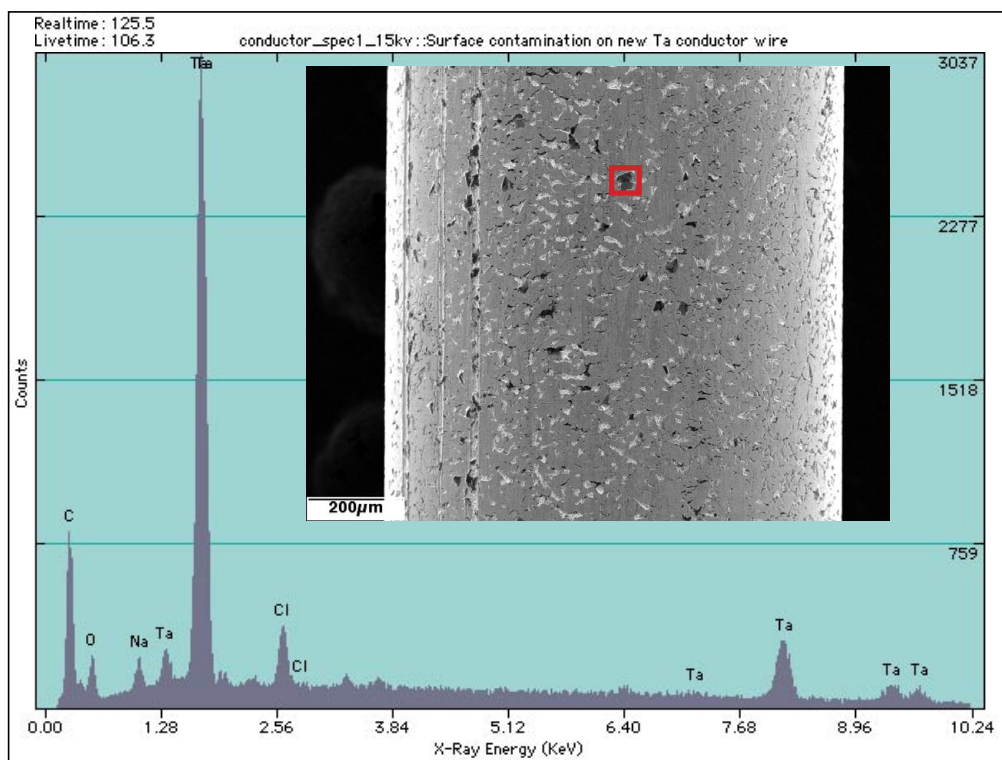


Figure 19. FESEM/EDS analysis of surface contamination on the new Ta wire from the same lot installed on the helical alumina insulator.

## **APPENDIX F—RHENIUM HEATER ELEMENT MATERIALS ANALYSIS**

Appendix F is a NASA memo dated February 4, 2005, concerning Re heater element materials analysis.





February 04, 2005

Reply to Attn of: (EM30 2005-006)

TO: MORGAN/P. Salvail

FROM: EM30/G. Jerman

SUBJECT: Analysis of a Discolored Helical Alumina Insulator, Wire Wrapped by a Rhenium Heater Wire (EM30 2005-0004)

### **Introduction**

A 0.040 inch diameter rhenium (Re) wire, twisted around a helically grooved alumina ( $\text{Al}_2\text{O}_3$ ) insulator, was resistively heated in a vacuum chamber to simulate nuclear fission heating. During testing, images of the hot Re element were taken at different power levels. Figure 1 shows the heater element early in its testing at a 1200 W power level. Figure 2 shows the heater element later at a 5000 W power level. Unlike the previous testing of a tantalum (Ta) heater element, documented in EM30 memorandum 2004-092, no differential heating was seen with the Re element. Upon removal from the test chamber, the white alumina insulator had a bluish-grey discoloration. The Re heater wire remained a shiny silver metallic color. The heater element was submitted to the EM30 Material Diagnostics Team to determine the cause of the insulator discoloration and document the condition of the alumina insulator and the Re heater wire.

### **Optical Microscopy**

The Re wire and the helical alumina insulator were separated for analysis. Figure 3 shows the heater assembly before separation. During unwinding, the Re wire was found to be ductile. No wire breakage occurred during unwinding. A small segment was cut from the middle of the heated Re wire for later analysis. A segment of new Re wire was also available for comparison. After removal of the conductor wire, variations in surface discoloration were noted on the alumina insulator. Figures 4, 5, and 6 show localized insulator surface coloration changes from general bluish-grey to white streaks and dark bluish-grey spots. In order to determine if the surface discoloration affected the alumina through its thickness, a small segment of the insulator was fractured. Figure 7 shows the insulator cross section. The general surface discoloration did not affect the alumina insulator thickness, but some shallow interactions did occur at the localized dark bluish-grey spots. Figures 8 and 9 show the surface condition of the new and heated wire and figures 10 and 11 show the wire cross sections. The surface texture of the Re wire did not change significantly after heating, but some grain growth did occur.

### **Scanning Electron Microscopy**

Surface morphology and chemistry information were collected from the insulator and conductor

wires in a Field Emission Scanning Electron Microscope (FESEM). Energy Dispersive x-ray Spectroscopy (EDS) was used to identify the surface chemistry in different regions of interest. In figure 12, FESEM/EDS identified the main constituents of the general bluish-grey discoloration as rhenium, aluminum, and oxygen. Figure 13 shows the surface morphology and chemistry of a dark bluish-grey spot. Although similar in color to the general surface discoloration, only a small amount of rhenium was detected on the alumina insulator. Boron and tungsten were also identified in relation to the dark bluish-grey discoloration. Figure 14 shows a region of white discontinuity in the general discoloration. This region was identified as mainly alumina with a little rhenium present. Figure 15 shows FESEM/EDS results for the new Re conductor wire. General EDS of the new Re wire surface revealed some surface contamination. Figure 16 shows the EDS results from a single location of surface contamination on the new wire. Significant amounts of sulfur, tungsten, oxygen, carbon, potassium, calcium, and chlorine were present in the contamination. Figure 17 shows FESEM/EDS results for the heated Re conductor wire. General EDS of the surface revealed some contamination was still present after heating the Re wire. Figure 18 shows the EDS results from a single location of surface contamination on the tested wire. Significant amounts of carbon, sulfur, chlorine, and potassium, are still present after heating the Re wire.

### **Discussion of Insulator Discoloration**

The general bluish-grey discoloration on the alumina insulator was caused by vapor deposition of rhenium oxides. White streaks in the discoloration probably formed due to contact with the hot conductor which prevented condensation of the vaporized rhenium oxide on the alumina surface. The lack of rhenium in the dark bluish-grey spots and the presence of tungsten and boron indicate these spots probably formed from vaporizing surface contamination on the Re wire. Since there was some depth to the interactions at the dark bluish-grey spots, there may have been some limited electrical arcing or high temperature interactions at conductor contact points on the alumina. None of the discoloration significantly affected the thickness of alumina, so the insulator's properties were not affected by rhenium oxide deposition. The discolored surfaces were somewhat conductive in the FESEM, so the bluish-grey deposits probably contained some metallic Re, but the significant presence of oxygen suggests no fully metallic layers were deposited on the insulator during heating.

### **Discussion of the Re Conductor Wire**

The rhenium wire surfaces contained significant volatile contamination which could negatively impact the alumina insulator. The presence of tungsten in the Re wire surface contamination indicates the Re wire was probably contaminated by debris left in wire drawing equipment utilized to draw both tungsten and rhenium wire. This contamination, however, did not play a significant role in insulator discoloration, and it did not result in degradation of the conductor wire. The observed ductility of the Re wire after testing precludes embrittlement due to diffusing surface contamination. Optical cross sections of the new Re wire found significant cracking. This cracking was probably due to over working the material during wire drawing. Subsequent heating of the wire healed many of the internal cracks, but small surface cracks are still present which could lead to later wire breakage

### **Comparison of Tantalum vs. Rhenium Heaters**

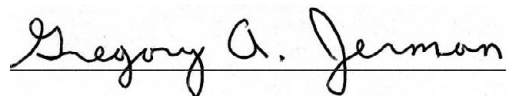
Previously tested Ta conductor wires and Re conductor wires both had surface contamination before use. Only the Ta wire degraded the alumina insulator. Why? The initial Re oxide vaporizes at 145 °C while the first Ta oxide vaporizes at 1870 °C. Thus rhenium oxide is present on the surface of the alumina insulator up to 1000 °C before it starts to decompose. The presence of a Re oxide layer would provide a buffer to alumina decomposition in the presence of carbon contamination under vacuum. In the Ta heater, alumina was reduced to metallic aluminum in the presence of carbon contamination before Ta oxide was vaporized and deposited on the insulator.

### **Conclusions**

1. The general bluish-grey discoloration on the alumina insulator was caused by the deposition of rhenium oxides.
2. The deposition of low temperature rhenium oxides protected the alumina insulator from high temperature degradation during thermal testing.
3. Because Re oxides preserved the alumina insulator integrity and the Re conductor wire retained a large amount of ductility, the Re/alumina combination was superior to the Ta/alumina combination.

### **Recommendations**

1. Because a small amount of vapor deposited rhenium oxide was beneficial to preserving the alumina insulator, and surface contamination on the conductor wire did not significantly affect the insulator, no operational changes are recommended.
2. Because the protective rhenium oxidation begins to degrade at 1000 °C, operation of the Re/alumina heater above 1000 °C is not recommended.



Gregory A. Jerman  
EM30 Material Diagnostics Team

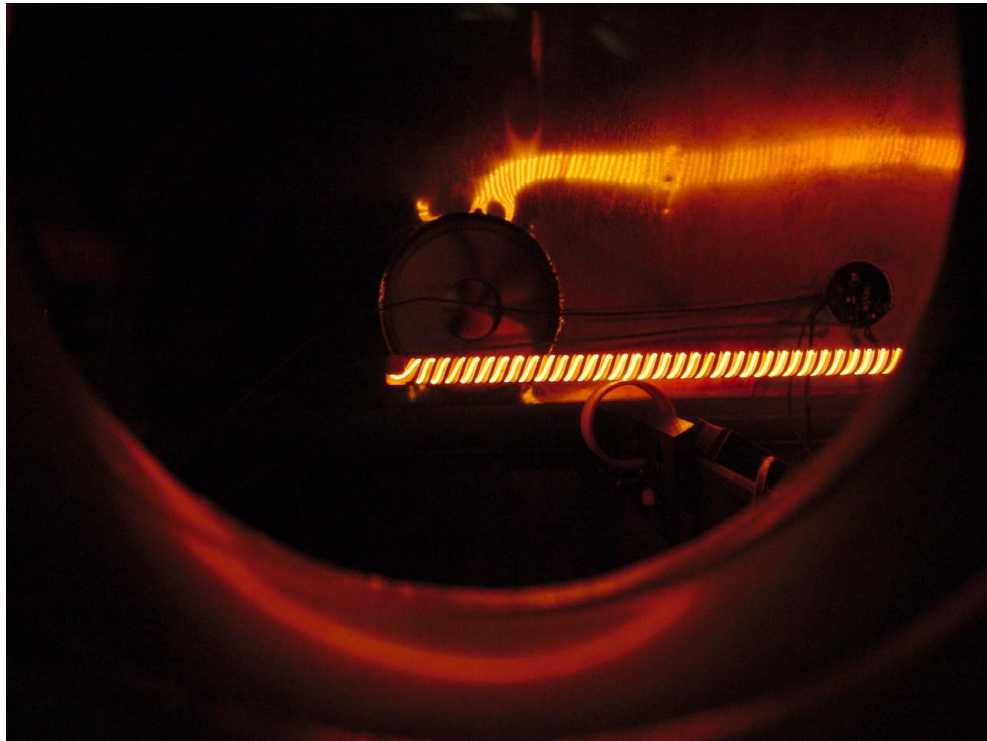


Figure 1. Initial Re wire thermal test image at 1200 W power setting.

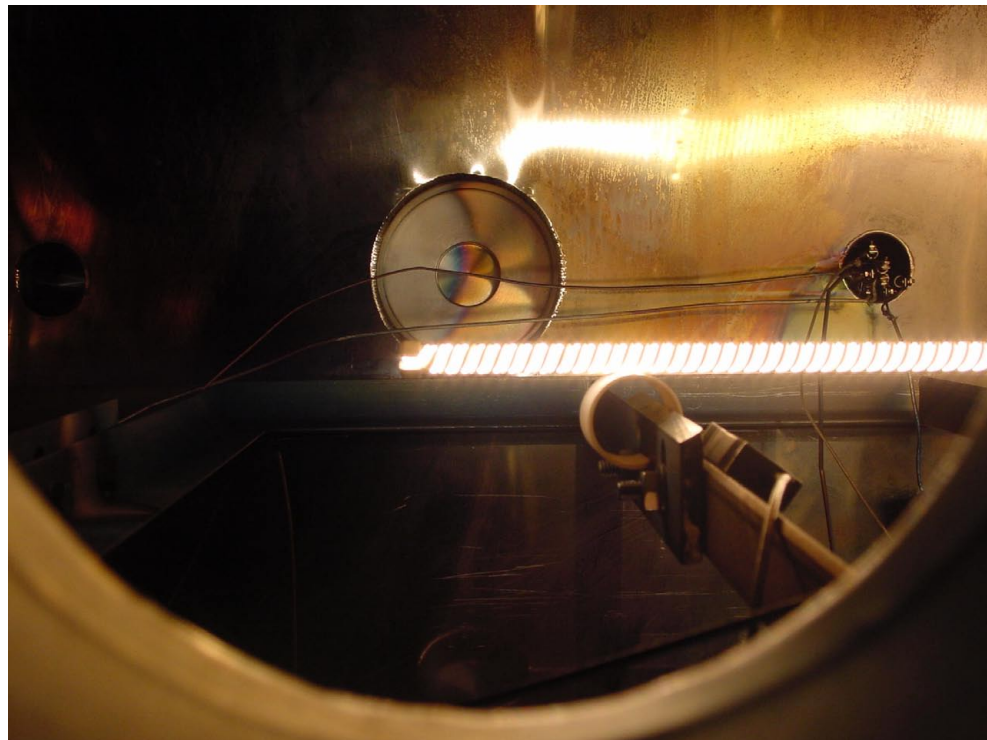


Figure 2. Later Re wire thermal test image at 5000 W power setting.

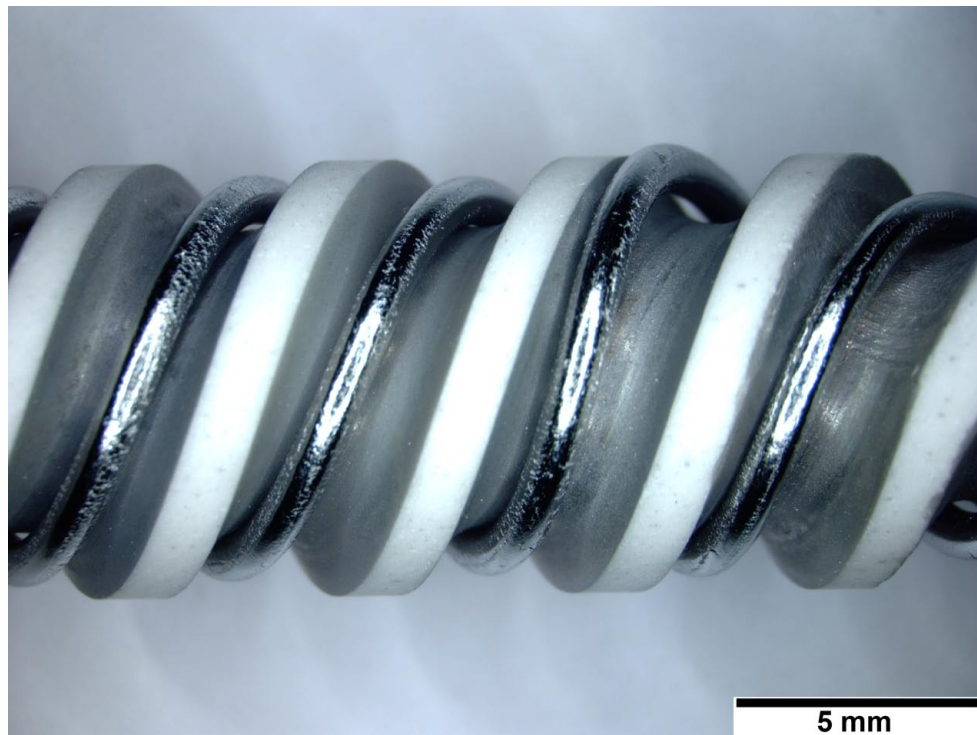


Figure 3. Re wire heater element as received. (7.1x)

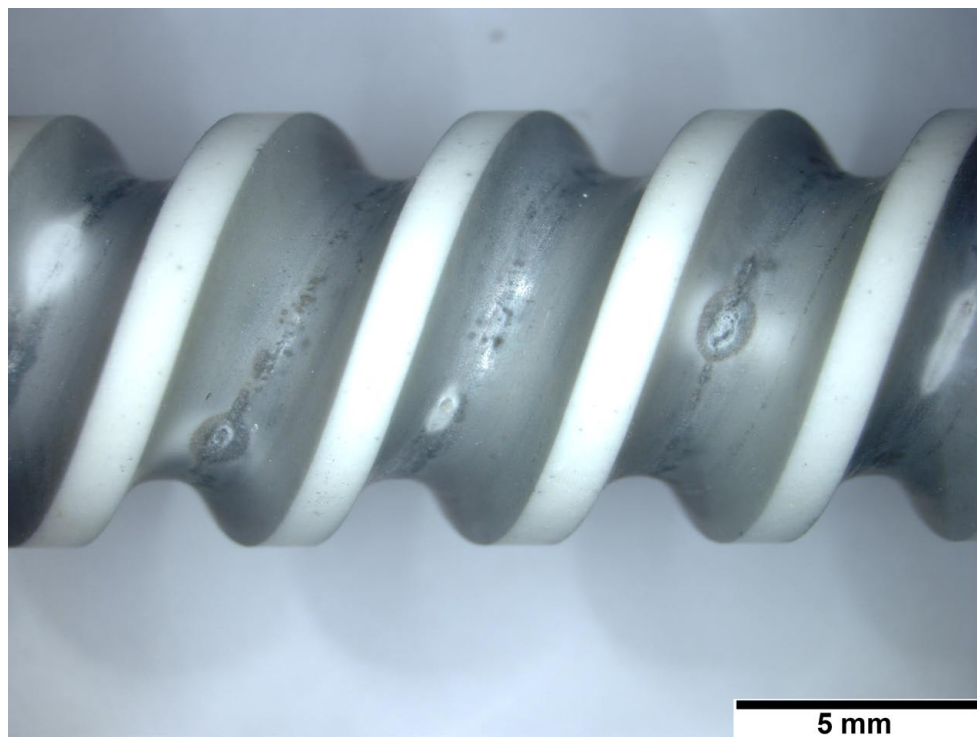


Figure 4. Surface discoloration after Re wire removal. (7.1x)



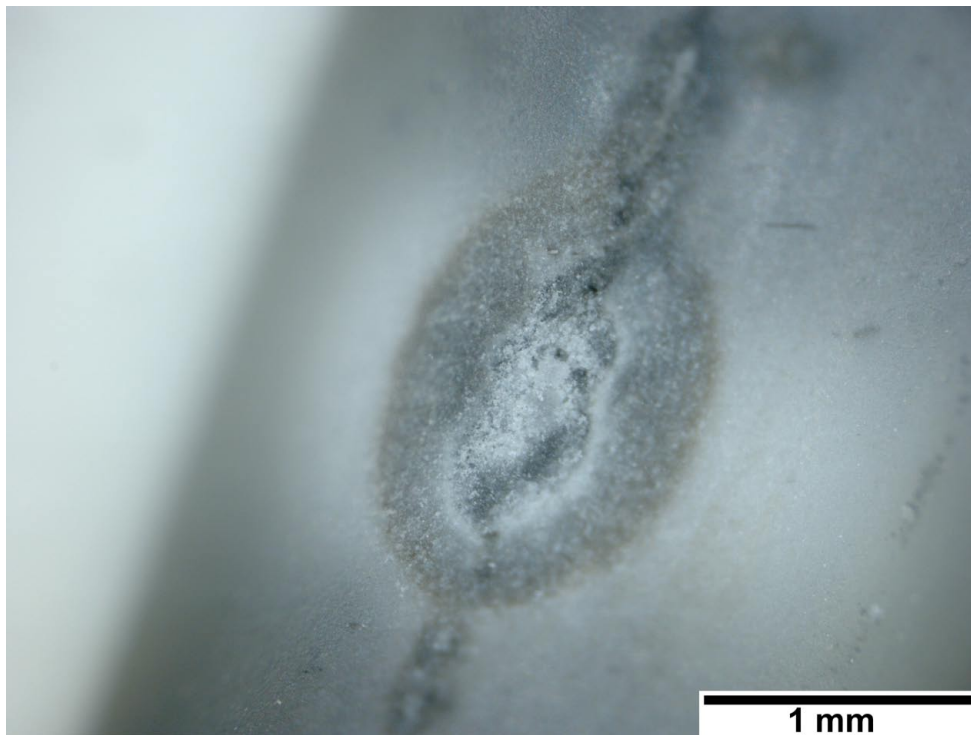


Figure 5. Surface discoloration zone 1 on the alumina insulator. (40x)

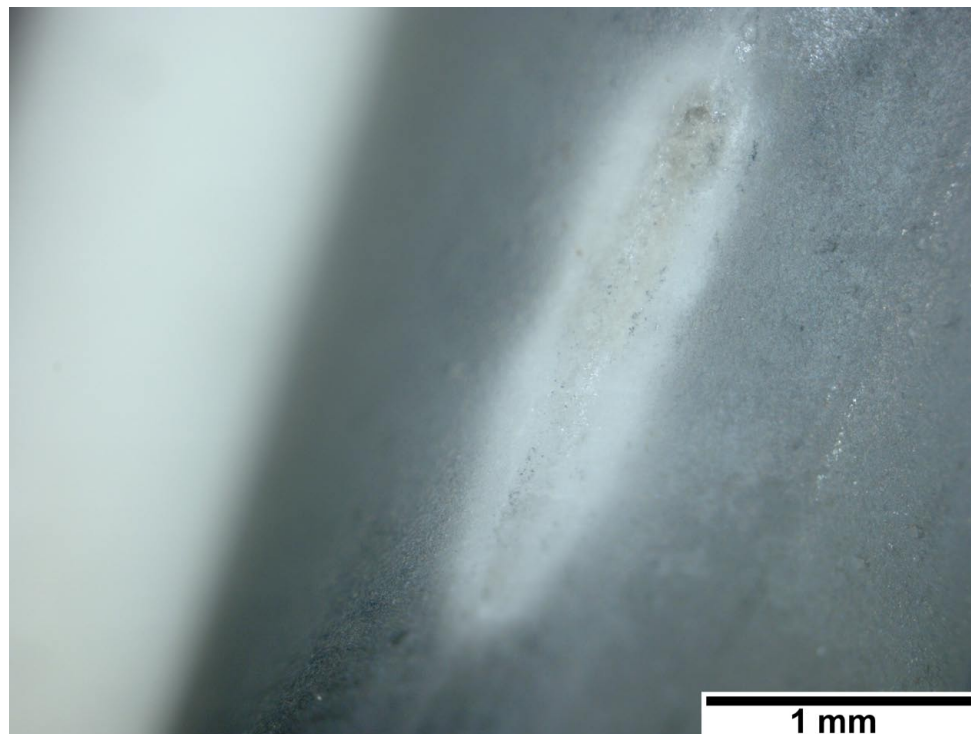


Figure 6. Surface discoloration zone 2 on the alumina insulator. (40x)



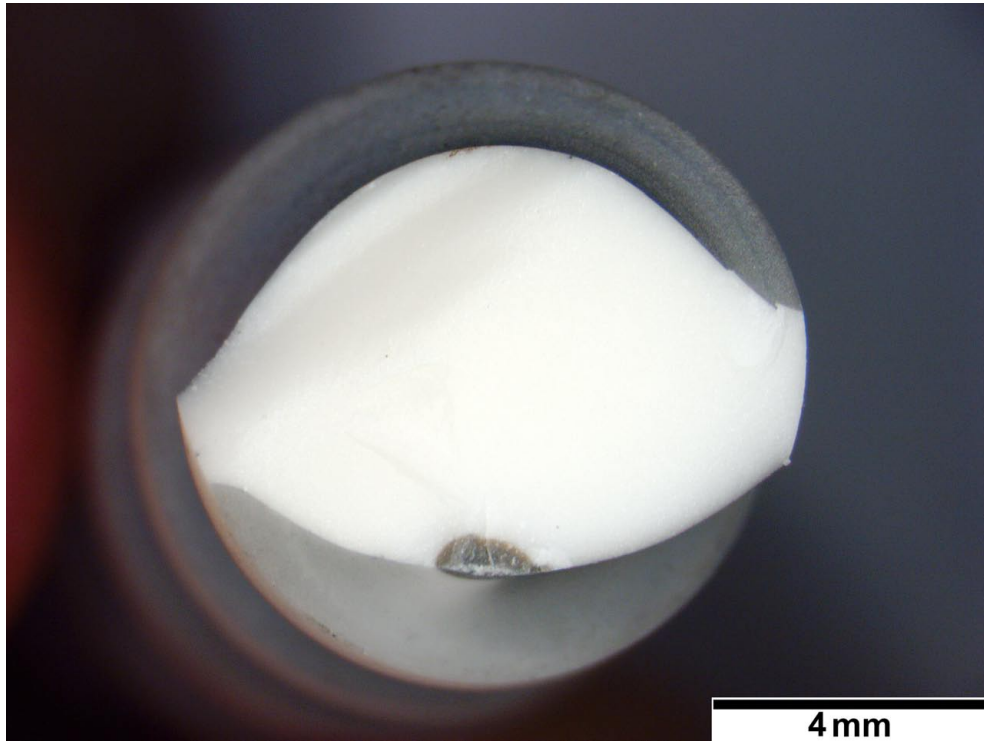


Figure 7. Fractured alumina cross section showing no through thickness interaction with the surface discoloration. (10x)

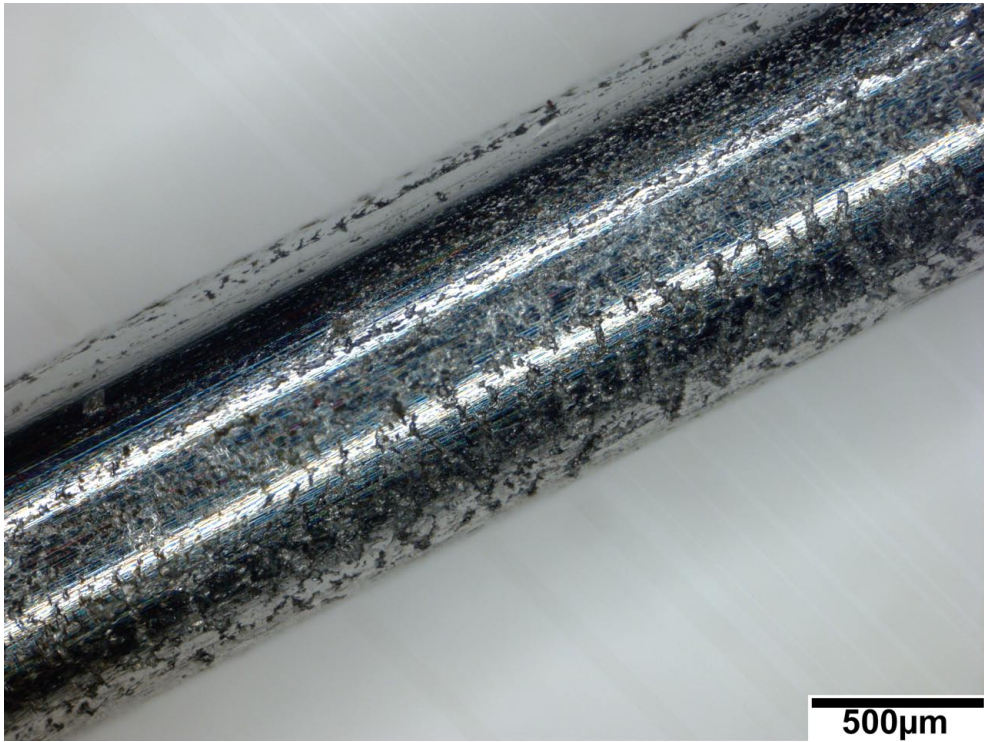


Figure 8. Optical view of the new Re wire surface condition. (50x)

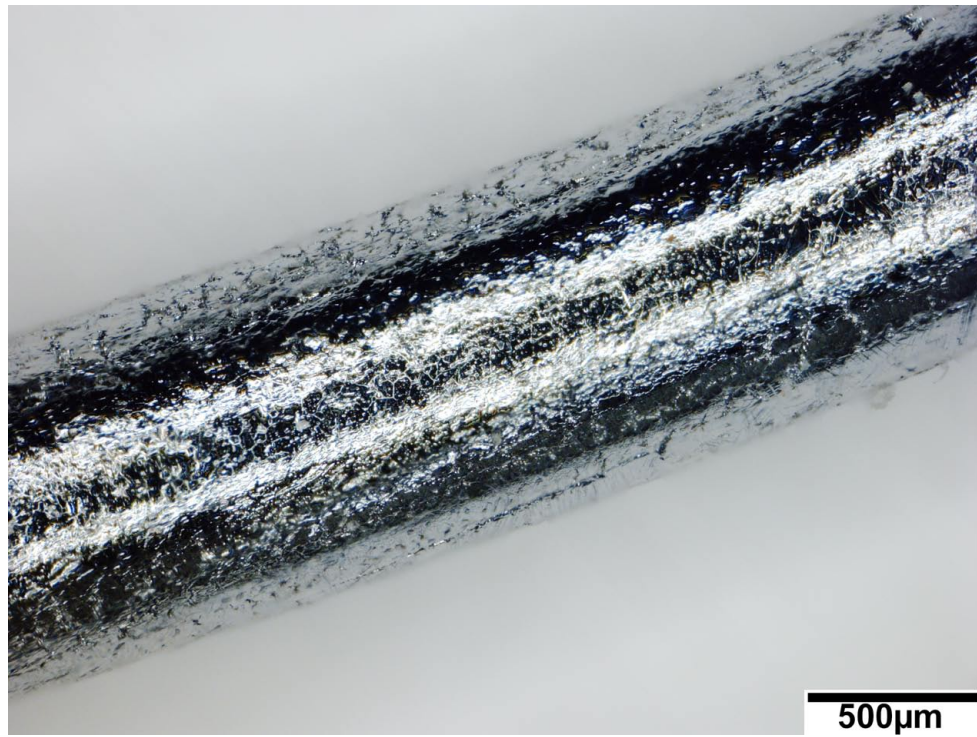


Figure 9. Optical view of the tested Re wire surface condition. (50x)

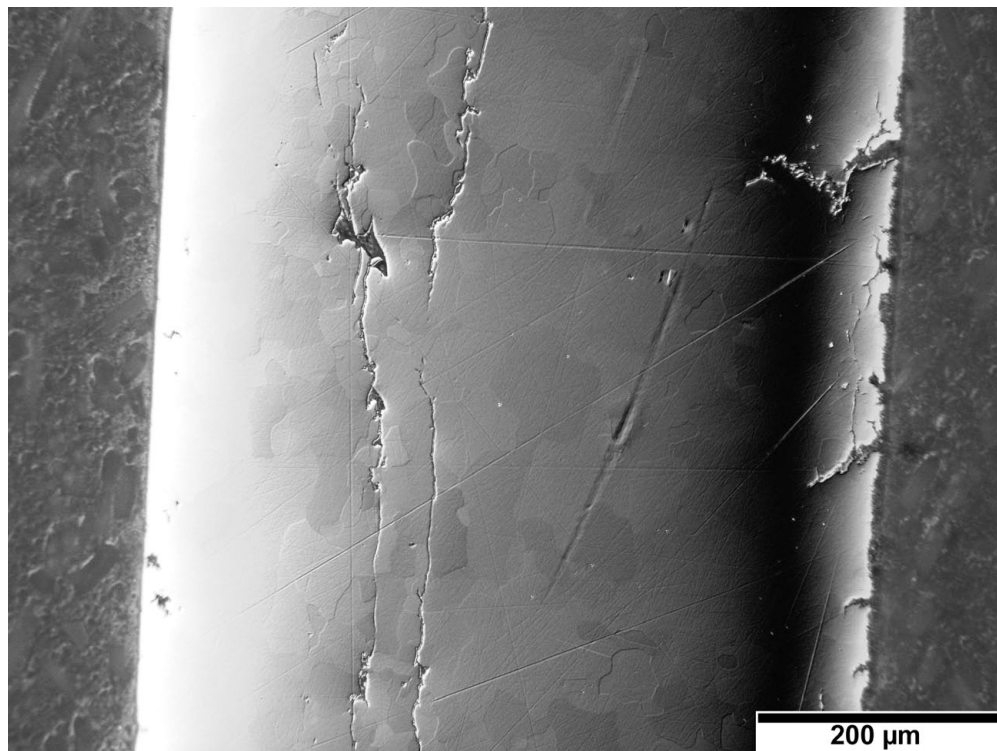


Figure 10. Optical cross sectional view of the new Re wire grain structure. (50x)



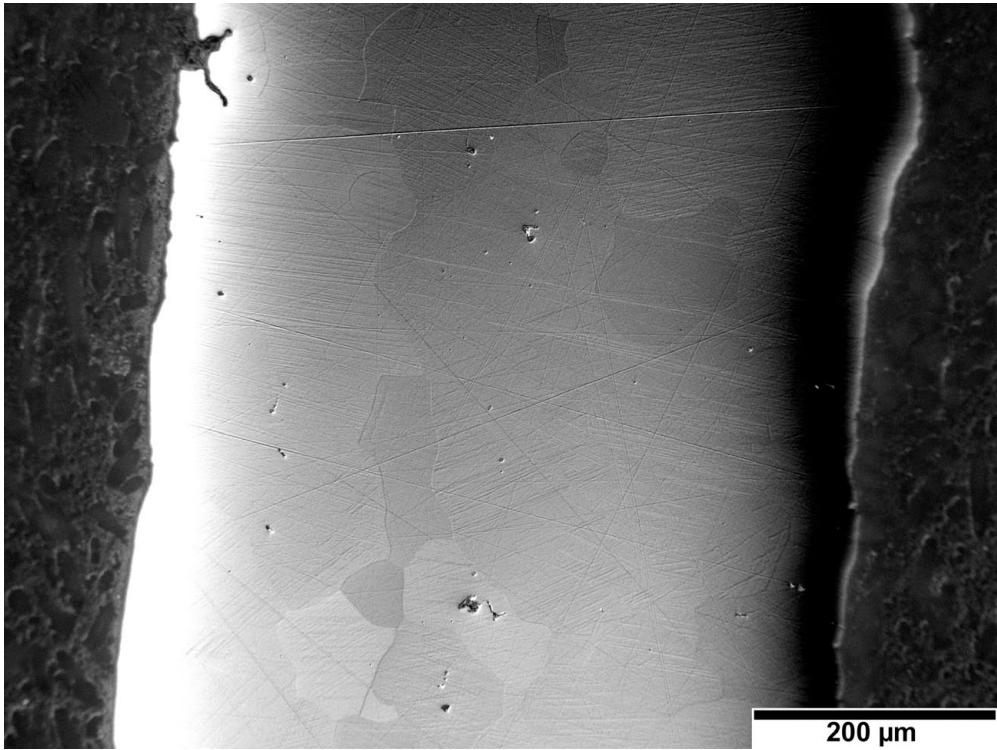


Figure 11. Optical cross sectional view of the tested Re wire grain structure. (50x)

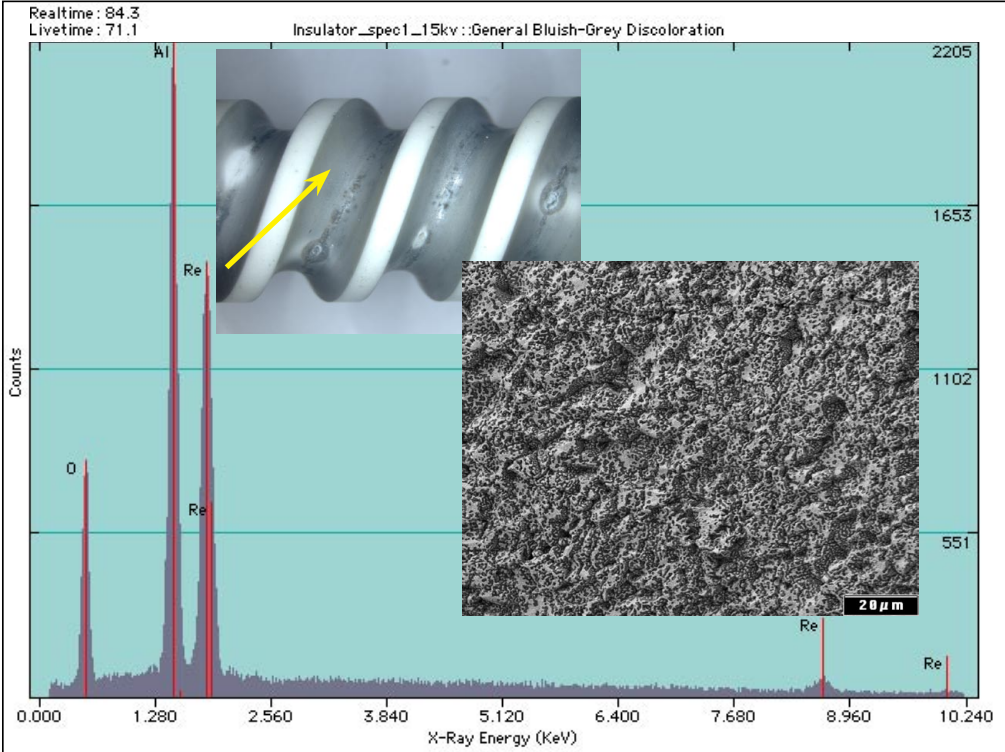


Figure 12. FESEM/EDS analysis of the uniform bluish grey coating that covers the most of the helical alumina insulator groove.

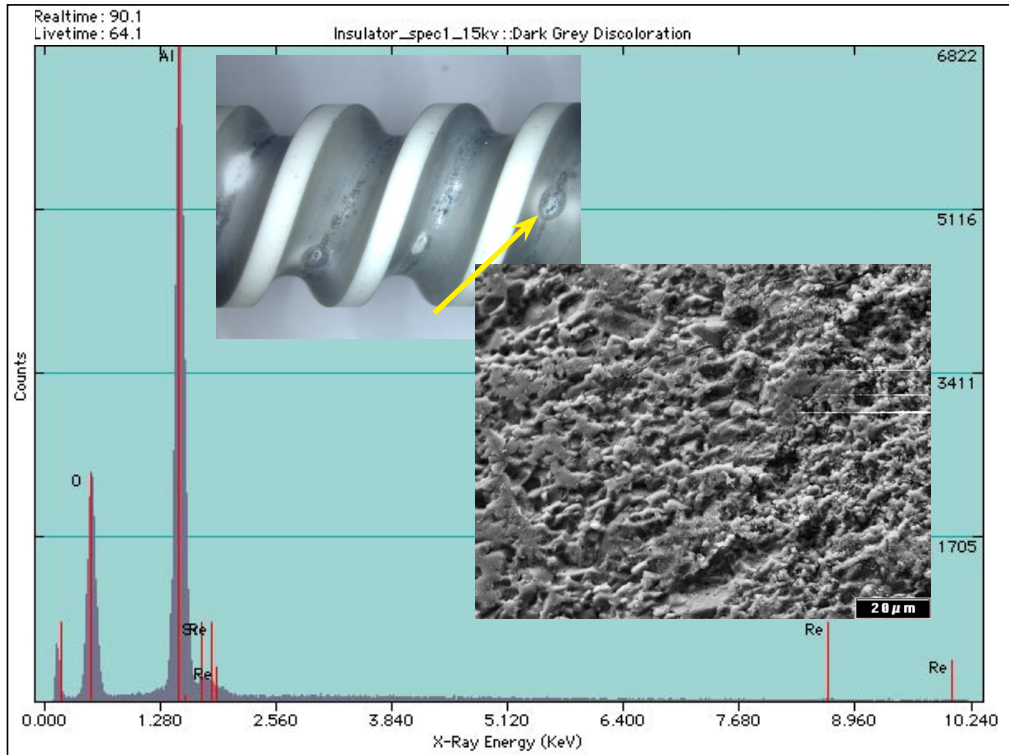


Figure 13. FESEM/EDS analysis of the dark bluish grey spot in the valley of the helical alumina insulator groove.

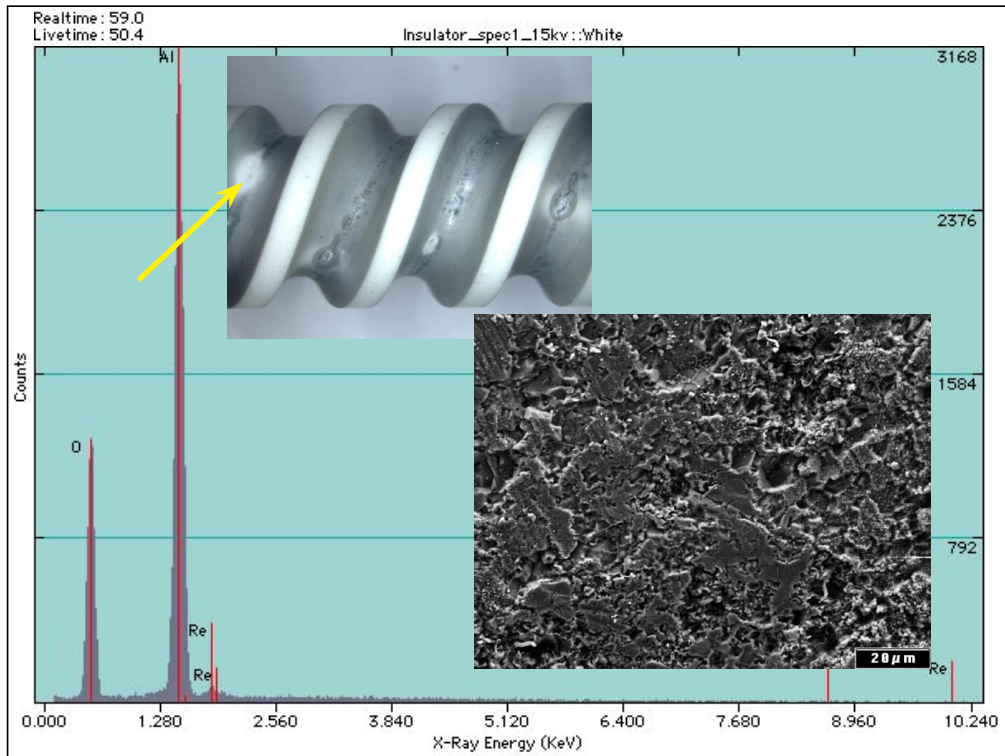


Figure 14. FESEM/EDS analysis of the white streak in the valley of the helical alumina insulator groove.

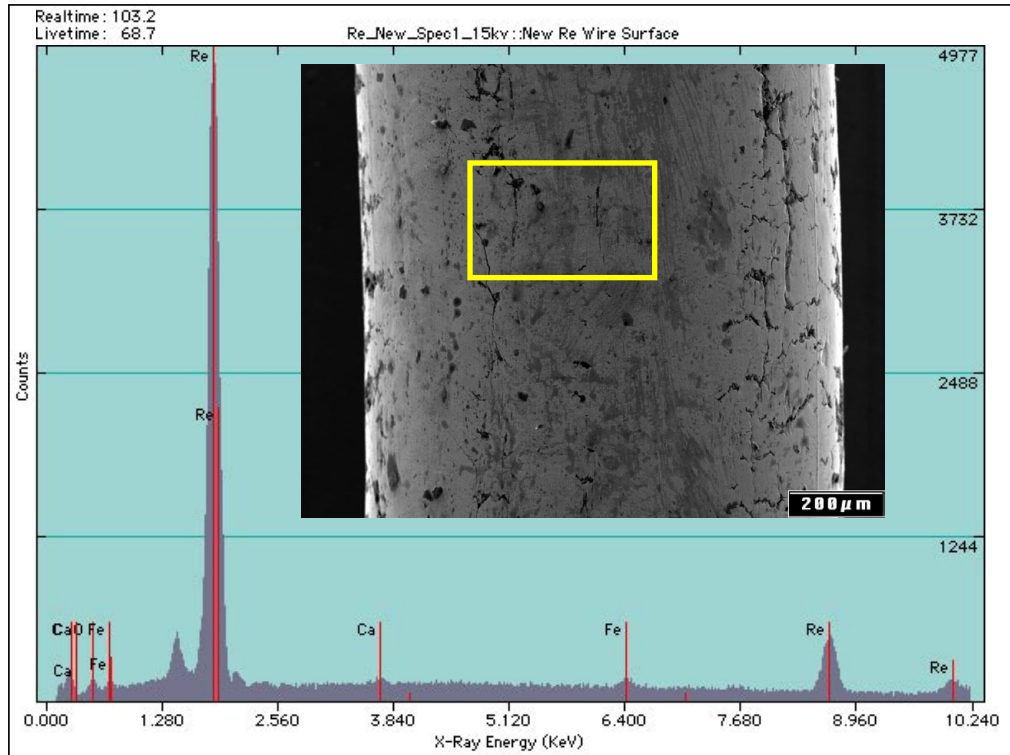


Figure 15. FESEM/EDS analysis of new Re wire from the same lot installed on the helical alumina insulator.

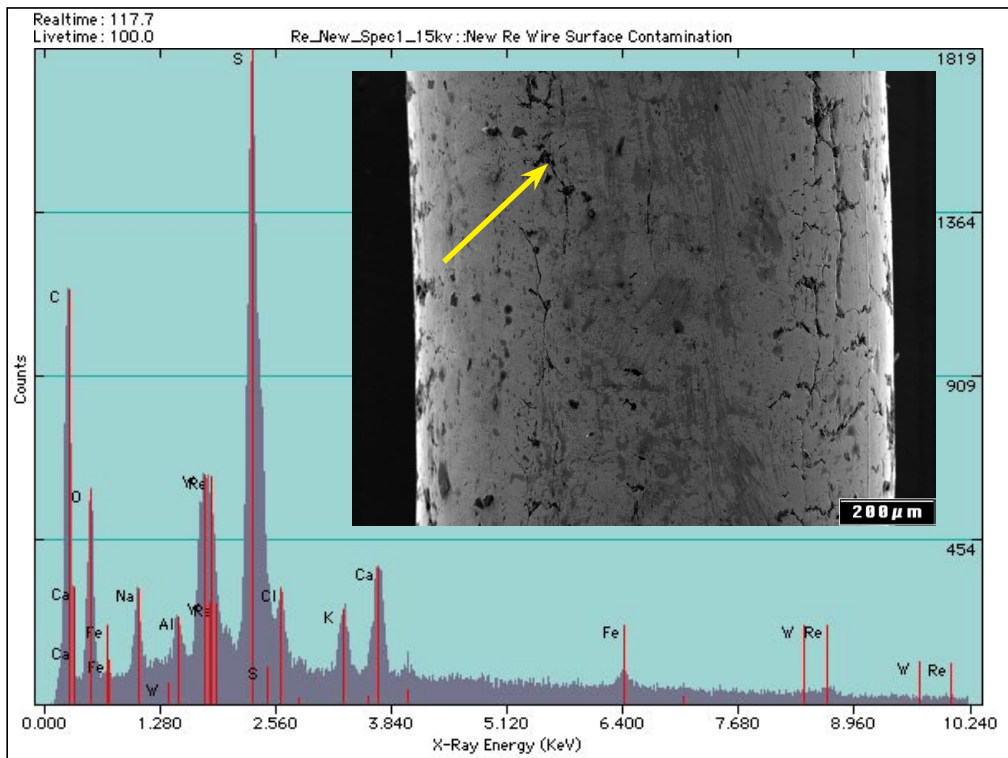


Figure 16. FESEM/EDS analysis of the surface contamination on the new Re wire.



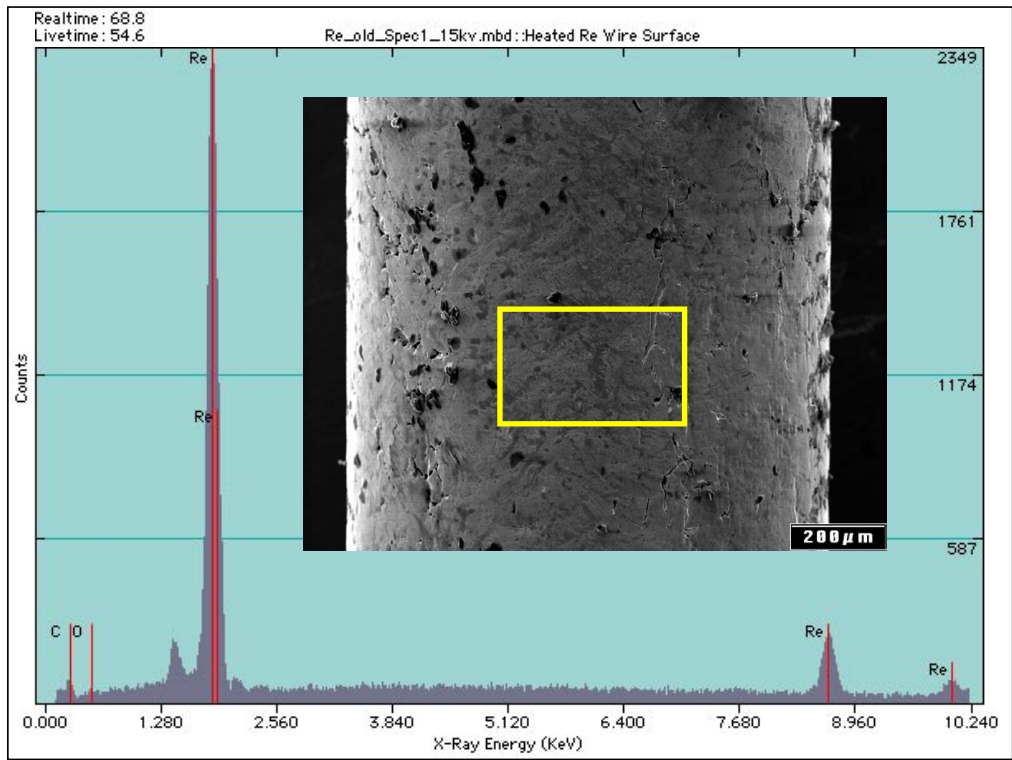


Figure 17. FESEM/EDS analysis of the thermally tested Re wire that was installed on the helical alumina insulator.

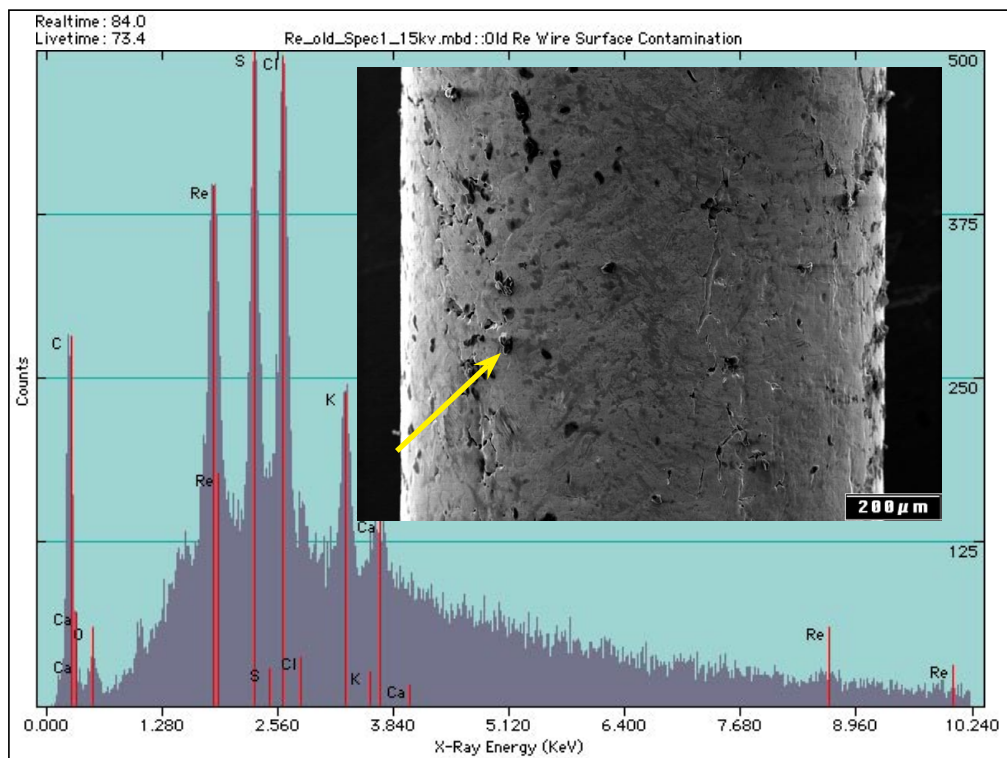


Figure 18. FESEM/EDS analysis of surface contamination on the thermal tested Re wire.



## APPENDIX G—KEY GOVERNING EQUATIONS AND SUPPORTING FORMULATIONS

### Concentric cylindrical gap conductive conductance (typically in W/K)

$$G_{gap} = \frac{2\pi L k}{\ln\left(\frac{D_{outer}}{D_{inner}}\right)}, \quad (6)$$

where  $L$  is the length of the gap,  $D_{inner}$  and  $D_{outer}$  are the inner and outer diameters of the gap, and  $k$  is the conductivity of the media in the gap.

### Concentric cylindrical gap radiative conductance (typically in W/K)

$$G_{rad,gap} = A\sigma E, \quad (7)$$

where  $A$  is the surface area of the inner surface that faces the gap,  $\sigma$  is the Stefan-Boltzman constant, and  $E$  is the emissivity function that takes into the account the two-dimensional geometry of the concentric cylinders. This assumes the axial length of the two opposing sides of the gap are very long compared the gap thickness. The emissivity function is:

$$E = \left( \frac{1}{\varepsilon_{inner}} + \frac{1 - \varepsilon_{outer}}{\varepsilon_{outer}} \left( \frac{D_{inner}}{D_{outer}} \right) \right)^{-1}, \quad (8)$$

where  $\varepsilon_{inner}$  and  $\varepsilon_{outer}$  are the emissivities of the inner and outer surfaces, respectively, encompassing the gap. This assumes that the surfaces are gray and diffuse. When there are more than two concentric cylinders making a series of gaps, these (radiative) gap conductances can be added in a serial fashion to obtain an overall conductance, which might be used, for example, to estimate the heat transfer between a heater wire and chamber boundary through a sheath.

### Heat balance equation

The conductances are then used to determine temperatures by solving equations such as the following for either temperature or heat transferred:

$$Q = G_{gap}(T_{inner} - T_{outer}) + G_{rad,gap}(T_{inner}^4 - T_{outer}^4), \quad (9)$$

where  $T_{inner}$  and  $T_{outer}$  are the temperatures of the inner and outer surface and the  $Q$  is the heat transferred between the surfaces.

### Conductive shape factors:

When the geometry is more complex than a concentric cylinder or slab, determining the conductive conductances can be performed by using what is referred to a conduction shape factor  $S$  as in the following equation:

$$Q_{con,12} = S_{12} k (T_1 - T_2) , \quad (10)$$

where  $T_1$  and  $T_2$  are the temperatures of two surfaces or thermal nodes,  $k$  is the thermal conductivity of the material between the two surfaces,  $Q_{con,12}$  is the net heat transferred by conduction between surfaces 1 and 2, and  $S_{12}$  is the conductive shape factor that takes into account the area of the surfaces and geometry of the thermal path between 1 and 2. In the current analysis, the shape factors were obtained using a partial finite element model of the gap between the heater wire, mandrel, and enclosing sheath. Shape factors were used to perform a preliminary level analysis or as part of a closed-form parametric solution to support trade studies. Because of the simplifications in the shape factors' development and computation, their use is subject to a number of restrictions and caution should be used when applying them. For more accurate estimates, complete finite difference and finite element solutions can be used.

### Radiative exchange factors:

When the geometry is more complex than flat plates or concentric cylinders and when radiation leaving or striking a surface is due to emission and reflection, radiative exchange factors can be computed that accurately (again, under certain restrictions) model the entire radiative transfer between an assembly of discrete surfaces. The following equation depicts, in a general sense, what is meant by radiative exchange factors:

$$Q_{rad,i} = A_i \sum_{j=1}^N f_{ij} \sigma (T_i^4 - T_j^4) , \quad (11)$$

where  $Q_{rad,i}$  is the net transfer into and out of a surface  $i$ , by radiative exchange with other surfaces in the enclosure,  $A_i$  is the surface area of the specific surface  $i$ ,  $f_{ij}$  is the radiative exchange factor from surface  $i$  to  $j$  and encompasses the surface emissivities and geometries of the various paths by which energy can be radiated from  $i$  and reach surface  $j$ ,  $T_i$  and  $T_j$  are the surface temperatures of surfaces  $i$  and  $j$ , respectively,  $N$  is the number of surfaces that contribute to the radiative enclosures, and  $\sigma$  is again the Stefan-Boltzman constant. The  $f_{ij}$ s are derived from calculated view factors and surface emissivities. These view factors and exchange factors can be calculated by hand per methods described in texts such as *Thermal Radiation and Heat Transfer* by Siegel and Howell,<sup>21</sup> as was performed in this case, or using a computer program such as TRASYS or Thermal Desktop or by a finite element modeler/solver such as FIDAP, as was used in this case as a backup solution.

### Heat balance equation part 2:

The radiative exchange factors and conductive shape factors can be combined along with an estimate of the heat generated in a component such as the heat in the wire arising from an applied voltage and the electrical resistance to compute the temperatures of the various components. The governing equation follows:

$$Q_{gen,i} = \sum_{j=1}^N S_{ij} k (T_i - T_j) + A_i \sum_{j=1}^N f_{ij} \sigma (T_i^4 - T_j^4) , \quad (12)$$

where  $Q_{gen,i}$  is the heat generated within a surface or thermal node  $i$ , and  $S_{ij}$ s are the conduction shape factors between nodes  $i$  and  $j$ . This equation can be written for each of the  $N$  surfaces in the enclosure then expanded and tailored, resulting in a set of equations that can be solved iteratively to obtain the unknown temperatures. This was performed in the Mathcad solution approach. For the SINDA solution, the radiative exchange factors and the conductive shape factors are submitted as part of the model; the conductors (both radiative and conductive) were calculated and the SINDA solution routines were applied to solve for temperatures.

## APPENDIX H—THERMAL CROSS-SECTION CALCULATIONS

The thermal conductivities of selected gases, at temperature, are provided in figure 76. Gas properties were obtained from: Incropera and DeWitt, Arp et al., Manglik, Bailey, and Jain.<sup>10-14</sup>

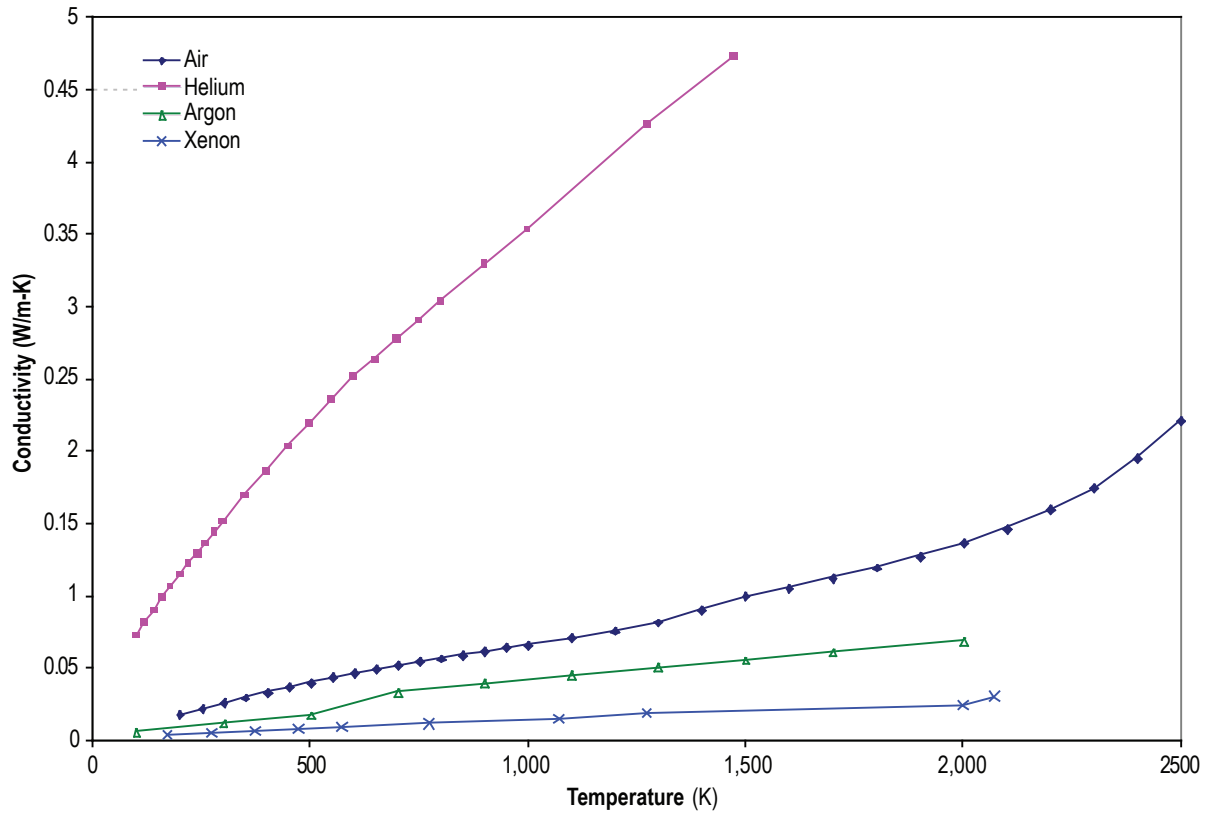


Figure 76. Thermal conductivity of selected gases.

## Summary of MathCad Calculations for Analysis of Sheathed Graphite Heater Elements

### One Dimension, Cross-Sectional Heat Transfer Calculations

#### Heater/Sheath Geometry

$$\text{IDcore} := 0.545 \text{ in}$$

$$\text{Lsheath} := 20 \text{ in}$$

$$\text{ODsheath} := 0.540 \text{ in}$$

$$\text{IDsheath} := .465 \text{ in}$$

$$\text{IDsheath} = 11.8 \text{ mm}$$

$$\text{ODheater} := .350 \text{ in}$$

$$\text{ODheater} = 8.9 \text{ mm}$$

$$\text{thsheath} := \frac{\text{ODsheath} - \text{IDsheath}}{2}$$

$$\text{thsheath} = 1 \text{ mm}$$

#### Geometric Calculations

$$\text{radialgap} := \frac{\text{IDsheath} - \text{ODheater}}{2}$$

$$\text{radialgap} = 0.1 \text{ in}$$

$$\text{Asrfsheath} := \pi \cdot \text{ODsheath} \cdot \text{Lsheath}$$

$$\text{radialgap} = 1.5 \text{ mm}$$

$$\text{Asrfheater} := \pi \cdot \text{ODheater} \cdot \text{Lsheath}$$

#### Design Conditions: Heater Power and Sheath Temperature


$$\text{Tsheat} := (1000 + 273.15) \text{ K}$$

$$\text{Qheater} := 6000 \text{ W}$$

## Gap Heat Transfer Calculations: Gas Gap, conduction only

Gas in gap is helium

Helium thermal conductivity

 Read in data from general gas properties spreadsheet  
(summarized in fig. 75)

TKheND :=

KheND :=



Adjust units of imported data

TKhe := TKheND · K

**Radial Conductor, G**

Khe := KheND ·  $\frac{\text{W}}{\text{m} \cdot \text{K}}$

Tgap := Tsheath

Kgas := linterp(TKhe, Khe, Tgap)

Kgas = 0.4  $\frac{\text{kg m}}{\text{s}^3 \text{K}}$

Gheonly :=  $\frac{2 \cdot \pi \cdot L_{\text{sheath}} \cdot K_{\text{gas}}}{\ln\left(\frac{ID_{\text{sheath}}}{OD_{\text{heater}}}\right)}$

Gheonly = 4.798  $\frac{\text{W}}{\text{K}}$

Theater :=  $\frac{Q_{\text{heater}}}{G_{\text{heonly}}} + T_{\text{sheath}}$

Theater = 2524 K

ΔThs := Theater – Tsheath

ΔThs = 1251 K



## Gap Heat Transfer Calculations: Gas Gap, conduction only

Gas in gap is Argon

### Argon thermal conductivity

Read in data from general gas properties spreadsheet

TKarND :=



KarND :=



Adjust for units of imported data

TKar := TKarND · K

Kar := KarND ·  $\frac{\text{W}}{\text{m} \cdot \text{K}}$

### Radial Conductor, G

Tgap := Tsheath

Kgas := linterp(TKar, Kar, Tgap)

Kgas = 0.1  $\frac{\text{W}}{\text{m} \cdot \text{K}}$

Garonly :=  $\frac{2 \cdot \pi \cdot \text{Lsheath} \cdot \text{Kgas}}{\ln\left(\frac{\text{IDsheath}}{\text{ODheater}}\right)}$

Garonly = 0.56  $\frac{\text{W}}{\text{K}}$

Theater :=  $\frac{\text{Qheater}}{\text{Garonly}} + \text{Tsheath}$

Theater = 11938 K

ΔThs := Theater - Tsheath

ΔThs = 10665 K

## Gap Heat Transfer Calculations: Gas Gap, conduction only

Gas in gap is Xenon

Argon thermal conductivity

Read in data from general gas properties spreadsheet

TKxeND :=



KxeND :=



Adjust for units of imported data

TKxe := (TKxeND + 273.15) · K

Kxe := KxeND ·  $\frac{\text{W}}{\text{m} \cdot \text{K}}$

**Radial Conductor, G**

Tgap := Tsheath

Kgas := linterp(TKxe, Kxe, Tgap)

Kgas = 0.018  $\frac{\text{W}}{\text{m} \cdot \text{K}}$

Gxeonly :=  $\frac{2 \cdot \pi \cdot \text{Lsheath} \cdot \text{Kgas}}{\ln\left(\frac{\text{IDsheath}}{\text{ODheater}}\right)}$

Gxeonly = 0.21  $\frac{\text{W}}{\text{K}}$

Theater :=  $\frac{\text{Qheater}}{\text{Gxeonly}} + \text{Tsheath}$

Theater = 30393 K

ΔThs := Theater - Tsheath

ΔThs = 29120 K

## Effect of gap size

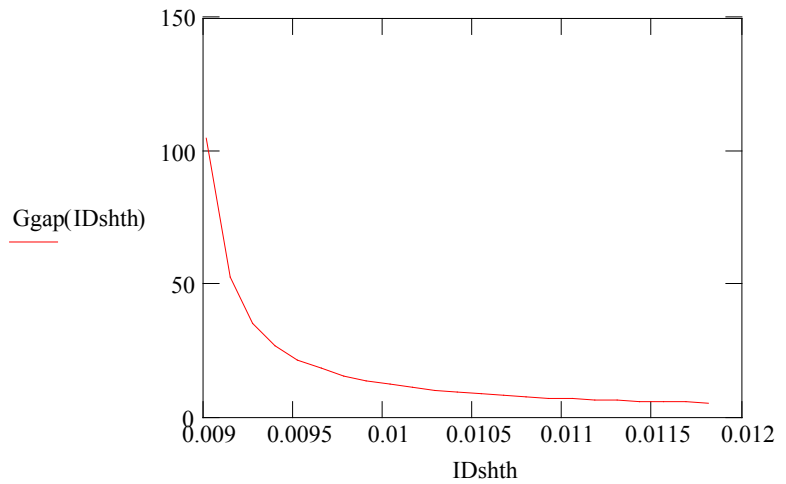
Since the OD of the sheath is fixed; the gap size can be reduced by thickening the sheath – decreasing the sheath ID or by increasing the heater diameter, which requires redesign of of the resistive element.

$$ID_{shth} := 0.465 \text{ in}, 0.460 \text{ in}.. 0.355 \text{ in}$$

$$K_{gas} := \text{interp}(TKhe, Khe, T_{sheath})$$

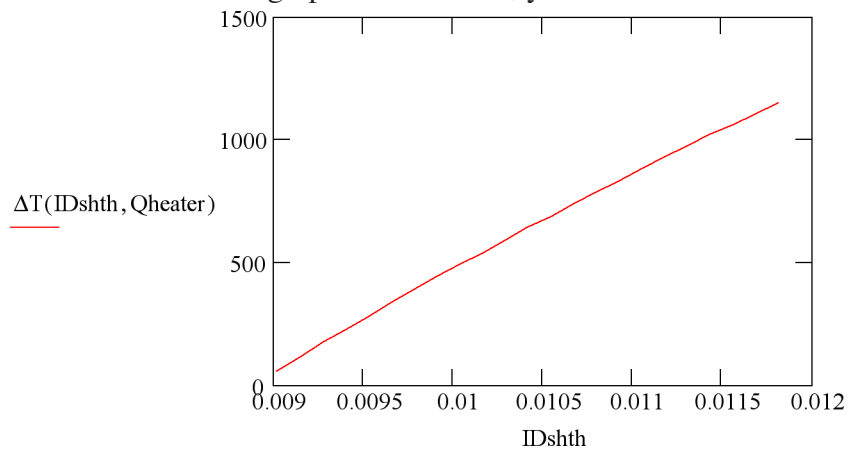
$$G_{gap}(ID_{sheath}) := \frac{2 \cdot \pi \cdot L_{sheath} \cdot K_{gas}}{\ln\left(\frac{ID_{sheath}}{OD_{heater}}\right)}$$

graph units: x -> m; y -> W/K



$$\Delta T(ID_{sheath}, Q_{heater}) := \frac{Q_{heater}}{2 \cdot \pi \cdot L_{sheath} \cdot K_{gas}} \cdot \ln\left(\frac{ID_{sheath}}{OD_{heater}}\right)$$

graph units: x -> m; y -> K or C



$$0.370 \text{ in} = 0.0094 \text{ m}$$

$$G_{gap}(.370 \text{ in}) = 26.7 \frac{\text{W}}{\text{K}}$$

$$\Delta T(.370 \text{ in}, 6000 \text{ W}) = 225.1 \text{ K}$$

## Gap Heat Transfer Calculations: Vacuum Gap, radiation only

### Assumed heater and wall emissivities and important constants

$$\sigma := 5.67 \cdot 10^{-8} \frac{\text{W}}{\text{m}^2 \cdot \text{K}^4}$$

$$\epsilon_h := .9$$

$$\epsilon_s := .7$$

$$E_{hs}(\epsilon_h, \epsilon_s) := \left[ \frac{1}{\epsilon_h} + \frac{1 - \epsilon_s}{\epsilon_s} \cdot \left( \frac{OD_{heater}}{ID_{sheath}} \right) \right]^{-1}$$

Heater surface emissivity;  
typical graphite emissivity

Sheath ID emissivity  
typical oxidized stainless steel; or potential emissivity  
enhanced refractory surface

$$T_{heater} := \left( \frac{Q_{heater}}{Asr_{heater} \cdot E_{hs}(\epsilon_h, \epsilon_s) \cdot \sigma} + T_{sheath}^4 \right)^{\frac{1}{4}} \quad T_{heater} = 1910 \text{ K}$$

Effective Radial conductor G normalized for the heater and sheath conditions;  
note that this radial conductor is highly temperature dependent.

$$G_{radonly} := Asr_{heater} \cdot E_{hs}(\epsilon_h, \epsilon_s) \cdot \sigma \cdot (T_{heater} + T_{sheath}) (T_{heater}^2 + T_{sheath}^2)$$

$$G_{radonly} = 9.4 \frac{\text{W}}{\text{K}}$$

$$\Delta T_{hs} := T_{heater} - T_{sheath}$$

$$\Delta T_{hs} = 637 \text{ K}$$

## Gap Heat Transfer Calculations: Vacuum Gap, radiation only, different radiative properties

Alternative emissivity combination #1

$$\epsilon_h := .9$$

Heater surface element emissivity  
Typical graphite emissivity

$$\epsilon_s := .2$$

Sheath ID emissivity  
Represents polished moly, tantalum sheath;  
uncertain of long term of stability of oxidized  
surfaces (TaO<sub>2</sub>, MoO<sub>2</sub>, etc)

$$T_{heater} := \left( \frac{Q_{heater}}{Asr_{heater} \cdot E_{hs}(\epsilon_h, \epsilon_s) \cdot \sigma} + T_{sheath}^4 \right)^{\frac{1}{4}} \quad T_{heater} = 2403 \text{ K}$$

Effective Radial conductor G normalized for the heater and sheath conditions;  
note that this radial conductor is highly temperature dependent.

$$G_{radonly} := Asr_{heater} \cdot E_{hs}(\epsilon_h, \epsilon_s) \cdot \sigma \cdot (T_{heater} + T_{sheath}) (T_{heater}^2 + T_{sheath}^2)$$

$$G_{radonly} = 5.3 \frac{\text{W}}{\text{K}}$$

$$\Delta T_{hs} := T_{heater} - T_{sheath}$$

$$\Delta T_{hs} = 1130 \text{ K}$$

## Gap Heat Transfer Calculations: Vacuum Gap, radiation only, different radiative properties

Alternative emissivity combination #2

$$\epsilon_h := .5$$

Heater surface element emissivity  
Carbon filament, could also represent ceramics such as boron nitride, alumina.

$\epsilon_s := .2$  Sheath ID emissivity  
Represents polished moly, tantalum sheath; uncertain of long term of stability of oxidized surfaces (TaO<sub>2</sub>, MoO<sub>2</sub>, etc)

$$T_{\text{heater}} := \left( \frac{Q_{\text{heater}}}{A_{\text{surfheater}} \cdot E_{\text{hs}}(\epsilon_h, \epsilon_s) \cdot \sigma} + T_{\text{sheath}}^4 \right)^{\frac{1}{4}} \quad T_{\text{heater}} = 2515 \text{ K}$$

Effective Radial conductor G normalized for the heater and sheath conditions; note that this radial conductor is highly temperature dependent. It is also dependent on geometry somewhat, although not as much.

$$G_{\text{radonly}} := A_{\text{surfheater}} \cdot E_{\text{hs}}(\epsilon_h, \epsilon_s) \cdot \sigma \cdot (T_{\text{heater}} + T_{\text{sheath}}) (T_{\text{heater}}^2 + T_{\text{sheath}}^2)$$

$$G_{\text{radonly}} = 4.8 \frac{\text{W}}{\text{K}}$$

$$\Delta T_{\text{hs}} := T_{\text{heater}} - T_{\text{sheath}}$$

$$\Delta T_{\text{hs}} = 1242 \text{ K}$$



## Gap Heat Transfer Calculations: Vacuum Gap, radiation only, different radiative properties

Alternative emissivity combination #3

$$\epsilon_h := .5$$

Heater surface element emissivity  
Carbon filament, could also represent ceramics such as boron nitride.

$$\epsilon_s := .7$$

Sheath ID emissivity  
typical oxidized stainless steel; or potential emissivity enhanced refractory surface

$$T_{heater} := \left( \frac{Q_{heater}}{A_{surfheater} \cdot E_{hs}(\epsilon_h, \epsilon_s) \cdot \sigma} + T_{sheath}^4 \right)^{\frac{1}{4}} \quad T_{heater} = 2113 \text{ K}$$

Effective Radial conductor G normalized for the heater and sheath conditions; note that this radial conductor is highly temperature dependent. It is also dependent on geometry somewhat, although not as much.

$$G_{radonly} := A_{surfheater} \cdot E_{hs}(\epsilon_h, \epsilon_s) \cdot \sigma \cdot (T_{heater} + T_{sheath}) (T_{heater}^2 + T_{sheath}^2)$$

$$G_{radonly} = 7.1 \frac{\text{W}}{\text{K}}$$

$$\Delta T_{hs} := T_{heater} - T_{sheath}$$

$$\Delta T_{hs} = 840 \text{ K}$$

## Gap Heat Transfer Calculations: Gap radiation and conduction combined

$$T_h := T_{\text{heater}} \quad \varepsilon_h := .5 \quad \varepsilon_s := .2$$

$$T_h := \text{root} \left[ G_{\text{heonly}} \cdot (T_h - T_{\text{sheath}}) + A_{\text{surfheater}} \cdot \sigma \cdot E_{\text{hs}}(\varepsilon_h, \varepsilon_s) \cdot (T_h^4 - T_{\text{sheath}}^4) - Q_{\text{heater}, T_h} \right]$$

$$T_h = 2036 \text{ K}$$

$$G_{\text{comb}} := \frac{Q_{\text{heater}}}{T_h - T_{\text{sheath}}}$$

$$G_{\text{comb}} = 7.9 \frac{\text{W}}{\text{K}}$$

$$\Delta T_{\text{hs}} := T_h - T_{\text{sheath}}$$

$$\Delta T_{\text{hs}} = 763 \text{ K}$$

## Gap Heat Transfer Calculations: Conductive gap filler; ceramic powder w/ helium

Boron Nitride conductivity dat

$$TK_{bnsng} := \begin{bmatrix} 80 \\ 392.0 \\ 752.0 \\ 1112.0 \\ 1472.0 \\ 1832.0 \\ 2192.0 \end{bmatrix} + 460 \cdot R$$

$$K_{bnsng} := \begin{bmatrix} 36.3 \\ 48.7 \\ 40.4 \\ 33.8 \\ 29.0 \\ 26.8 \\ 27.2 \end{bmatrix} \frac{\text{BTU}}{\text{hr}\cdot\text{ft}\cdot\text{R}}$$

Computation of packed bed conductance; based on scott gilley's method/research in development of microgravity processing SACA's with power filled gaps

BSF := .5      BSF => Bulk Solid Fraction

XN := 11.6 · BSF

$K_{gas} := \text{linterp}(TK_{he}, K_{he}, T_{gap})$        $K_{gas} = 0.4 \frac{\text{W}}{\text{m}\cdot\text{K}}$

$K_{pwr} := \text{linterp}(TK_{bnsng}, K_{bnsng}, T_{gap})$        $K_{pwr} = 46.4 \frac{\text{W}}{\text{m}\cdot\text{K}}$

$$K_{bulk} := K_{gas} \cdot \left[ 0.5 \cdot XN \cdot BSF \cdot \frac{K_{pwr}}{K_{pwr} - K_{gas}} \cdot \left( \frac{K_{pwr} \cdot \ln\left(\frac{K_{pwr}}{K_{gas}}\right)}{K_{pwr} - K_{gas}} - 1 \right) + 0.2146 \right]$$

$K_{bulk} = 2.4 \frac{\text{W}}{\text{m}\cdot\text{K}}$

Equation for  $K_{bulk}$  is based on Hengst-Kaganer formulation for  $K_{eff}/K_{gas}$

$$GBN_{filler} := \frac{2 \cdot \pi \cdot L_{sheath} \cdot K_{bulk}}{\ln\left(\frac{ID_{sheath}}{OD_{heater}}\right)}$$

$GBN_{filler} = 27.2 \frac{\text{W}}{\text{K}}$

$$T_{heater} := \frac{Q_{heater}}{GBN_{filler}} + T_{sheath}$$

$T_{heater} = 1494 \text{ K}$

$$\Delta T_{hs} := T_{heater} - T_{sheath}$$

$\Delta T_{hs} = 220 \text{ K}$

## Gap Heat Transfer Calculations: Conductive gap filler; ceramic liner w/ helium

### Calculate thickness of liner

$$th := 0.8 \cdot \text{radialgap}$$

$$th = 0.046 \text{ in}$$

### Calculate thickness of gaps between liner and heater and liner and sheath

$$\text{gapsmall} := \frac{\text{radialgap} - th}{2}$$

$$\text{gapsmall} = 0.006 \text{ in}$$

$$\text{IDliner} := \text{ODheater} + 2 \cdot \text{gapsmall}$$

$$\text{IDliner} = 0.361 \text{ in}$$

$$\text{ODliner} := \text{ODheater} + 2 \cdot \text{gapsmall} + 2 \cdot th$$

$$\text{ODliner} = 0.454 \text{ in}$$

$$\text{Ghesmallinner} := \frac{2 \cdot \pi \cdot L_{\text{sheath}} \cdot K_{\text{gas}}}{\ln\left(\frac{\text{IDliner}}{\text{ODheater}}\right)}$$

$$\text{Ghesmallinner} = 42.161 \frac{\text{W}}{\text{K}}$$

$$\text{Ghesmallouter} := \frac{2 \cdot \pi \cdot L_{\text{sheath}} \cdot K_{\text{gas}}}{\ln\left(\frac{\text{IDsheath}}{\text{ODliner}}\right)}$$

$$\text{Ghesmallouter} = 54.43 \frac{\text{W}}{\text{K}}$$

$$K_{\text{liner}} := K_{\text{pwr}}$$

$$\text{Glineronly} := \frac{2 \cdot \pi \cdot L_{\text{sheath}} \cdot K_{\text{liner}}}{\ln\left(\frac{\text{ODliner}}{\text{IDliner}}\right)}$$

$$\text{Glineronly} = 653.02 \frac{\text{W}}{\text{K}}$$

$$\text{GBNliner} := \left( \frac{1}{\text{Ghesmallinner} + \text{Gradonly}} + \frac{1}{\text{Ghesmallouter} + \text{Gradonly}} + \frac{1}{\text{Glineronly}} \right)^{-1}$$

$$\text{GBNliner} = 26.277 \frac{\text{W}}{\text{K}}$$

$$\text{Theater} := \frac{Q_{\text{heater}}}{\text{GBNliner}} + T_{\text{sheath}}$$

$$\text{Theater} = 1501 \text{ K}$$

$$\Delta T_{\text{hs}} := \text{Theater} - T_{\text{sheath}}$$

$$\Delta T_{\text{hs}} = 228 \text{ K}$$

$$\text{GBNlinernogas} := \left( \frac{1}{\text{Gradonly}} + \frac{1}{\text{Gradonly}} + \frac{1}{\text{Glineronly}} \right)^{-1}$$

$$\text{GBNlinernogas} = 3.551 \frac{\text{W}}{\text{K}}$$

$$\text{Theater} := \frac{Q_{\text{heater}}}{\text{GBNlinernogas}} + T_{\text{sheath}}$$

$$\text{Theater} = 2963 \text{ K}$$

$$\Delta T_{\text{hs}} := \text{Theater} - T_{\text{sheath}}$$

$$\Delta T_{\text{hs}} = 1690 \text{ K}$$

## Task 1a: effect of sheath on heater temperatures–low power

$$Q_{\text{heater}} := 1000 \text{ W}$$

$$T_c := (50 + 273.15) \cdot \text{K} \quad \text{Temperature of Vacuum Chamber Wall}$$

$$\epsilon_h := .9 \text{ heater emissivity; represents graphite heater type radiative performance}$$

$$\epsilon_c := .2 \text{ chamber wall emissivity; represents clean ss wall}$$

$$ID_{\text{chamber}} := 3 \text{ ft} \quad \text{Approximate interior diameter of vacuum chamber housing heater and sheath}$$

$$\epsilon_s := .2 \text{ sheath interior and exterior emissivity representing bare (clean) stainless, moly or tan}$$

### No sheath configuration

$$E_{hc}(\epsilon_h, \epsilon_c) := \left[ \frac{1}{\epsilon_h} + \frac{1 - \epsilon_c}{\epsilon_c} \cdot \left( \frac{OD_{\text{heater}}}{ID_{\text{chamber}}} \right) \right]^{-1}$$

$$T_{\text{heater}} := \left( \frac{Q_{\text{heater}}}{Asr_{\text{heater}} \cdot \sigma \cdot E_{hc}(\epsilon_h, \epsilon_c)} + T_c^4 \right)^{\frac{1}{4}} \quad T_{\text{heater}} = 1096 \text{ K}$$

### With Polished stainless steel sheath surrounding heater

$$E_{sc}(\epsilon_s, \epsilon_c) := \left[ \frac{1}{\epsilon_s} + \frac{1 - \epsilon_c}{\epsilon_c} \cdot \left( \frac{OD_{\text{sheath}}}{ID_{\text{chamber}}} \right) \right]^{-1}$$

$$T_{\text{sheath}} := \left( \frac{Q_{\text{heater}}}{Asr_{\text{sheath}} \cdot \sigma \cdot E_{sc}(\epsilon_s, \epsilon_c)} + T_c^4 \right)^{\frac{1}{4}} \quad T_{\text{sheath}} = 1422 \text{ K}$$

$$T_{\text{heater}} := \left( \frac{Q_{\text{heater}}}{Asr_{\text{heater}} \cdot \sigma \cdot E_{hs}(\epsilon_h, \epsilon_s)} + T_{\text{sheath}}^4 \right)^{\frac{1}{4}} \quad T_{\text{heater}} = 1742 \text{ K}$$

## Task 1a: effect of sheath on heater temperatures - high power

$$Q_{\text{heater}} := 6000 \text{ W}$$

Same optical properties and chamber temperature conditions

With no sheath

$$T_{\text{heater}} := \left( \frac{Q_{\text{heater}}}{A_{\text{surfheater}} \cdot \sigma \cdot E_{\text{hc}}(\epsilon_{\text{h}}, \epsilon_{\text{c}})} + T_{\text{c}}^4 \right)^{\frac{1}{4}} \quad T_{\text{heater}} = 1712 \text{ K}$$

With Polished stainless steel sheath surrounding heater

$$T_{\text{sheath}} := \left( \frac{Q_{\text{heater}}}{A_{\text{rfsheath}} \cdot \sigma \cdot E_{\text{sc}}(\epsilon_{\text{s}}, \epsilon_{\text{c}})} + T_{\text{c}}^4 \right)^{\frac{1}{4}} \quad T_{\text{sheath}} = 2224 \text{ K}$$

$$T_{\text{heater}} := \left( \frac{Q_{\text{heater}}}{A_{\text{surfheater}} \cdot \sigma \cdot E_{\text{hs}}(\epsilon_{\text{h}}, \epsilon_{\text{s}})} + T_{\text{sheath}}^4 \right)^{\frac{1}{4}} \quad T_{\text{heater}} = 2726 \text{ K}$$

With sheath having modified optical properties

$$\epsilon_{\text{s}} := .7$$

$$T_{\text{sheath}} := \left( \frac{Q_{\text{heater}}}{A_{\text{rfsheath}} \cdot \sigma \cdot E_{\text{sc}}(\epsilon_{\text{s}}, \epsilon_{\text{c}})} + T_{\text{c}}^4 \right)^{\frac{1}{4}} \quad T_{\text{sheath}} = 1638 \text{ K}$$

$$T_{\text{heater}} := \left( \frac{Q_{\text{heater}}}{A_{\text{surfheater}} \cdot \sigma \cdot E_{\text{hs}}(\epsilon_{\text{h}}, \epsilon_{\text{s}})} + T_{\text{sheath}}^4 \right)^{\frac{1}{4}} \quad T_{\text{heater}} = 2057 \text{ K}$$



## Temperature differential across sheath

$$K_{ss} := 28 \frac{\text{W}}{\text{m}\cdot\text{K}}$$

$$K_{nb} := 69 \cdot \frac{\text{W}}{\text{m}\cdot\text{K}}$$

$$ID_{shth} := OD_{heater} + 0.005 \text{ in}$$

$$K_{mo} := 96 \frac{\text{W}}{\text{m}\cdot\text{K}}$$

$$G_{sheath}(K_{sheath}, ID_{shth}) := \frac{2 \cdot \pi \cdot L_{sheath} \cdot K_{sheath}}{\ln\left(\frac{OD_{sheath}}{ID_{shth}}\right)}$$

### Thick sheath

$$\Delta T_{sheathss} := \frac{6000 \text{ W}}{G_{sheath}(K_{ss}, ID_{shth})}$$

$$\Delta T_{sheathss} = 28.2 \text{ K}$$

$$\Delta T_{sheathnb} := \frac{6000 \text{ W}}{G_{sheath}(K_{nb}, ID_{shth})}$$

$$\Delta T_{sheathnb} = 11.4 \text{ K}$$

$$\Delta T_{sheathmo} := \frac{6000 \text{ W}}{G_{sheath}(K_{mo}, ID_{shth})}$$

$$\Delta T_{sheathmo} = 8.2 \text{ K}$$

### Thin Sheath

$$\Delta T_{sheathss} := \frac{6000 \text{ W}}{G_{sheath}(K_{ss}, ID_{sheath})}$$

$$\Delta T_{sheathss} = 10 \text{ K}$$

$$\Delta T_{sheathnb} := \frac{6000 \text{ W}}{G_{sheath}(K_{nb}, ID_{sheath})}$$

$$\Delta T_{sheathnb} = 4.1 \text{ K}$$

$$\Delta T_{sheathmo} := \frac{6000 \text{ W}}{G_{sheath}(K_{mo}, ID_{sheath})}$$

$$\Delta T_{sheathmo} = 2.9 \text{ K}$$

## APPENDIX I—SINDA RESULTS: TEMPERATURE PROFILES

SINDA heater simulation results are shown in table 17.

Table 17. Summary of results from SINDA heater simulation (temperatures are given in Kelvin).

Case	Cu Lead		Mo Transition		Heater Element		Sheath		Comments
	Min	Max	Min	Max	Min	Max	Min	Max	
Case 1	778	1,069	1,107	1,475	1,468	1,471	1,348	1,349	1 kW; *PPF=1
Case 2	778	1,085	1,126	1,547	1,545	1,813	1,362	1,417	3 kW; PPF=1.33
Case 3	778	1,119	1,165	1,707	1,709	1,712	1,394	1,395	3 kW; PPF=1
Case 4	778	1,122	1,168	1,720	1,723	2,153	1,398	1,508	6 kW; PPF=1.33
Case 5	778	1,176	1,232	1,985	1,993	2,001	1,462	1,464	6 kW; PPF=1
Case 6	332	1,121	1,168	1,720	1,723	2,153	1,398	1,508	6 kW; PPF=1.33; cooled lead end

\* PPF corresponds to the peak to average power peaking factor.

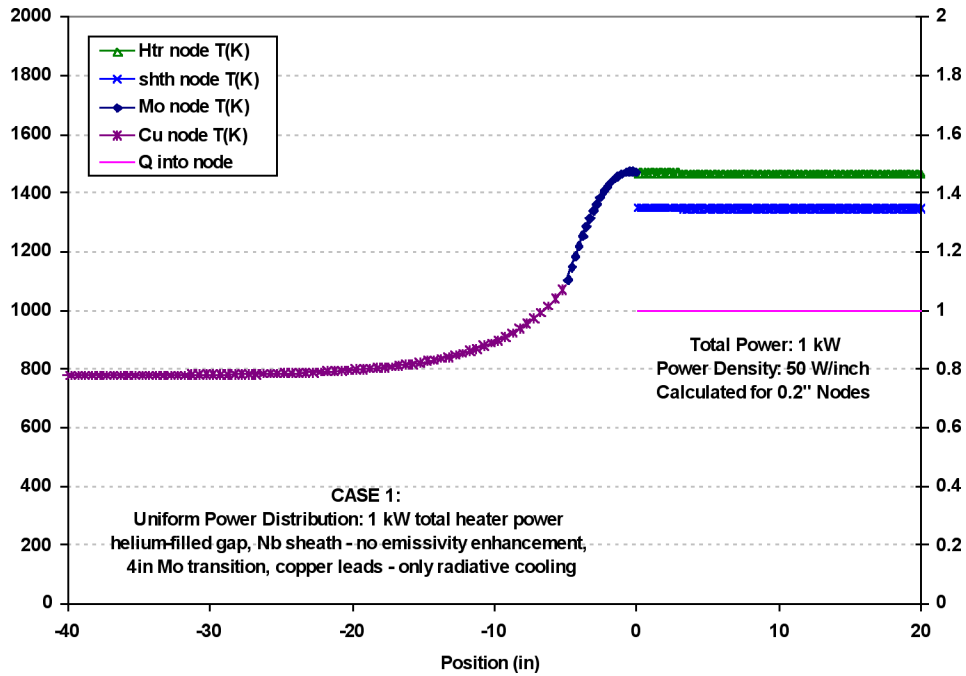


Figure 77. Axial temperature profile for case 1.

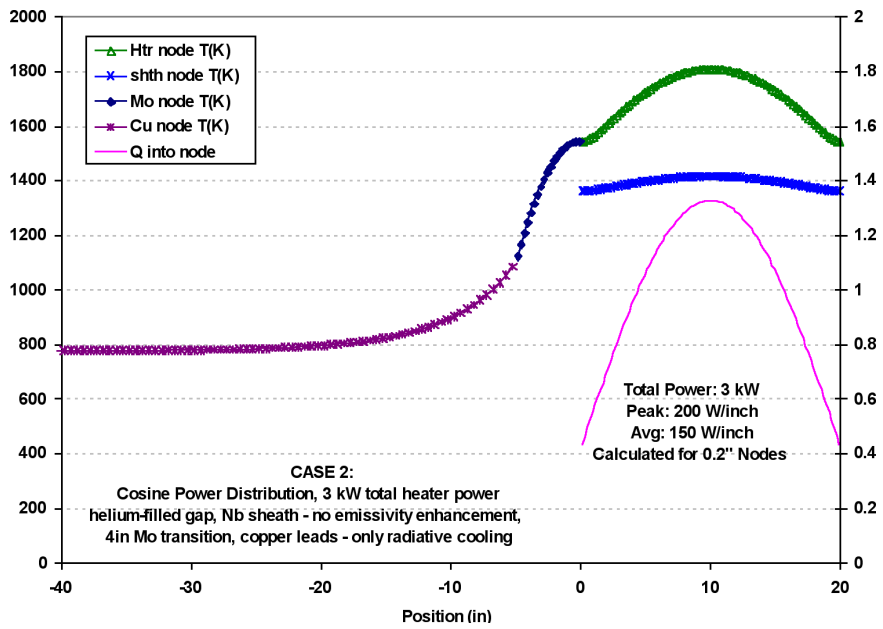


Figure 78. Axial temperature profile for case 2.

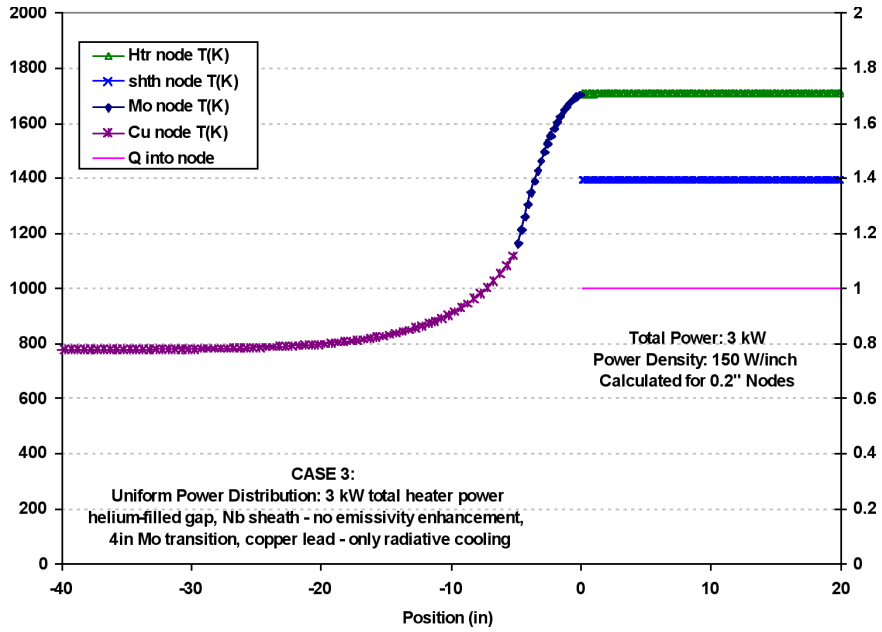


Figure 79. Axial temperature profile for case 3.

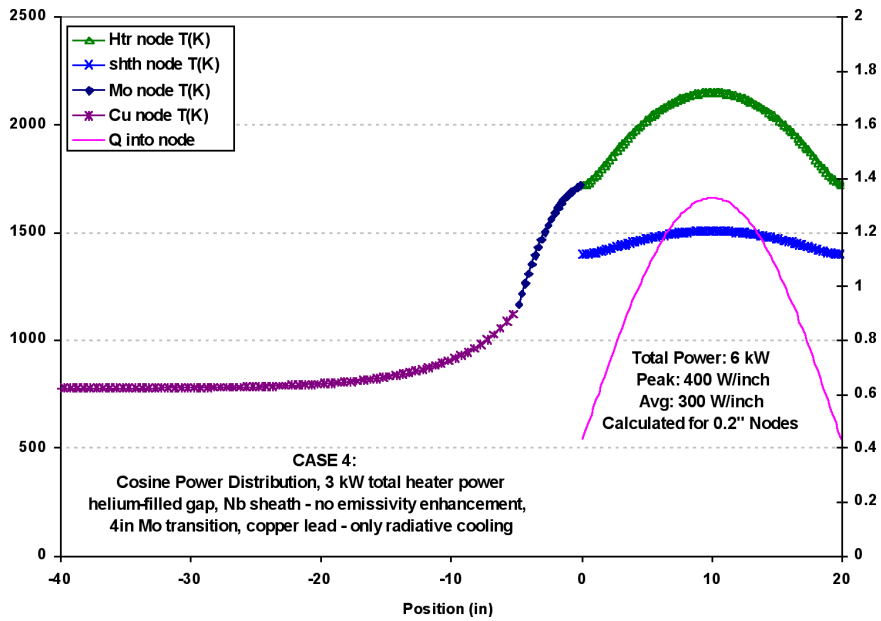


Figure 80. Axial temperature profile for case 4.

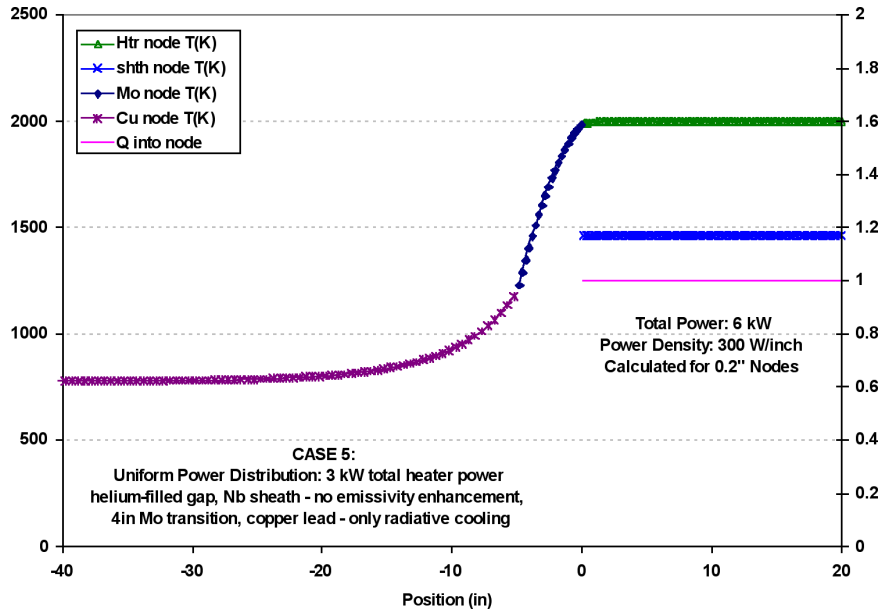


Figure 81. Axial temperature profile for case 5.

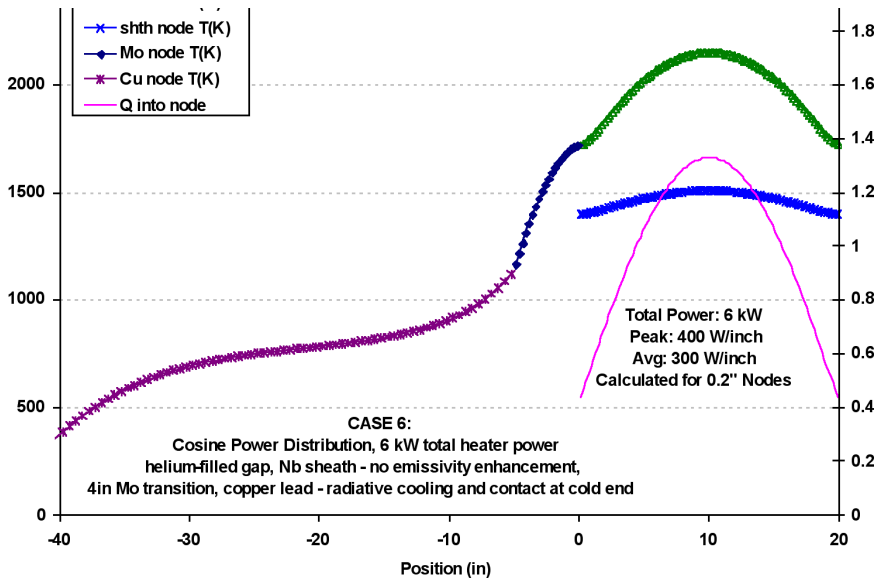


Figure 82. Axial temperature profile for case 6.

## APPENDIX J—THERMAL ANALYSIS: CALORIMETER

### Thermal Analysis of the Cold Wall Calorimeter and Proposed Sheath Instrumentation for Fuel Pin Thermal Simulator Testing

#### Abstract

In order to perform high power testing of the fuel pin thermal simulator concepts, a cold wall calorimeter was designed and constructed. This cold wall calorimeter was intended to remove a large amount of heat (~6000 W) from a single simulator while maintaining the simulator temperature at levels more representative of actual-use conditions in an electrically heated reactor core array. The calorimeter is also designed to allow for improved instrumentation in single element testing, necessary to determine element temperature at various positions and to measure the total heat removal by the calorimeter. While preliminary thermal analyses were considered in this design, a more detailed thermal analysis of the as-built design was required to verify the operation of the calorimeter and to determine operating ranges and thermal behavior in different ambient conditions. The analysis data will be compared to test data to correlate the model for use in other simulator analyses. An additional analysis was performed in an attempt to quantify the conduction error inherent in the compression-based thermocouples intended to measure the temperature of the simulator external sheath surface.

#### Calorimeter and Thermal Model Description

The calorimeter is composed of a primary large diameter copper tube (ID = 0.68", OD = 0.75", Length = 24"), surrounded by six coiled copper tube water loops, and associated instrumentation. Each of these water loops is connected in parallel to a central water supply loop. The loops are helically wrapped around the primary tube with spacing between the loops to allow both thermocouple and optical pyrometer access to the fuel pin simulator sheath through small holes in the primary tube. The coils are not physically attached to the primary tube but are wrapped to minimize the gap between each coil and the primary tube outer diameter. There is limited contact between the coiled loops and the primary tube, but the amount of contact (contact area and pressure) is not controlled nor has it been quantified.

The analysis model consists of both hydraulic and thermal elements. The hydraulic element serves to estimate the distribution of mass flow and the ensuing temperature increase in water that flows in each coil as it removes heat from the portion of the primary tube (or cold wall) to which that coil is thermally coupled. The hydraulic element consists of sets of fluid nodes and paths representing each coil in addition to supply and return lines and a mass flow source. There are also thermal ties associated with each fluid node and the adjacent thermal node to determine the amount of heat that is convected away from the surface by each node in the water circuit. The



thermal element consists of sets of thermal nodes and connecting conductive and radiation conductors that represent the following components: copper tubing in the water lines and primary tube, molybdenum fuel pin simulator sheath, graphite rod heater, and associated alumina spacers that electrically isolate the graphite from the sheath.

The thermal model considers the convective heat transfer from the cold wall to the water loops, conductive heat transfer within the various solid components, conductive heat transfer across any narrow gas gaps and radiative heat transfer between components and to the environment. The ambient conditions considered pure helium gas, pure argon gas and vacuum. Appropriate constant and temperature dependent material properties (e.g. thermal conductivity and total emissivity) were included in the model. While density and specific heat were also included in the model, only steady state analyses were performed.

The thermal and hydraulic model, shown in figure 83, was created using Thermal Desktop (by Culimore and Ring). Only the primary tube and the fluid circuit are shown; all other components are located concentrically within the cold wall. The blue arrows in the figure represent the fluid path, and each arrow adjacent to the cold wall represents one loop around the cold wall. The radiative exchange calculations were performed using RADCAD, a module of Thermal Desktop, and were incorporated into the thermal/hydraulic solution computed by SINDA/FLUINT.

Figures 84–87 provide typical contour results for the cold wall, sheath and heater for the case of a helium environment, a heater power of 6000 W, and a total cooling water mass flow rate of 5 gal/min. A more quantitative depiction of the results for this case is provided in figure 88.

The model assumes an inlet water temperature of 293 K (20 °C). The outlet water temperature from each branch is slightly different, as indicated by the contours applied to the fluid nodes in figure 85. After all branches merge, however, the temperature of the water flow return is approximately 317.7 K (24.7 °C). The cold wall contour is provided here for reference; its scale is not shown in figure 85 but is identical to that shown in figure 84.

Banding is seen in the cold wall temperature profiles in both the contour plots (fig. 84–87) or the quantitative x-y plot (fig. 88). This characteristic results from the spacing between coils where no direct cooling is applied to the cold wall. This is the area where small holes are placed in the cold wall for the sheath thermocouples and optical pyrometers. The heat received from the sheath in these ‘uncooled’ regions conducts axially to the nearest cooled portions of the primary tube where it is removed by the water flow. The effect of this banding on the sheath and heater temperature profiles appears to be negligible.

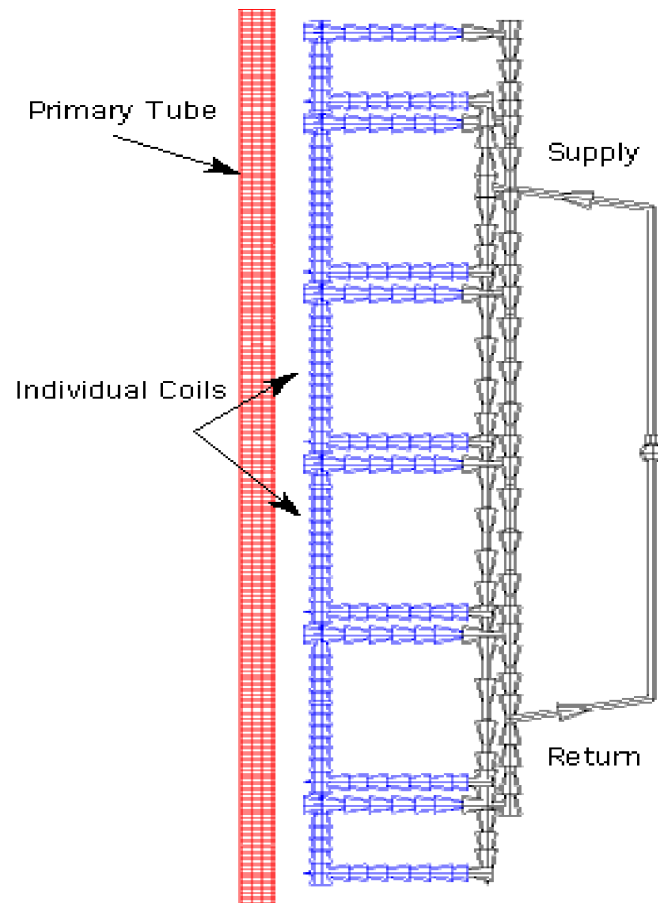
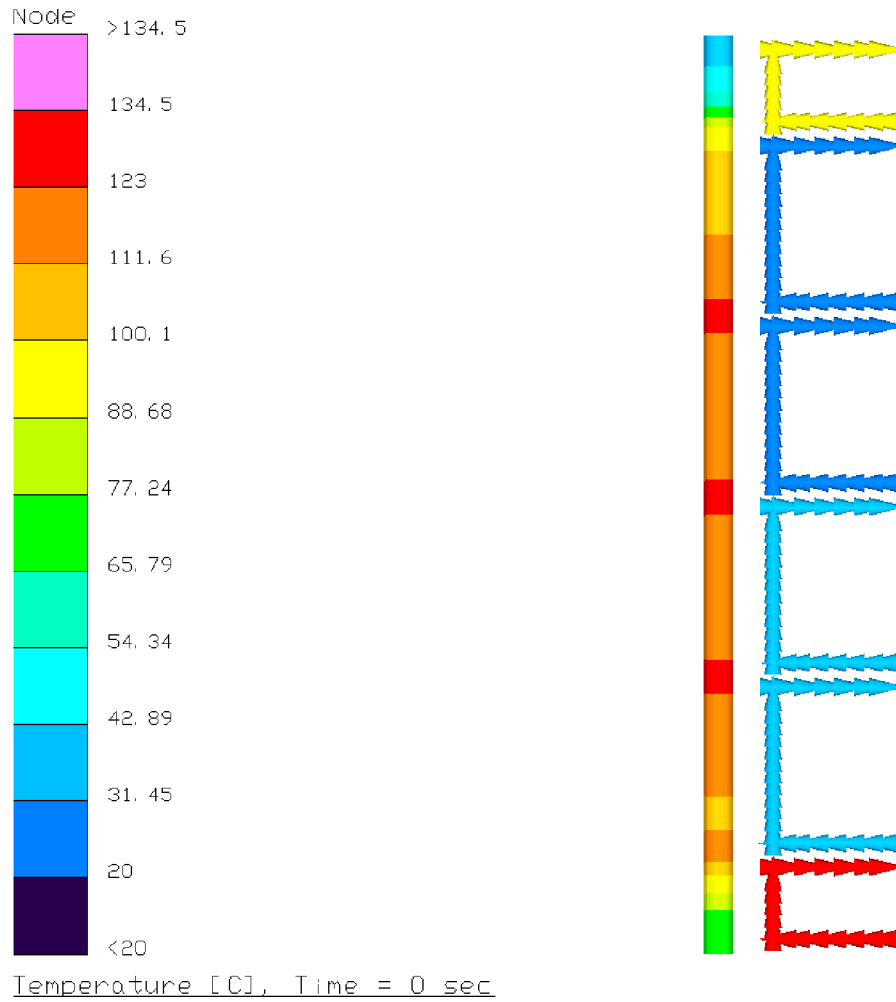


Figure 83. Cold wall/calorimeter primary tube and fluid circuit.



*Note: The colors applied to the fluid paths represent flow rate (scale not provided).*

Figure 84. Predicted cold wall temperatures for the case of 6,000 W, He atmosphere, 19 L/min (5 gal/min) water flow.

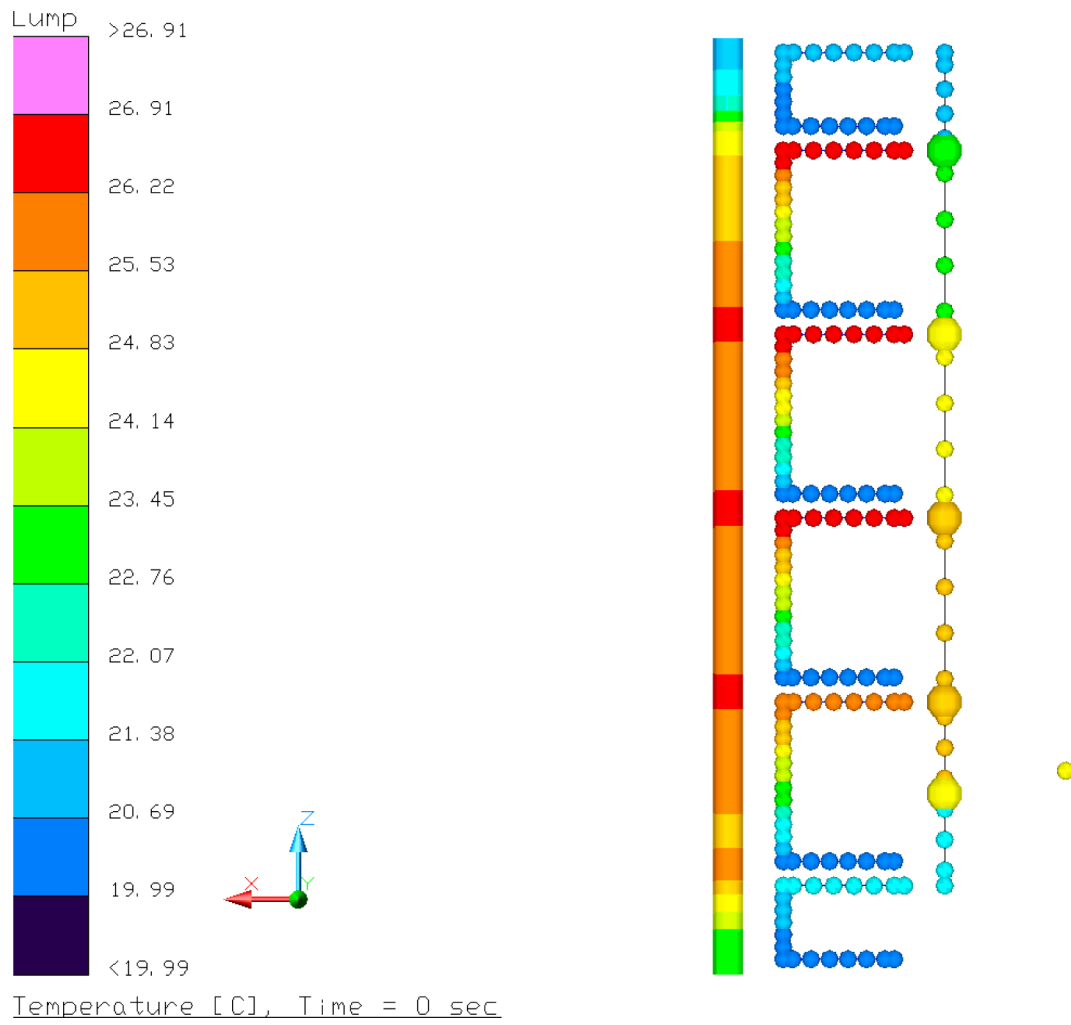


Figure 85. Water temperatures for the case of 6,000 W, He atmosphere, 19 L/min (5 gal/min) water flow.

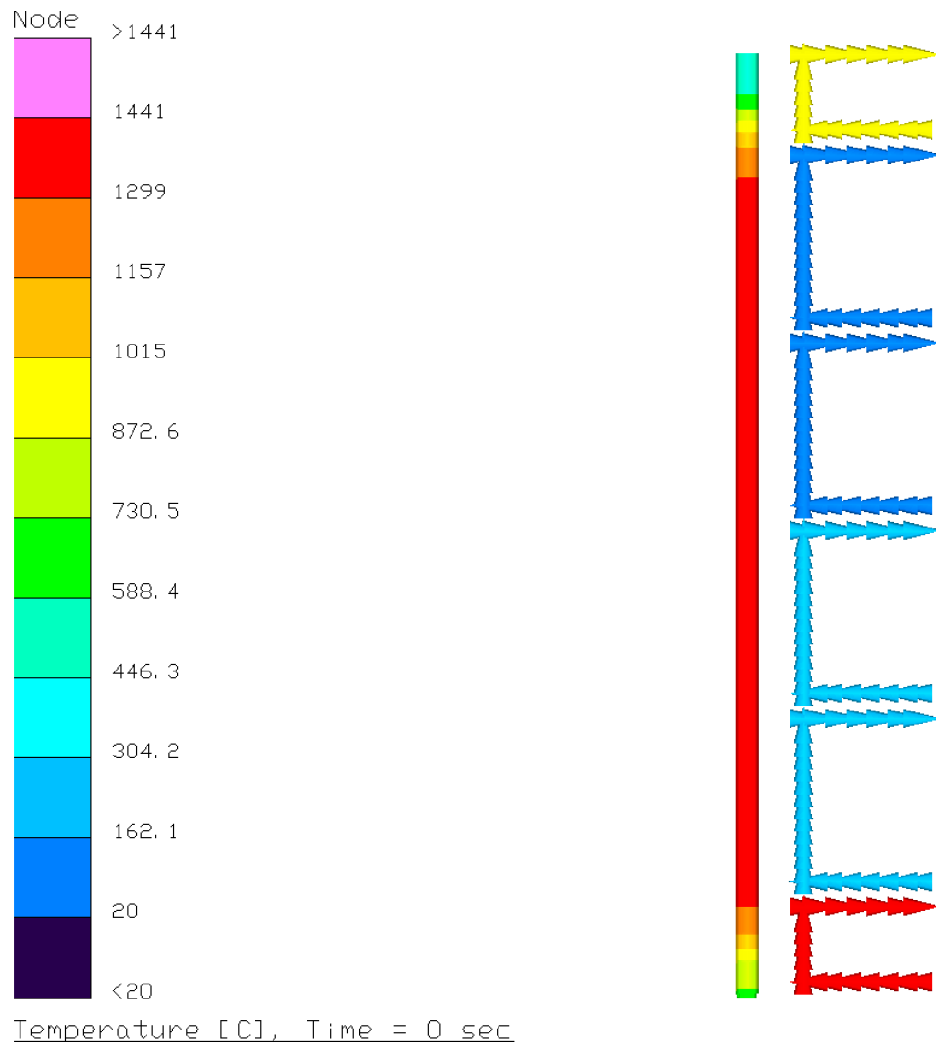


Figure 86. Sheath temperature profile for the case of 6,000 W, He atmosphere, 19 L/min (5 gal/min) water flow.

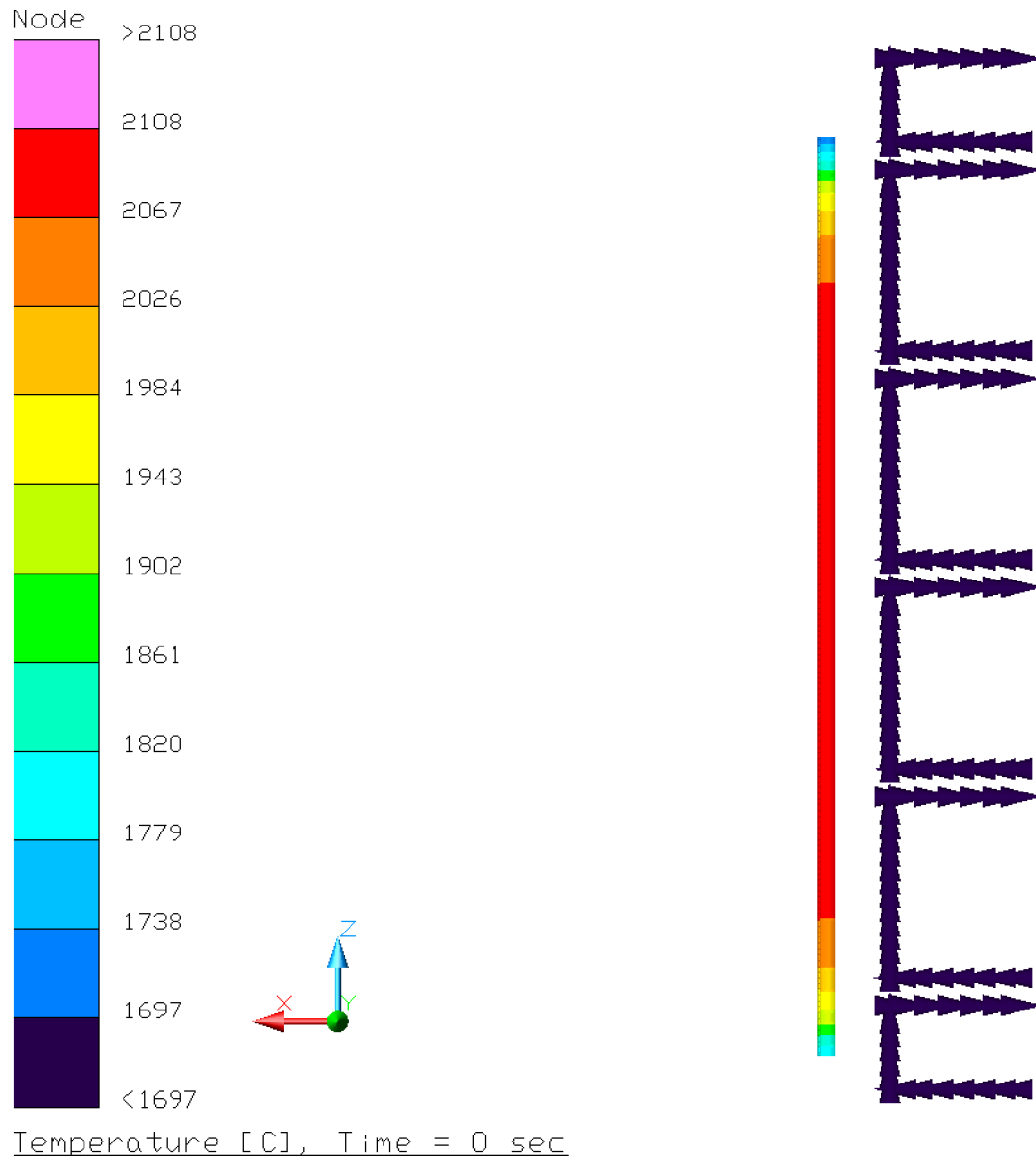


Figure 87. Heater temperature profile for the case 6,000 W, He atmosphere, 19L/min (5 gal/min) water flow.



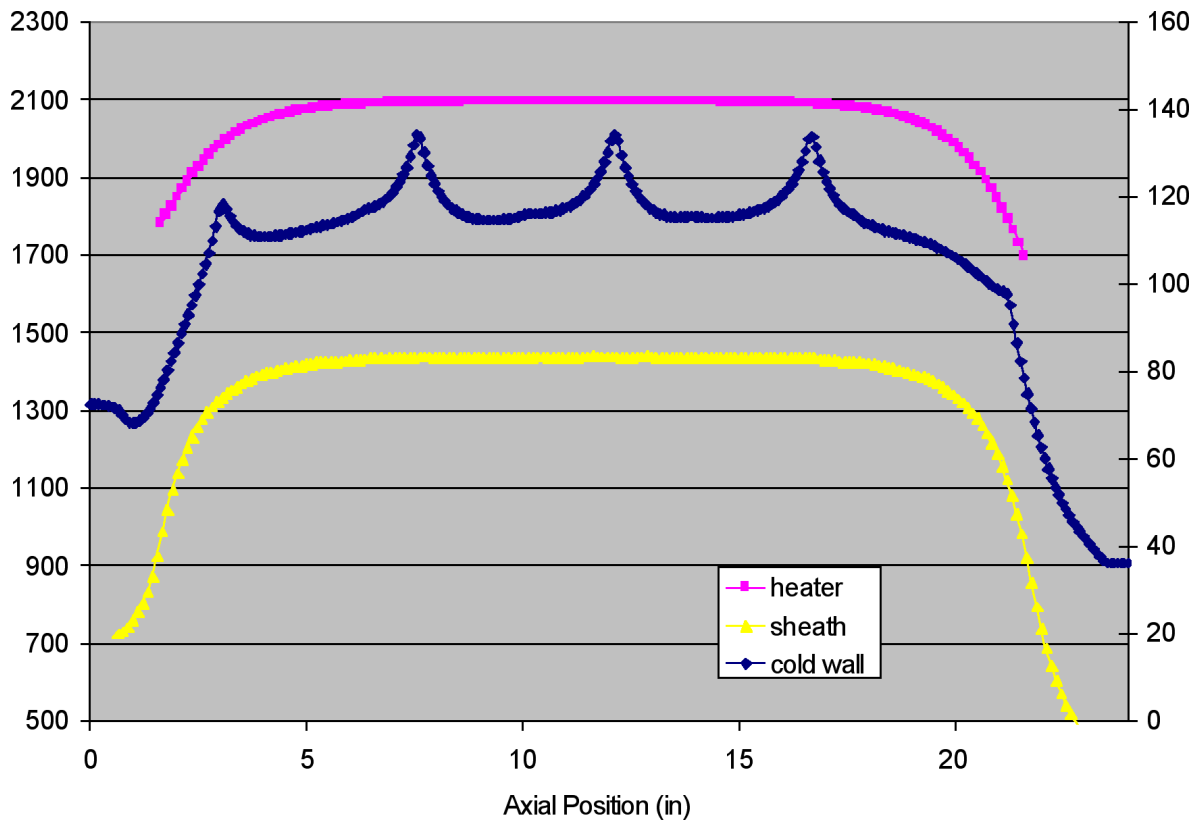


Figure 88. Temperature vs. axial position for the sheath, heater, and cold wall for the case of 6,000 W, He atmosphere, 19L/min (5 gal/min) water flow. (Axial position is the position along the longitudinal axis of the heater/sheath and zero represents the end of the cold wall.)

Table 18 contains a comparison of predicted temperatures for the three different ambient conditions (He, Ar, or vacuum), three heater power levels, and three total cooling water flow rates. Results for the argon and vacuum conditions at 6,000 W heater power indicate excessive heater and sheath temperatures, as well as elevated cold wall temperatures. These temperature estimates may be conservative in that the cold wall (and, in turn, the sheath and the heater) is coupled to the cooling coils primarily by gas gap conduction and radiation; i.e. negligible metal-to-metal contact conductance is modeled between the cooling coils and the primary cold wall. Consequently, when the gap is filled with a low conductivity gas such as argon or a vacuum exists, the conductance between the primary tube and cooling tubes is small or nonexistent. The assumption of minimal metal-to-metal contact may be overly conservative as there is probably some contact between the coils and the primary tube. This contact can be estimated from early testing and results and implemented into the thermal model which can then be used to revise the predicted temperatures. If the assumption of poor or no contact is found to be valid through initial testing, it may be advisable to improve the coupling between the cooling coils and primary tube. In the original calorimeter design, the cooling coils were brazed to the primary tube to enhance this conductance. Early attempts to apply this braze were inconsistent and unrepeatable. Additional

development may still be necessary. Alternatively, a thermally conductive glue (e.g. Ecco bond) or vacuum compatible thermal grease (e.g. arctic alumina or other) could be applied in the gap between the coils and primary cold wall to improve this coupling and lower cold wall, sheath and heater temperatures.

Table 18. Comparison of temperatures for various atmospheres and conditions.

Configuration/Conditions			Heater Temperature		Sheath Temperature		Cold Wall Temperature		Water Temp	Branch Flow Rate	
Ambient Condition	Heater Power (W)	Total Flow Rate (gal/min)	Tmax (°C)	Tmin (°C)	Tmax (°C)	Tmin (°C)	Thot (°C)	Tcold (°C)	Tmax (°C)	Max (gal/min)	Min (gal/min)
Helium	6,000	5	2,108	1,697	1,441	450	135	36	27	1.134	0.676
Argon	6,000	5	3,810	3,095	2,991	1,855	539	240	27	1.134	0.676
Vacuum	6,000	5	4,141	3,441	3,395	2,350	1,511	967	26	1.135	0.676
Helium	1,000	5	632	534	408	161	41	24	21	1.136	0.677
Argon	1,000	5	1,948	1,674	1,431	968	141	81	21	1.136	0.677
Vacuum	1,000	5	2,534	2,162	2,062	1,630	849	639	21	1.136	0.677
Helium	6,000	1	2,113	1,699	1,448	454	150	39	56	0.223	0.136
Helium	1,000	1	634	536	410	161	43	24	26	0.225	0.137
Vacuum	500	3.5	2,078	1,806	1,680	1,389	657	524	20.4	.827	.476

Model results indicate that at a heater power of 6,000 W, the calculated sheath temperatures still slightly exceed the maximum target temperature of 1,700 K (1,427 °C) even when high conductivity helium is used to fill the gaps between the primary tube and the sheath. This precludes the possibility of ‘tunability’ to achieve a specific sheath temperature below 1,700 K (1,427 °C). If lower sheath temperatures are required at the higher power settings, then additional cooling techniques or higher conductivity gap fillers will be needed. Alternatively, shrinking the gas gap between the primary tube and sheath would increase the conductance between the sheath and the primary tube, resulting in the possibility for lower sheath temperatures. Further, an increased axial conductance down the cold wall would decrease temperature banding in the results. To achieve both of these enhancements, a thicker walled tube with same outer diameter could be used. The tube used to assemble the current calorimeter was the thickest available off-the-shelf when the system was assembled; a thicker primary tube may require a customized order or may require the adoption of a variety of approaches to fabricate a cold wall for this application.

## APPENDIX K—THERMOCOUPLE THERMAL ERROR ANALYSIS

### L.1 Thermal Model

The primary purpose of the development of the thermocouple thermal model was to evaluate the potential error associated with spring loaded thermocouples, similar to those depicted in figure 14, employed in the calorimeter to measure sheath surface temperature. While thermocouple error can result from a number of causes, this modeling and analysis effort focuses on those factors that affect how close the thermocouple bead temperature is to the temperature of interest: that of the sheath surface.

In order for the bead temperature to closely resemble the sheath surface temperature, the bead must be closely thermally coupled to the surface of interest and uncoupled from the surroundings as much as possible. Therefore the thermal model considers these two key aspects: the contact conductance between the thermocouple bead and the sheath surface and the heat losses from the bead to other parts of the thermocouple and the surroundings.

The contact and the associated thermal contact conductance between the bead and the sheath surface depend on a number of characteristics. Key characteristics include the contact force and area (i.e., contact pressure), the relative hardness and roughness of the contacting surfaces, thermal conductivity of both the bead and sheath surface materials and the presence and properties of any intervening media (gas, liquid, etc.) between the two contacting surfaces. Typically, the contact conductance increases as the contact pressure increases, the materials become softer and smoother, or the materials on either side of the interface become more conductive. The presence of a gas such as air or helium can also significantly increase the contact conductance. The compilation of these parameters makes it very difficult to predict the contact conductance. Therefore, the analysis presented here considers a number of cases in an attempt to bound the estimated error. The conductance values are provided in table 19. The conductances for cases B and D were based on a 5 MPa contact pressure (an estimated 1.0 N contact force) and bead contact area of  $\approx 0.2 \text{ mm}^2$  in addition to the conditions stated in the table. The other conditions were included as bounding cases. All values of the contact coefficient were obtained from empirical data found in Manglik (1984); the associated contact conductances were derived by dividing the contact area by the contact coefficient.

Table 19. Bounding contact coefficient and conductance between TC bead and sheath surface.

Case	Contact Configuration	Contact Coefficient ( $^{\circ}\text{C}^2/\text{KW}$ )	Conductance ( $\text{W}/^{\circ}\text{C}$ )
A	High resistance	1	0.0002
B	Nickel on stainless steel (vacuum)	0.6	0.0003378
C	Medium resistance	0.1	0.002
D	Aluminum on Aluminum (air)	0.05	0.004054
E	Low Resistance	0.01	0.02

In the case of the spring loaded K type thermocouples, the thermocouple bead consists predominately of nickel and the sheath has, thus far, typically consisted of molybdenum. Because molybdenum is more conductive and is similar to or softer than stainless steel, the contact conductance should be higher than that in case B. However, both nickel and molybdenum are harder and less conductive than aluminum, so the conductance will likely be less than that in case D (a helium ambient environment might raise the conductance a bit compared to that of air). As there is an appreciable amount of scatter in the empirical data in Manglik (1984) and since the exact conditions of bead and sheath surface contact are unknown, it is important to keep in mind that these are only estimates. In addition, since the potential exists to operate the calorimeter in different ambient gases, the contact conductance for this spring loaded thermocouple may vary. Finally, while it may be tempting to apply more contact force to increase the contact pressure and the associated contact conductance, excessive force can be applied that can buckle or break the exposed lead wire or bead connections. None the less, the 1N force used to obtain these numbers was only an estimate of that force actually applied by the spring, and improvements in contact conductance could be realized if the actual force was or could safely be made higher than this value.

The thermal losses to the surroundings and along the thermocouple leads were modeled using a geometric thermal model that considers solid conduction and surface radiation. The full model, as is apparent from figures 89–91, consists of a sheath wall held constant at 1,441 °C, the cold wall held constant at 135 °C, and a representative thermocouple that contacts the sheath and passes through the cold wall. The thermocouple is in turn composed of a bead, an exposed wire lead section, a long metallic sheathed lead section, a spring section and a plastic connector. Heat is exchanged between the thermocouple sheath via a contact conductance, as listed in table 19, as well as by radiation; heat is also exchanged between the thermocouple and the cold wall and the surrounding ambient environment via radiation.

## **L.2 Predicted Thermocouple Error**

Figures 89–91 depict contour plots showing temperatures for the highest conductance case considered (case E). Figure 89 shows the complete mode and figures 90 and 91 show successively zoomed in shots to provide a closer view at the exposed lead and contact regions. A temperature scale is provided for reference.

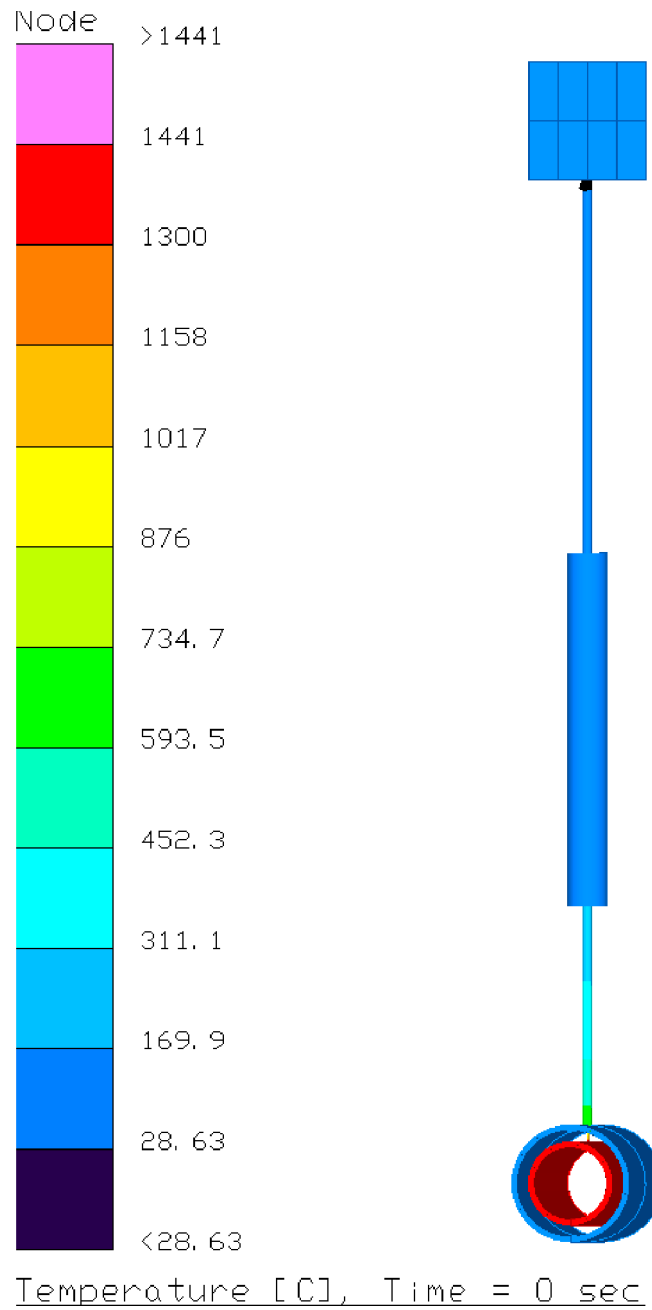


Figure 89. Temperature profile for TC error model; temperature profile corresponds to a bead contact conductance of  $0.02 \text{ W/}^\circ\text{C}$ .

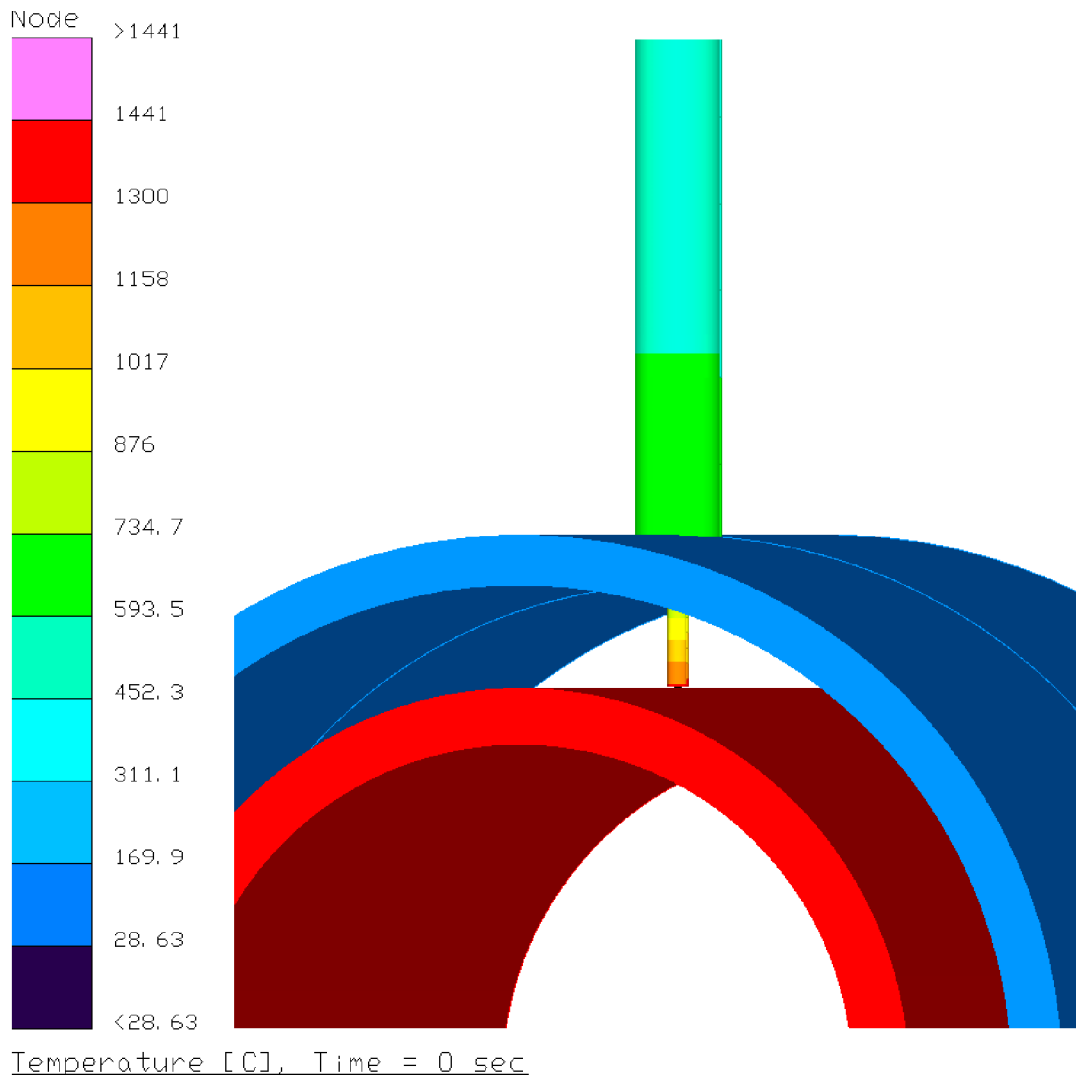


Figure 90. Close-up view of exposed TC wires in vicinity of the sheath and primary tube cold wall; temperature profile corresponds to a bead contact conductance of  $0.02 \text{ W/}^\circ\text{C}$ .



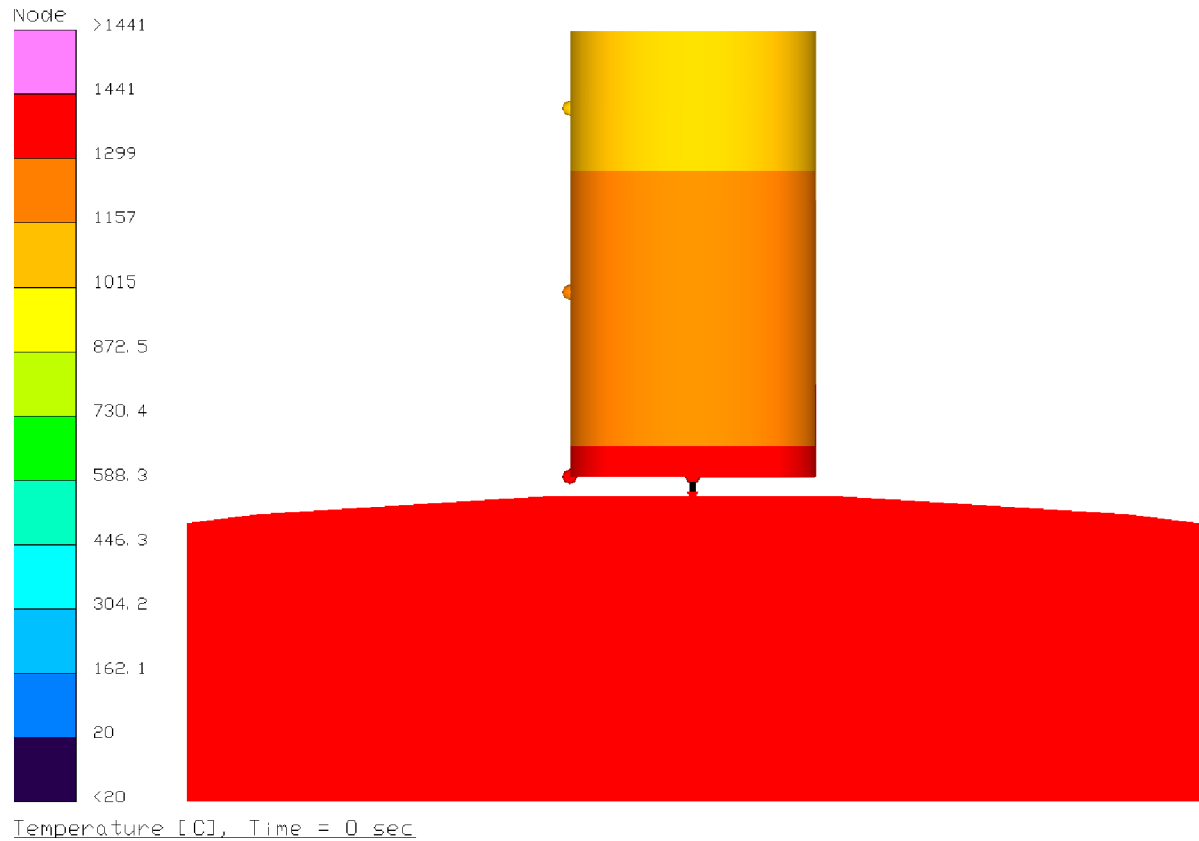


Figure 91. Close-up view of conductor between the TC bead and sheath wall; temperature profile corresponds to a bead contact conductance of  $0.02 \text{ W}/^\circ\text{C}$ .

Figure 92 summarizes the percent error in temperature for the various conductance cases. The percent error calculation technique is shown on the figure.  $T_{bead}$  is the temperature calculated for the thermal node on the wire closest to the sheath surface. As can be seen from the summary data, the temperature error can vary quite a bit for the range of conductance values evaluated. For example, the predicted error varies from near 60% for case B to less than 20% for case D.

Based on this information, a means for improving the overall conductance and the certainty of that conductance needs to be considered to avoid the ambiguity that might result from using this configuration of thermocouple contact and to improve the overall usefulness and reliability in sheath temperature instrumentation.

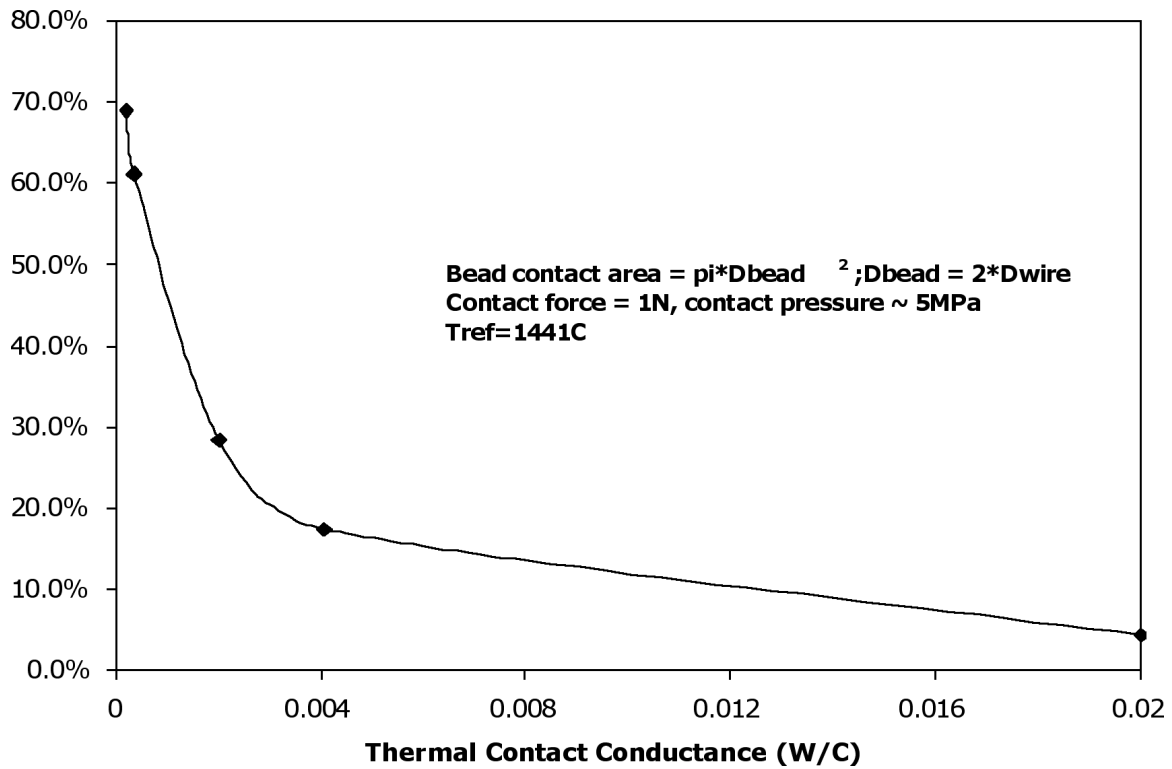


Figure 92. Comparison of TC error versus bead contact conductance.

### References

Manglik, R. (technical editor), "Imperfect Metal-to-Metal Surface Contact (May 1991 Update)," *Heat Transfer Data Book*, Section 502.5, Genium Publishing Corporation, 1984.

## APPENDIX L—DESIGN DRAWINGS: MODIFIED POWER INTERFACE

Figures 93–97 show design drawings for the modified power interface.

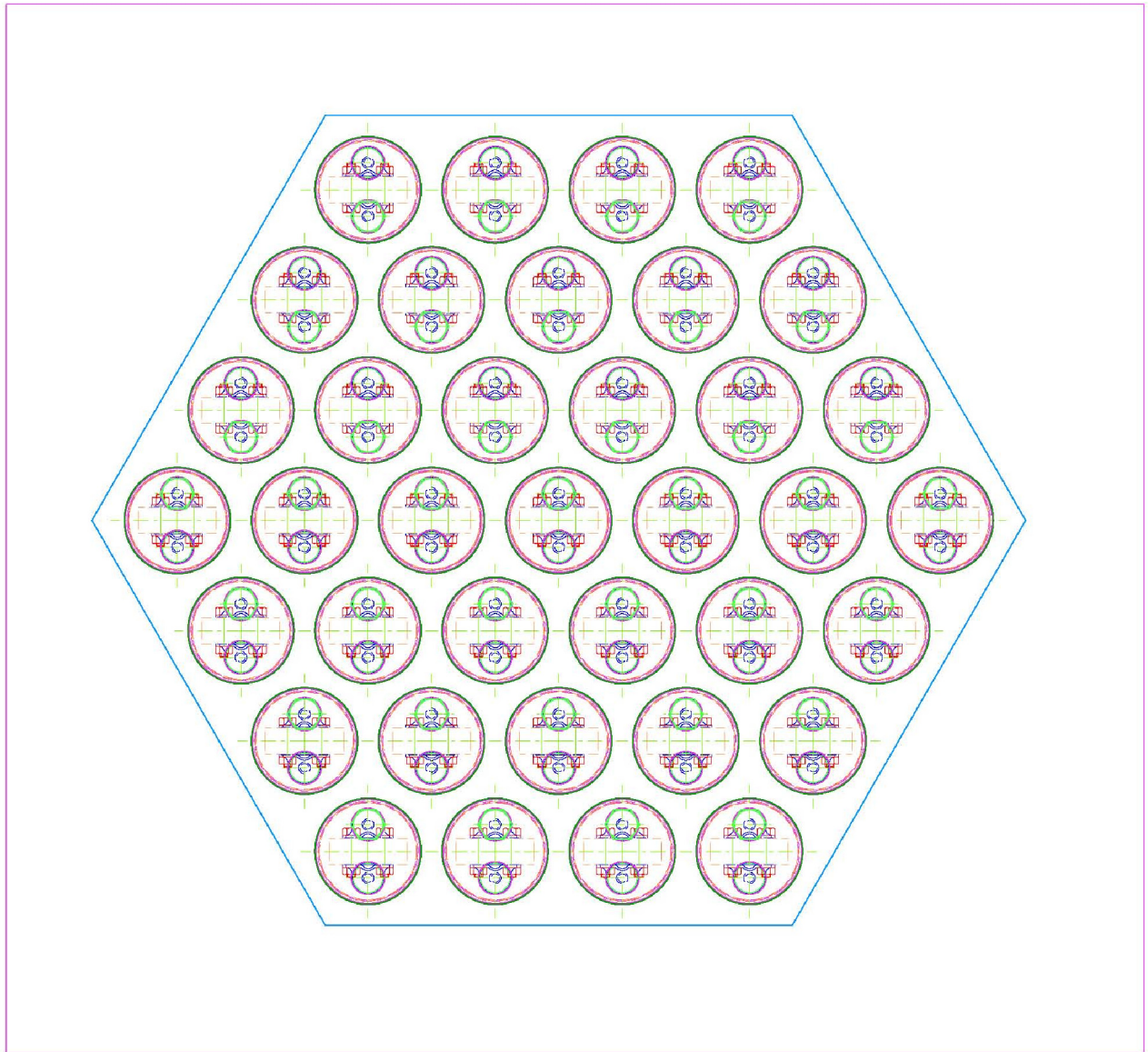


Figure 93. Cross-sectional view showing heater element pin formation for modified power interface.

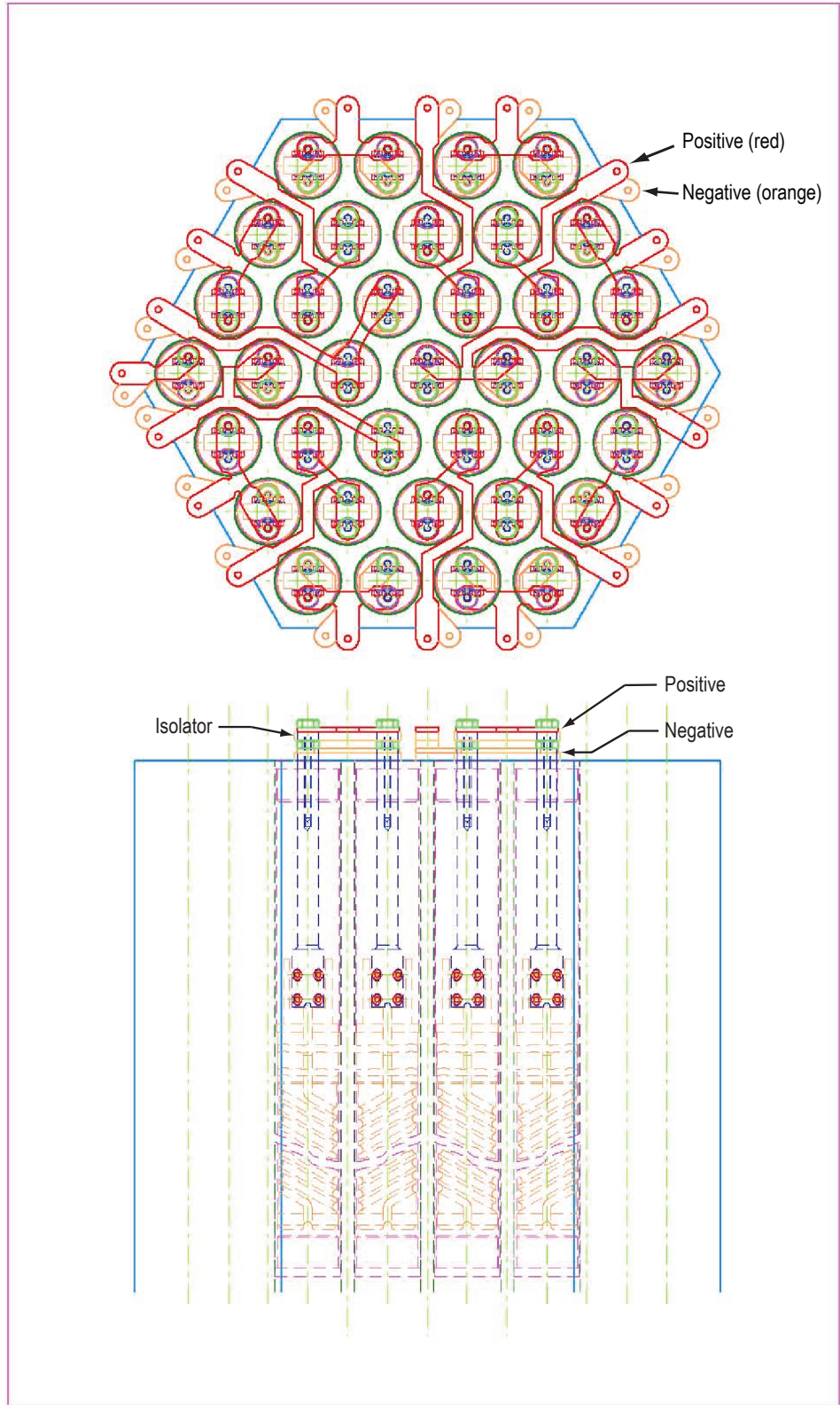


Figure 94. Modified (conceptual) power interface showing positive and negative leads to heater element power terminals.

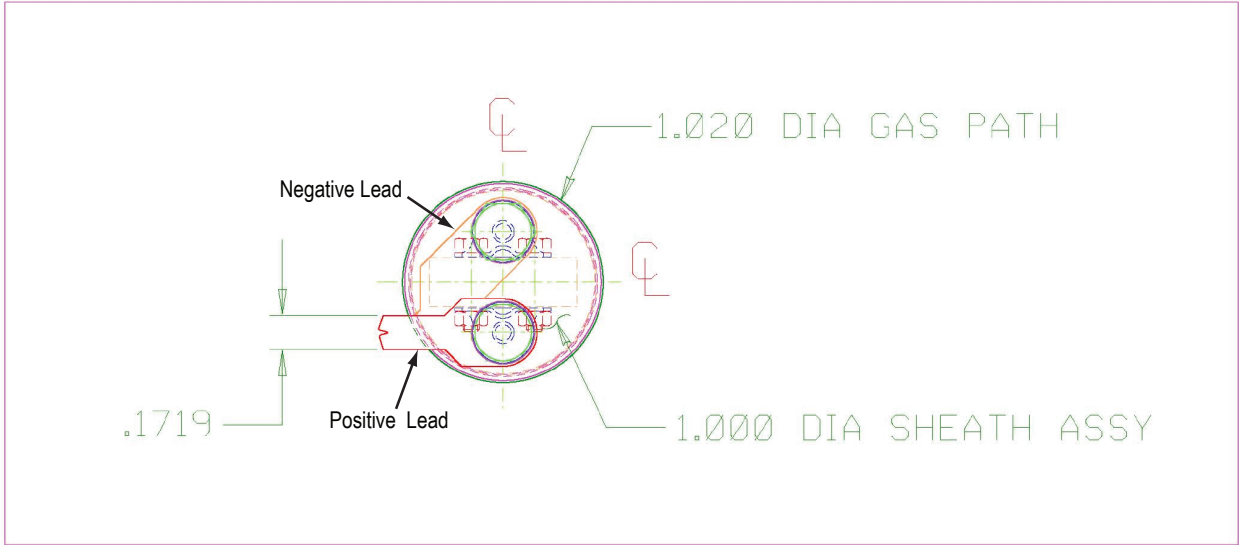


Figure 95. Modified power terminal connections for a single pin.

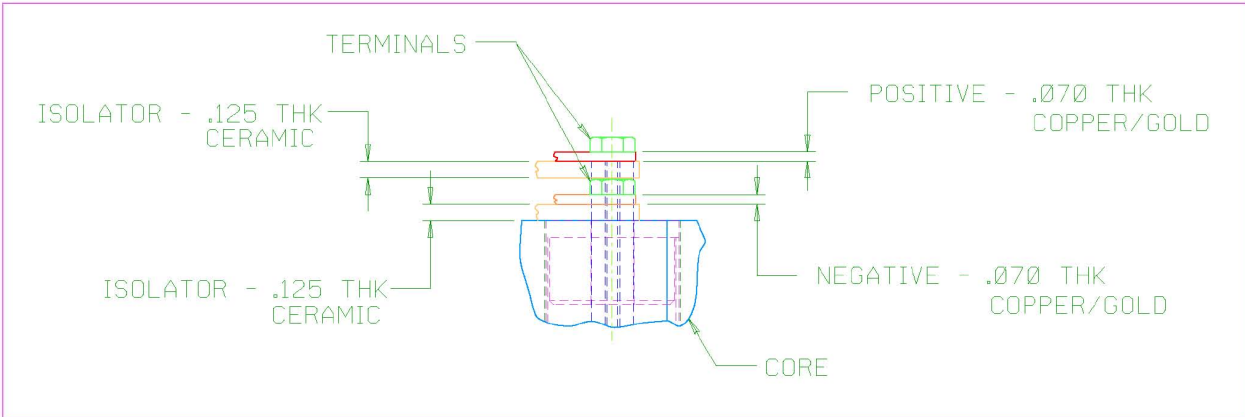


Figure 96. Modified power terminal connections for a single pin; axial view.

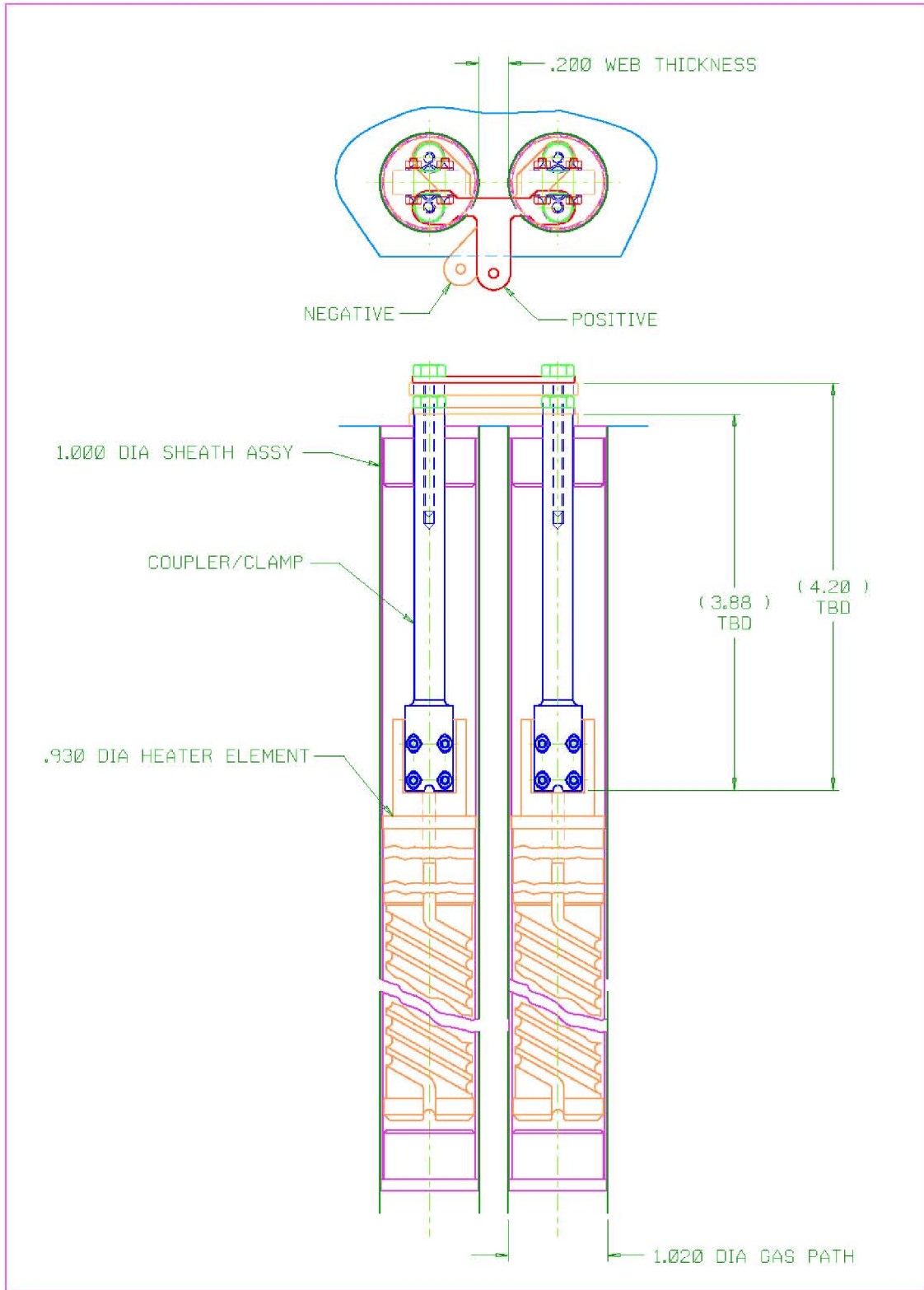


Figure 97. Modified power interface conceptual design showing series connection between neighboring pins.



## APPENDIX M—BASIC MATERIAL CLEANING PROCEDURES

All components that will be used in the heater assembly and test chamber should be cleaned prior to initial checkout testing and prior to integration with any reactor test article. The following steps outline the basic approach to cleaning various materials that may be used in these components. In all procedures, the terms ‘wash’ and ‘rinse’ constitute full immersion in fluid. The procedures differentiate between simple cleaning (to remove oil, dirt and grease) and pickling. During the pickling process, contaminant metals, especially low melting point metals, are removed. In this case, the cleaning process will include an additional immersion in aqua regia. The more aggressive aqua emporis ( $\text{Hf}/\text{HNO}_3$ ) immersion should not be necessary and is not as desirable, as it actually removes some of the prime metal. The proposed procedures are employed by Applied Methods and Materials in handling by stainless steel and refractory metal heat pipe components and should be applicable to the heater assembly components.

### Basic Cleaning Procedure – All Metals

This Basic Cleaning procedure is to be used for parts requiring minimal cleaning (e.g. freshly machined parts with light contamination). *Note: This should not be taken to preclude the requirement for acid pickling if specified.*

1. Wash in Freon, acetone or approved substitute until all signs of oil /grease contaminants have been removed.
2. Wash in hot Tri-sodium phosphate solution.
3. Soak in solution of caustic cleanser (11 parts de-ionized water, 1 part NaOH, 1 part hydrogen peroxide).
4. Flush in hot distilled water.
5. Repeat step 2 three times.
6. Rinse piece for 5 minutes in hot distilled de-ionized water inside an ultrasonic cleaner.
7. Rinse piece for 5 minutes in distilled water using ultrasonic vibration.
8. Rinse piece for 5 minutes in ethanol using ultrasonic agitation.

## Stainless Steel Cleaning Procedure

This procedure applies to austenitic stainless steel in the as-milled condition. It may be used for screen and wire cloth for heat pipes, tubing, plate, and other forms of material that although machined in part, contain surfaces in the as-milled condition.

1. Wash part in Freon TF in an ultrasonic cleaner for at least 5 minutes to remove all signs of grease.
2. Wash part in ultrasonic cleaner containing a caustic solution consisting of 11 parts (by volume) de-ionized water, 1 part sodium hydroxide, and 1 part hydrogen peroxide for up to 5 minutes.
3. Wash part in hot de-ionized water for at least 5 minutes.
4. Repeat Steps 2 and 3 three times.
5. Wash part in hot de-ionized water in ultrasonic cleaner for at least 5 minutes.
5. Wash part in ethanol in ultrasonic cleaner for at least 5 minutes.
6. Proceed to vacuum baeout; establish a pressure of  $10^{-6}$  torr and a temperature  $50\text{ }^{\circ}\text{C}$  over the maximum operating temperature, baeout for a minimum of 3 hours.

## Nb-1%Zr Cleaning Procedure (may be adopted with modifications for Ta and W)

This procedure may be used for Nb-1%Zr material, and may be adopted for Ta, assuming that a small amount of metal loss is tolerable. For tungsten alloys aqua regia should be used as a substitute for the Hf/HNO<sub>3</sub>, as the rate of attack on the base metal is much slower. This procedure can be applied to screen and wire cloth (as would be employed in heat pipe wicks), tubing, plate, and other forms of material that, although machined in part, contain surfaces in the as-milled condition.

1. Wash part in Freon TF in an ultrasonic cleaner for at least 5 minutes to remove all signs of grease.
2. Rapidly dunk part (initially for 5 seconds) in cleaning solution consisting of two parts (by volume) HNO<sub>3</sub>, two parts deionized water, and one part hydrofluoric acid (HF). Part should be immersed long enough to thoroughly remove scale, but not long enough to remove measurable amounts of material from the part.
3. Flush part in hot de-ionized water.
4. Rinse part in hot de-ionized water in ultrasonic cleaner for at least 5 minutes.
5. Rinse part in ethanol in ultrasonic cleaner for at least 5 minutes.
6. Proceed to vacuum baeout; establish a pressure of  $10^{-8}$  torr and a temperature  $50\text{ }^{\circ}\text{C}$  over the maximum operating temperature, baeout for a minimum of 3 hours.

### **Tantalum Cleaning Procedure (the Triple Threat)**

Alternately, the following procedure may be used for tantalum, assuming that a small amount of metal loss is tolerable. This procedure can be applied to screen and wire cloth (as would be employed in heat pipe wicks), tubing, plate, and other forms of material that, although machined in part, contain surfaces in the as-milled condition.

1. Wash part in Freon TF in an ultrasonic cleaner for at least 5 minutes to remove all signs of grease.
2. Rapidly dunk part (initially for 5 seconds) in cleaning solution consisting of two parts (by volume) sulfuric acid, one part nitric acid, and one part hydrofluoric acid (HF). Part should be immersed long enough to thoroughly clean, but not long enough to remove measurable amounts of material from the part.
3. Flush part in hot de-ionized water.
4. Rinse part in hot de-ionized water in ultrasonic cleaner for at least 5 minutes.
5. Rinse part in ethanol in ultrasonic cleaner for at least 5 minutes.
6. Proceed to vacuum baeout; establish a pressure of 10<sup>-8</sup> torr and a temperature 50 °C over the maximum operating temperature, baeout for a minimum of 3 hours.

### **Mo-Re Alloy Cleaning Procedure**

This procedure may be used for molybdenum and rhenium alloys. It can be applied to screen and wire cloth (as would be employed in heat pipe wicks), tubing, plate, and other forms of material that, although machined in part, contain surfaces in the as-milled condition.

1. Wash piece in PF solvent until all signs of grease have been removed.
2. Soak piece for 1 to 2 minutes in 1 part by volume HCl and 1 part by volume de-ionized water to remove residual iron surface impurities.
3. Soak piece for 5 minutes in caustic cleaning solution consisting of 11 parts by volume de-ionized water, 1 part by volume NaOH, and 1 part by volume H<sub>2</sub>O<sub>2</sub>. Remove piece from caustic bath. Replenish or replace solution as required.
4. Wash part in hot de-ionized water for at least 5 minutes.
5. Repeat step 3 and 4 three times.
6. Rinse piece for 5 minutes in ethanol inside an ultrasonic cleaner.
7. Vacuum-fire at 200 to 400 °C for 12 to 24 hours at a vacuum level of 10<sup>-6</sup> torr or lower.

An additional pickling procedure can be used to chemically remove surface oxides (scales) and other surface contaminants by immersion in an aqueous acid solution.

### **Mo-Re Alloy Pickling Procedure**

1. Submerge in mixture of acetic, nitric and HF in a ratio of 10:4:1.
2. Immerse in pure HCl to remove staining.
3. Rinse with de-ionized water.
4. Rinse with alcohol.
5. Following pickling, handle components with clean gloves.

### **Alumina**

A detailed cleaning procedure for alumina is currently being investigated; this procedure is likely to include the following steps:

1. Abrasive blasting using glass bead or alumina grit (alumina grit would produce higher erosion).
2. Cleaning in acetone, possibly in an ultrasonic cleaner.
3. Dry in a furnace (in air) up to 1000 °C.

## APPENDIX N—PURIFIED INERT GAS CONDITIONING

*The following discussion was adapted from the purified inert gas conditioning system that will be adopted for heat pipe life testing, as discussed in Report ER11-05-WI2-003, Section 5 (Martin, et al., 2005). Because similar materials and fill gases may be applied in the initial heater assembly check out tests, the analysis is applicable to the present discussion.*

The ambient oxygen concentration is critical to the lifetime of refractory metals operated at increased temperature for a relatively long time. For the proposed testing, refractory metal components will be operated in either a vacuum environment or in a low-pressure, ultra high purity (UHP) noble gas environment (argon and helium mixed to a predetermined partial pressure of each gas). To achieve the desired gas purity, successive dilutions and pump down of the system are required. The pump down procedure will also include an initial bakeout of the system at ~525 K to drive off water vapor (and other volatiles) from the gas lines, vacuum chamber and test components. A generally accepted vacuum level for testing Mo-Re alloys is in the  $10^{-6}$  torr range; given a direct pump down from air to  $10^{-6}$  torr, the oxygen concentration is 0.28 ppb in the vacuum test environment. Hence, the target maximum oxygen concentration in the test chambers will be 0.28 ppb at the desired operating pressure of approximately 76 torr (the set pressure used in calculating gas conditioning requirements).

### Sizing and Performance

As discussed in Report ER11-04-WI2-1.1 (Martin, 2004), a series of calculations was performed to assess the oxygen concentration in the heat pipe test chambers over successive dilutions with UHP fill gas, assuming an initial oxygen concentration of 209,500 ppm in the air filling the test chambers (20.95% oxygen by volume). Calculations were performed assuming three cylindrical test chambers having approximate dimensions of 24" diameter (23.625" ID) by 36" length (total volume 48000 in<sup>3</sup> (0.78 m<sup>3</sup>) for all three chambers), which will be constructed for use in heat pipe life tests. All heat pipe life testing will be performed with a low pressure fill of mixed helium and argon in the test chambers. The UHP He and Ar, purchased from Sexton Supply (Huntsville, AL), have a guaranteed minimum purity of 99.999%. The UHP He has a maximum oxygen content of 3 ppm (by volume); UHP Ar has a maximum oxygen content of 1 ppm (by volume).

To obtain the oxygen concentrations shown in figure 93, the test chambers are first pumped from atmospheric pressure to  $10^{-3}$  torr (e.g. operating only the roughing pump connected to the test chambers). Note that the plots correspond to a 76-torr chamber pressure, the approximate pressure at which the heat pipe life tests will be performed. Initially pumping the chamber to a pressure below the desired operating pressure results in a drastic reduction in the oxygen concentration from 209,500 ppm to 0.3 ppm at  $10^{-3}$  torr; direct pump down to only 76 torr reduced the oxygen concentration to  $\sim 2 \times 10^4$  ppm, as shown in figure 89 prior to fill with ultra high purity gas at 76 torr. After this initial pump down, the chambers were back-filled to 76 torr of UHP He or Ar

and again pumped down to  $10^{-3}$  torr to further reduce the oxygen concentration in the test chambers. After just two dilutions with UHP gas (He or Ar), the test chambers reach the minimum purity level achievable given the purity of the supply gas. While these calculations ignore any additional contamination from impurities in the lines and test chamber, they do provide an ultimate baseline for the minimum achievable oxygen concentration for a given fill gas and operating pressure without additional gas purification. The test procedure will also include an initial bakeout of the system (under vacuum), which will assist in driving out volatile impurities (primarily water if the system is thoroughly cleaned and degreased) from the test components and fill lines to reduce additional impurities in the system.

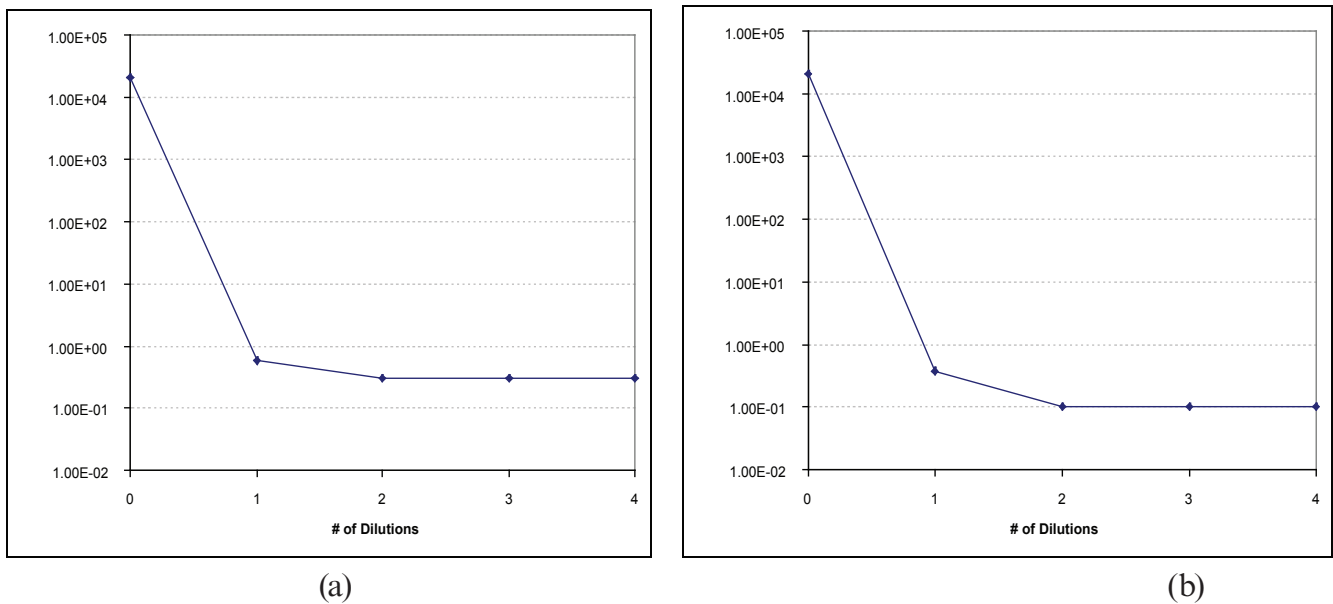


Figure 98. Oxygen concentration (ppm by volume) in the heat pipe test chambers following successive dilutions with (a) UHP He or (b) UHP Ar fill gas.

A smaller test chamber will be utilized for heater assembly testing (approximate diameter of 24", length of 72", yielding a total volume of 5400 in<sup>3</sup> (0.09 m<sup>3</sup>). Because the same supply gases will be used in this chamber, the ultimate minimum purity level of the fill gas will be limited to the same levels shown in figure 93 (0.3 ppm O<sub>2</sub> for He, 0.1 ppm O<sub>2</sub> for Ar) without additional gas purification.

As discussed in Report ER11-04-WI2-001.1 (*Design of a Refractory Metal Life Test Heat Pipe and Calorimeter*, Section 4.2.1), the gas mixture used in the heat pipe tests will be selected to achieve the desired gas conductivity across the gap between the heat pipe condenser and the calorimeter. A similar approach will be adopted in the heater assembly tests. In this case the gas mixture will be selected to achieve the desired conductivity between the heater assembly and the representative core surface (fuel clad or core block), and between this surface and the calorimeter that will be designed to remove heat from the heater assembly in the absence of the full reactor test article (which would include active cooling). The gas mixture selected for the lower power (1 – 4 kW) heat pipe tests was He-32%Ar (molar fraction). The increased heat flux for the 5 kW heat pipe test and the minimum gap width established for fabrication purposes (0.020") requires



that the Ar content in the gas mixture be reduced to 6% (molar fraction) for this test. The partial pressure of each gas in the mixture is given by the molar fraction multiplied by the total gas pressure. For instance, for a total pressure of 100 psig and a 32% Ar mix, the partial pressure of argon will be 32 psig and the partial pressure of helium will be 68 psig. Partial pressures will be used to establish the proper gas ratios in the helium/argon mixing procedure.

## **Gas Purification**

Additional purification of the UHP gases will be required to meet the required oxygen concentration for long term testing of refractory metals, established at less than 0.28 ppb (comparable to  $10^{-6}$  torr) for testing Mo-Re alloys. To accomplish this purification a SAES ambient temperature MicroTorr gas purifier, which has an advertised performance for purifying both helium and argon to a final oxygen concentration of 1 ppb, can be used to clean the incoming gases prior to entry into the test chamber. A recirculating gas system, which would include additional purification using a SAES MonoTorr point-of-use purifier, will not be considered at this time. Additional information on gas purification systems can be found in Report ER11-04-WI2-003.

The design of the gas mixture and purification system is such that the recirculating gas system can be fully isolated from the gas mixing/fill system using the hand valve G-HOV9, allowing the gas mixture bottle to be charged with an appropriate helium/argon mixture prior to test chamber fill. The small test chamber fill system will be connected to the main fill system just after the MicroTorr Purifier (G-HOV5 opens the fill line to this chamber), such that the same He and Ar supply bottles and initial purification system may be used for both systems. The pre-mixed fill gas can be mixed to the desired partial pressures of helium and argon to meet both test requirements using separate gas mixture bottles and recirculating gas systems.

## **References for Appendix O:**

Martin, J.J., Reid, R.S., and Bragg-Sitton, S.M. (2004), *Design of Refractory Metal Life Test Heat Pipe and Calorimeter*, ER11-04-WI2-001.1, December 16, 2004.

Martin, J. J., Bragg-Sitton, S.M., Reid, R.S., Stewart, E. and Davis, J. (2005), *Design of Refractory Metal Heat Pipe Life Test Environment Chamber, Cooling System, and Radio Frequency Heating System*, NASA MSFC Report submitted to NRPCT, Report Number ER11-05-WI2-003, February 22, 2005.

**APPENDIX O—ADVANCED HEATER ELEMENT DESIGNS:  
CHANGING POWER PROFILE**

Figures 99–101 are conceptual designs with varying power profiles.

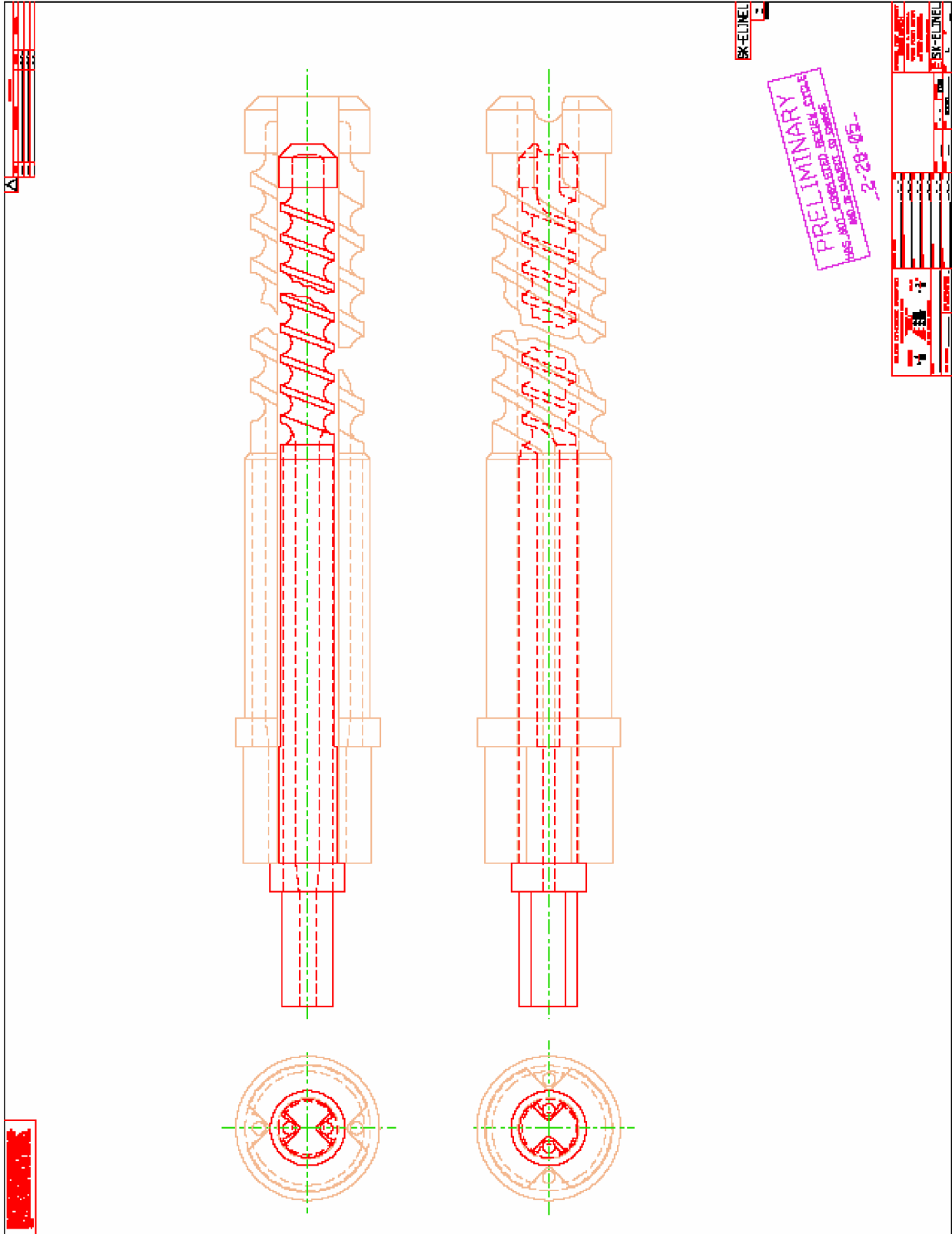


Figure 99. Conceptual design, varying power profile.

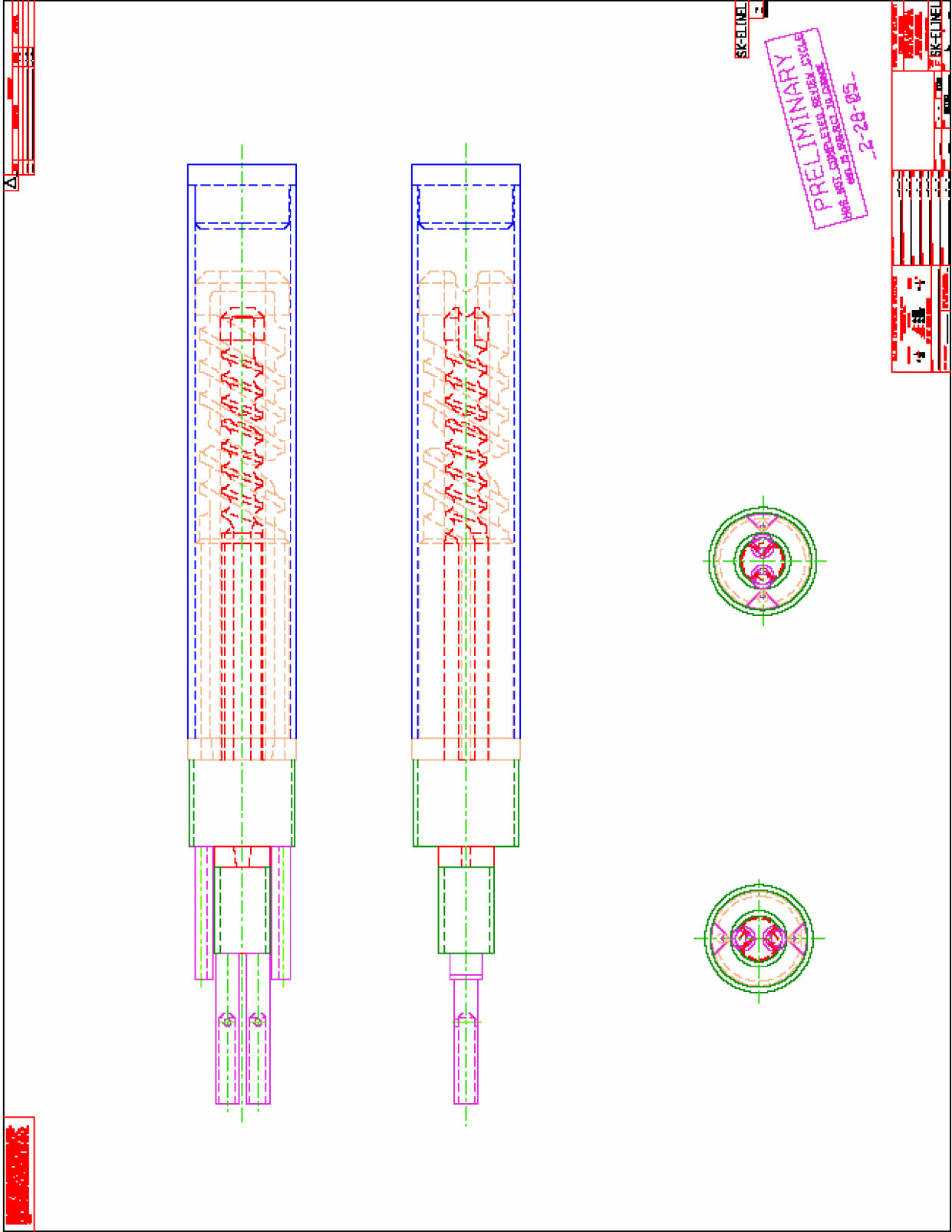


Figure 100. Conceptual design, varying power profile.

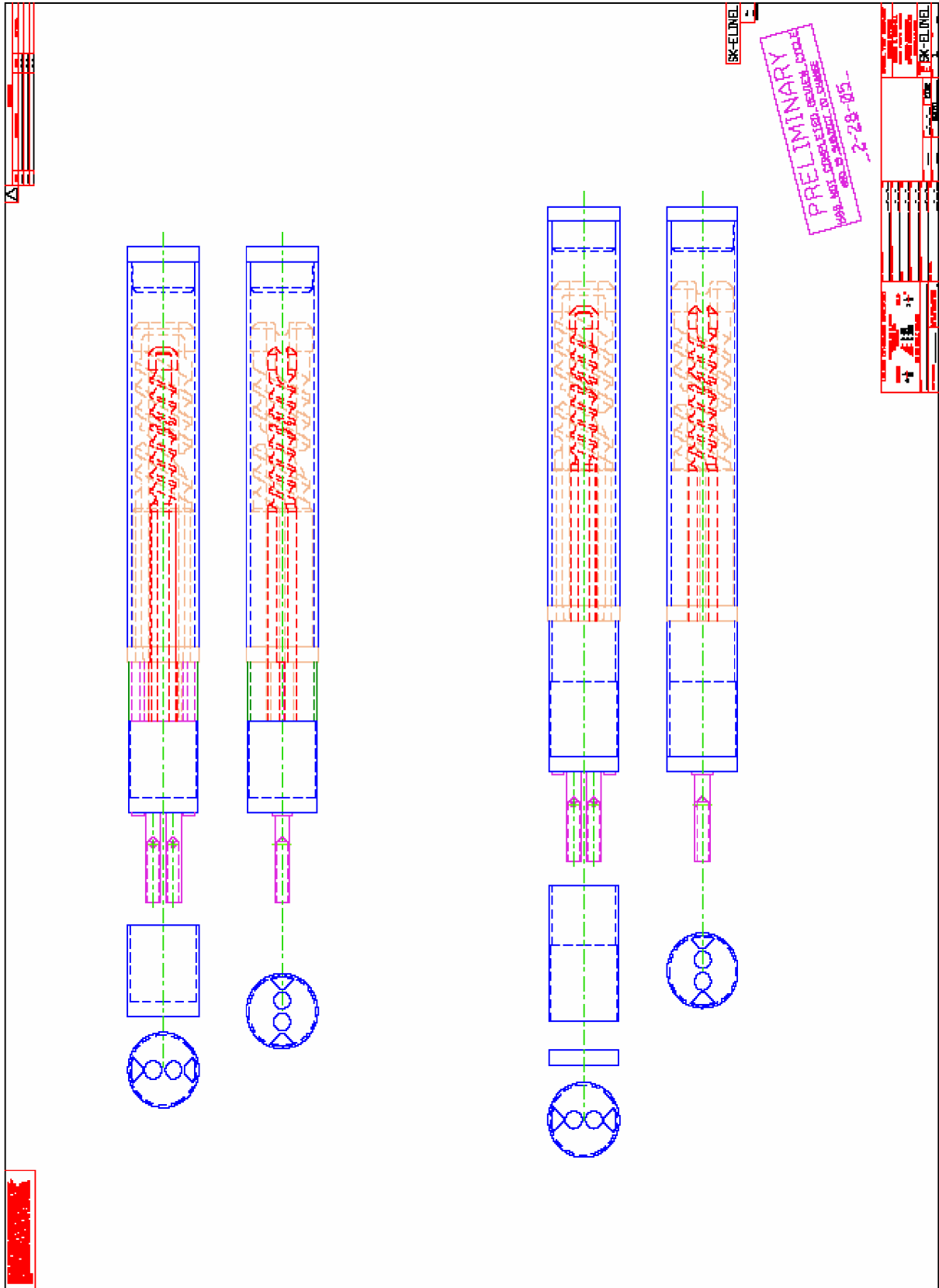


Figure 101. Conceptual design, varying power profile.

**APPENDIX P—ADVANCED HEATER ELEMENT DESIGNS:  
HEXAGONAL CROSS SECTION**

Figure 102 is a conceptual design for the hexagonal cross section.



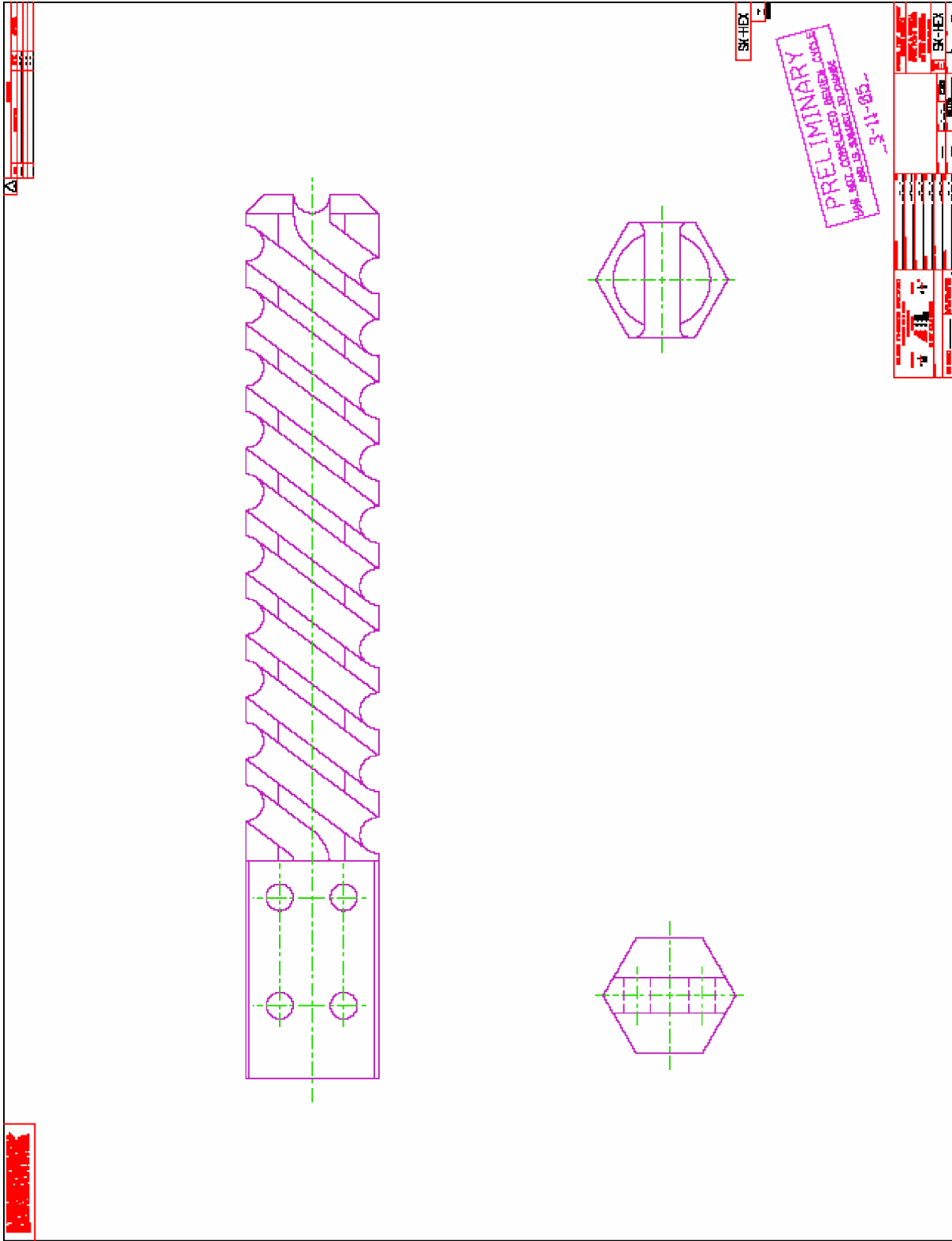


Figure 102. Conceptual design for hexagonal cross section, spiral-wound mandrel heater element.

## REFERENCES

1. VanDyke, M.K.; Houts, M.G.; Pederson, K.; et al.: "Phase I Space Fission Propulsion System Testing and Development Process," *Space Technology and Applications International Forum*, American Institute of Physics, Albuquerque, NM, Vol. 552, pp. 837–842, 2001.
2. VanDyke, M.K.; Houts, M.G.; Godfroy, T.J.; et al.: "Phase I Space Fission Propulsion System Testing and Development Progress," *Space Technologies and Applications International Forum*, American Institute of Physics, Albuquerque, NM, Vol. 608, pp. 692–697, 2002.
3. VanDyke, M.K.; Houts, M.G.; Godfroy, T.J.; et al.: "Test Facilities in Support of High Power Electric Propulsion Systems," *Space Technology and Applications International Forum*, American Institute of Physics, Albuquerque, NM, Vol. 654, pp. 451–456, 2003.
4. VanDyke, M.K.; Martin, J.J.; and Houts, M.G.: "Overview of Nonnuclear Testing of the Safe, Affordable 30-kW Fission Engine Including End-to-End Demonstrator Testing," *NASA/TM—2003–212930*, Marshall Space Flight Center, AL, November 2003.
5. VanDyke, M.K.: "Early Flight Fission Test Facilities (EFF-TF) To Support Near-Term Space Fission Systems," *Space Technology and Applications International Forum*, American Institute of Physics, Albuquerque, NM, Vol. 699, pp. 713–719, 2004.
6. VanDuyn, L.B.; Poston, D. I.; and Reid, R.S.: "Analysis of the SAFE-30 Resistance-Heated Test Data," *Space Technologies and Applications International Forum*, American Institute of Physics, Albuquerque, NM, Vol. 608, pp. 698–710, 2002.
7. Godfroy, T.J.; Bragg-Sitton, S.M.; and VanDyke, M.K.: "Thermally Simulated Testing of a Direct-Drive Gas-Cooled Nuclear Reactor," *International Congress on Advances in Nuclear Power Plants (ICAPP-2003)*, Cordoba, Spain, Paper 3343, 2003.
8. Bragg-Sitton, S.M.; and Forsbacka, M.: "Application of a Virtual Reactivity Feedback Control Loop in Non-Nuclear Testing of a Fast Spectrum Reactor," *International Congress on Advanced Nuclear Power Plants (ICAPP-2004)*, American Nuclear Society, Pittsburgh, PA, pp. 2259–2268, 2004.
9. ESPI Corporation, <[www.espimetals.com](http://www.espimetals.com)>, March, 2005.
10. Incropera, F.P.; and DeWitt, D.P.: *Fundamentals of Heat and Mass Transfer*, 3rd Ed., 981 pp., John Wiley & Sons, New York, NY, 1990.
11. Arp, V.; McCarty, B.; and Fox, J.: "GASPAK®," Ver.3.401, Cryodata, Inc., October 16, 2002.

12. Manglik, R. (ed.): *Fluid Flow Data Book*, Genium Publishing Corp., Schenectady, NY, Section 410.2, pp.1–6, 1982.
13. Jain, P.C.: “The Prediction of Thermal Conductivity of Xenon,” *Journal of Physics D: Applied Physics*, Vol. 11(17), printed in Great Britain, The Institute of Physics, 1978.
14. “Thermal Design Data Book for Coupled Growth in Hypermonotectics and Particle Engulfment and Pushing by Solidifying Interfaces Sample Ampoule Cartridge Assembly,” Teledyne Brown Engineering Inc., Report #480MMSC0071, Huntsville, AL, June 2003.
15. Ott, L.J.; and McCulloch, R.: “Overview of Fuel Rod Simulator Usage at ORNL,” in *Proceedings of Space Technology and Applications International Forum (STAIF-2004)*, American Institute of Physics, Albuquerque, NM, Vol. 699, pp. 703–712, 2004.
16. Ott, L.J.; and McCulloch, R.: “Electric Fuel Rod Simulator Fabrication at ORNL,” in *Proceedings of Space Technology and Applications International Forum (STAIF-2004)*, American Institute of Physics, Albuquerque, NM, Vol. 699, pp. 720–727, 2004.
17. Stinson-Bagby, K.L.; and Fielder, R.S.: “Fiber Bragg Gratings for High-Temperature Thermal Characterization,” *International Congress on Advances in Nuclear Power Plants (ICAPP-2004)*, Pittsburgh, PA, Paper 4299, pp. 2288–2294, 2004.
18. Fielder, R.S.; Klemer, D.; and Stinson-Bagby, K.L.: “High-Temperature Fiber Optic Sensors, an Enabling Technology for Nuclear Reactor Applications,” *International Congress on Advances in Nuclear Power Plants (ICAPP-2004)*, Pittsburgh, PA, Paper 4298, pp. 2295–2305, 2004.
19. Bragg-Sitton, S.M.; and Webster, K.: “Application of Simulated Reactivity Feedback in Nonnuclear Testing of a Direct-Drive Gas-Cooled Reactor,” *NASA/TM-2007-21495*, Marshall Space Flight Center, AL, 2007.
20. Siegel, J.R.; and Howell, R.: *Thermal Radiation Heat Transfer*, 4th Ed., 1072 pp., Taylor and Francis, New York, NY, 2002.

REPORT DOCUMENTATION PAGE			Form Approved OMB No. 0704-0188	
Public reporting burden for this collection of information is estimated to average 1 hour per response, including the time for reviewing instructions, searching existing data sources, gathering and maintaining the data needed, and completing and reviewing the collection of information. Send comments regarding this burden estimate or any other aspect of this collection of information, including suggestions for reducing this burden, to Washington Headquarters Services, Directorate for Information Operation and Reports, 1215 Jefferson Davis Highway, Suite 1204, Arlington, VA 22202-4302, and to the Office of Management and Budget, Paperwork Reduction Project (0704-0188), Washington, DC 20503				
1. AGENCY USE ONLY (Leave Blank)	2. REPORT DATE July 2008	3. REPORT TYPE AND DATES COVERED Technical Memorandum		
4. TITLE AND SUBTITLE Heater Development, Fabrication, and Testing: Analysis of Fabricated Heaters			5. FUNDING NUMBERS	
6. AUTHORS S.M. Bragg-Sitton, R.E. Dickens, J.T. Farmer, J.D. Davis, M.R. Adams, J.J. Martin, and K.L. Webster				
7. PERFORMING ORGANIZATION NAME(S) AND ADDRESS(ES) George C. Marshall Space Flight Center Marshall Space Flight Center, AL 35812			8. PERFORMING ORGANIZATION REPORT NUMBER M-1235	
9. SPONSORING/MONITORING AGENCY NAME(S) AND ADDRESS(ES) National Aeronautics and Space Administration Washington, DC 20546-0001			10. SPONSORING/MONITORING AGENCY REPORT NUMBER NASA/TM-2008-215466	
11. SUPPLEMENTARY NOTES Prepared by the Propulsion Systems Department, Engineering Directorate				
12a. DISTRIBUTION/AVAILABILITY STATEMENT Unclassified-Unlimited Subject Category 18 Availability: NASA CASI 301-621-0390			12b. DISTRIBUTION CODE	
13. ABSTRACT (Maximum 200 words) Thermal simulators (highly designed heater elements) developed at the Early Flight Fission Test Facility (EFF-TF) are used to simulate the heat from nuclear fission in a variety of reactor concepts. When inserted into the reactor geometry, the purpose of the thermal simulators is to deliver thermal power to the test article in the same fashion as if nuclear fuel were present. Considerable effort has been expended to mimic heat from fission as closely as possible. To accurately represent the fuel, the simulators should be capable of matching the overall properties of the nuclear fuel rather than simply matching the fuel temperatures. This includes matching thermal stresses in the pin, pin conductivities, total core power, and core power profile (axial and radial). This Technical Memorandum discusses the historical development of the thermal simulators used in nonnuclear testing at the EFF-TF and provides a basis for the development of the current series of thermal simulators. The status of current heater fabrication and testing is assessed, providing data and analyses for both successes and failures experienced in the heater development and testing program.				
14. SUBJECT TERMS fission power systems, nonnuclear testing, thermal simulators, space power, early flight fission test facility, heater elements for nuclear simulation			15. NUMBER OF PAGES 224	
			16. PRICE CODE	
17. SECURITY CLASSIFICATION OF REPORT Unclassified	18. SECURITY CLASSIFICATION OF THIS PAGE Unclassified	19. SECURITY CLASSIFICATION OF ABSTRACT Unclassified	20. LIMITATION OF ABSTRACT Unlimited	



National Aeronautics and

Space Administration

IS20

**George C. Marshall Space Flight Center**

Marshall Space Flight Center, Alabama

35812